Structure and neutron decay of the unbound Beryllium isotopes 15,16Be

Belen Monteagudo Godoy

Normandie Université

THÈSE

Pour obtenir le diplôme de doctorat

Spécialité PHYSIQUE

Préparée au sein de l'Université de Caen Normandie

Structure and neutron decay of the unbound Beryllium isotopes 15,16Be

Présentée et soutenue par
Belen MONTEAGUDO GODOY

Thèse soutenue publiquement le 08/11/2019 devant le jury composé de		
M. DIDIER BEAUMEL	Directeur de recherche au CNRS, Institut de Physique Nucléaire d'Orsay	Rapporteur du jury
M. BERTRAM BLANK	Directeur de recherche au CNRS, Université Bordeaux 1 Sciences et Techno	Rapporteur du jury
Mme MARIA JOSE GARCIA BORGE	Professeur, Instituto de Estructura de la Materia	Membre du jury
M. ETIENNE LIENARD	Professeur des universités, Université Caen Normandie	Président du jury

Thèse dirigée par F. MIGUEL MARQUES MORENO, Laboratoire de physique corpusculaire (Caen)

UNIVERSITÉ CAEN NORMANDIE

ED 591 PSIME

lpc caen
Laboratoire de physique corpusculaire

Remerciements

D'abord un grand merci aux membres du Jury: Bertram Blank, Didier Beaumel, María José García Borge et Etienne Liénard pour avoir pris le temps de lire attentivement et corriger ce manuscrit. Le travail présenté dans cette thèse n'aurait pas été possible sans bien sûr mes deux directeurs de thèse Miguel Marqués et Julien Gibelin (même si ce n'est pas officiel). Merci pour le soutien et toutes les connaissances que vous m'avez transmises. De la même façon, j'aimerais remercier le groupe "exotic", dirigé par Nigel Orr pour m'avoir integrée si bien dans l'équipe. Merci spécialement à Anna Corsi, pour m'avoir cédé des données si interessantes et m'avoir aidé lors des analyses, et à Jesus Casal, avec qui j'ai pu comprendre un peu plus ce que j'observais.

Merci également aux personnes avec qui j'ai pu partager des bons moments. Aux gens du LPC pour mettre la bonne ambiance au travail, et surtout, aux thésards et postdocs du LPC et GANIL que j'ai rencontrés au cours de ces trois années. Ceux qui sont déjà partis: Yiyan, Daniel et Debi, qui m'ont accueillie et appris le français, le trio brésilien Guilherme, Kendi et Bira, Sophia, Benoit, Aldric. Mais aussi à ceux qui restent: Sylvain, Thomas, Joel, Pierrick, Yoann (meilleur informaticien du monde!), Jianqi, Armel, Blaise et à mes collègues d'escalade Edgar et Cyril. Je souhaite bon courage à ceux qui sont en troisième année et ceux qui viennent de commencer: Chloé, Alex, William et Savitri.

Por supuesto, me gustaría agradecer a mi familia cuyo apoyo, aunque lejos, siempre está presente dondequiera que yo vaya. Finalmente agradecer a Simon, una persona maravillosa.

Contents

List of Figures

List of Tables

Chapter 1

Introduction

Contents

After more than 100 years of research and despite the joint efforts of experimental and theoretical studies, a complete picture of nuclear structure and its dependence on the number of protons and neutrons is still an unsolved question in nuclear physics. Given the complexity of describing the N-body interactions in nuclear systems, even for systems of very few nucleons, many phenomena still lack a firm theoretical support. Yet an enormous progress has been achieved over the past years with the development of new experimental techniques and the improvement of theoretical methods.

This thesis work is focused on very neutron-rich nuclei which lie at the limits of binding and beyond, in the light-mass region of the nuclear chart. In particular, we will present a study on the spectroscopy and two-neutron decay of the unbound isotope ^{16}Be. The nn correlations of the decay have been extensively probed and interpreted from a microscopical point of view. In order to complete the picture and give a better insight on the evolution of nuclear properties towards ^{16}Be, the two previous isotopes of the isotopic chain, the unbound ^{15}Be and the last bound beryllium isotope ^{14}Be, are also investigated.

This work is divided into 6 chapters. The current chapter presents the context and the motivations of this thesis. Following the introductory chapter, the experimental setup

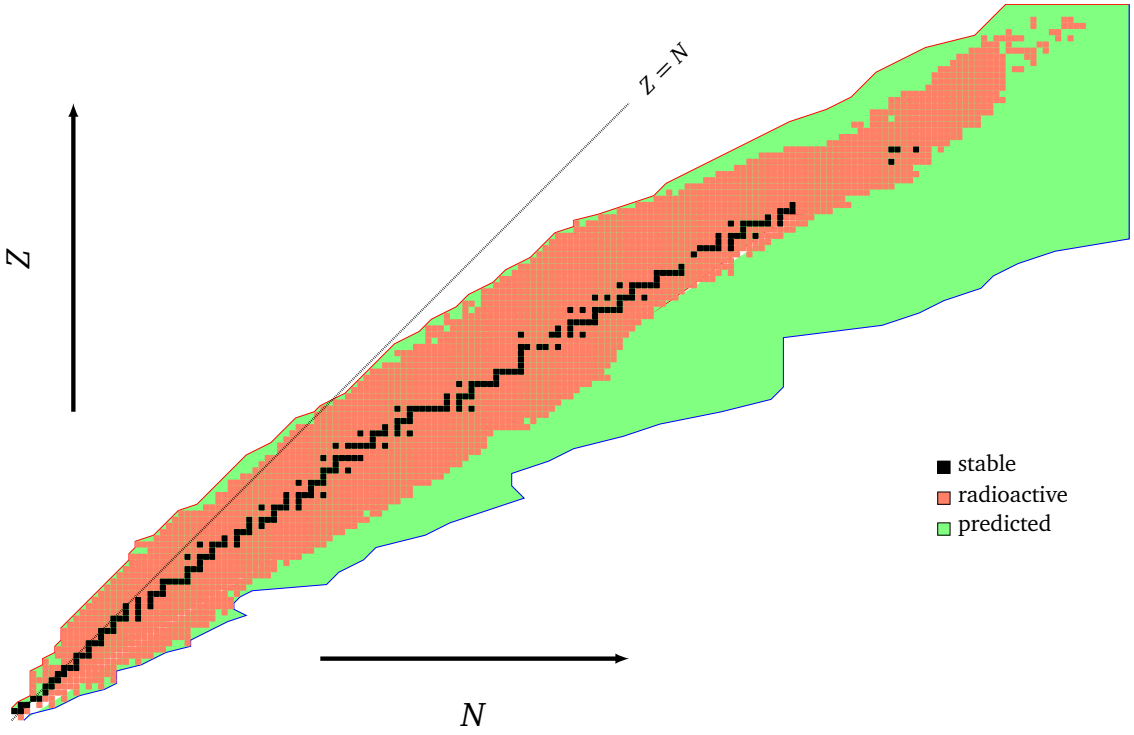

Figure 1.1: *Nuclear chart representing the existing nuclei with respect to the proton Z (vertical axis) and neutron N (horizontal axis) numbers. Black squares represent stable nuclei, orange bound unstable nuclei in both neutron-rich and neutron-deficient sides, and in green predicted nuclei [1] which have not been observed yet. The predicted limits of proton and neutron particle stability, the driplines, are shown with red and blue solid lines, respectively.*

employed to populate the nuclei of interest is presented. The techniques related to the analysis of the experimental data as well as the simulations performed are described in the third chapter. The next chapter describes the results on the spectroscopy of ^{14,15,16}Be. The analysis of the *nn* correlations for the states decaying by two-neutron emission is detailed in chapter 6. Finally, the conclusions and perspectives are summarized in the last chapter.

1.1 Nuclear properties at the extremes

1.1.1 The limits of nuclear binding

The stability of a nucleus depends on its number of protons Z and neutrons N. In the light-mass region, stable nuclei show a ratio $N/Z \sim 1$, which corresponds to the same number of neutrons and protons. As we go towards heavier systems composed of a bigger number of protons, an excess of neutrons is needed in order to compensate the increasing electrical repulsion between protons. Heavy nuclei find therefore the stability with larger N/Z ratios. The excess or deficiency of neutrons beyond that optimal ratio leads to bound systems that are unstable with respect to β decay. One of the basic questions in nuclear structure is where the limits of the nuclear existence are situated, *i.e.*, the boundaries of the nuclear chart where no more protons or neutrons can be bound to the nucleus. These

frontiers are commonly known as the *nuclear driplines*, namely the proton and neutron driplines, for the neutron-deficient and neutron-rich side respectively.

With the improvement of the experimental techniques and the development of radioactive ion beams (RIBs), it has been possible to reach isotopes very far from stability. In particular, the impact of RIBs, which allow us to probe reactions involving very unstable isotopes, has been prominent in nuclear structure providing very detailed information, not only about unstable nuclei, but also about stable ones. Nowadays more than 3000 nuclei are known to exist, 254 of which are stable, and yet a similar amount are predicted and remain unobserved, specially on the neutron-rich side. As we move towards the neutron dripline, to more extreme ratios $N/Z \gg 1$, isotopes become very unstable and thus very short-lived, with lifetimes that can be as low as several milliseconds at the dripline. This makes them very difficult to produce and study experimentally.

Figure 1.1 illustrates the predicted isotopes (green) in relation to the already observed ones (orange, black). As a consequence of the Coulomb interaction between protons, there exists more neutron-rich than proton-rich isotopes. Due to the limitations associated with the production of beams, the neutron dripline is indeed very difficult to reach experimentally for heavy isotopes than it is on the neutron-deficient side. Accordingly, the neutron dripline is very much unexplored and has only been reached for very light nuclei, with a small number of protons $Z \lesssim 10$. A fact that can be clearly appreciated in Fig. 1.1, where the green color dominates in the neutron-rich region, being the last observed isotope very far from the predicted limits of particle stability for most of the heavier elements.

1.1.2 Neutron-rich nuclei

Neutron-rich nuclei have been a main research field in nuclear physics for many years as they provide a powerful insight on nuclear structure and its evolution. However, as mentioned above, the investigation of the nuclear evolution at and beyond the neutron dripline is, so far, only possible in the light part of the nuclide chart. In this work, we will push these studies further by probing the structure of Beryllium isotopes up to $2n$ beyond the dripline.

Over the years, anomalous phenomena have been discovered in a number of neutron-rich nuclei, and some have been found to be relatively common in nuclei very far from stability. The ordinary properties of stable nuclei, which had been studied for decades, were found not to be universally applicable. Instead, other "exotic" phenomena appear in unstable nuclei, which include larger and longer tails in the density distribution, the so-called *halo nuclei*, cluster structures, emergence of new magic numbers, or unusual decay patterns, among others, which are a consequence of the evolution of the nuclear structure with the number of nucleons.

Figure 1.2 schematically shows the evolution of the single-particle neutron and proton configurations with the number of neutrons N. For stable nuclei, both proton and neutron potentials are approximately similar. The only difference comes from the Coulomb interaction which makes the proton potential slightly shallower. As we go far from stability on the neutron-rich side, proton and neutron configurations may be decoupled. A bigger number of neutrons implies a deeper proton potential as a consequence of the n-p attractive interaction, which makes more difficult to remove one proton from the nucleus.

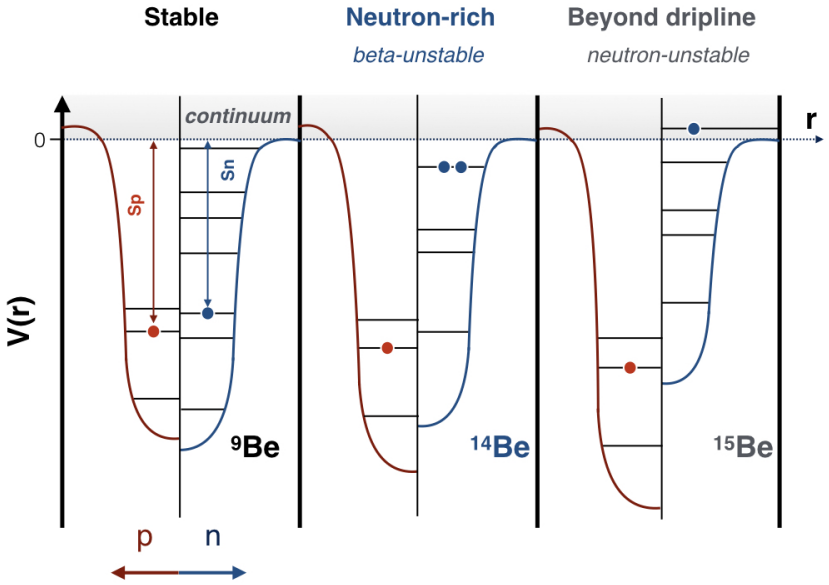

Figure 1.2: *Schematic view of the evolution of proton and neutron single-particle configurations for the Beryllium chain. For the only stable isotope of the chain, ^{9}Be, the neutron and proton separation energies are very similar. The increase of the number of neutrons makes the proton potential become deeper while the neutron potential becomes shallower. For ^{14}Be, the valence neutron level lies very close to the continuum and there is a significant difference in the proton and neutron separation energies. For ^{15}Be, the highest occupied level for neutrons is already in the continuum.*

On the contrary, the separation energy of one neutron decreases for neutron-rich nuclei, being at the neutron dripline close to zero. As a result, the most neutron-rich isotopes may have bound ground states that are very close to the continuum and very few or even no excited bound states. If we go beyond the neutron dripline, nuclei become unstable with respect to neutron emission. All states from these nuclei, both ground and excited states, are unbound states which exhibit resonances in the continuum.

The decoupling of neutron and proton configurations may give rise to special structures in which the nucleon correlations can overcome the collective effects. Such is the case of the already mentioned halo nuclei, with a structure that can be visualized as a core surrounded by a low density halo of "orbiting" valence neutron(s). The formation of a halo is a threshold effect that appears as a combination of a low separation energy of the valence neutron(s), which makes barely bound states very close to the continuum, and the short-range part of the nuclear force that leads to an "inert" core in which all other nucleons are contained. As a result, the valence neutron(s) can decouple and tunnel out into regions well beyond the potential range created by the core. The radial distribution of these nuclei is very different for protons and neutrons, the later being much larger and presenting longer tails. This results in an overall radius size much bigger than the one predicted by the empirical equation $R \propto A^{1/3}$ that works so well for stable nuclei.

Neutron halos can be formed of one or several neutrons. In particular, two-neutron halo nuclei are of special interest. Their properties arise from their three-body character core$+n+n$: they are a bound system only when the three are together but each of the two-

body subsystems is unbound. Systems with this kind of structure are commonly denoted as *borromean* systems. Many nuclei near the neutron dripline, such as ^{6}He, ^{11}Li or ^{14}Be, exhibit this behavior. The neutron halo is therefore expected to be a general phenomenon, not only in the light-mass region but also possibly in heavier nuclei.

So far, no current nuclear theory can fully explain the ensemble of phenomena occurring in the neutron-rich side, nor the exact position of the dripline itself. In this sense, the single-particle shell model, which is a benchmark for the description of the properties of stable nuclei, can no longer be naively applied for very neutron-rich systems. The magic numbers (2, 8, 20, 28, 50, 82, 126) associated with the closed shells have been shown to change locally for very exotic nuclei. New magic numbers emerge in neutron-rich nuclei since the order of neutron and proton orbitals evolves with the number of neutrons. The exact determination of the neutron dripline is an important test for theoretical formalisms as it can help verify the accuracy of their assumptions by comparing with the experimental data. In addition, the study of the properties of nuclei near and beyond the dripline should reveal valuable information about the shell evolution that leads to phenomena like the ones described above.

1.2 Beyond the driplines

1.2.1 Nucleon emission

Induced emission

New exotic decay modes are also encountered as we move further away from stability. Nuclei for which the number of neutrons or protons is in excess become more weakly bound and, as a consequence, nucleons may more easily "escape" from the nucleus. Nucleon emission from neutron- or proton-rich nuclei has been established as a characteristic phenomenon occurring as we approach the driplines, where the energy needed to remove a proton or neutron becomes low enough or even negative. The emission of nucleons has been extensively observed following a preceding β decay [9, 10, 11]. In the neutron-rich side, the β-delayed neutron emission becomes possible when the Q-value of the β decay is large enough to overcome the neutron separation energy of the daughter nucleus. In this case, the β decay induces the neutron emission by populating excited states which are neutron unbound. This phenomenon, analogously found in proton-rich nuclei, is increasingly important as we approach the driplines since the Q_β values become larger while the particle separation energies decrease.

Spontaneous emission

Near the driplines, as the particle separation energy becomes negative, ground-state nucleon emission becomes a dominant or at least significant decay mechanism. Because of the Coulomb interaction, ground-state proton and neutron emission present different features. The lifetime with respect to nucleon emission depends on the height of the barrier which prevents the valence nucleon(s) from escaping the nucleus as well as the energy of the state with respect to this barrier. In general, proton emitters present measurable long lifetimes, compared to neutron emitters, as the Coulomb barrier reduces the proton penetration probability and constrains the valence proton(s) in the nucleus for longer time.

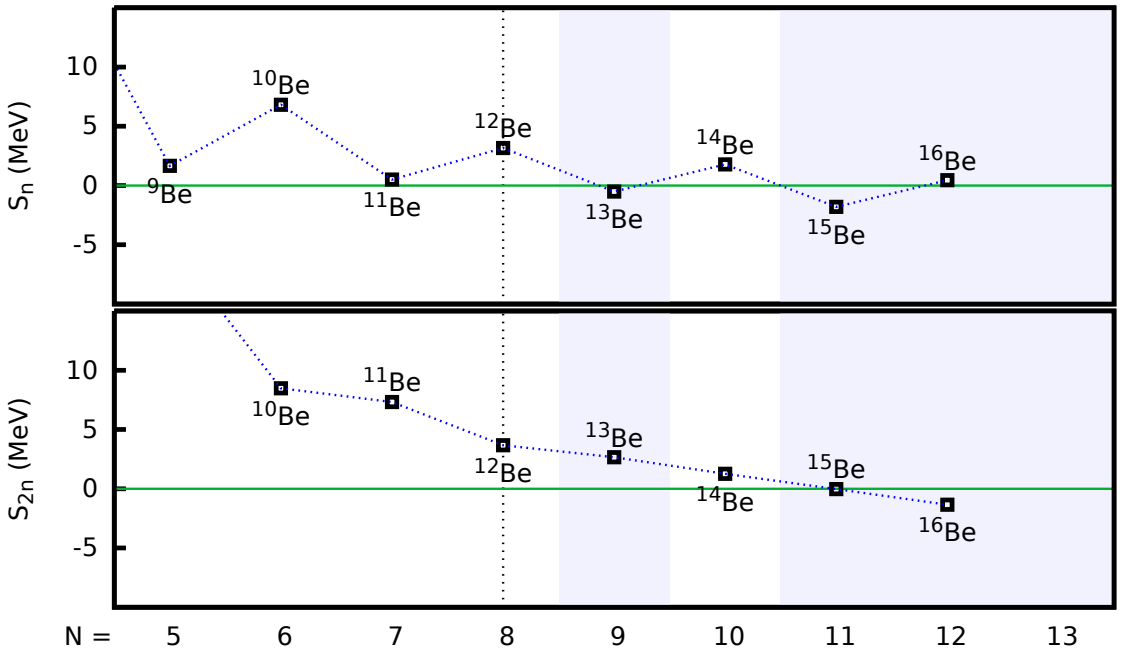

Figure 1.3: *Evolution of the* $1n$ *and* $2n$ *separation energy for the isotopic chain of Beryllium.*

Consequently, proton decays are usually discussed in terms of proton radioactivity[1]. On the contrary, neutron decaying states, which are constrained only by centrifugal barriers, are expected to have shorter lifetimes. While proton radioactivity is slow enough to be in competition with β decay, neutron emission is the dominant decay mechanism for neutron-unstable nuclei.

Ground state two-nucleon emission may occur once we go beyond the driplines as a result of the evolution of the nucleon-nucleon pairing interaction. One of the clearest manifestations of these correlations is exhibited in the odd-even oscillations of the neutron separation energies S_n. Fig. 1.3 shows the S_n evolution along the Beryllium isotopic chain. As for any isotopic chain, this effect is specially remarkable near the driplines, where the oscillations close to zero make even-N nuclei bound and odd-N neighbors unbound with respect to one-neutron emission. Such is the case of ^{13}Be and ^{14}Be in Fig. 1.3, for which the neutron separation energy is negative and positive respectively. On the contrary, the trend of the two-neutron separation energy S_{2n} is to decrease monotonously towards the dripline. Beyond the neutron dripline, the S_n oscillations can give rise to situations in which the S_{2n} reaches negative values while S_n stays positive. This translates into systems which are bound with respect to single-neutron emission and unbound with respect to two-neutron emission, as we can see for ^{16}Be in Fig. 1.3. In these systems beyond the dripline where the one-neutron decay channel is energetically inaccessible, a spontaneous two-neutron decay from the ground state is more likely to happen.

This scenario applies as well to the proton dripline. Indeed, the possibility of promptly emitting two nucleons from the ground state was first predicted for the two-proton ra-

[1]Radioactivity is understood as a process by which an atom loses energy. The time of this process must be superior to the time required for the atom to form, *i.e.*, around 10–100 fs.

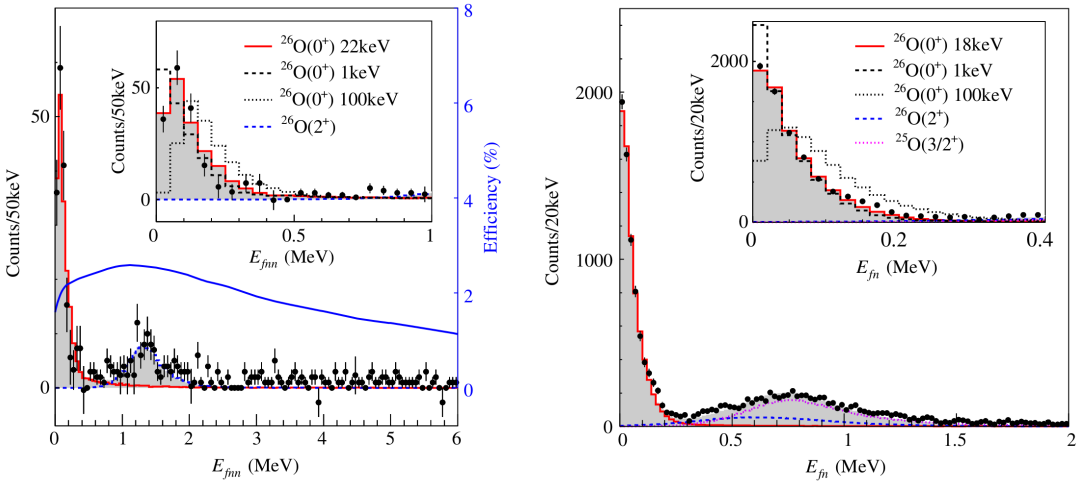

Figure 1.4: *On the left, relative energy spectrum of ^{26}O reconstructed from its decay products $^{24}O+n+n$ from $^{27}F(-1p)$ reactions. The red solid line represents the best fit for the 0^+ ground state at 22 keV. The blue line is the 2n detector efficiency. On the right, decay energy spectrum of $^{24}O+n$ from the same reaction. This spectrum is fitted with three contributions, the decay of ^{26}O through both its 0^+ (red solid line) and 2^+ (blue dashed line) states and the direct population of the ground state $3/2^+$ of ^{25}O at 749 keV (pink dotted line). This fit provides a more accurate value of the ^{26}O ground state, represented by the shadowed histogram, of only 18 keV. Taken from Ref. [2].*

dioactivity by Goldansky in 1960 [12]. It was only in 2002 that this decay was observed for the first time [13]. In analogy to the neutron dripline, all two-proton emitters are even-Z nuclei located beyond the proton dripline such as ^{19}Mg or ^{45}Fe. However, since the neutron dripline is only attainable for light nuclei, very few two-neutron emitters are known. The only two candidates are ^{26}O and ^{16}Be.

The case of ^{26}O is of special interest. With two more neutrons than the last bound Oxygen isotope ^{24}O and the one-neutron channel forbidden by more than 700 keV [2], ^{26}O is a strong candidate for the study of a spontaneous two-neutron emission. In addition, its lifetime has been measured to be 4.5 ps [14] (although with relatively large uncertainties of about ± 4 ps), an unexpected value for neutron-emitters which have only centrifugal barriers. Long-living two-neutron decaying states, however, are reasonably possible according to some theory works, as the position of the energy of the state with respect to the centrifugal barrier plays also an important role. According to [15], ^{26}O would exhibit such a lifetime for a decay energy of < 1 keV. A recent experimental study [2] using a proton knock-out reaction from ^{27}F has found the ^{26}O ground state to be barely unbound with respect to two-neutron emission by 18 ± 5 keV. This energy, although very small, does not attain the low value required by theory to support ps lifetimes. The left panel in Fig. 1.4 shows the $^{24}O+n+n$ relative energy spectrum where a very narrow peak at ~ 0.1 MeV can be observed together with a broader structure at around ~ 1.5 MeV. These two structures correspond to the 0^+ ground state and the 2^+ first excited state of ^{26}O which can be equally seen in the $^{24}O+n$ spectrum (right panel). Moreover, the energy resolution of the experiment was shown to be sufficiently sensitive to changes of few keV at low decay energies (see both insets of Fig. 1.4). Further studies will confirm whether ^{26}O represents the first case of two-neutron radioactivity.

Another important aspect of three-body decays such as the one of ^{26}O is the study of the correlations between the decay particles. Because of the very low energy of the ground state, the *nn* correlations could not be studied in Ref. [2]. At an energy as low as 18 keV, neutron detection is a very important factor as several hits in the detector may come from multiple interactions of a single neutron, a phenomenon known as *cross-talk*. Space-time conditions are applied in order to extract the real number of neutrons interacting in the neutron array. At very low decay energies, the emitted neutrons do not have much energy to share and follow very close trajectories. As a consequence, the very low-energy pairs of ^{26}O ground state were detected in bars that covered the same angular range, and therefore angular correlations in the ground state could not be probed in detail. A new detector array with better spatial resolution is under construction and a new experimental campaign for ^{26}O is already planned. On the other hand, the other two-neutron emitter candidate, ^{16}Be, with a presumably ground state at much higher energy, would be more suitable for the study of the *nn* correlations. This unbound nucleus, which is the main subject of this thesis work, is discussed in detail in section 1.4.1 of this chapter.

1.2.2 Resonant states

As we approach either the proton or neutron dripline, the low-lying excited states are usually no longer bound. Beyond the driplines, even the ground states are above the particle emission threshold. If these states are located not too far from the threshold, they may manifest themselves as resonances in the continuum. In this thesis work, the role of resonances is specially important since we only investigate unbound states with respect to neutron emission, which may present resonant states. A brief description of the formalism used is presented in this section. For further details the reader can refer to [16].

Resonant states are experimentally difficult to observe due to their very short lifetime, *a priori* of the order of $\sim 10^{-22}$ s, which makes impossible the direct measurement of their energy. As the resonance has a finite lifetime τ, its energy has a certain width Γ, both linked by the Heisenberg uncertainty principle as follows,

$$\Gamma \times \tau \ \sim \ \hbar \tag{1.1}$$

If we consider a nucleus unbound to single-neutron emission, a resonant state can appear as a consequence of the interaction between the valence neutron with the bound core formed by the other nucleons. In this case, it is possible to formalize a neutron resonance as a scattering phenomenon. From this perspective, the effective potential "felt" by the neutron will be given by [17],

$$V_{eff}(r) \ = \ V_N(r) + V_\ell(r) \ = \ V_N(r) + \frac{\hbar^2 \ell(\ell+1)}{2\mu r^2} \tag{1.2}$$

where r is the core-neutron distance, μ the reduced mass, V_N the attractive nuclear potential created by the core and V_ℓ the repulsive centrifugal potential. The centrifugal barrier that confines the neutron in the potential depends on the value of the angular momentum of the neutron ℓ. For $\ell = 0$, the centrifugal term V_ℓ is zero and the neutron will not encounter any centrifugal barrier. This situation may give rise to *virtual states*, for which

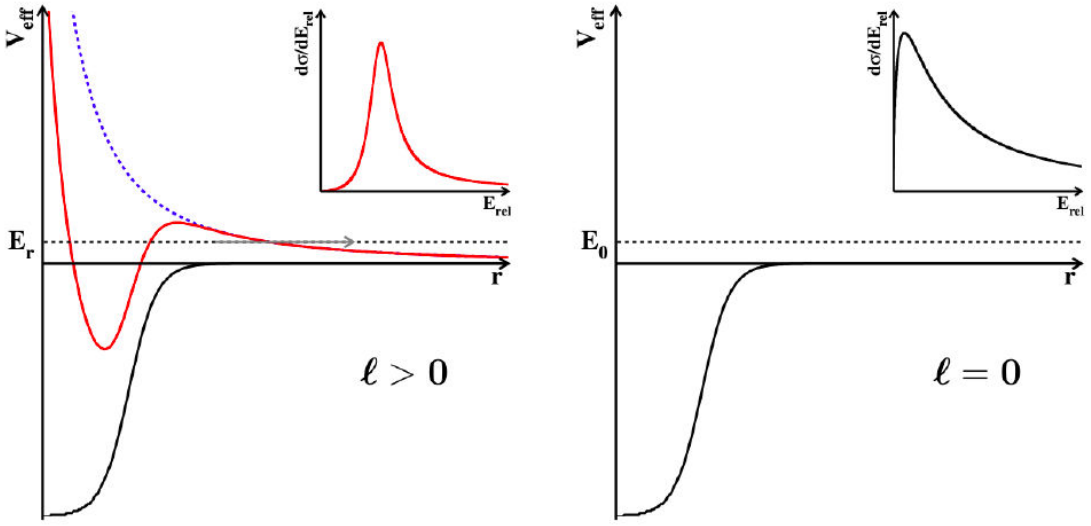

Figure 1.5: *On the left, effective potential felt by a neutron with $\ell > 0$ angular momentum. The blue dashed line represents the centrifugal barrier that confines the neutron inside the nucleus and the black line the attractive nuclear potential of the core. The red line is the effective potential that includes these two contributions. On the right, the centrifugal barrier disappears in the case of a neutron with $\ell = 0$. In this case, the effective potential coincides with V_n, in black line. Both insets represent the corresponding differential cross-section as a function of the relative energy between the neutron and the core. Taken from [3].*

the cross-section increases towards zero energies [18] showing an exponential-like behavior. In such a case, we cannot define a width or an energy, and therefore no lifetime τ. Its cross-section can be described using a single parameter, the scattering length a_s.

On the contrary, values of angular momentum $\ell > 0$ will display a centrifugal barrier, with its penetrability dependent on its height. The larger ℓ is, the higher this barrier and therefore the longer the neutron remains inside the potential. In such cases, the neutron+core system can form resonant states with a lifetime τ that increases (and width decreases) with larger ℓ.

If we describe the resonance from a scattering point of view, we can treat the core as a target, neglecting its structure, and the neutron as the incident particle. Following a partial-wave analysis and applying the corresponding boundary conditions [16], the differential cross-section for a partial wave with angular momentum ℓ is found to be,

$$\frac{d\sigma_\ell}{dE} = \frac{4\pi}{k^2}(2\ell+1)\frac{1}{1+\cot^2\delta_\ell(E)} \tag{1.3}$$

where k is the wave number of the core-neutron relative momentum and δ_ℓ the scattering phase shift for a given ℓ induced by the interaction of the incident neutron with the potential. The cross-section σ_l takes its maximum value for a phase shift $\delta_\ell = \pi/2$. Near this value, $\delta_\ell(k)$ increases very rapidly and the cross-section exhibits a narrow peak as a function of energy that is interpreted to be a resonance. Near the resonance, δ_ℓ will be

negligible for all the partial waves except for the resonant component. In such a case, δ_ℓ can be approximate by,

$$\cot \delta_\ell \;=\; \frac{E_r - E}{\Gamma_\ell} \tag{1.4}$$

where E_r is the energy of the resonance and Γ_ℓ the width, both dependent on the angular momentum ℓ of the resonance. The shape of the phase shift leads to a resonance that can be described as a *Breit-Wigner distribution* for which the cross-section is defined as,

$$\sigma \;\propto\; \frac{\Gamma_\ell^2}{(E - E_r)^2 + (\Gamma_\ell/2)^2} \tag{1.5}$$

Following this description, the parameters E_r, Γ_l allow us to characterize the unbound state. By way of example, Fig. 1.5 shows the potential and energy distribution for a Breit-Wigner resonance with $\ell > 0$ and a virtual state for $\ell = 0$, being the absence of a centrifugal barrier for the latter the main difference between them.

1.2.3 Three-body resonances and FSI

In the above section, we have introduced the formalism for resonances which couple with a two-body channel. However, resonances can involve two, three or more particles. In this context, light neutron-rich nuclei, such as ^{6}He or ^{11}Li, often show structures with a manifest three-body character consisting of a bound core plus two weakly-bound neutrons. Beyond the neutron dripline, unbound systems show similarly core$+n+n$ structures in their resonant states.

These neutron-rich systems, which would be almost impossible to describe solving a N-body problem, can be more easily approached in terms of two- and three-body interactions between the few clusters, that is, using a Hamiltonian of the kind,

$$H \;=\; \sum_i (-\frac{\hbar^2}{2m}\nabla_i^2) + \sum_{i<j} V_{ij} + \sum_{i<j<k} V_{ijk} \tag{1.6}$$

Indeed, the study of unbound three-body nuclei is an important source to investigate the nuclear interaction between nucleons as well as the effect of the three-nucleon forces in nuclear structure. In this sense, the experimental study of core$+n+n$ resonances can reveal direct properties from the core$+n$ or nn interactions that may help theories develop more realistic nuclear interactions. In particular, the nn interaction can be thoroughly investigated in three-body decays involving a two-neutron emission: the *final state interaction* (FSI) between neutrons, which are no longer interacting with the core, leads to characteristic correlations in their relative energy and angles. Unlike protons, the absence of Coulomb barrier makes the correlation between neutrons easier to identify as it is better conserved during the decay. In the relative energy, these correlations manifest, in either sequential or direct decays, as low-energy enhancements which clearly deviate from the energy distribution that we would obtain following only kinematic constraints.

Strong signals in the nn relative energy will, as well, have an impact on the core+n relative energies, and eventually, on the three-body relative energy. In order to fully understand the decay of three-body resonances, it is essential to take into consideration the effect of the interaction between neutrons. This can be achieved using two main approaches:

- *Phenomenological.* The low-energy increase towards zero in the nn relative energy observed in many three-body decays is very similar to what a nn virtual state would look like. As for virtual states, the exponential-like behavior of the cross-section distribution can be well reproduced by the asymptotic part of the nn potential, which can be characterized by a single parameter, the nn scattering length $a_s = -18.5$ fm. Such description would correspond to a simple FSI analysis for which we would assume that the asymptotic part of the nn potential dominates the final state, neglecting the structure of the source.
- *Microscopical.* Another approach is to consider the complete three-body interactions which may lead to internal correlations in the original system. These internal correlations, when propagated during the decay towards our detectors, would reveal themselves as correlations in the energy distributions. In this case, the nn interaction would be no longer described with the single parameter a_s but with a realistic $V_{nn}(r)$ potential, coupled to a core-n potential and eventually a three-body force.

In this work, we investigate several systems that present two-neutron emission. The measured nn correlations from the decay of these nuclei have been studied from both perspectives: a phenomenological model, the FSI formalism [19] which has been long used in the study of nn emissions, and a microscopical model [20] that carries out complete three-body calculations. The interpretation of the decay correlations as well as the comparison between the two approaches are presented in chapter 6.

1.3 Experimental approach

We aim at the study of very neutron-rich nuclei located far from stability, beyond the neutron dripline. The experimental techniques employed must take into account their nature and adapt to their "exotic" features. One of the most important characteristics is the fact that they are short-lived systems difficult to produce. In this context, the techniques developed for the study of unstable nuclei represent a complete turn around with respect to the conventional techniques so long used for stable nuclei: the nucleus of interest, which is now unstable, can no longer be at rest as a target. The study of radioactive nuclei implies experiments performed in *inverse kinematics*, where the nucleus of interest becomes the beam and a stable nucleus the target.

The production of radioactive beams, though challenging, can be achieved in different ways. In our case, the most adequate is the production by *fragmentation* from a primary stable beam. This production technique, explained in more detailed in Sec. 2.1, has been proved to be a very powerful tool to explore new regions of the nuclear chart, particularly useful for the neutron-rich side. One of the most high-performing facilities in the world providing RIBs produced by this technique is the RIKEN-RIBF facility in Japan. All experiments presented in this thesis have been performed at the RIBF, primarily using

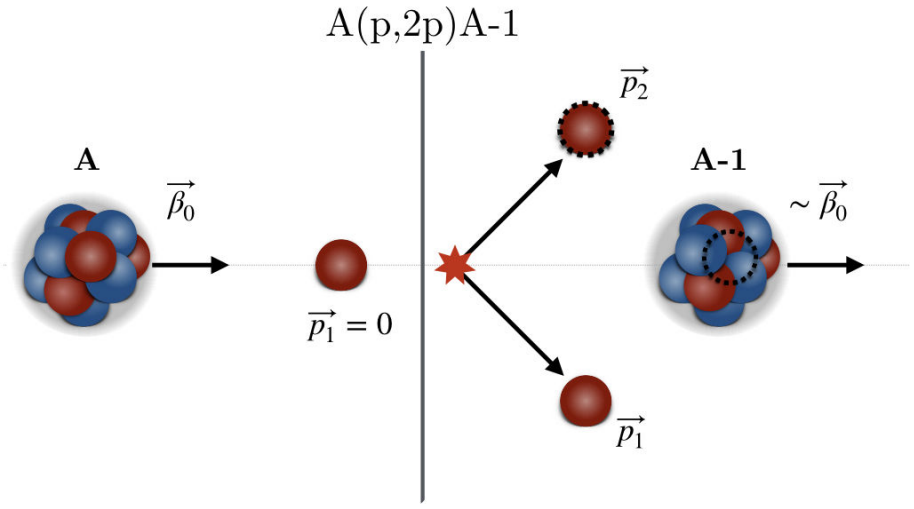

Figure 1.6: *Schematic representation of a proton knock-out reaction process on a proton target in inverse kinematics.*

the SAMURAI setup. The high intensity and energy of the primary beam at RIBF are able to produce secondary beams of unstable nuclei at high energies, 200–300 MeV/nucleon within our experimental conditions, that allow the population of unbound systems far from stability.

With radioactive beams at energies of several hundred MeV/nucleon, fast nucleon-removal reactions, or *knock-out reactions*, are the key tool for spectroscopy. These reactions, performed in inverse kinematics, imply the population of the nucleus of interest by removal of one or few nucleons from the beam caused by the collision with the target nucleus. A schematic picture showing a proton knock-out reaction on a proton target is illustrated in Fig. 1.6. The cross-section of the reaction is determined by the choice of the beam, being higher when closer in A and Z to the nucleus of interest. The production rate depends on two main factors: *i)* the intensity of the beam, *ii)* and the thickness of the target. The use of fast beams makes it possible to use relatively thick targets that compensate their low intensity. In most cases, a solid target of ^{9}Be or ^{12}C is used. Recently, the development of active targets, such as the liquid-hydrogen MINOS target described in Sec. 2.2, has allowed the use of thicker targets that improve significantly the statistics without worsening the resolution and even improving it. Both ^{16}Be and ^{15}Be presented in this work have been populated via knock-out reactions, the former using the active target MINOS and the latter, a solid carbon target.

Moreover, other reactions can be used in order to explore different aspects that knock-out reactions cannot cover, such as *inelastic scattering*, very useful to study the excited bound and unbound states of a given initial nucleus. In this case, the nucleus of interest, which is already in the beam, is excited in its interaction with the target but none of its nucleons is removed. Within this idea, the third isotope investigated in this thesis, ^{14}Be,

has been populated from an inelastic scattering reaction.

Independently of the reaction, experiments involving the investigation of very short-lived nuclei, which are expected to decay inside the target immediately after the reaction takes place, must be performed in *complete kinematics measurement*. Using a multidetector setup all decay particles are tracked and momentum-tagged in order to reconstruct the energy of the original system. In particular, unbound states of neutron-rich systems will decay by emission of one to several neutrons. The detection system must be able to detect these neutrons as well as the remaining charged fragment within the conditions of the experiment. Because of the high incident energy regime, all decay products are emitted forward focused covering a small angular aperture, with velocities close to the initial velocity of the beam. The higher the energy of the beam, the smaller the angular aperture. This implies that most of the detectors have to be located in forward angles and at big distances from the target in order to improve the angular acceptance and resolution respectively.

At the RIBF, the SAMURAI multi-particle spectrometer ensures the kinematically complete reconstruction. This setup comprises a large variety of detectors that include the fast-neutron array NEBULA, situated at around 11 m, a gamma detector DALI2 and several charged-particle detectors to identify and track all fragments in an event-by-event basis. The main part is a superconducting magnet, from which the SAMURAI setup gets its name, that enables the separation of the charged fragments for their identification. An overview of all the detectors included in the setup is presented in chapter 2.

When all decay products are detected and identified, the reconstruction of the energy can be done *via invariant-mass spectroscopy*. This technique is independent of the reaction mechanism or the incident beam used to populate the nucleus. The invariant mass, which is just the total relativistic energy, can be reconstructed from the measured 4-momenta of all decay particles in any reference frame. If we subtract the masses of the decay particles from the total energy, we will obtain the *relative energy* describing the relative motion between particles. The peaks shown in the spectrum of relative energy will be associated with the resonances of the original system. A detailed explanation of this method is given in section 4.1.4.

1.4 Beryllium isotopic chain

The exploration of isotopic chains of light nuclei, and in particular at the limits of stability, provides valuable information to test theoretical models, essential to not only explain experimental data but also predict the behavior of still unknown heavier nuclei. In this context, the Beryllium isotopes are of particular interest as they exhibit a wide range of interesting phenomena and structures. With a small number of protons, $Z = 4$, the evolution of the isotopic chain of Beryllium can be experimentally assessed from the proton to the neutron driplines, which are known to be ^{7}Be and ^{14}Be respectively, and beyond.

Indeed, special phenomena are not restricted to isotopes very far from stability. The $N = 4$ member of the Beryllium chain, the unbound ^{8}Be, represents a classic α clustering example. Although the α particle has a high binding energy, the ^{8}Be system lies at around 90 keV of the $\alpha+\alpha$ threshold. The addition of one more neutron to the 2α structure makes the system bound and gives rise to the only stable nucleus of the chain, ^{9}Be. The effect of

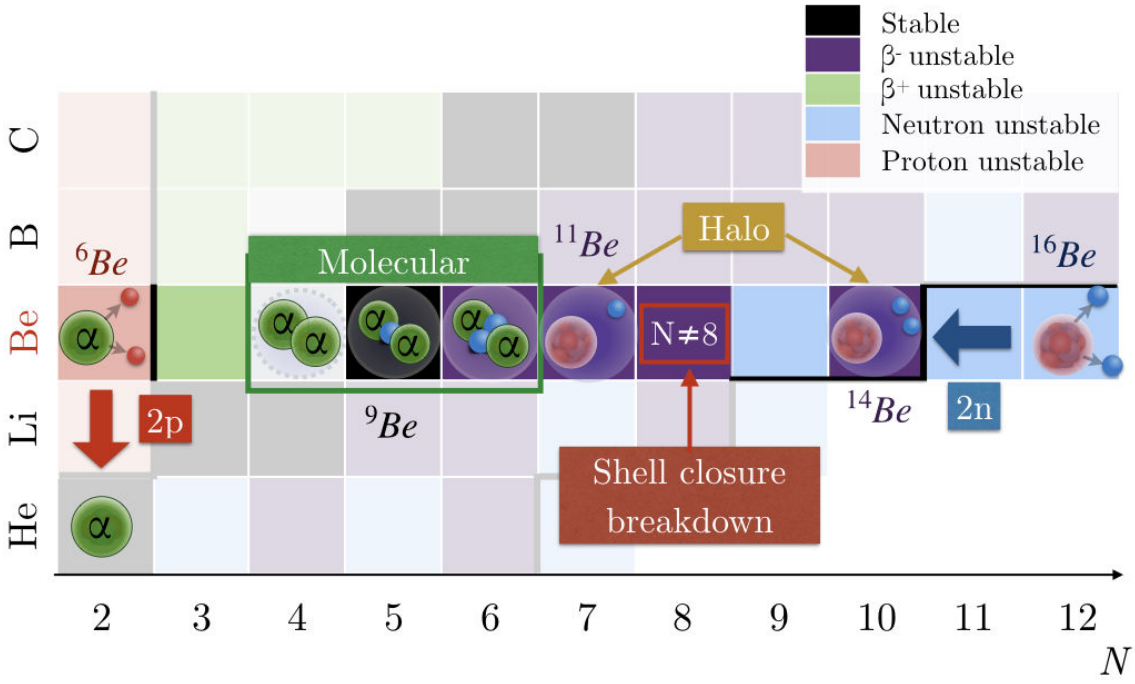

Figure 1.7: *Representation of the most important phenomena occurring in the beryllium isotopic chain ranging from proton and neutron emission beyond the driplines, the molecular behavior of ^{8-10}Be, the neutron halos in $^{11,14}Be$ to the breakdown of the magic number $N = 8$ for ^{12}Be.*

the "extra" neutron can be naively understood in terms of "molecular orbitals", similarly as valence electrons in covalent bonds [21]. This molecular character of 2α-xn structures can be also found in both ground state and first excited state of the next nucleus ^{10}Be [22], with the covalent bond orbital occupied by two neutrons instead of one, and in other isotopic chains such as ^{9}B [23], the mirror of ^{9}Be, which replaces the valence neutron with a valence proton.

Moving forward to more neutron-rich Beryllium we encounter the breakdown of the $N = 8$ magic number. In contrast with its isotone, ^{14}C, the very mixed ground state configuration of ^{12}Be [24, 25, 26] indicates a breakdown of the p-shell closure for neutrons. The shell evolution manifests itself already in the neighboring isotope, the weekly bound ^{11}Be, that exhibits an intruder configuration with the level inversion of the states $1/2^+$ and $1/2^-$ [27], by which the intruder $1/2^+$ becomes the ground state.

On the other hand, ^{11}Be is the benchmark single-neutron halo nucleus. Since it is bound by only 0.5 MeV to neutron emission, the wave function of its valence neutron extends to large distances as a consequence of the low binding energy. Its even more weekly-bound single excited state, $1/2^-$, also exhibits a halo structure. The extent of the radius of both halo states in ^{11}Be [28] are very similar and are far beyond normal nuclear radii, resulting in distances of about ~ 7 fm [29] between the neutron and the ^{10}Be core,

which itself is $\sim$ 2.5 fm in size. Another example of a halo nucleus is the last bound isotope of the isotopic chain, the borromean ^{14}Be with $N = 10$. In this case, the system is described as a two-neutron halo with a ^{12}Be core [30, 31, 32], for which the subsystem ^{12}Be+n is neutron unbound.

Due to the lightness of the beryllium isotopes, it is also possible to experimentally explore the isotopic chain beyond both driplines where other phenomena such as spontaneous nucleon emission may emerge. The very short-lived ground state of ^{6}Be has been known to decay by emission of two protons since the seventies [33]. In this case, single-proton decay to ^{5}Li is energetically very unlikely to happen as its ground state lies above the ground state of ^{6}Be. Instead the $\alpha + p + p$ decay channel is much more favored. Such behavior occurs beyond the driplines as a result of the pairing interaction that makes even-Z nuclei more bound than their odd-Z neighbors. Similarly, the even-N isotopes beyond the neutron dripline are expected to be more bound than their odd-N neighbors. Within this context, ^{16}Be is a perfect candidate for the study of the spontaneous two-neutron emission from a ground state.

In this thesis work, we focus on the study of the unbound states of the Beryllium isotopes at and beyond the neutron dripline, with special emphasis in ^{16}Be and its presumably two-neutron decay. In order to better understand its structure, the spectroscopy and decay of the ^{14,15}Be nuclei are also investigated. In the following, a summary of what is known to date about these three systems is given as well as the challenges and objectives that we face in their study.

1.4.1 Beryllium-16

The $N = 12$ member of the Beryllium isotopic chain is ^{16}Be which has two more neutrons than the last bound isotope ^{14}Be and thus is found beyond the neutron dripline. Shell-model calculations predict the single- and two-neutron separation energy to be +1.8 MeV and −0.9 MeV respectively [34]. Accordingly, ^{16}Be is expected to be bound with respect to neutron emission and unbound with respect to two-neutron emission. Moreover, the available information suggests that its neighbor ^{15}Be is presumably unbound by at least 1.54 MeV with respect to neutron emission. This creates a good candidate for a direct two-neutron decay to ^{14}Be, making ^{16}Be one of the few known candidates for which the spontaneous two-neutron emission may occur.

The ^{16}Be system has been investigated in [4] by means of a $(-1p)$ knock-out reaction from a ^{17}B beam at an energy of 53 MeV/nucleon using a Beryllium target. A broad structure at an energy of 1.35(10) MeV above the ^{14}Be+$n + n$ threshold was identified with its ground state, with a width of $\Gamma = 0.8(1)$ MeV and an assigned spin and parity of 0^+. In addition, significant enhancements were observed at low nn relative energies (E_{nn}) and angles (θ_{nn}). Particle correlations were compared to three different models: *a)* direct phase-space three-body decay of non-interacting particles, *b)* sequential decay through the tail of the only observed state in ^{15}Be at 1.8 MeV and *c)* dineutron emission which then breaks up into two neutrons later in the decay, corresponding therefore to a "sequential" decay process described as ^{14}Be+$^{2}n \longrightarrow ^{14}$Be+$n + n$.

Fig. 1.8 shows the comparison of these three hypothesis for the decay mode with the experimental relative energy of ^{14}Be+$n + n$ (left panel), and the nn relative energy (right

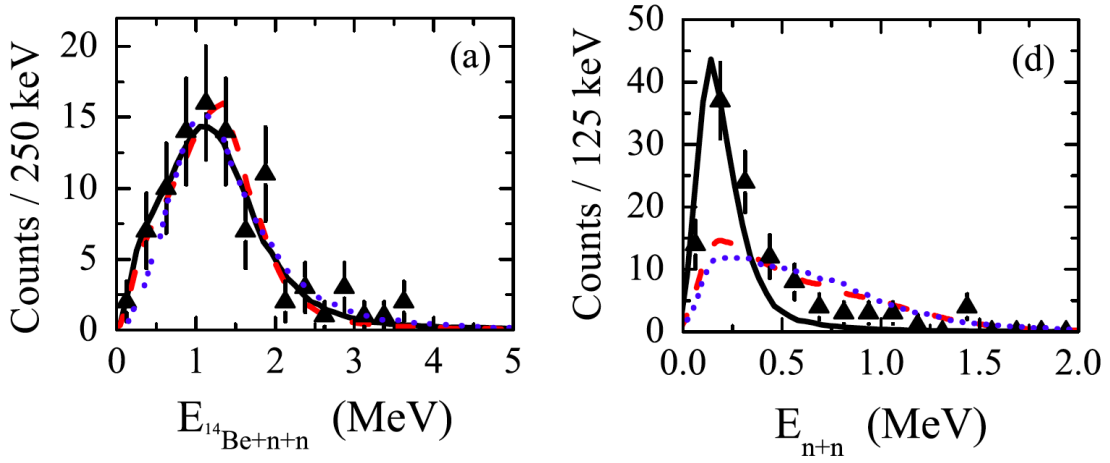

Figure 1.8: *On the left (a),* ^{14}*Be+n + n relative energy spectrum. On the right (d), relative energy between the two neutrons emitted in the decay of* ^{16}*Be. In both figures, the direct three-body decay with no FSI interaction is shown as a red dashed line, the sequential decay via the only known state of* ^{15}*Be at 1.8 MeV as a blue dotted line, and the dineutron as a black solid line. Adapted from [4].*

panel). The total relative energy shows a broad structure with very low statistics that can be reproduced with any of the assumed decay models, since this distribution is the input for all of them. On the contrary, among the three hypothesis used the low-energy signal observed in the *nn* channel can be only described with the one that assumes a dineutron decay (solid black line). It was concluded than the dineutron model was the best fit of the experimental data, claiming the first observation of a dineutron decay from a ground state.

The aim of this work

However, the absence of the *nn* interaction in the description of the direct three-body decay was pointed out [35, 36]. Indeed, and in contrast with two-proton decays, the lack of Coulomb barrier leads to a better conservation of the *nn* correlations during the decay. The *nn* interaction in the final state leads to a characteristic low-energy enhancement (see for example [37, 38, 39]) which is present in most of the channels where the emission of two neutrons is involved. Furthermore, the structure identified with the ground state is quite broad, possibly due to low resolution and statistics. As each resonance can have a different decay mode and therefore present a different signature, a good resolution and a broad acceptance are necessary to unambiguously determine the origin of the observed correlations. In addition, the first excited state 2^+ of ^{16}Be remains unobserved. Its observation would provide the whole set of 2^+_1 energies for all known Beryllium isotopes, from which very important information about the shell evolution can be extracted. Since it is predicted to be at an energy above 2 MeV, the $2n$ acceptance of the neutron detector should be large enough between about 0–5 MeV in order to avoid the cut-off of the signal.

This thesis work presents the results on ^{16}Be in the s018 campaign at RIKEN using the SAMURAI setup, which includes the neutron array NEBULA and the active target MINOS. ^{16}Be was populated using the same reaction as in [4], a one-proton removal reaction from a ^{17}B beam, but with a simpler proton target and an expected improvement

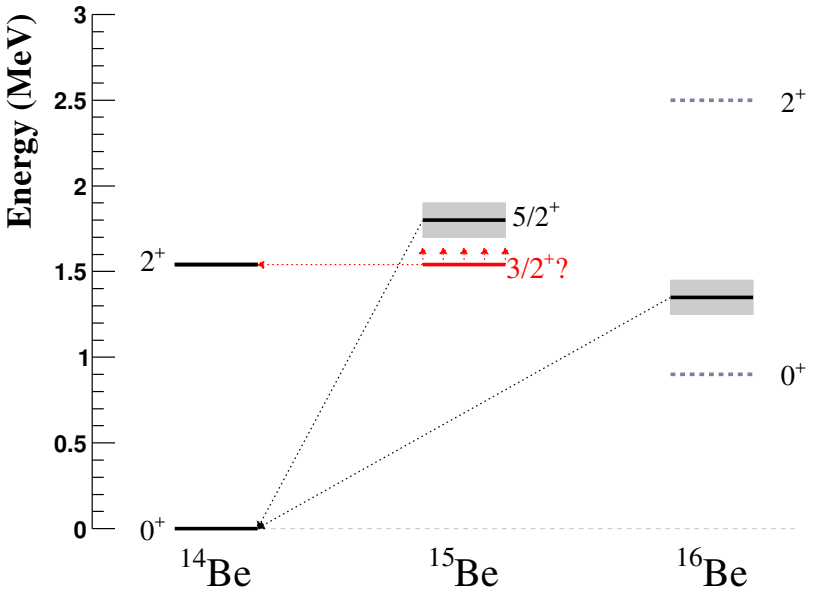

Figure 1.9: *Level scheme for the most neutron-rich isotopes of Beryllium. The black solid lines represent the experimental values. The dashed black lines correspond to the shell model predictions for ^{16}Be. The still unobserved $3/2^+$ state in ^{15}Be is the red solid line.*

in resolution, statistics, and two-neutron detection efficiency. In addition to these experimental improvements, another aim will be the study of the two-neutron emission within a more realistic formalism. In this sense, the unfolding of the FSI is essential for the investigation of the correlations between the decay particles. Given the recent progress in the theoretical description of light exotic nuclei, it would be important to probe the $2n$ emission, for both ground and first excited states in ^{16}Be, within a formalism built from microscopic principles, as we aim at a better understanding of the structure of three-body resonances and the role of the nn interaction.

1.4.2 Beryllium-15

The neighbor of ^{16}Be, ^{15}Be, is expected to be unbound with respect to single-neutron emission. The existence of an intermediate state in ^{15}Be is fundamental for the interpretation of the two-neutron decay of ^{16}Be. Yet its level structure is not completely determined and understood. Shell-model calculations using the code NUSHELLX [40] and the WBP interaction [41] predict two low-lying states, a $3/2^+$ ground state and a $5/2^+$ first excited state at 300 keV. A large spectroscopic overlap between $3/2^+$ and the neutron unbound 2^+ excited state of ^{14}Be is also predicted.

The ground state of its isotone ^{17}C, with $N = 11$, has been shown to be a $3/2^+$ state [42]. Consequently, the first attempt to populate ^{15}Be used a two-proton knock-out reaction from a 55 MeV/nucleon ^{17}C beam that was expected to have a high selectivity and mostly populate the $3/2^+$ state in ^{15}Be. No events in the ^{14}Be+n were observed and a lower limit for the energy of the $3/2^+$ state of 1.54 MeV [34] was established. The analysis of the ^{12}Be+$3n$ channel [43] concluded that no ^{15}Be component was needed to describe the experimental data. In a second experimental attempt, the neutron transfer ^{14}Be$(d,p)^{15}$Be

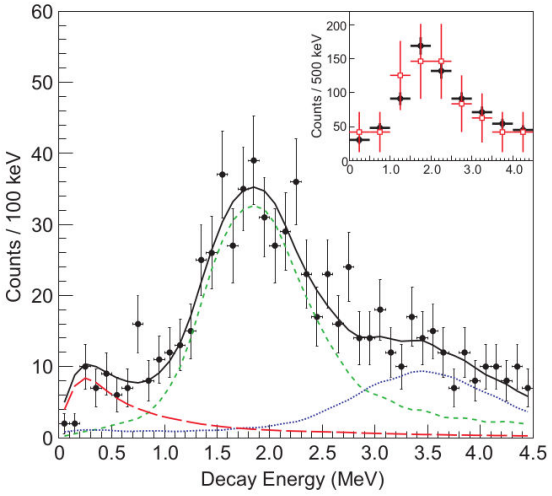

Figure 1.10: *^{15}Be decay energy spectrum populated from a neutron transfer reaction with a ^{14}Be beam. The best fit to the data is shown in black solid line which has contributions from a resonant state at 1.8 MeV (green short-dashed line) and other contributions identified with the background (red long-dashed and blue dotted lines). Taken from [5].*

was used to populate states in ^{15}Be [5]. The ^{14}Be+n relative energy obtained from this experiment is illustrated in Fig. 1.10. Based on the decay patterns predicted by shell-model calculations, one resonance-like structure observed in this spectrum was identified with the $5/2^+$ state at an energy of 1.8(1) MeV.

The aim of this work

The previous spectroscopy studies of ^{15}Be do not resolve the question of which of the two states, either $3/2^+$ or $5/2^+$, corresponds to the ground state. For the moment the $3/2^+$ state, which was the most suitable candidate to correspond to the ground state in the first place, is still unobserved. In order to fully understand the decay of ^{16}Be, it would be important to know the level structure of ^{15}Be as the sequentiality of its two-neutron emission highly depends on it. The goal of new experiments on ^{15}Be would be to populate the unobserved $3/2^+$ state as well as to confirm the energy of the $5/2^+$ state at 1.8 MeV. Within this context, we have probed the spectroscopy of ^{15}Be populated from different experiments performed at RIKEN using the SAMURAI setup that include a wide range of knock-out reactions. The results obtained from these experiments and the influence of ^{15}Be in the decay of ^{16}Be are presented in this thesis work (see Sec. 5.2).

1.4.3 Beryllium-14

The ^{14}Be isotope is the heaviest beryllium isotope with a known bound state. As mentioned before, it is also a classic example of a halo nucleus, which can be described as a core of ^{12}Be plus two loosely-bound neutrons. While its 0^+ state is bound, the first 2^+ excited state has been observed to be unbound with respect to two-neutron emission by 280(10) keV [6]. ^{14}Be* was studied using inelastic scattering on a carbon target. The only observed state, identified with $\ell = 2$ by comparison with angular distributions, was found to decay

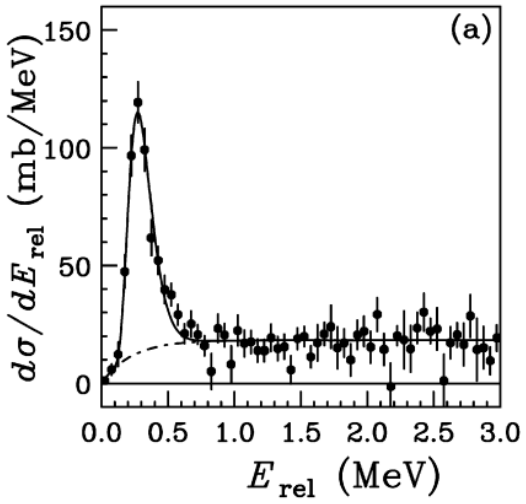

Figure 1.11: *^{12}Be+$n+n$ relative energy reconstruction [6]. The low-energy peak corresponds to the first excited state of ^{14}Be located at 0.28 MeV over the two-neutron emission threshold.*

to the ground state of ^{12}Be by emission of two neutrons. In Fig. 1.11 the reconstruction of the three-body relative energy ^{12}Be+$n+n$ is shown, where a clear peak at ~ 0.3 MeV can be seen. The excitation energy of ^{14}Be(2^+), $E_x = S_{2n} + E_{rel}$ with $S_{2n} = 1.27(13)$ MeV [44], results thus in an energy of 1.55±0.13 MeV.

The aim of this work

Even though the error of E_{rel} is significantly small (10 keV), the error of E_x is much bigger as it is completely dominated by the uncertainty of S_{2n}.Therefore, a more precise mass measurement of ^{14}Be will considerably reduce the uncertainty of the 2^+ energy. In terms of relative energy, it seems very unlikely to reduce the attained uncertainty of 10 keV. The above-mentioned study [6] confirmed the direct decay of ^{14}Be* to ^{12}Be by emission of two neutrons, but it did not investigate the correlations of the decay particles. Later studies indicated that the relative energy of the two neutrons emitted in the decay could be reproduced by simply taking into consideration three-body kinematics without the inclusion of any final state interaction [45].

In the context of this thesis, the study of the two-neutron decay from ^{14}Be(2^+) would provide an insight to a better understanding of characteristic features encountered in three-body decays involving the emission of two simultaneous neutrons. Although the decay of both ^{16}Be and ^{14}Be involve the emission of two neutrons, they show different features: *i)* ^{14}Be does not follow a spontaneous neutron decay. Instead, we need to energetically promote ^{14}Be to an unbound excited state (2^+) to induce a two-neutron emission. *ii)* While the FSI seems to be very important in the decay of ^{16}Be, the nn relative energy in ^{12}Be+$n+n$ shows no correlations coming from the FSI. In order to determine whether these differences are important or not, it would be noteworthy to compare the spontaneous two-neutron emission that we find in the ground state of ^{16}Be with the "induced" one that occurs in ^{14}Be. Moreover, it would be specially important to investigate and compare the correlations shown in the decay of both systems within the same formalism. The aim of

this work is to cover all these aspects. With that purpose, we have probed the inelastic scattering reaction ^{14}Be(C,X)^{14}Be* from the SAMURAI commissioning campaign in order to populate the 2^{+} excited state and to most importantly investigate the decay correlations using the same formalism and techniques employed for ^{16}Be.

Chapter 2

Experimental setup

Contents

The experimental campaign SAMURAI 18 (s018), performed at the **R**adioactive **I**sotope **B**eam **F**actory (RIBF) at RIKEN Nishina Center [46], is the main experiment analyzed as part of this thesis work. The aim of this campaign was to probe the halo nuclei such as ^{11}Li or ^{14}Be, given the RIBF capability to produce high-intensity unstable beams. In our particular case, the nucleus of interest was ^{16}Be, populated using a knockout reaction from a ^{17}B beam on the MINOS target, and detected by means of the standard SAMURAI setup and the NEBULA neutron array. To achieve a better understanding of ^{16}Be, the nuclear structure of the previous most neutron-rich isotopes of beryllium, ^{15}Be and ^{14}Be, has also been investigated through a series of experiments during the SAMURAI commissioning and DayOne campaign, performed also at RIKEN.

This chapter describes the setup of the experiment s018, the main features of which apply to the DayOne and SAMURAI experiments. First, a brief explanation about the radioactive isotope (RI) beam production is provided as well as the techniques utilized for its identification and transportation. The SAMURAI experimental setup is then described, including the target MINOS and the ensemble of detectors employed in the detection of the decay products. Other detectors of the experiment that are not significant for the analysis are also mentioned. Finally, the differences in the experimental conditions and setup

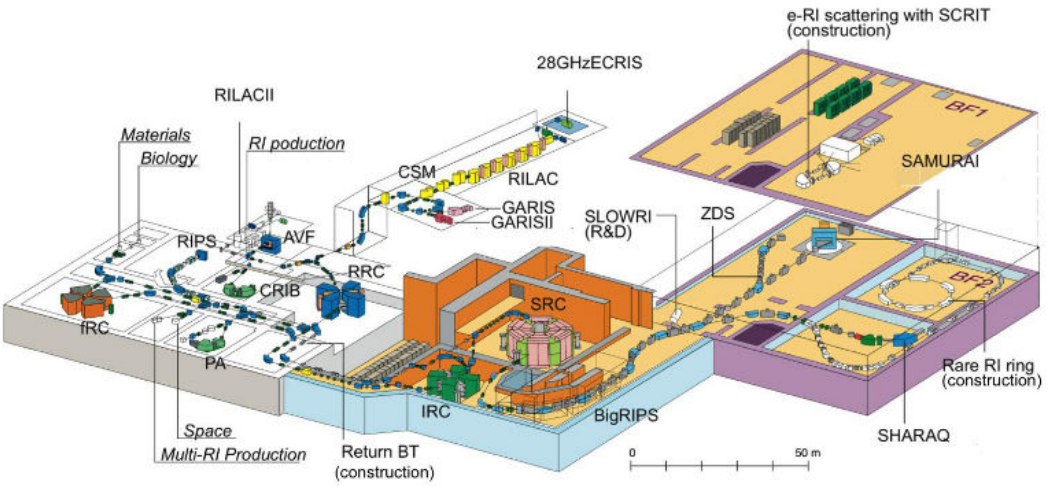

Figure 2.1: *Schematic overview of RIBF at RIKEN Nishina Center. The primary beam of ^{48}Ca is first accelerated by the heavy-ion accelerator system coupled for injection to the SRC from where it is conducted to the primary Be target. After fragmentation, the beam species are identified and selected in the BigRIPS separator and sent to the experimental area SAMURAI.*

between the campaign s018 and the commissioning and DayOne campaign are introduced. Additional details on these setups can be found in [3, 7, 47, 48].

2.1 Beam Production

The most feasible way to reach neutron-rich nuclei very far from stability ($N/Z \gg 1$) is by means of intense radioactive isotope beams. A beam of this kind can be produced by several techniques. However, if the study of very short-lived exotic nuclei is the goal, the most appropriate technique is the **in-flight fragmentation** technique: the high-intensity RI beam is produced via the projectile fragmentation of a primary heavy-ion beam, previously accelerated. The secondary beam resulting from the fragmentation is then conducted to a secondary target where the very neutron-rich isotope is populated.

At the RIBF facility, the superconducting fragment separator BigRIPS [49] is specially conceived for the production of very intense RI beams via this technique. Figure 2.1 presents the schematic configuration of RIBF. The production, selection and characterization of the beam, from the heavy-ion system accelerator to the BigRIPS separator, is outlined in this first section.

2.1.1 Primary beam: RIBF accelerators

The RIBF heavy-ion accelerator system integrates a set of cyclotrons and injectors, for which several operational modes are available depending on the mass and charge of the accelerated particle. In the particular case of the acceleration of ^{48}Ca, the mode applied is the one intended for variable-energy experiments of medium-mass ions.

The Calcium ions are extracted by an ECR ion source and then accelerated up to

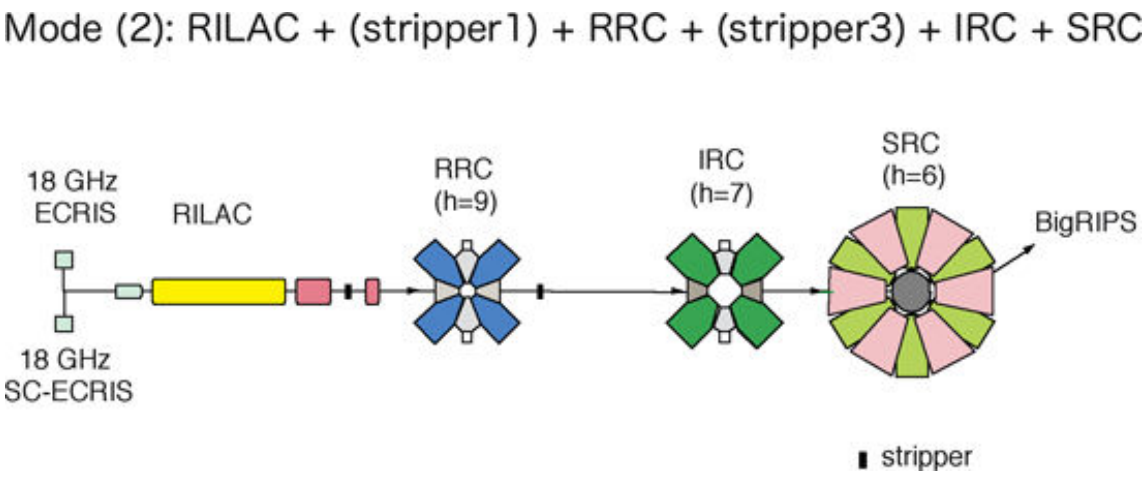

Figure 2.2: *Schematic representation of the RIBF acceleration system used for the primary beam.*

345 MeV/nucleon in several steps using a combination of different accelerators. The first one in the acceleration scheme is a linear accelerator (RILAC), followed by a number of cyclotrons: RRC, IRC and finally the **S**uperconducting **R**ing **C**yclotron (SRC) [50]. Along the beam line, strippers are located to remove electrons, the isotope being fully stripped at the entrance of IRC. The acceleration mode is represented in Fig. 2.2. This heavy-ion accelerator system provides a wide range of stable beams, from very light isotopes, as Helium, to heavy ones, as Uranium, at intensities starting from 10^9 pps. The beam intensity attained during the experiment was about 400 pnA. Once the desired energy is reached, the stable beam is sent to the primary Beryllium target.

2.1.2 Secondary beam: BigRIPS

As mentioned above, the RI secondary beam is produced in the BigRIPS separator by fragmentation of the accelerated stable beam. The production target consists of a thick target of Beryllium, located at the beginning of the separator. RI beams produced by the in-flight technique are widely referred to as **cocktail beams**, as these types of heavy-ion collisions at high energies generate a large variety of nuclei. All resulting radioactive ions have a lower mass and charge than the former primary isotope. Since the amount of generated species is substantial, the purification of the beam becomes an essential part. Throughout the 78 m of the BigRIPS spectrometer, the beam is first purified in order to select and finally identify the nuclei of interest. An overview of BigRIPS is shown in Fig. 2.3.

The BigRIPS separator is featured in two stages. In the first part of the separator, the RI beam is both produced and selected. This stage includes the production target situated at F0 and continues to the second focal plane F2. The main purpose of the second stage is the identification of beam species as, although purified, the beam is always composed of a mixture of isotopes. This part of the separator starts at F3 and contains all focal planes up to F7. Altogether, BigRIPS comprises six superconducting dipoles (D1-D6) and a collection of quadrupoles (STQ1-14) that play a key role ensuring beam focusing and transportation at every focal plane.

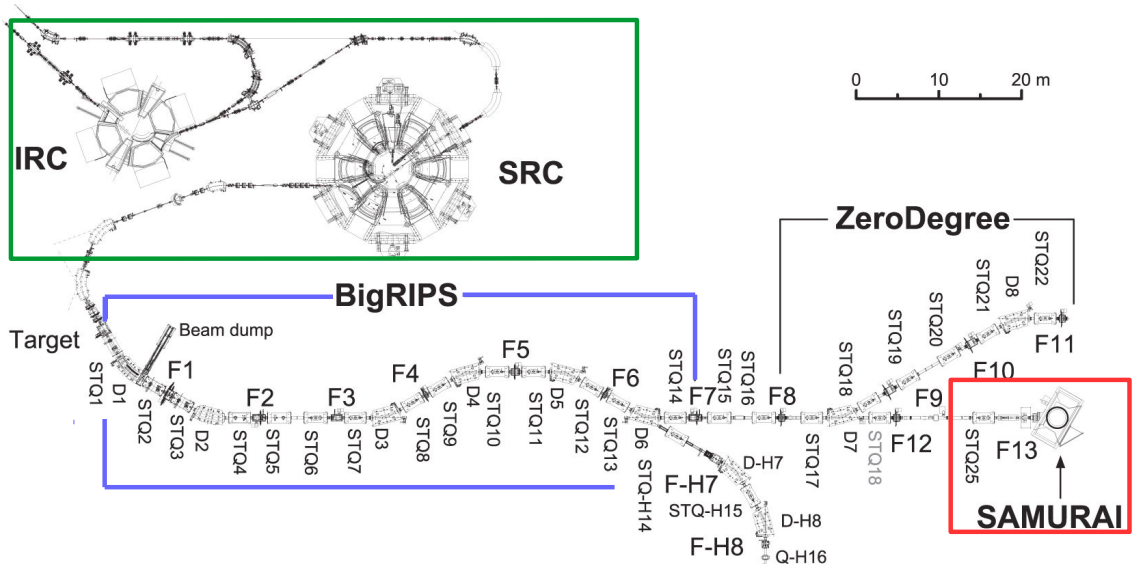

Figure 2.3: *Distribution of the beam lines with a schematic overview of the heavy-ion accelerator system (green), the BigRIPS separator (blue) and the SAMURAI experimental room(red).*

Production and selection of the secondary beam. The selection of the secondary beam species is made in flight in the first part of the separator (F0-F2) by using the momentum-loss achromatic technique. This technique comprises the use of the first two dispersive dipoles (D1 and D2) and an energy degrader situated at F1. Considering that the trajectory of a particle in a constant magnetic field depends on its charge, mass and velocity, nuclei can be separated according to their nature. This dependency is described by the concept of rigidity, $B\rho$, defined as the product of the magnetic field B times the radius of the trajectory ρ. The $B\rho$ of a given particle is calculated as follows:

$$B\rho = \frac{p}{Q} = \frac{\gamma m v}{Q} \sim \frac{A}{Z}\frac{u_a}{e}\gamma v \tag{2.1}$$

where p is the momentum of the particle, v its velocity, Q its charge, m its mass and $\gamma = 1/\sqrt{1-\beta^2}$ with $\beta = v/c$. The atomic mass and the electron charge are represented by u_a and e respectively. The selection in $B\rho$ is therefore equivalent to a selection by mass-over-charge, represented by the A/Z ratio, when the velocity of the species is similar. The magnetic field along the beam line is thus adjusted to control the motion of particles. In order to achieve high intensity and purity, different parameters are applied depending on the desired nature of the final RI beam.

In this stage, the $B\rho$ method is enhanced by adding an Aluminum energy-degrader between the two bending dipoles. Given that different species can have the same mass-over-charge ratio, a selection by $B\rho$ is not sufficient. According to the Bethe-Bloch equation for charged heavy-ions, the energy loss due to the passage of a particle through matter depends on the charge of the isotope and its velocity, $\Delta E \propto Z^2/v^2$. Assuming a similar velocity of the beam isotopes, the energy loss is approximately proportional to Z^2. This

permits the isotopic selection of the beam species by the properties of mass-over-charge and atomic number. The $B\rho$-ΔE-$B\rho$ combined method is similarly implemented in the second stage, at F5, to increase purity and remove remaining contaminants.

Beam identification and transportation. The energy loss (ΔE), time of flight (ToF) and position (x,y) are measured in the second part of the spectrometer by beamline detectors located at the focal planes. Particles are identified event by event by the ToF-$B\rho$-ΔE method from which the mass-over-charge ratio A/Z and atomic number Z can be deduced. The ToF is measured by plastic scintillators between the focal planes F3-F7 and F7-F13 (at the entrance of SAMURAI). The energy-loss measurement is performed with a multi-sampling ionization chamber (MUSIC) or a stack of silicon detectors situated at F7. The magnetic rigidity is calculated by trajectory reconstruction of the ions at the focal planes with PPACs detectors.

The BigRips separator is followed by a delivery line that conducts the beam to the SAMURAI experimental room, starting at F13. Depending on the experimental requirements, the settings in the optics of the beam lines can be adjusted to achieve the desired characteristics. The optics mode determines the acceptance and the momentum resolution of the beam line. The larger the acceptance, the lower the resolution. In the experiment s018, with the MINOS target, the optics for the transport at the end of the beam line were tuned to make the beam size small on the target spot.

2.1.3 Beam characterization at SAMURAI

SAMURAI stands for **S**uperconducting **A**nalyser for **MU**lti-particle from **RA**dio **I**sotope beam [51] and it is specially designed to detect multiple particles in coincidence in kinematically complete measurements. A schematic view is shown in Fig. 2.4. The standard SAMURAI setup consists of a large amount of detectors that include heavy-ion detectors (HODOSCOPEs, BDCs, FDCs), a neutron detector (NEBULA), a gamma detector (DALI), and a superconducting dipole magnet, the SAMURAI magnet. Some other additional detectors can be added depending on the specifications of the experiment. For the s018 campaign, notably intended for quasi-free (p,pn) reactions on a proton target (MINOS), a supplementary neutron detector (WINDS) and two proton detectors (RPD, RPTOF) were added to the standard setup. More details on these detectors will be given in next sections.

SBTs. At the entrance of SAMURAI (F13) two 2-mm-thick fast-timing scintillators (SBT1 and SBT2) are employed to provide a trigger signal (see Sec. 2.5), as well as the ToF of the beam particles between the focal planes F7 and F13. The plastics are equipped with two PMTs positioned at the left and right edges. The timing for each SBT is calculated as the average of both PMTs:

$$T_{SBT} = \frac{T_{left} + T_{right}}{2} \tag{2.2}$$

The determination of the time-of-flight of the beam particles using the SBTs is detailed in Sec. 3.1.

Beam Position: BDCs. The incoming beam is tracked using two identical drift

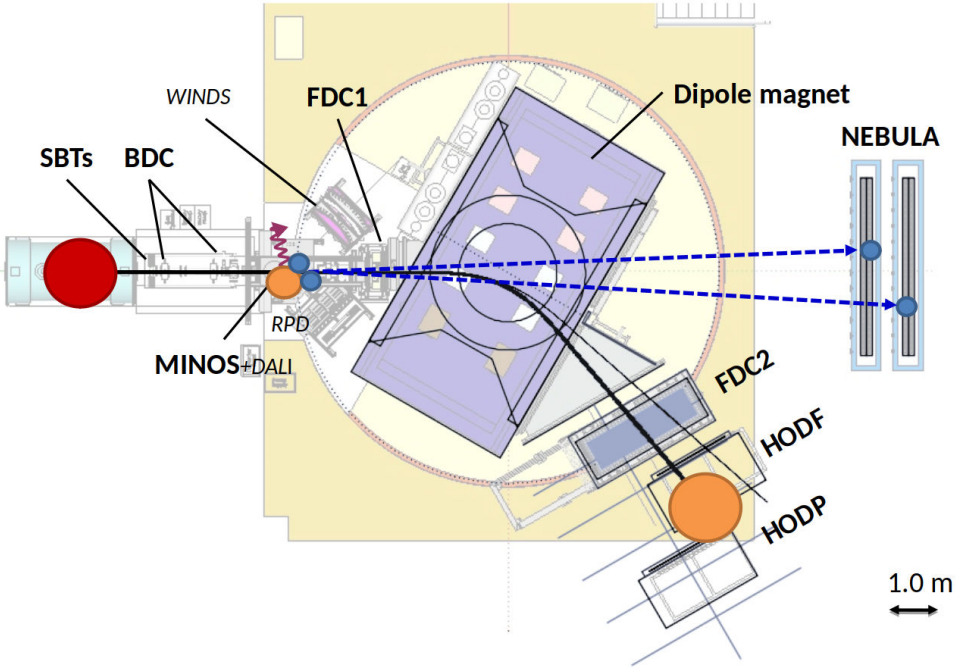

Figure 2.4: *Schematic view of the SAMURAI setup. The red dot represents the beam that interacts in MINOS giving as a result an unbound system with a core+two neutron structure. The decay products will be measured by NEBULA (neutrons in blue) and the HODOSCOPEs (charged fragment in orange).*

chambers called BDC1 and BDC2 (**B**eam **D**rift **C**hamber). These two detectors are separated by 1 m and located between the beam trigger (SBTs) and the target. By combining the position measured by the two drift chambers, the trajectories of the incident isotopes are determined event-by-event.

The dimensions are 320(H)×320(V)×120(T) mm^3 with an effective area of 80(H)×80(V) mm^2. They are composed of 8 planes of 16 wires used as anodes and arranged either horizontally (y) or vertically (x). Planes with the same orientation are set together following the configuration: $x_1x'_1y_1y'_1x_2x'_2y_2y'_2$. Wires in the same plane are separated by 5 mm while the distance between two consecutive planes is 4.8 mm. Spatial resolution is improved by shifting the wires from one consecutive plane to the other of the same orientation by 2.5 mm. BDCs are operated at 50 Torr using a gas of isobutane. See Sec. 3.3 for details on the calibration for the drift chambers.

2.2 Target: MINOS

MINOS (**Mag**ic **N**umbers **O**ff **S**tability) [52] is the reaction target used in the experiment. It is composed of a 15 cm thick target cell of liquid Hydrogen coupled with a **T**ime **P**rojection**C**hamber (TPC) of 30 cm length. It is specially designed for proton-induced knock-out reactions, where the TPC is used as a vertex tracker. The trajectories of the emitted protons in the TPC are reconstructed in three dimensions, from which the interaction point in the target can be determined. The vertex reconstruction method depends on the reaction involved. For (p, np) reactions, the recoil proton detected in the TPC and the beam are used. In the case of $(p, 2p)$ reactions, where two protons are

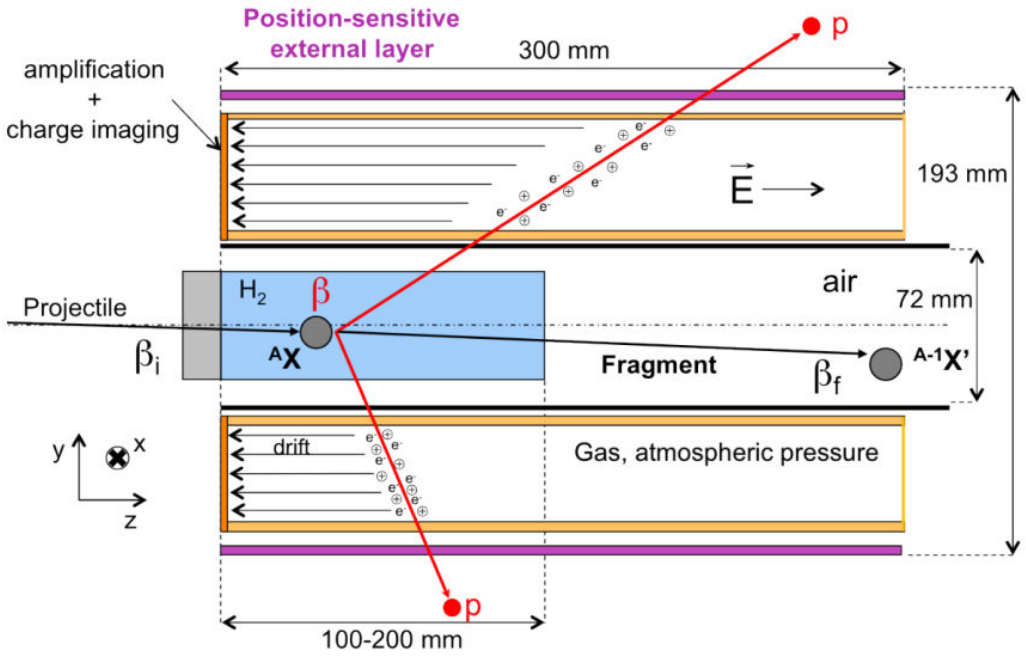

Figure 2.5: *Cross-sectional view of MINOS. The blue area shows the target cell filled with liquid hydrogen. Around it, the orange part is the TPC that is used as a vertex tracker.*

detected in coincidence, the vertex is deduced from their reconstructed trajectories. In Fig. 2.5 a view of the vertex determination scheme is presented.

A major issue in experiments with secondary beams intended to populate very exotic nuclei relies on reaction rates. The probability of a nuclear reaction proportionally depends on the thickness of the target. The larger the target, the bigger the number of target nuclei and consequently, the higher the number of reactions. However, a thicker target also implies a more important energy loss. In regular solid targets, the thickness will have a significant effect on the final resolution, as the energy-loss calculation is approximated by considering the reaction point in the center of the target. A technical problem arises when trying to optimize the thickness of the target while maintaining a good energy resolution. A compromise is needed in order to meet the requirements for statistics as well as for energy resolution.

Moreover, other approaches have been developed to overcome the pitfall. The ensemble of MINOS+TPC is part of a technology, commonly known as active targets, aiming at the use of very thick targets in direct secondary reactions. The determination of the reaction point in MINOS gives us the possibility to calculate more precisely the energy loss of either the outgoing reaction products or the incoming particles of the beam (see Fig. 2.6). This allows the employment of thicker targets, not only without degrading the energy resolution, but even improving it while considerably increasing statistics, which is specially useful in reactions where rare isotopes are studied.

The shape of the target cell is cylindrical, with an effective surface of Ø= 38 mm. The inner part is filled with liquid Hydrogen, kept at very low temperatures, and located inside a sealed vacuum chamber. The average temperature during the experiment was

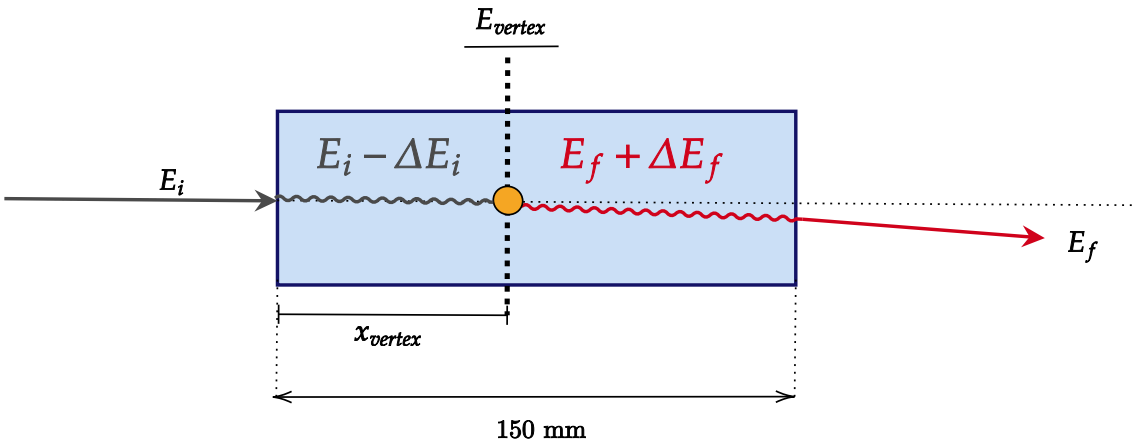

Figure 2.6: *The determination of the reaction point allows us to calculate the energy loss of the beam particles as well as of the reaction products.*

about 15 K resulting in an effective target thickness of 1.16 g/cm^2. See Ref. [53] for more technical information.

2.3 Detection of decay products

2.3.1 SAMURAI magnet

The SAMURAI magnet is a H-type dipole with a cylindrical pole of 2 m diameter. The size of the magnet is 6.7(H)×4.64(V)×3.5(T) m^3. The geometry with a pole-gap width of 0.8 m allows a large angular acceptance for fast projectile neutrons. Due to the intense magnetic field (2.9 T during the experiment), the projectile fragment is momentum-tagged, which is fundamental for invariant-mass measurements.

In experiments where very short-lived nuclei are populated, the decay is expected to happen inside the target immediately after the reaction. If the unbound system has a core+n+n structure, as in the case of ^{16}Be, the two neutrons will be emitted forward while the trajectory of the heavy fragment will be bent by the SAMURAI magnet according to its properties of mass, charge and momentum as described by the magnetic rigidity (see Eq. 2.1). The SAMURAI magnet permits thus the separation of heavy fragments produced in the target allowing, in conjunction with the other SAMURAI detectors, the identification and complete kinematics of all decay products (see Fig. 2.4).

2.3.2 Fragment Position: FDCs

Such as for the incoming beam, the outcoming fragment direction is measured using two drift chambers named **F**orward **D**rift **C**hambers (FDC). Heavy fragments produced after the reaction are tracked at the entrance and at the exit of the SAMURAI magnet by means of the FDC1 and the FDC2 respectively. From the reconstructed trajectory between the two detectors, magnetic rigidity is uniquely calculated for particle identification.

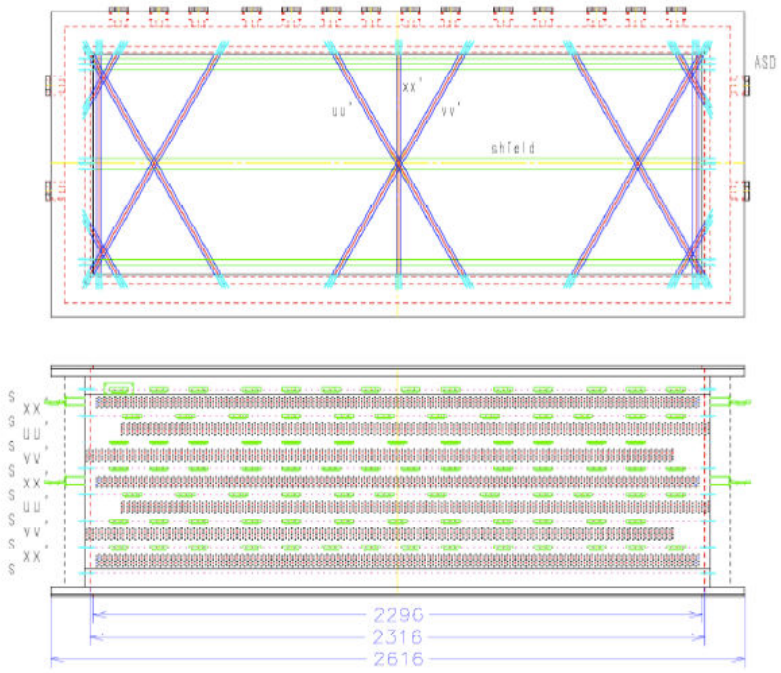

Figure 2.7: *FDC2 structural plane. A side (upper) and a top (lower) view are showed.*

The technique employed for the reconstruction of heavy-fragment trajectories and the $B\rho$ calculation are detailed in Sec. 4.1.2.

FDC1 is located after the target and before the entrance window of SAMURAI. The operational mode is similar to BDC's. The difference between them is based on the dimensions and configuration of the planes.

The FDC1 is rectangular with a dimension of 1000(H)×696(V)×336(T) mm^3 and a cylindrical active area of diameter 310 mm. It is composed of 14 planes and 32 wires/plane. There are no horizontal planes (y). Instead, planes at angles of $+30°$(u) and $-30°$(v), together with vertical planes (x), are used. The configuration is the following: $x_1x'_1u_1u'_1v_1v'_1$ $x_2x'_2u_2$ $u'_2v_2v'_2x_3x'_3$. Consecutive planes are separated by 10 mm and wires from the same plane by 5 mm. As for the BDC, wires of successive planes with same orientations are shifted by 2.5 mm to improve detection efficiency and resolution. The position is reconstructed with a resolution of 100 μm (rms) and a efficiency of 100% [51].

FDC2 is the second drift chamber used in the analysis of the rigidity of the charged fragment. It is located after the exit window of SAMURAI. Since the trajectories spread due to the increasing distance from the target and the variety of fragments produced, the dimensions of the FDC2 are much larger compared to the previous drift chambers in order to detect the maximum number of projectiles.

The FDC2 is also rectangular with a size of 2616(H)×1156(V)×876(T) mm^3 and an active zone of 2296(H)×836(V)×653(T) mm^3. Equally to the FDC1, there are 14 planes with directions x,u,v (no horizontal planes) and they follow the same distribution. The number of wires composing a single plane is however much higher, 112 wires/plane. Wires in a same plane are separated by 10 mm and are distributed forming a hexagonal cell

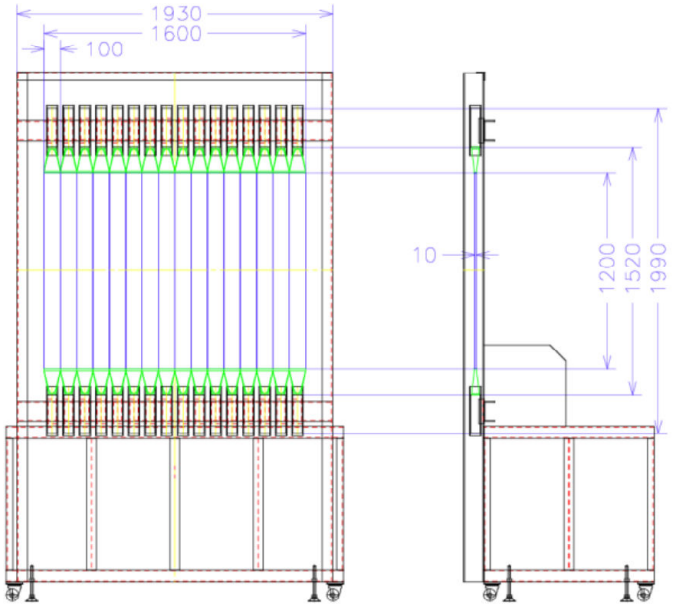

Figure 2.8: *HODOSCOPE structure from a front (left) and a side (right) view.*

structure. Two planes of the same orientation are assembled together, named as superlayer, such as xx′. In a superlayer, planes are separated by 15 mm and shifted by 5 mm. Superlayers are separated by 100 mm with shield planes in between. The operating gas is a mixture of Helium and isobutane at 1 atm. The structure of the FDC2 is shown in Fig. 2.7.

2.3.3 Fragment Identification: HODOSCOPEs

Two conventional scintillator hodoscopes (HODOF and HODOP) are placed after the FDC2 in order to measure the ToF and the charge of the fragments. The use of two hodoscopes permits the acceptance of a larger number of particles comprised in a wide range of mass and charge. Depending on the magnetic rigidity and momentum of the nucleus of interest, the position of the detectors can be optimized. In combination with the detection position given by the FDC2, charged particles are identified by using the ToF and charge measured by the HODOSCOPEs. The method followed to identify fragments is described in Sec. 3.2.

Each hodoscope is composed of 16 bars of plastic scintillator of dimensions 1200(V)× 100(H)×10(T) mm^3. As in the case of the SBTs, the end edges of the plastics are equipped with two PMTs. In the s018 campaign, the HODOP was located $\sim$ 1.5 m behind the HODOF. Both detectors were aligned in a straight line to cover the maximum possible area as the aim of the experiment was the study of a large variety of nuclei. Figure 2.8 shows a schematic representation of one HODOSCOPE.

2.3.4 Neutron Detection: NEBULA array

NEBULA stands for "**NE**utron-detection system for **B**reakup of **U**nstable-Nuclei with **L**arge **A**cceptance" [54]. The detector is designed to measure fast neutrons at energies

Figure 2.9: *Photo of the NEBULA detector in the SAMURAI experimental room at RIKEN.*

of some hundreds of MeV with a wide range of acceptance and high efficiency. NEBULA is placed at around 11 m from the target after the SAMURAI magnet. Unlike charged particles, emitted neutrons coming from the target will travel straightforward through SAMURAI, as neutrons do not feel the magnetic field. This makes possible the reconstruction of the momentum directly from the measured ToF between the vertex of the reaction and the detection position in NEBULA. See Sec. 3.5 for further details on the momentum reconstruction of neutrons.

The neutron array is composed of a total of 120 organic plastic scintillators arranged in two walls. The two walls are separated by a distance of 1 m and each of them is equally divided in two consecutive layers. Each layer contains 30 plastics of rectangular dimensions $120\times1800\times120$ mm^3. Two PMTs are coupled to the ends of each plastic. The total detection area is 3.6×1.8 m^2.

A good position resolution is essential for the reconstruction of the momentum and energy of the detected neutrons. When a plastic is triggered, the two coupled PMTs are used to calculate the vertical Y position, as the time difference between them is proportional to the vertical coordinate of the detection point. As for X and Z, the fixed position of the plastic, *i.e.*, its middle position, is estimated as the interaction point. The resolution in X and Z is, consequently, ±6 cm, half the width of one plastic.

A key problem regarding neutron detection is the identification. Charged particles can be misidentified as neutrons, since they both can interact in NEBULA, just as a single neutron can generate several signals that can be misinterpreted as multiple-neutron events.

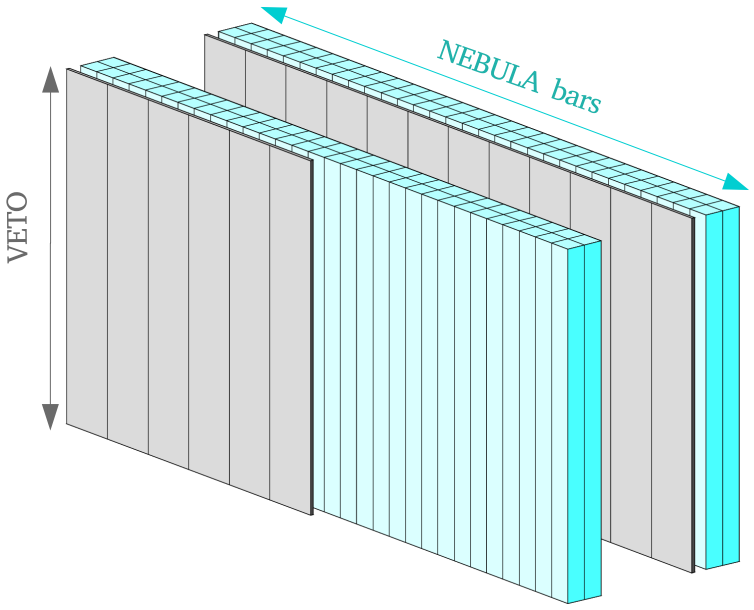

Figure 2.10: *Schematic view of the NEBULA walls. The VETOs are represented by the gray layers while the NEBULA bars are shown in blue. A total of 120 neutron detectors are distributed in two walls, each of them constituted of two layers.*

- To avoid misidentification of charged particles as neutrons, charged particle detectors (VETOs) are located before each wall, as shown in Figs. 2.9 and 2.10. These detectors are thin enough (approximately 1 cm thick) to have a very low neutron detection efficiency although sufficiently large to detect charged particles. In the case in which both, VETO and NEBULA, are triggered the event is then rejected.
- Multi-neutron detection is a more challenging issue. Given that neutrons can only interact by strong interaction, their detection cannot be direct, but indirect. The main mechanism involved in the detection is the collision between the neutron and the Hydrogen and Carbon nuclei. The deposited energy in the detector is not proportional to the energy of the incident neutron, as it is the recoil of the charged particles from the collision that induces the signal in the detector. As a consequence of the interaction in NEBULA, a neutron losses some of its energy but not necessarily the totality. The same neutron can be therefore detected multiple times in NEBULA, a phenomenon commonly known as **cross-talk**. The identification of the number of real neutrons is essential for the study of channels where more than one neutron are expected in the final state. An analysis method for the rejection of cross-talk is explained in Sec. 3.6.

2.4 Additional detectors

The complete setup of s018 includes several other detectors that will not be explained in detail since they were not used for this thesis work. The main objective of the campaign was to measure quasi-free (p,pn) reactions following either a missing-mass or an invariant-mass analysis. Through the use of a collection of detectors, positioned at an angle of $\sim 45°$ with respect to the target, the outgoing reaction products were detected to make possible the missing-mass analysis. In particular, the knocked-out neutron and the recoil proton

energy and ToF were measured by using WINDS and the RPD-RPTOF combination, respectively. Since our reaction of interest is a (p,2p) knock-out reaction, from which the relative energy is reconstructed by the invariant-mass method, we only need particles involved in the decay to be detected. The standard SAMURAI setup is therefore enough for our analysis. The following is a brief description of the additional detectors used for the missing-mass analysis:

RPD and RPTOF are proton detectors used to determine the timing (RPTOF) and position (RPD) of the recoil proton of MINOS. The full kinematics of the ejected protons can be obtained in combination with the trajectories in the TPC and the point of interaction in MINOS, by which the energy loss can be calculated.

WINDS is a slow-neutron detector, covering emission angles from 25–60° with respect to the center of MINOS. In this setup, WINDS is used to detect the recoil neutron from (p,pn) knock-out reactions.

The SAMURAI standard setup also includes a γ-ray detector named **DALI**, which is located surrounding the MINOS target. The use of DALI is important for invariant mass measurements, however, gamma-rays are only emitted from bound excited states. Since no bound excited states are expected in our analysis, the DALI information will not be used.

2.5 SAMURAI commissioning and DayOne campaign

The setup described in this chapter corresponds to the SAMURAI campaign s018 but can be, in general terms, applied to the other series of experiments analyzed in this work, namely the commissioning of SAMURAI and the DayOne campaign. There exists, however, some differences in the setup and the experimental conditions which are relevant.

Setup. The commissioning and DayOne campaign made use of the standard SAMURAI setup. Therefore the SAMURAI detectors used in the three series of experiments were the same with the exception of:

- As mentioned, the use of WINDS, the RPD and RPTOF detectors, which are related to the selection of quasi-free reactions, and the second of the hodoscopes, the HODOP, in the s018 experiment.
- The use of the thick proton target MINOS in s018 instead of a carbon solid target, as used in DayOne and the commissioning, is one of the most important differences in the setup. The coupling of MINOS with a TPC allows the vertex of the reaction to be determined and improves significantly the resolution and statistics. Since the vertex cannot be reconstructed in solid targets, the depth of the reaction vertex was assumed to be at the target mid-thickness (X and Y coordinates were extrapolated from the BDCs). As a consequence, solid targets are generally thinner because of the limitations in the energy resolution. While MINOS had a length of 150 mm, the carbon targets used were approximately 10 mm thick in order to preserve a good resolution.

Trigger logic. In multidetector setups as the one described in this thesis, the data

Experiment	Trigger
s018	(DS)Beam
	(DS)Beam(×HODO)×Proton
	(DS)Beam(×HODO)×Proton×WINDS× $\overline{\text{VETO}}$
	(DS)Beam(×HODO)×Proton×NEBULA
Commissioning	(DS)Beam × $\overline{\text{VETO}}$
	(DS)Beam×NEBULA
DayOne	(DS)Beam
	(DS)Beam×NEBULA
	(DS)Beam×DALI

Table 2.1: *General triggers for the experiments s018, the SAMURAI commissioning and DayOne. In the case of s018, the main triggers imply the detection of a proton. As for the commissioning and DayOne, a signal in NEBULA or DALI in coincidence with the SBTs triggered the record of the event. The beam trigger alone, which is present in all three experiments, allows to record events with no extra coincidences with a certain downscale (1/X). In some cases, a beam VETO is included in the trigger. This VETO was fired when the trajectory of the beam particles was out of the target cell. The beam trigger in coincidence with this VETO rejected the event.*

acquisition system (DAQ) must ensure the processing of all signals synchronously. The DAQ at RIKEN is based on a common trigger scheme, the RIBFDAQ [55], that interprets the logic signals received from all detector units and, based on the requested trigger signal, decides to record or reject the event. Due to the high rates of triggered events that we are dealing with, the dead time of the detectors plays an important role in the acquisition. In order to take into account this effect, only a fraction of the total triggered events (downscale) is normally recorded (1/10, 1/100, etc.). The choice of the trigger logic as well as the downscale depends mainly on the special requirements of every experiment. In particular, the trigger logic between the s018 and the commissioning and DayOne campaign was importantly different:

- The main triggers of the s018 campaign required that at least the SBTs (beam trigger) and the RPTOF (recoil proton trigger) were in coincidence. Consequently, mostly events where protons were emitted at average angles of 45° were taken into account. This strict trigger logic is considerably useful to select quasi-free reaction channels, which was the main goal of the experiment, as it reduces the "background" coming from other undesired channels. However, it also forbids some channels such as, for instance, elastic or inelastic scattering channels, to be observed. The list of main triggers is listed in table 2.1. Note that the beam trigger, which does not have any constraint on the reaction channel, was used with a significant downscale (1/500), implying very low statistics.

- The commissioning and DayOne campaign, which did not have this peculiar trigger logic, provide a large variety of different channels. In the commissioning, the main goal was to test the capability of the SAMURAI setup for spectroscopy studies of neutron-rich systems by using very well-known reaction channels. The DayOne cam-

paign, performed after the commissioning, aimed at the study of a big number of unknown neutron-rich nuclei populated from knock-out reactions. In both experiments, the main trigger involved the detection in coincidence of the beam with some other decay particle, such as one neutron in NEBULA or gamma-rays in DALI (see table 2.1). For more detailed information on the electronics and DAQ of Dayone see [7].

Chapter 3

Calibrations

Contents

This chapter presents the description of the detector calibrations of the experiment s018. The other experiments included in this work, the SAMURAI DayOne campaign and the SAMURAI commissioning, have comparable analysis techniques, with the exception of the methods followed for the analysis of MINOS. For detailed information related to their specific calibrations and experimental conditions the reader can refer to [3, 7].

3.1 Identification of the beam

Beam isotopes are separated and selected in the BigRIPS separator, as explained in section 2.1.2. The identification of the beam species is performed event-by-event from the reconstruction of the ion atomic number Z and the mass-over-charge ratio A/Z. At F13, corresponding to the entrance of the SAMURAI experimental room, a rough beam **p**article

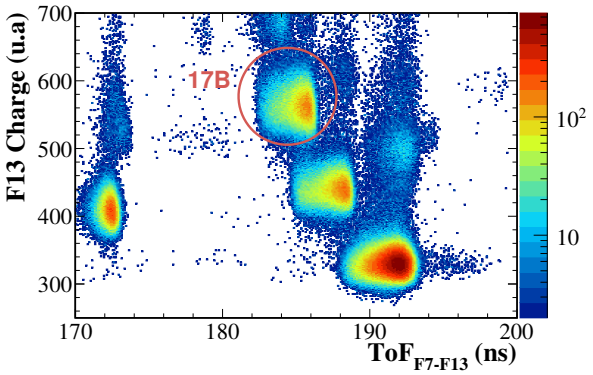

Figure 3.1: *Identification of the isotope of interest in the beam using the deposited energy in F13 and the ToF between the focal planes F7 and F13. The ions included in the beam are* ^{11}Li, ^{12}Be, ^{14}Be *and* ^{17}B.

identification (PID), from the BigRIPS original matrix, can be obtained. The reconstructed Z and A/Z can be improved by applying a set of corrections based on the particle position and/or the $B\rho$ at the focal planes where a PPAC is implemented. As the selectivity resolution is not a major issue for our experiment due to the small number of species present in the beam, only modifications in the F13 focal plane have been taken into consideration.

SBT: Time calibration As already mentioned in the previous chapter, two scintillators (SBT1 and SBT2) are located at F13 in order to measure the time (beam trigger) and charge of the incoming beam at the entrance of SAMURAI. The two PMTs positioned at the edges of each detector permit the two-fold collection of light. The evolution of the charge collected by a PMT as a function of the hit position in the plastic can be described as,

$$Q_{L/R} \;=\; Q_0 \exp\left(-x_{L/R}/\lambda\right) \tag{3.1}$$

where $Q_{L/R}$ is the charge deposited in the PMT left (L) or right (R), $x_{L/R}$ the distance from the interaction in the detector to the corresponding PMT, Q_0 is the initial charge deposited by the particle and λ the light attenuation parameter. Hence $Q = \sqrt{Q_L \times Q_R}$ is, within the assumption of Eq. 3.1, proportional to the total deposited energy of the detected particle. Since the isotopes are supposed to be fully stripped, the deposited energy can be assumed to be proportional to the atomic number Z of the nucleus. As for isotopic identification, taking into consideration the time-of-flight between F13 and F7 is enough to separate the beam species with no further corrections in BigRIPS, given that only one nucleus per isotopic chain is expected or at most, two of them with very different A/Z (see Fig. 3.1).

In order to reduce the background, the average time of both SBTs is used to determine the time at the focal plane F13. The ToF can be easily calculated by the time difference between the focal planes F7 and F13 as,

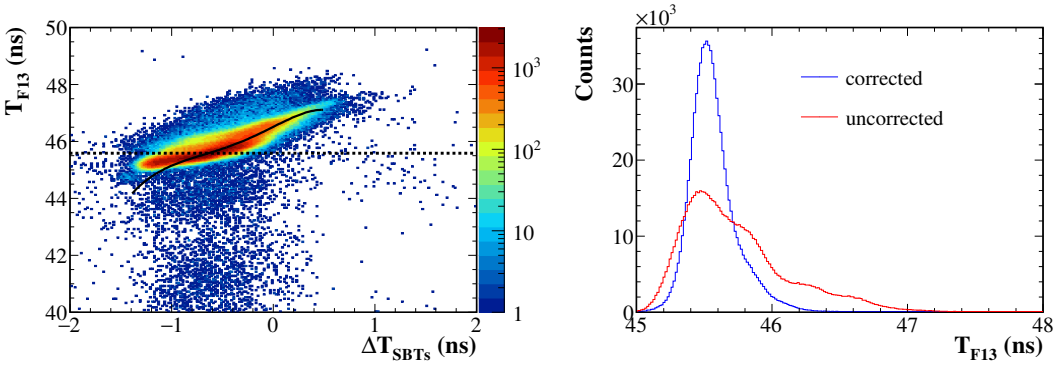

Figure 3.2: *F13 time correction. On the left, dependence of the time signal at F13 with respect to the vertical position Y obtained from the time difference. The dotted line represents the average of the time distribution and the plain line the fifth-order fit used to correct the distribution. On the right, T_{F13} resolution before (red) and after corrections (blue).*

$$\mathrm{ToF_{F7\text{-}F13}} = \frac{T_{\mathrm{SBT1}} + T_{\mathrm{SBT2}}}{2} - T_{\mathrm{F7}} + T_{\mathrm{offset}} \tag{3.2}$$

where T_{offset} is an offset included to take into account the time propagation delay. This offset is estimated from the central value of the magnetic rigidity, $B\rho_0$, measured at F7, using a small dispersive momentum run in which slits prevent particles out of the central trajectory to continue. The velocity β of a given isotope with known A/Z can be calculated by employing the relation between the velocity and the magnetic rigidity described by Eq. 2.1, as the $B\rho_0$ is assumed unchanged from F7 to F13 (delivery line). Since the distance between focal planes is known, an offset is then deduced from $\beta = L/\mathrm{ToF}/c$ in order to match the estimated velocity.

Furthermore, the F13 time resolution is particularly relevant as it is the reference time for the whole analysis at a later stage, such as the calculation of the ToF of neutrons. In this sense, the time measured at F13 has to be independent from the nature of the particle, *i.e.* from the deposited charge in the detector, and the position of the interaction. The time dependence with the charge is a very well-known effect commonly known as *slew effect* and its correction is detailed in Sec. 3.5.2. As an example, Fig. 3.2 illustrates how the time resolution is improved by reducing the position-related dependency of the time signal, in this case, applying a fifth-order polynomial correction.

3.2 Fragment PID

Scintillator HODOSCOPEs (HODOF, HODOP) are employed to identify the heavy fragments by means of the reconstruction of the atomic number Z and mass-over-charge ratio A/Z. The position of the detectors with respect to the SAMURAI magnet and to FDC2 is such that, generally, the highest A/Z ratios are detected in the first plastics of the HODOF, moving to the HODOP as A/Z decreases. Since beam ions do not have the same velocity, the determination of Z and A/Z is done separately for each of the beam species. The next section describes the methods used for the fragment identification that,

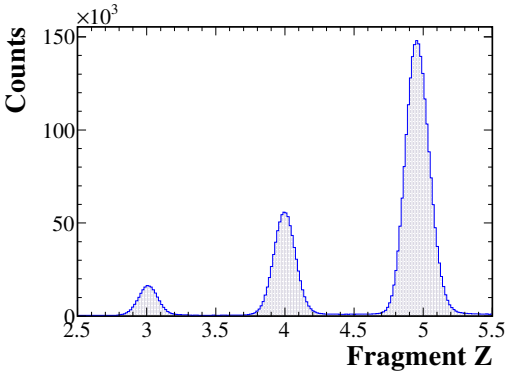

Figure 3.3: *Identification in Z from the ^{17}B beam.*

unlike previous works[3, 7], did not involve the reconstruction of the $B\rho$ of fragments.

3.2.1 Z calibration

Similarly to other plastic scintillators taking part in the experimental setup, the presence of two PMTs permits to improve significantly the time and charge resolution, as their correlation discards spurious events. The time and charge are, therefore, calculated as in section 3.1, like the average of both PMTs signals. In a similar fashion to the beam PID, the atomic number Z can be deduced from the proportional relation with the deposited energy of the fragment in the detector. Taking into account that an ion can interact in several plastics of the HODOSCOPE, only the plastic corresponding to the maximum deposited energy is used for the Z reconstruction.

In order to improve the resolution, some corrections over the charge are performed to remove slew-related effects. As detailed in the NEBULA part of the analysis, in Sec. 3.5, the detection position can be related to the difference between both PMTs signals. In the case of plastics in the HODOSCOPEs, their PMTs are positioned at the upper and lower edges of the detector, giving the information about the vertical Y position. First, plastics are aligned vertically one by one, assuming that the average of the $\Delta T = T_{up} - T_{\text{down}}$ distribution must be centered on zero. A second-degree polynomial correction is followed to rectify the dependence of the light collection with the position $\Delta T \sim Y$ in the plastic.

However, the major contribution to bad resolution is the artificial reliance of the charge collection on the average time given by the PMTs. This dependence is corrected with a linear function separately for every plastic. The Z value is automatically found as the projection of the corrected charge, as illustrated in Fig. 3.3.

3.2.2 AoZ determination

Contrary to the identification of the beam, the ToF alone is not sufficient for selectivity, as a wide variety of fragments are created in knock-out reactions. The isotopic separation for a given Z is achieved in conjunction with the reconstructed position in the HODOSCOPE given by FDC2. The method presented below does not involve the reconstruction of the $B\rho$ of the fragment, which can be necessary when a high resolution in A/Z is required. Since our goal is to identify ^{14}Be isotopes, whose neighbour isotope ^{13}Be is unbound, a

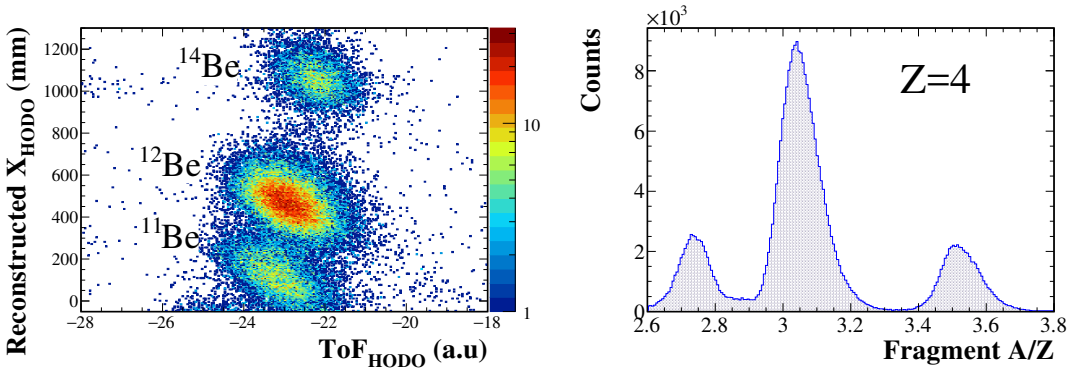

Figure 3.4: *Identification in A/Z for Beryllium isotopes, $Z = 4$, from a ^{17}B beam. On the left, reconstructed X position in the HODOSCOPE as a function of the ToF. On the right, reconstructed A/Z.*

very good resolution is not needed in order to select unambiguously the nucleus of interest.

Plastics are aligned in time by using empty target runs with decreasing magnetic field values. This allows all plastics to have enough statistics as isotopes swipe all the long from HODOP to HODOF as the magnetic field decreases. The time of one of the plastics is taken as a reference, the other plastics being aligned to this referent time. In order to do this, we take into account only events where a same charged particle has interacted twice in two consecutive bars in the HODOSCOPE. Since the time difference of these two close hits should be centered around 0, we can easily extract an offset to align the pair of plastics.

The position of the interaction in the HODOSCOPE can be extrapolated with the angle and position measured in FDC2. The trajectory of a particle in the drift chamber is defined by the position at the center of the detector, X_{FDC2}, and the angle in the XZ plane, θ_{XZ}. With these parameters, the position X_H in the HODOSCOPE is calculated as

$$X_H = X_{\mathrm{FDC2}} + (Z_H - Z_{FDC2}) \tan(\theta_{XZ}) \tag{3.3}$$

where $Z_H - Z_{\mathrm{FDC2}}$ is the distance to FDC2 in the Z-axis. Isotopes are isotopically separated when plotting X_H as a function of the ToF. A/Z is identified with each of the $X-$ToF lines, as shown in Fig. 3.4 (left). Note that in this figure no offset for ToF is added, and the ToF presented does not correspond to physical values. The A/Z ratio can be derived as a projection of these lines onto a perpendicular line (see the right panel in Fig. 3.4).

3.3 Drift chambers

3.3.1 Drift Time Calibration

The particle tracking in the drift chambers is possible by determining the **drift distance** D of the electron-ion pairs towards the closest anode (or cathode). In order to calculate

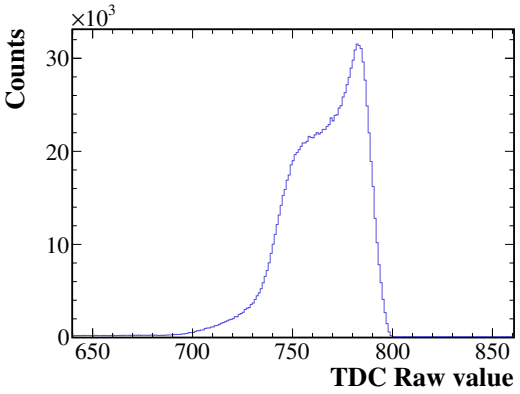

Figure 3.5: *Raw TDC distribution of the first wire plane of the BDC2.*

this distance, the drift time of the electrons is measured by a TDC located between the SBTs and the drift chamber, from which a START and STOP signal is obtained. The relation between the two drift values is the following,

$$D = \int_{t_{start}}^{t_{stop}} v(t)dt \tag{3.4}$$

where t_{start} and t_{stop} are the beam trigger and the stopping time respectively, and $v(t)$ the drift velocity. If a cylindrical symmetry around the wires is considered, the drift velocity can be simplified as

$$v(t) = \frac{dr}{dt} = \frac{dr}{dN}\frac{dN}{dt} \tag{3.5}$$

Using this approximation, the velocity can be written as the multiplication of two independent terms: $\frac{dr}{dN}$ corresponding to the radial distribution of the ionized particles, and $\frac{dN}{dt}$ that corresponds to the drift time distribution. Assuming a non-dependent radial distribution, the drift velocity can be calculated as

$$D = \int_{t_{start}}^{t_{stop}} v(t)dt = \frac{dr}{dN}\int_{t_{start}}^{t_{stop}} \frac{dN}{dt}dt \tag{3.6}$$

Since the time distribution dN/dT is experimentally accessible and it can be measured, the integral is easily calculated. The drift distance and this integral are proportional and dependent on the radial distribution. However, this proportionality can be found as the two extreme values for the drift distance are well-known: The maximum value corresponds to half of the distance between two near wires, while the minimum distance is 0, meaning that the ions have been ionized next to a wire. For further details see [7].

3.3.2 Tracking algorithm

The detection position in the vertical and horizontal directions is calculated independently and in the center of the drift chamber. For that purpose, the trajectory in the chamber is reconstructed from the triggered wires using a linear regression by which the best χ^2 is chosen. The linear regression takes into account the position of the triggered wire plus the drift distance. Since the direction of the incident particle with respect to the wire is unknown, the ion is supposed to be from the wire at a distance equal to the drift distance but either on the left, right, in front or behind the wire. The four possibilities are tested as a part of the linear regression to improve the precision of the tracking. Along with these combinations, the linear trajectory is reconstructed using as many points as planes the drift chamber has, which implies the use of just one wire per plane. When several wires are triggered in a same plane, all combinations with the other wire planes are tested. The multiple combinations result in a very computationally demanding algorithm, specially in the case of FDC2.

3.3.3 Alignment of the drift chambers

The BDCs, located at 1300 mm and 200 mm upstream the hydrogen target, are used as beam trackers. The trajectory of the beam is fundamental to reconstruct the exact position where the reaction has taken place in the target, especially in (p, pn) reactions. In these types of reactions, where only one proton is emitted, it becomes necessary to determine the reaction point along the Z-axis using the beam trajectory given by the BDCs (see next Sec. 3.4.2). An important aspect to consider in order to accurately calculate the position of the beam is the relative alignment between the drift chambers.

The alignment is achieved by using all three drift chambers in the beam line: BDC1 and BDC2, positioned before the target, and FDC1, located after the target. FDC1 and BDC1 are chosen to be fixed while BDC2 is to be aligned with respect to the other two. The method is only valid if the MINOS-TPC is emptied, so that the unreacted beam can reach FDC1 and be measured. From the positions X and Y measured in BDC1 and FDC1, the position of the beam particles are interpolated in BDC2 supposing a linear trajectory (see Fig. 3.6). The equation of the reconstructed line connecting BDC1 and FDC1 along the XZ plane is presented by the equations

$$\theta_x = \arctan\left(\frac{X_{FDC1} - X_{BDC1}}{Z_{FDC1} - Z_{BDC1}}\right) \tag{3.7}$$

$$X_{BDC2} = X_{BDC1} + (Z_{BDC2} - Z_{BDC1})\frac{X_{FDC1} - X_{BDC1}}{Z_{FDC1} - Z_{BDC1}} \tag{3.8}$$

which are similar in the YZ plane. The difference between the measured and the interpolated position in BDC2 will give us the offset that has to be applied in order to align the drift chambers. BDC2 is shifted along the X- and Y-axis according to this offset. As an example, in Fig. 3.7 (right) the distribution used to align the Y position of BDC2 is shown. Once the offset is applied, the alignment can be checked by comparing the detected

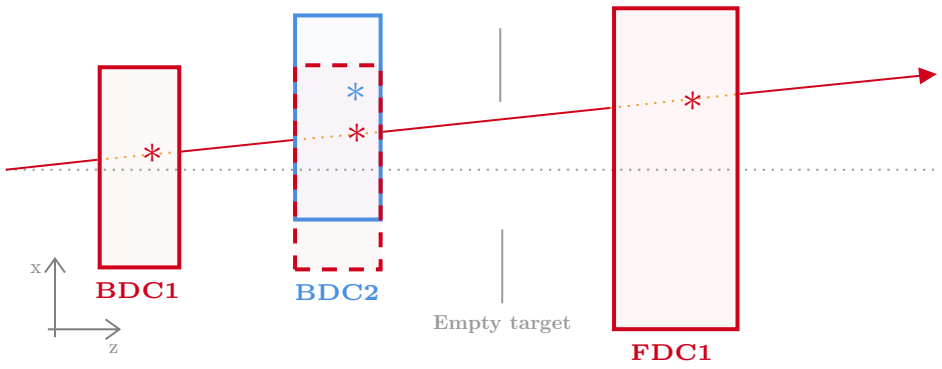

Figure 3.6: *Schematic overview of the drift chambers alignment. BDC1 and FDC1 are fixed. BDC2 (blue) represents the BDC2 original relative position. The asterisks represent the detection position of the beam in the drift chambers. The position in BDC2 is interpolated using BDC1 and FDC2, and an offset is added in order to align BDC2 with respect to the other drift chambers (red).*

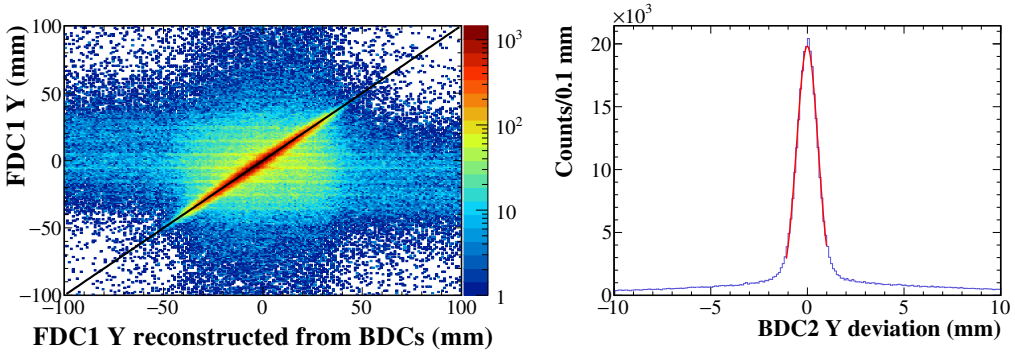

Figure 3.7: *Drift chambers alignment. On the left, correlation plot between the Y position measured in FDC1 with respect to the reconstruction position using the BDCs, once BDC2 is already aligned. On the right, deviation of the measured and the interpolated position along the Y-axis for BDC2.*

position in FDC1 with its reconstructed position from BDC1 and BDC2, as shown in the left panel of Fig. 3.7. Note that the alignment is done only for X and Y directions, as Z position is unambiguously determined.

3.4 MINOS Calibration

3.4.1 TPC drift velocity

The reaction point is determined from the reconstructed trajectories of the emitted protons, detected by the TPC surrounding the target. As in the case of the drift chambers, position detection in the TPC is defined from the drift velocity of the electrons and can be calculated as

$$V_{drift} = \frac{L_{TPC}}{t_{stop} - t_{start}} \tag{3.9}$$

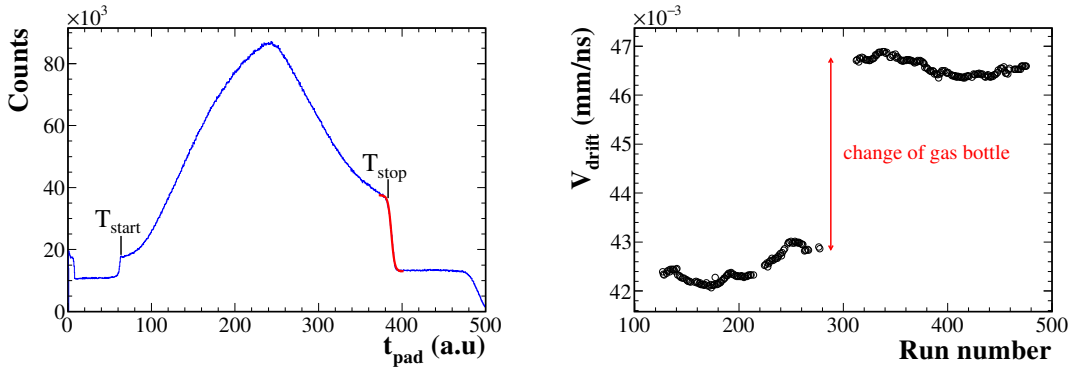

Figure 3.8: *On the left, time distribution t_{pad} of the TPC. The maximum of the distribution is determined by a fit with the Fermi function described by the Eq. 3.10. On the right, evolution of the drift velocity as a function of the run number. The gap is due to a change of the gas bottle of the TPC.*

where L_{TPC} is the length of the TPC, 300 mm. The time t_{start} corresponds to the time at which the first primary electron reaches the micromegas mesh. Since these electrons have been ionized at the level of the micromegas, the drift is equal to 0. As a consequence, t_{start} is independent from the drift of the electrons and will remain constant over time. Electrons which have been drifted from the end of the TPC will define t_{stop} of the time distribution. Contrary to t_{start}, t_{stop} can be very changing over time as the drift path of the electrons is modified by impurities in the gas, as well as by small changes in the conditions of temperature and pressure in the TPC.

For a good reconstruction of the vertex, the drift velocity is calculated run by run in order to take these changes into account (see Fig. 3.8, right). As the minimum drift time is set constant for all runs, the only parameter that varies in the determination of the drift velocity is t_{stop}. The maximum of the drift time is thus represented by the mid-point in the downward slope of the TPC time distribution t_{pad}, as illustrated in Fig. 3.8 (left). For each run, this point has been calculated by fitting the slope by a Fermi function,

$$f(t) = \frac{p_0}{1 + exp((t - t_{stop})/p_1)} + p_2 \tag{3.10}$$

where p_0, p_1 and p_2 are constants.

3.4.2 Calibration of vertex position

Once the drift velocity is determined, the position of the drift electrons in the TPC can be calculated. As only a longitudinal electric field is applied, tracks detected in the TPC are linear (see Fig. 3.10). The tracking of the emitted protons is achieved using the **Hough transform** method, a graphical technique to recognize straight lines. This method is applicable for 3D as well as for 2D space using the same principle: for every point, all possible lines to which the point may belong are scanned. Each of these lines can be associated with the parameters (ρ, θ), ρ being the closest distance to the origin and θ the angle with respect to the horizontal axis (see Fig. 3.9). The parameters (ρ, θ) define the *Hough space*, where lines passing through a single point define an unique sinusoidal curve.

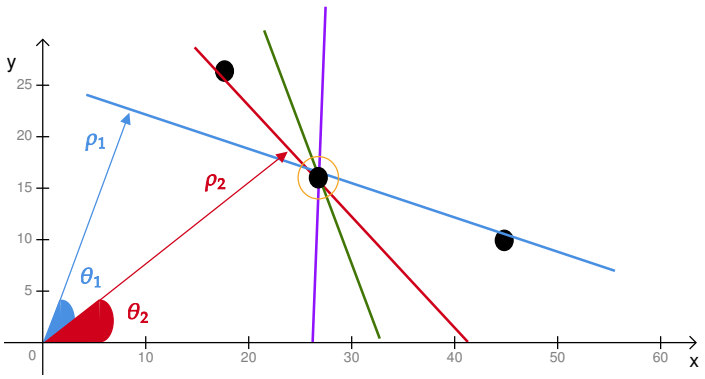

Figure 3.9: *Hough transform example for a 2D case. The parameters ρ and θ are calculated for each of the possible lines passing through a given point, in the example, the point of the middle. Colinear points will give the same ρ, θ values.*

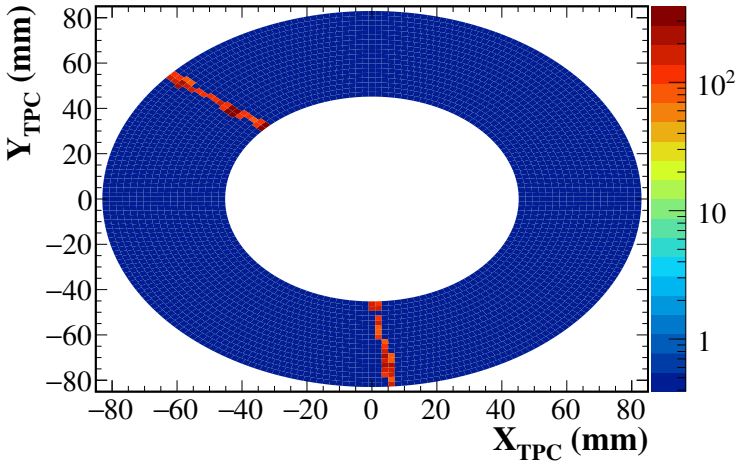

Figure 3.10: *Example of tracking in the TPC of two protons emitted during the reaction. The two trajectories are recognized and reconstructed by the Hough transformation. The extrapolation of the proton trajectories will determine the reaction vertex in the target cell.*

The curves corresponding to co-linear points will cross at a common ρ and θ by which the straight line containing all points can be calculated. A more detailed explanation about this method and how it is implemented in MINOS can be found in [53].

As shown in Fig. 3.11, the reconstruction of the vertex in the target cell is determined by the intersection of the tracks of the outgoing particles. However, due to the tracking resolution of the TPC and the straggling of particles through the target, the tracks do not intersect in a common crossing point. The reaction point is thus calculated as the mid-point corresponding to the minimum distance of the two tracks. In $(p, 2p)$ knockout reactions these two tracks are the two proton tracks detected in the TPC, while one proton track is combined with the trajectory of the beam for (p, pn) knockout reactions. By way of example, Fig. 3.10 shows the tracking of two protons in the TPC for a single event.

Since the vertex calculation is performed within the TPC reference frame, the MINOS-TPC has to be aligned with respect to the drift chambers in order to obtain the position

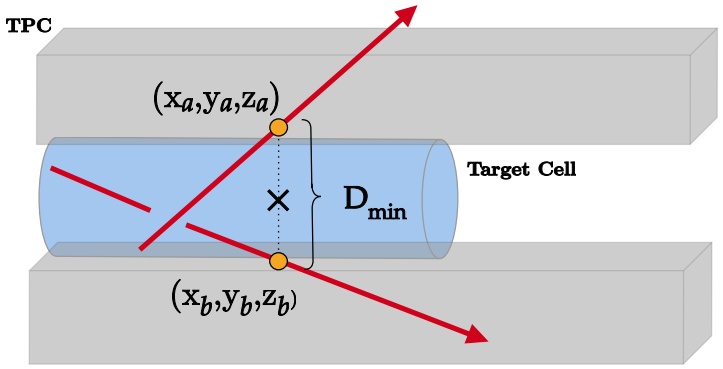

Figure 3.11: *In the case of detection of two protons, the point of the reaction, noted* $\times$ *here, is determined by the intersection of the two reconstructed trajectories given by the TPC. The crossing point of two 3D straight lines is defined as the mid-point of the minimum distance* D_{min} *between them.*

of the reaction point as precisely as possible.

X and Y positions are aligned by means of the BDCs. In the case of a reaction involving the emission of two protons, the point of interaction in MINOS should be common to the trajectories of the two protons, depending entirely on the TPC, and to the trajectory of the beam reconstructed by the BDCs. Following this principle, the Z vertex position is calculated using only the events for which two protons are emitted. The reconstruction of the vertex is performed with the two proton tracks detected in the TPC, without taking into account the BDCs. The vertex positions X and Y are then compared to the X and Y positions extrapolated from the trajectory of the beam given by the BDCs for a same Z position. A difference between them indicates a misalignment from which an offset can be calculated.

Z position of the vertex is calibrated from empty target runs, where MINOS is still present but the liquid hydrogen cell has been emptied. Reactions can only take place in the extremes of the target cell, *i.e.*, at positions Z=0 mm and Z=150 mm. A shift is then applied to match these positions. Moreover, the calculation of the drift velocity in the TPC can also be checked from empty target runs: as the entrance and exit of the target cell is very well defined (see Fig. 3.12), the size is easily calculated. This gives us a good idea of the accuracy of the drift velocity calculation, which is closely related to the size of the target.

The resolution of the reconstructed vertex can be calculated using proton knockout reaction channels. In these reactions, the two protons tracked in the TPC are normally used to determine the reaction point, however, it is not the only possible way. The vertex can also be calculated using the beam trajectory and one of the protons. In total, three different combinations can be applied to derive the vertex and all three should be in agreement. The resolution is, therefore, checked by comparing the vertex position obtained with the two proton tracks and with the trajectory of the beam in combination with one of the protons, as shown in Fig. 3.13. The resolution obtained for the reconstructed positions

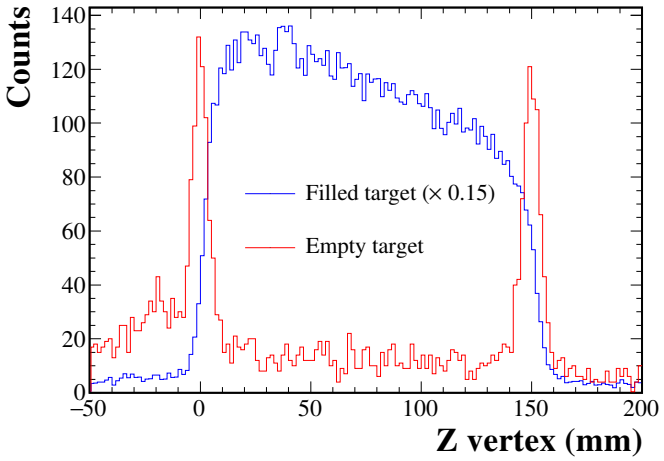

Figure 3.12: *Calibrated Z vertex of MINOS. In red and blue, runs with empty and filled target cell are compared. The peaks at Z=0 and Z=150 mm represent the entrance and exit of the MINOS target cell.*

is 5.6 (X), 2.6 (Y) and 7.7 (Z) mm.

3.5 NEBULA

The first contribution to the resolution of the relative energy comes from the precise determination of the vertex in the target. It is followed by the resolution of the neutron energy reconstruction, which is dominated by the spatial resolution since the momentum of neutrons is deduced from the ToF and the distance between NEBULA and the target. It is thus essential to properly calibrate the detection position and time in NEBULA. Moreover, the neutron momentum is taken as a reference for the momentum reconstruction of all other particles (see Sec. 4.1.3).

In this section, the methods used in the calibration of the position, time of flight and charge in NEBULA are explained, as well as the cross-talk rejection algorithm.

3.5.1 Light output calibration

The charge collected from each photomultiplier (*up* and *down*) for each detector has to be calibrated separately according to the equation,

$$Q_{cal} = a\,(Q_{raw} - Q_{ped}) \tag{3.11}$$

where Q_{cal} and Q_{raw} are the calibrated and raw charge respectively, and a and Q_{ped} the parameters of calibration to be found. Three points of reference are used in order to determine these parameters: the pedestal, the cosmic rays and a source of AmBe.

- The **pedestal** is the signal observed in the absence of radiation. It is induced by

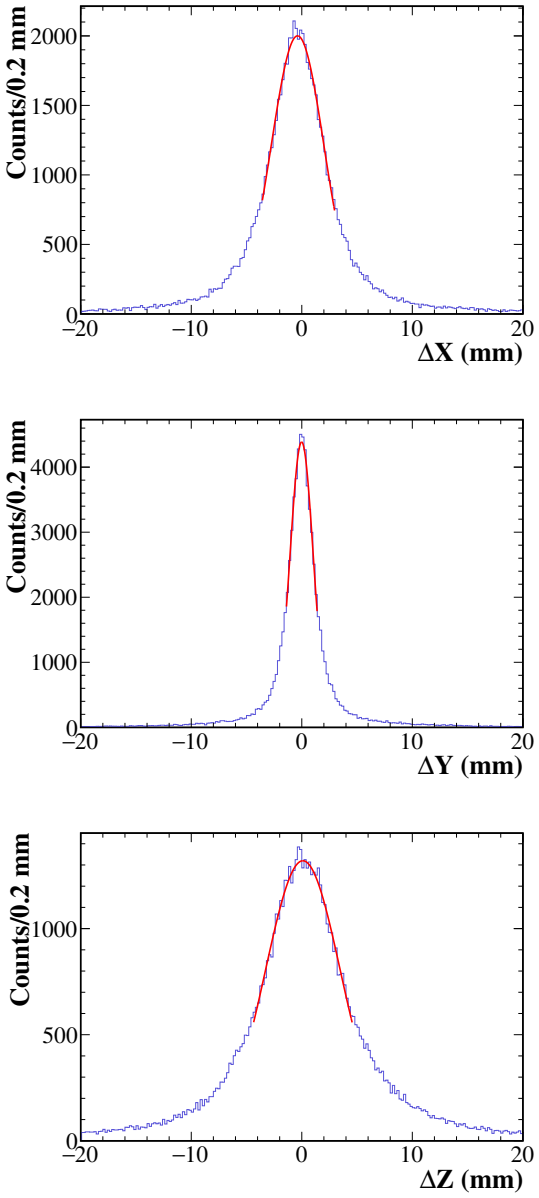

Figure 3.13: *Resolution of the reaction point in MINOS for the X, Y and Z position.*

the electronic noise of the acquisition system and corresponds to a charge equal to 0. The determination of the pedestal is therefore the first step.

- The **cosmic rays** are used for the calibration of the bars at energies of ∼1/6 of the dynamic range. The energy of the muons, produced in the atmosphere from collisions of cosmic particles, is very well known, around 4 GeV at the earth surface. Taking into account the incident angle of muons, the average energy loss in NEBULA is estimated to be at about 29.9 MeV [56]. The shape of this energy loss is fitted with a Landau function [57] convoluted with an exponential function in order to describe the background.
- An **AmBe source** is used as a source of γ-rays at an energy of 4.4 MeV. However, the cross section of the photoelectric effect in an organic scintillator as NEBULA (BC408) is very low compared to the Compton effect. Since the value of the Compton edge is fixed kinematically and can be calculated from the known energy of the γ-ray, this point serves as a reference. Its theoretical value is easily calculated as $E_{edge} = E_\gamma/(\frac{mc^2}{2E_\gamma} + 1) = 4.158$ MeV. Due to the detector response, it is difficult to determine where the Compton edge lies. A common procedure is to determine the mid-point of the slope, although other techniques are also consistent [7]. In our case, a Fermi function similar to the Eq. 3.10, is chosen to calculate the Compton edge.

These three reference points have to be determined for the upper and lower PMTs, located at the extremes of every bar in NEBULA. An example of results obtained by these calibrations is shown in Fig. 3.14. Once each PM is calibrated, the total charge is calculated in a similar way to that of other scintillators equipped with two PMTs, as the product of both PMTs charge signals

$$\mathrm{Q}_{total} = \sqrt{\mathrm{Q}_{up}\mathrm{Q}_{down}} \tag{3.12}$$

3.5.2 Time Calibration

TDC Calibration

The **T**ime to **D**igital **C**onverter, TDC, is a unit that digitalizes the output pulse proportional to the time period between two logic pulses, *START* and *STOP*. It is used by a large number of detectors taking part in the SAMURAI setup (Plastic scintillators, NEBULA, HODOSCOPE...). The time calibration for TDCs and therefore for all these detectors is done using a *timing calibrator* that generates pulses at a very well known frequency. By knowing the time interval between two pulses, the proportional coefficient between the output signal registered in the TDC and the real physical time can be found as shown in Fig. 3.15.

Time slew correction

One of the main problems affecting the time resolution is the **Slew or Walk effect**. The slew effect refers to a dependency of the generated time signal on amplitude and comes directly from the method used to discriminate signals. As represented in Fig. 3.16, in the

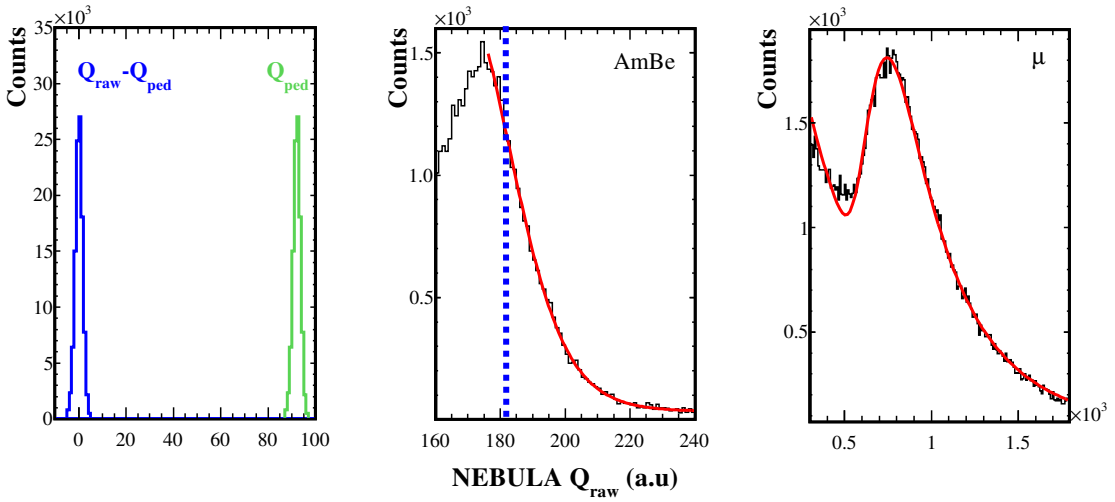

Figure 3.14: *Calibration example for upper PMT in detector 15 of NEBULA. On the left, pedestal signal. On the right, Fermi function fit to determine the compton edge of a gamma emission of 4.4 MeV from a AmBe source. On the right, high-energy calibration using cosmic rays. The energy distribution is fit by a Landau function plus an exponential function to describe the background.*

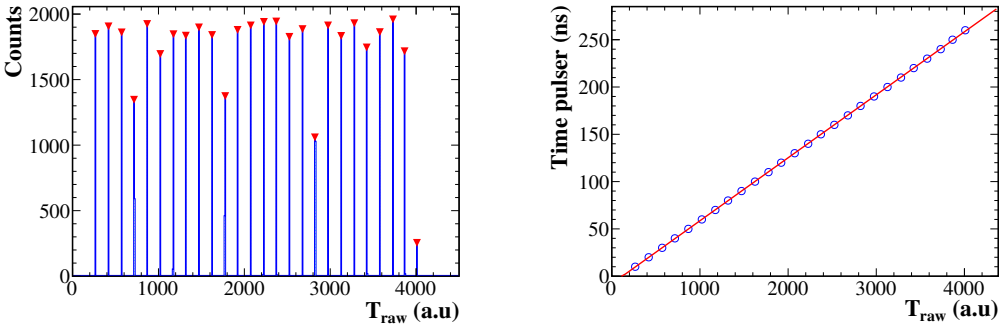

Figure 3.15: *TDC calibration for ID=15 in NEBULA. A pulser time is used to relate the electronic time to a physical time. On the left, detection of time pulses by the TDC. On the right, correlation between the TDC raw time with the time pulser in ns.*

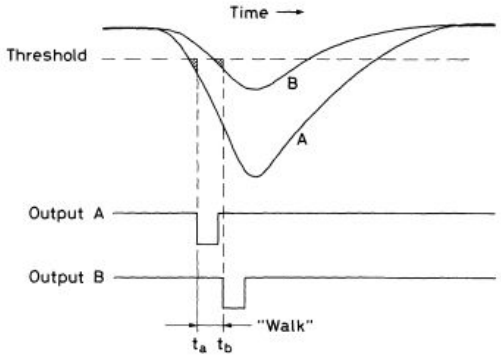

Figure 3.16: *Walk effect produced by a fixed threshold discriminator (leading-edge).*

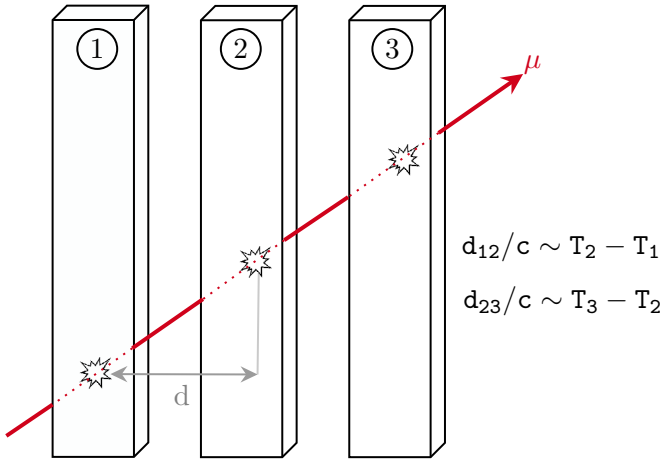

Figure 3.17: *Schematic representation of the procedure used to calibrate the time slew effect using the cosmic rays. The trigger condition for muons is that at least 15 out of 120 detectors are fired. The interaction point is calculated from the reconstructed trajectory and the ToF calculated assuming a speed equal to the speed of light.*

case of using a fixed threshold as discriminator, given two signals with different amplitude but coincident in time, these will be triggered at different times due to the difference in the pulse height, though being exactly coincident in time. In order to improve the time resolution of the TDCs, the slew effect is corrected. The procedure varies slightly according to the detector but follows the same idea.

The method used for the time calibration in NEBULA is based on the detection of cosmic-ray muons. As explained above, the utility of the constant flux of cosmic muons as a calibration source is the fact that their properties, such as the energy, are well known. Since a single muon traverses several detectors in NEBULA, the time difference between bars can be related from the reconstruction of their trajectory (see Fig. 3.17). Assuming a speed for the muons equal to the speed of light, the slew effect can be corrected by means of the time of flight of muons between two consecutive detectors in one layer. The ToF can be deduced either directly from the time difference registered by the TDCs or from the distance between the two points of interaction in the detectors. The difference in the shape of the ToF distribution between these two methods manifests the walk effect and

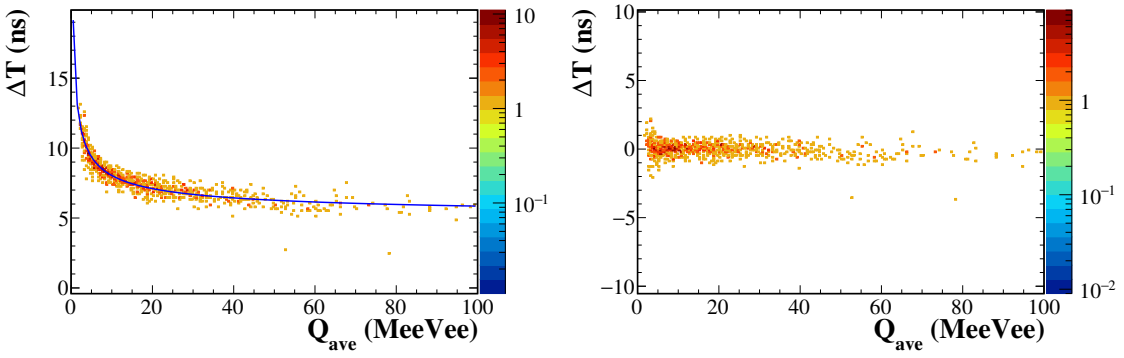

Figure 3.18: *Time slew calibration for ID=15 in NEBULA. On the left, the time difference as a function of the average charge in the detector before the slew correction. On the right, the same distribution once the correction is applied.*

can be corrected if plotted as a function of the deposited charge. The dependency of the time with respect to the charge is described with the following equation

$$T = A + \frac{B}{\sqrt{Q}} \tag{3.13}$$

where T represents the time and Q the measured charge in the detector. An independent correction is applied for each detector in NEBULA. In Fig. 3.18, a typical time distribution before and after the correction is shown for one of the detectors.

Neutron Time of Flight

The time of each detector is calculated as the average of the measured time by the TDCs in the extremities

$$T = \frac{T_{up} + T_{down}}{2} \tag{3.14}$$

However, the time measured by each detector is independent and does not correspond to the real physical time of the detected particle. For the reconstruction of the neutron time of flight, all detectors must be aligned together in time with respect to a common reference. To this aim, an aluminum solid target, instead of MINOS, has been used to produce γ-rays that are used as reference: the distance between the target and the interaction point in NEBULA is known and the ToF can be easily calculated for γ-rays. The standard procedure implies a first relative alignment of all plastics using the γ-rays detected in NEBULA, unambiguously discriminated from neutrons by ToF. Due to a problem occurred during the experiment, the statistics of γ-rays are too low for most of the detectors and therefore, cosmic rays are used instead for this first alignment. The relative alignment is followed by a global alignment by which an offset T_0 is added to the ensemble of detectors.

- *Relative Alignment.* The objective of the relative alignment is to correlate the time with respect to a reference detector. In our case, this is done with the reconstruction

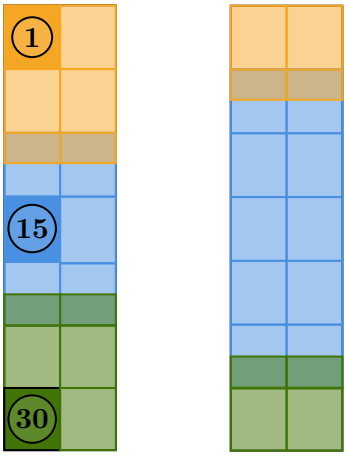

Figure 3.19: *Cluster method to calibrate relative time in NEBULA. The alignment is performed by groups for which a reference bar is designated. The alignment of groups is achieved with the overlap detectors.*

of the trajectories of the cosmic muons traversing NEBULA. The time of two hits belonging to the same trajectory, and therefore, corresponding to the same particle, can be related as

$$T_1 = T_2 + d_{12}/c + T_{off} \tag{3.15}$$

where T_1 and T_2 are the times measured for the two hits, d_{12} the distance between their detection point and T_{off} the offset time applied to align both times to the same value. Unfortunately, it is almost impossible to relate all detectors to only one reference detector, as the flux of cosmic muons strongly depends on the incident angle. Instead, several detectors are chosen as reference and the relative alignment is performed by groups. These groups are then aligned together with respect to the most centered group (ID=15 in our case) using the detectors located in the overlap of the groups. An schematic view of the method can be seen in Fig. 3.19.

- *Global Alignment (T_0).* While neutrons are slower and have an energy-dependent speed, γ-rays, faster and with a constant speed, give rise to a very narrow time distributions very well separated from the broad distribution coming from neutrons. The time of flight between NEBULA and the target is calibrated using the ToF of γ-rays, by shifting the time distribution by an offset T_0. This offset is calculated as the difference between the expected ToF that γ-rays should have and the measured ToF in the detector number 15, which is in the center and has the maximum statistics. The calibrated time-of-flight is shown in Fig. 3.20, where the two structures (neutrons and γ-rays) can be distinguished.

3.5.3 Y position

As the neutron is assumed to interact in the center of the bar in the X-axis, the horizontal position of the interaction is determined by the fixed position of the detector, giving a resolution of ± 6 cm. Considering that the vertical size of one bar in NEBULA is 180 cm, the detection position along the Y-axis cannot be similarly assumed to be the center of the

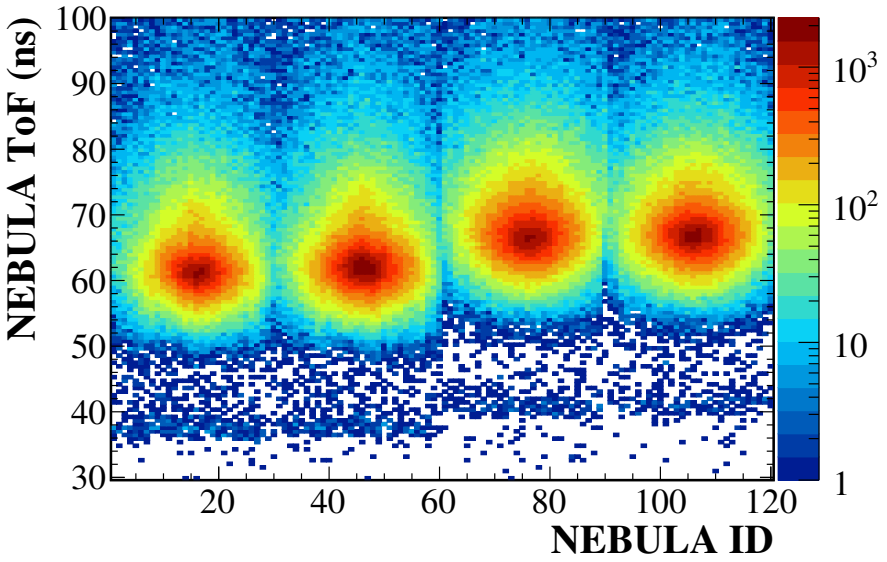

Figure 3.20: *Time of flight between NEBULA and the Al solid target as a function of the ID in NEBULA. The γ-rays distributions are centered around 40 ns, though statistics is very limited in comparison with neutrons (big structure at higher times).*

bar since that would result in a very bad resolution. The Y detection position is, instead, reconstructed based on the time difference between the two PMTs of each bar, following the linear proportionality

$$Y \sim \delta T = T_{up} - T_{down} \tag{3.16}$$

Assuming T_{up}=T_{down} to correspond to the middle of the bar and T_{up} or T_{down} equal to 0, being the extremes of the detector, the proportionality is found. The vertical position has been calibrated using again the reconstructed trajectories of the cosmic rays. From the reconstructed trajectory, the vertical position of the interaction point can be determined, by which the correlation between the position and the time difference is deduced. In Fig. 3.21, the reconstructed Y position before and after the calibration is shown.

3.6 Cross-talk Method

As mentioned in the previous chapter, a neutron can induce a signal in several detectors of NEBULA, a phenomenon commonly called **cross-talk**. At an energy of around 250 MeV, collisions are the main mechanism of interaction by which neutrons deposit a part of their energy in the detector. One neutron can therefore interact several times in different bars of NEBULA, since it will likely pass through the neutron array without losing all its energy. These multihits can be wrongly interpreted as events coming from the detection of independent neutrons, entailing misleading results. Moreover, multihits can also be caused by the detection of other particles such as charged particles. Although VETOS located in front of each wall of NEBULA reject charged particles arriving the detector, recoil protons produced by the collisions of neutrons cannot be *a priori* distinguished

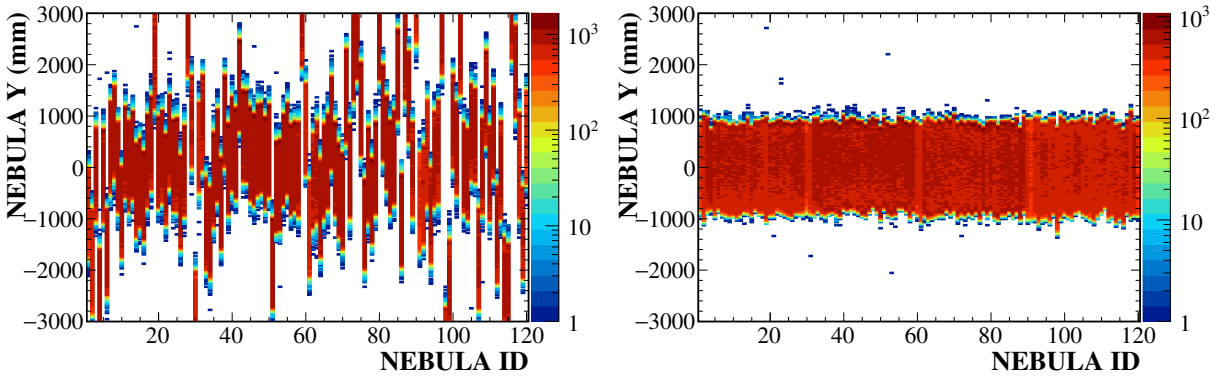

Figure 3.21: *NEBULA Y using the reconstructed trajectory of cosmic rays before (left) and after (right) the calibration of the position is applied.*

from real neutron events. These protons can travel to the neighbouring detectors and be erroneously interpreted as "neutrons". A cross-talk rejection algorithm, by which the real number of neutrons is found, becomes essential for the analysis of multineutron events.

The cross-talk rejection is not of great importance when analyzing channels where only one neutron is emitted, but indispensable when analysing multineutron channels. In the one-neutron case, only the first neutron interaction, that is, with the shortest time of flight, is taken into account and considered as a real neutron. Any other particle detected after the time of this first neutron is rejected as being considered as a cross-talk event. The "fastest" neutron is also used as a reference for multineutron channels. Since all cross-talk events come later in time, the first neutron can always be considered as a real neutron event. Taking the first neutron as the starting point of the algorithm, cross-talk rejection is applied to all combinations of neutron pairs.

The goal of the algorithm is to identify real neutrons by rejecting the "fake" neutron events while keeping the "good" ones. However, the conditions applied to reject the cross-talk rejects also a portion of the real neutron-pair events. In order to optimize the algorithm, suitable conditions, representative of cross-talk events, have to be found along with a compromise, based on how severe we want these conditions to be. The stricter the condition is, the more cross-talk is rejected, however, the more good events are also eliminated. The algorithm is developed based on a combination of cluster- and causality-based conditions and put to the test by means of simulations and experimental channels where only one neutron is emitted. In general, the rejection algorithm consists of two main steps:

First step: Cluster Analysis. Clusterization in NEBULA aims to identify events where the interaction of a neutron has induced a recoil proton to travel to neighbouring detectors. Same-wall hits which are very close to each other are grouped together in clusters and treated as a whole for further analysis. This clusterization based on the proximity of the hits rejects not only recoil protons that could be wrongly identified as neutrons, but also real neutrons that interact in adjacent bars, which is typically the case of neutrons emitted at very low decay energies. Whether an adjacent bar has been triggered as a consequence of a (p, n) diffusion or the interaction of another neutron, cannot be distinguished. The cluster analysis implies thus a reduction in the spatial resolution of the

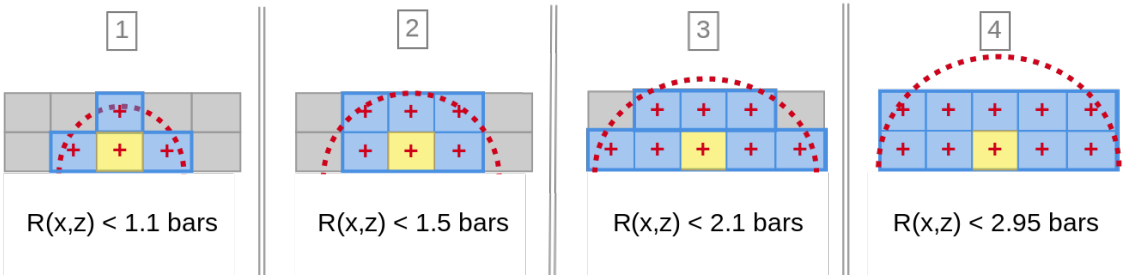

Figure 3.22: *Different conditions tested for 2D cluster method. In yellow, the reference bar is represented. The blue squares show the adjacent bars that will be included in the cluster of the reference bar.*

detector. However, the resolution can be optimized using different clusterization models.

Two methods have been tested in order to achieve the most suitable technique to identify multineutron events: the Hypersphere and the 2D clusters method.

- *Hypersphere method*: A pair of hits are grouped together if the spatial and time distance between them are content in the radius of the hypersphere defining adjacent detectors in NEBULA. The radius $\Omega(r,t)$ is a continuum variable constructed from the time and spatial distribution between two hits as,

$$\Omega^2 = \frac{(\frac{\Delta x}{r})^2 + (\frac{\Delta y}{r})^2 + (\frac{\Delta z}{r})^2 + (\frac{\Delta t}{r/\beta_{01}c})^2}{4} \tag{3.17}$$

  where $r = \sqrt{\Delta x^2 + \Delta y^2 + \Delta z^2}$, Δt the time interval between the pair of hits and $\beta_{01}c$ represents the velocity of the fastest neutron. This method is favorable to distinguish cases where, although interacting in contiguous detectors, the vertical position of the interaction of the two neutrons is rather different (*i.e.* close to the upper and lower PMT of the bar respectively for which $\Delta Y = Y_{n2} - Y_{n1} \sim$1.8 m) or the time span between the two interactions is big. Since neutron and proton masses are similar, recoil protons are not expected to be emitted in the opposite direction, as well as the time of flight is expected to be similar. Nevertheless, the radius being a continuum variable, it is difficult to determine the radius signature of cross-talk for adjacent bars.

- *2D Clusters method*: From a more intuitive point of view, cluster analysis can be conceived in 2D dimensions by taking into account uniquely the interaction position in X and Z, which results equivalent to a discrete radius when defined as,

$$R^2 = \frac{(\Delta x)^2 + (\Delta z)^2}{120} \tag{3.18}$$

  where the radius is divided by the width of a bar, 120 mm, in order to discretize the variable with respect to the number of detectors. All pairs of hits for which this 2D radius is content within a certain constant, $R(x,z) < R_{cluster}$, are considered to be in the same cluster. For instance, clusters considering only adjacent bars would translate into a cluster condition of approximately $R(x,z) < 1$, while $R(x,z) < 3$

would represent a distance of 3 adjacent bars (see Fig. 3.22). The advantage of this method is to avoid any possible error coming from calibrations, since X and Z positions are always given in the center of the detector.

Second step: Causality condition. Once clusters are identified, each of them is treated as a unique hit. The total number of hits is the result of the interaction of an unknown number of neutrons in the detector. To figure out what the number of neutrons is, a causality condition based on velocity is applied. If a neutron interacts twice in the detector, the velocity of the interaction of the cross-talk neutron, since it is the same neutron, would be smaller or at most equal to the velocity of the first neutron interaction, never greater. If the first neutron has the time to arrive to the position of the second interaction, then, this second hit would be considered as cross-talk. The condition for a pair of neutrons to be considered as two real neutrons interacting in NEBULA can be thus formulated as

$$v_{12} = \frac{\vec{r_2} - \vec{r_1}}{t_2 - t_1} > v_{01} \tag{3.19}$$

where v_{12} represents a virtual velocity reconstructed from the difference of positions and times of the two neutrons and v_{01} the reconstructed velocity for the fastest neutron. The causality condition is applied in a iterative way, starting with the first neutron arriving in NEBULA, which is always used as a reference. In the first iteration, the condition will be applied to all combinations of hits with the first one. The process is repeated successively taking as reference the next neutron that has not been identified as cross-talk in the precedent iteration. An explanation of the procedure of the algorithm is schematically represented in Fig. 3.23. As it happens with the cluster conditions, the causality selection implies eliminating not only cross-talk but a significant part of independent neutron pairs for which the velocity is quite close[1].

Performance evaluation. Tests are performed in order to evaluate the ratio of rejected cross-talk/good two-neutron events, as well as to check the performance of the algorithm. As the algorithm is strongly dependent on the distance at which two hits are considered to be in the same cluster, efficacy to reject cross-talk has been tested in terms of radius range. Four cluster conditions are examined in each model, $\Omega(r,t) < \Omega_{cluster} = \{1.0, 1.5, 2.0, 2.5\}$ and $R(x,z) < R_{cluster} = \{1.1, 1.5, 2.1, 2.95\}$. $R(x,z)$ being a discrete variable, the values chosen for the test correspond to a distance expressed in number of adjacent bars, $R_{cluster}$ = {1 bar, 1 bar+ 1 diagonal, 2 bars, 2 bars+ 2 diagonals} as illustrated in Fig. 3.22). The analysis of the cross-talk filter has been performed with the following set of data:

- **One-neutron channel**, the experimental ^{15}B+$n+n$. The neutron from the knock-out reaction used to populate ^{16}B from the ^{17}B$(p,pn)^{15}$B reaction, is ejected at an angle of approximately 45º with respect to MINOS. Only the neutron corresponding to the decay of ^{16}B can be detected in NEBULA, located at around 11 m from the target. Therefore, all $2n$ events detected in NEBULA are due to cross-talk.

[1] which is typically the case for two neutrons emitted with small relative energy[2].

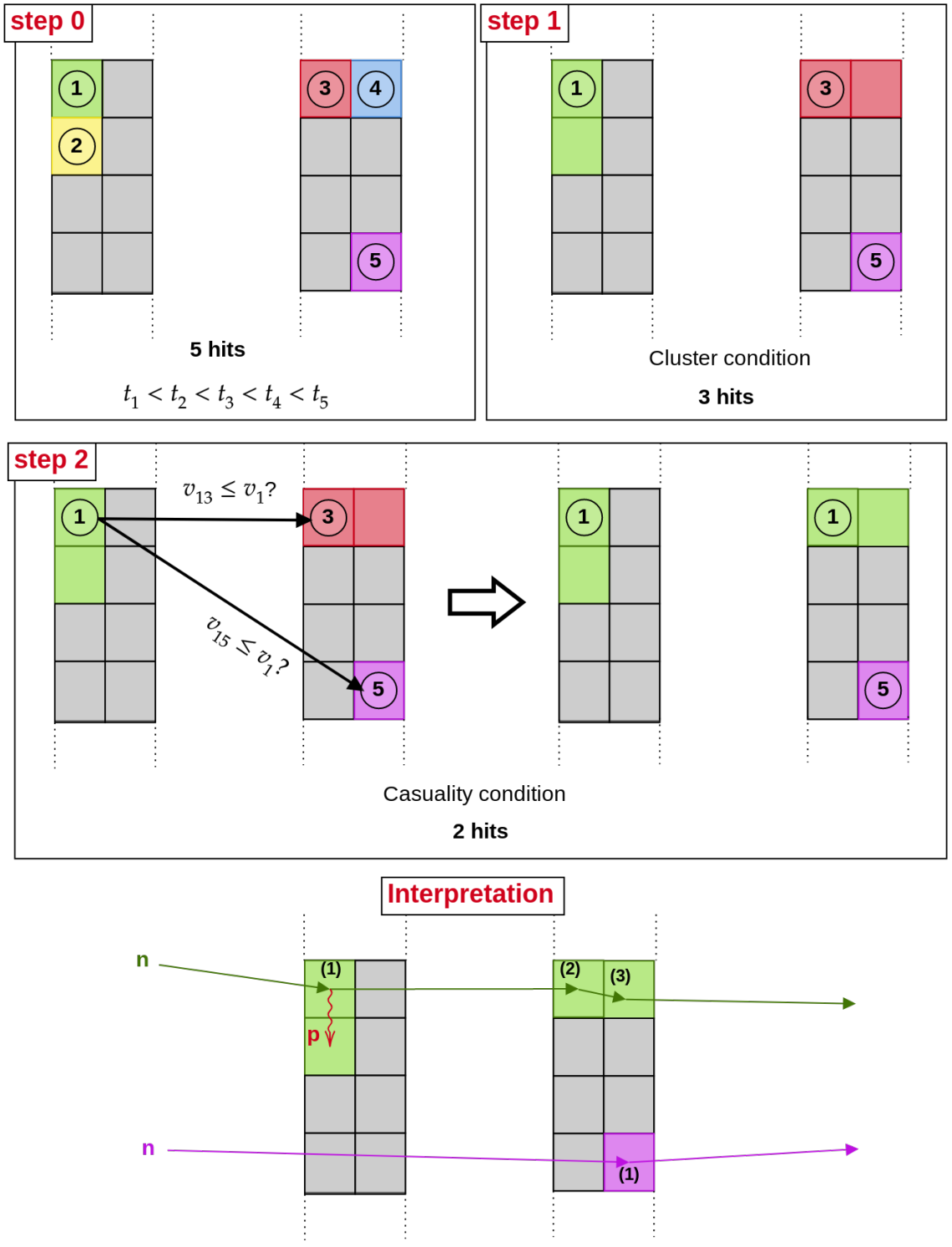

Figure 3.23: *Schematic representation of the cross-talk identification of five initial hits. The clusterization reduces the number of hits from 5 to 3, corresponding to the number of found clusters. The causality condition is then applied between these clusters, by which only two independent hits are left and identified as neutrons. The lower picture represents a hypothesis of the interaction of these two neutrons in five different detectors in NEBULA.*

- **Well-known two-neutron channel**, the experimental ^{12}Be+$n+n$ channel populated by inelastic scattering from a ^{14}Be beam. The inelastic scattering populates an unbound excited state (2^+) that decays into two neutrons and ^{12}Be. In this case, actual $2n$ events are mixed with cross-talk.
- **Simulations** on the ^{12}Be+$n+n$ channel. We can check the number of good events that we reject as only real $2n$ events are generated.

First, an estimation of the number of rejected cross-talk $2n$ events as well as of the rejected good $2n$ events, is performed according to the method and the severity of the conditions. The estimation on the total number of rejected cross-talk is studied via the ^{15}B+$n+n$, for which only cross-talk is generated, while the simulated ^{12}Be+$n+n$ is taken into consideration for the study of the good $2n$ events. For both, the cross-talk filter is applied and compared. Figure 3.24 reports a comparison between the two clusterization methods. We estimate that both methods eliminate as much of cross-talk, around 90-98% depending on the radius size, while rejecting approximately the same proportions of good events. As we can see in Fig. 3.24, the detection of real $2n$ events decreases more significantly than cross-talk rejection increases, meaning a more important rejection on good $2n$ rejection as cluster conditions become more restrictive. In order to reject the maximum of cross-talk without losing too many $2n$ events, a radius of $\Omega(r,t) < 2.0$ or $R(x,z) < 1.5$ is chosen, for which $2n_{CT} \sim 98\%$ ($2n_{simulated} \sim 53\%$) and $2n_{CT} \sim 96\%$ ($2n_{simulated} \sim 58\%$) respectively.

Both cluster and causality conditions are compared for the same two channels in Fig. 3.25 where the distribution of $2n$ events with respect to the velocity and the hypersphere radius can be found. The 2D cluster method is selected for our cluster algorithm as it eliminates less $2n$ events with very low relative energy, typically, within a small radius. The final conditions applied in the cross-talk filter are

$$\begin{aligned} &\beta_{12}/\beta_{01} < 1 \\ &R(x,z) < 1.5 \end{aligned} \tag{3.20}$$

where β_{12} and β_{01} represent the ratio of the velocity v_{12} and v_{01}, respectively, to the light constant c. The methods and conditions selected for the cross-talk filter are put to the test with the experimental ^{14}Be+$n+n$ channel, known to have a narrow state at low energy. The spectrum in relative energy and the application of cross-talk can be found in Sec. 5.2.

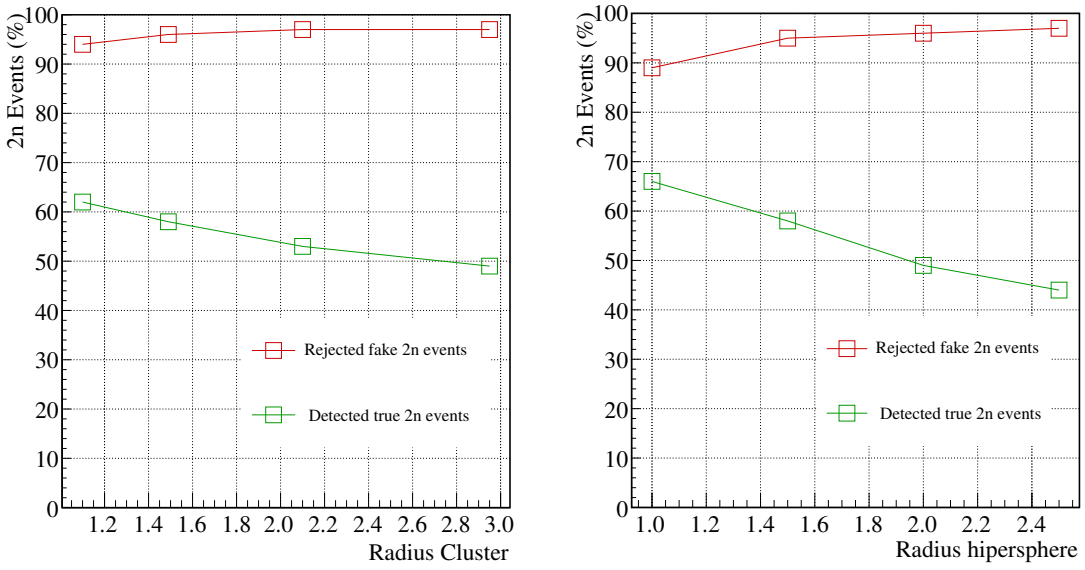

Figure 3.24: *Rejection of 2n events using the hypersphere (left) method and the clusters method (right). In green, the detected 2n events in comparison with the 2n cross-talk events that are rejected for the same conditions. The best conditions represent the best compromise between these two parameters.*

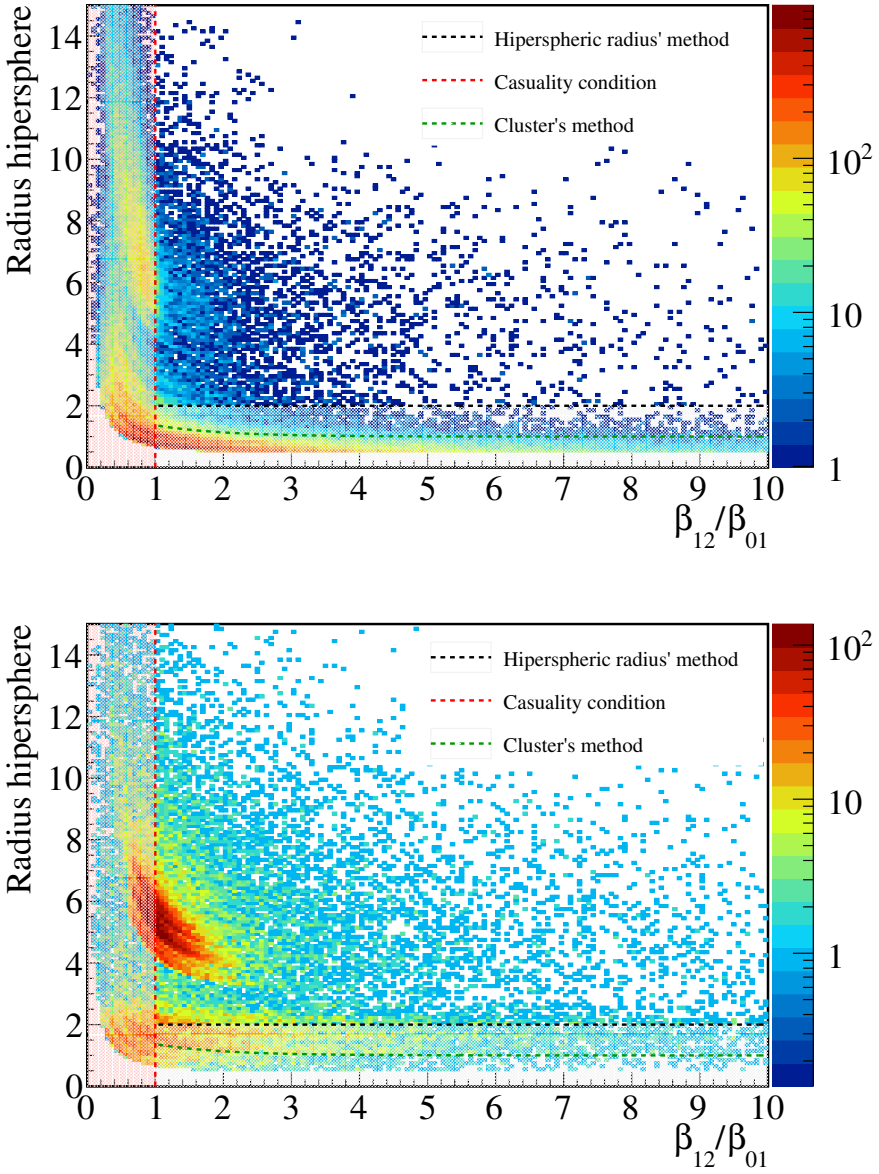

Figure 3.25: *Distribution of the hypersphere radius with respect to the relative velocity of the pair of neutrons divided by the fastest one of the pair. Upper, reconstructed data from ^{15}B+$n+n$ channel. Lower, simulated true $2n$ events for ^{14}Be+$n+n$. The dashed lines define the areas of rejected events when we apply the causality conditions (red) and the clusterization using either the hypersphere method (blue) or the 2D clusters method (green).*

Chapter 4

Analysis techniques and Simulations

Contents

As discussed in previous sections, the setup has a complex multidetector configuration for which many calibrations have to be performed in order to convert and make raw data "readable". The reconstruction of physical observables, such as the momenta of particles, combines the calibrated data from individual detectors or, at a later stage, group of detectors. As a result, the global resolution is a convolution of the individual detector resolutions for amplitude, time, position, *etc.* In this respect, simulations are an essential part of the analysis as they allow the deduction of the global resolutions and detector responses. Moreover, they are also a key point to physically interpret the spectra. In order to make simulations unambiguously comparable with experimental data, both are analyzed using a common analysis technique and filter (see Fig. 4.1).

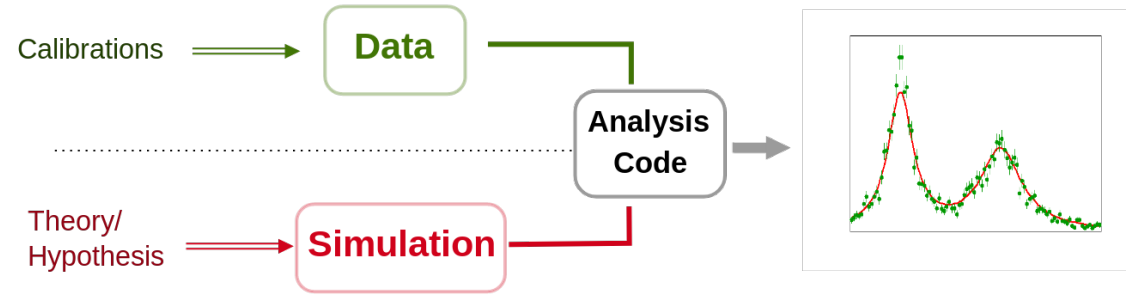

Figure 4.1: *Schematic overview of the data analysis process. In order for simulations to be directly comparable with experimental data, a common and unique analysis code, which includes all filters and conditions, is applied for the reconstruction of the observables of interest.*

In this chapter, we give an overview of the techniques involved in the data analysis. We first describe how the physical observables are obtained from calibrated data. The invariant-mass method used to reconstruct the relative energy of the system is also outlined. Next, the different simulation tools employed to generate the setup and physical processes are detailed. Finally, the Dalitz plot method used for the analysis of the three-body correlations of the decay is explained.

4.1 Reconstruction of physical observables

4.1.1 Event selection

In order to reconstruct the relative energy of the unbound systems produced in the target, the momenta of the decay products have to be determined. A precise identification of the fragment and the neutrons is essential to reject spurious events and obtain a clean spectrum.

Selection in the target

The reconstruction of the vertex of the reaction in MINOS is an important aspect of the analysis that allows to precisely calculate the energy loss of the charged particles. The reaction point is determined by the intersection of the 3D trajectories of the ejected particles detected in the TPC surrounding the target. As mentioned in Sec. 3.4.2, only events for which the minimum distance D_{min} between trajectories is less than 5 mm are selected. This selection includes 90% of the events and corresponds to the double of the FWHM of the D_{min} distribution that we can see in Fig. 4.2.

Events for which the reconstructed vertex is outside the cylindrical target cell of MINOS are also rejected. Taking into consideration the finite resolution of the reaction point, the

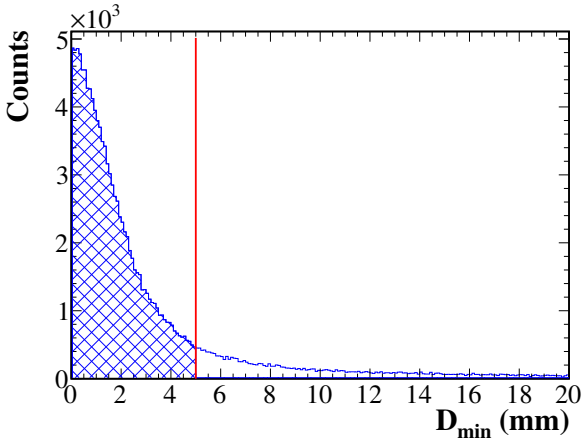

Figure 4.2: *Distribution for the minimum distance between two reconstructed trajectories in MINOS, either beam+p or p+p trajectories. The striped area shows selected events.*

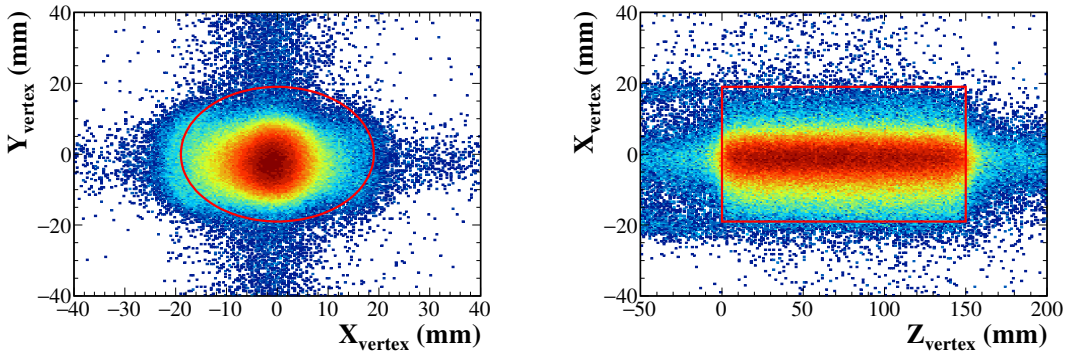

Figure 4.3: *Reconstruction of the vertex position in MINOS in the XY plane (left) and the XZ plane (right). The red squares and circles represent the selected events according to the dimensions of the LH_2 target cell.*

area selected is slightly bigger than the actual size. As can be seen in Fig. 4.3, the length Z_{vertex} is selected in a range from 0 to 150 mm, while the selected radius in the XY plane is $R(X,Y) = \sqrt{X^2_{\text{vertex}} + Y^2_{\text{vertex}}} < 19$ mm.

Conditions for neutrons

Neutron detectors based on plastic scintillators are not only sensitive to neutrons but also to other particles such as γ-rays or charged particles. As mentioned in Sec. 3.5, charged particles are identified by VETOs located in front of each wall of NEBULA. When one of these VETOs is fired, neutrons belonging to the same wall are rejected. As γ-rays and other particles generated by the interaction of neutrons in the detector cannot be fully differentiated by means of VETOs, neutron event discrimination is enhanced by the use of conditions related to the time of flight and light output.

In this sense, gamma particles coming from the de-excitation of a nucleus in the target are easily distinguished from neutrons by their ToF. Given the distance between MINOS and NEBULA, gamma events are considered to have a ToF of less than $\sim$ 44 ns, which

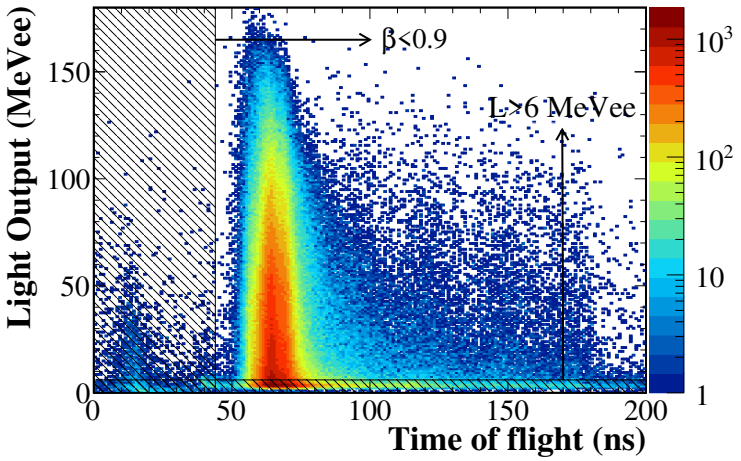

Figure 4.4: *Neutron selection in NEBULA. γ-rays are discriminated from neutrons by their time of flight, $\beta < 0.9$, and the light output, $L > 6$ MeVee. The shadowed areas represent the rejected events.*

would correspond to a velocity of $\beta > 0.9$. In addition, the energy of neutrons, close to the beam energy ($\sim$ 250 MeV, *i.e.*, $\beta \sim 0.6$), is significantly different from the energy of γ-rays (of about several MeV) or other secondary particles produced by the interaction of a neutron with a carbon or an hydrogen in the plastic. Even though the deposited energy is not proportional to the energy of particles, the energy loss cannot, however, be superior to it. This implies that most of γ-rays will concentrate at low values of light output while a very small fraction of neutrons will coexist at the same range. According to [56], applying a threshold of $L > 6$ MeVee is sufficient to eliminate up to 80% of γ-rays. In combination with a lower limit of ToF $>$ 44 ns, we can select about 90% of neutrons. In Fig. 4.4 the distribution of light output with respect to the ToF is shown. Here the main structure corresponds to the detection of neutrons. The stripped areas represent the rejected events.

Selection for fragment events

Besides the fragment identification in the HODOSCOPE, fragment events are selected according to their measured position in FDC2. As illustrated on the right plot of Fig. 4.5, if the reconstructed X_{FDC2}, Y_{FDC2} positions are out of the dimensions of the FDC2 ($|Y| > 200$ mm and $|X| > 1000$ mm) the event is rejected as being considered wrongly reconstructed. Furthermore, the reconstruction of X_{FDC2} can be as well checked by looking at the correlation with the ID of the HODOSCOPEs. Since trajectories between FDC2 and the HODOSCOPE are linear, their correlation in X axis is expected to be equally linear. If for example a particle is tracked at the beginning of the drift chamber, which corresponds to the first bars of the HODOSCOPE, but is detected in one of the last plastics of the HODOSCOPE, we conclude that the position reconstruction in FDC2 is wrong. As shown in Fig. 4.5, only events showing a linear correlation between the two detectors are selected to ensure the good reconstruction of the fragment.

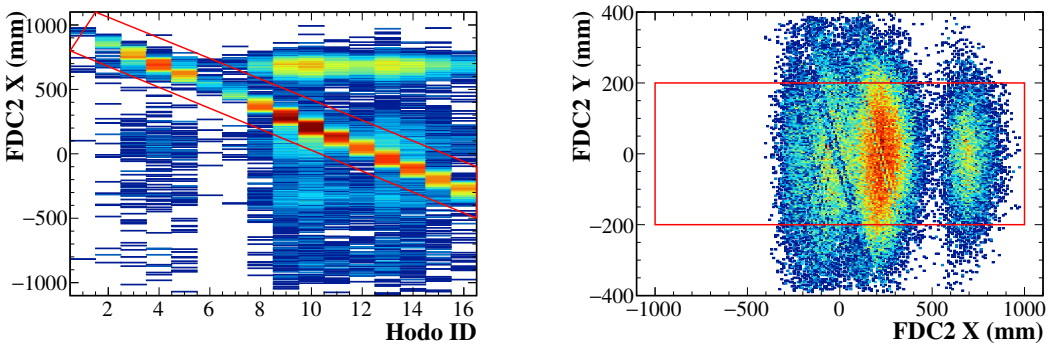

Figure 4.5: *Event selection for the fragment. On the left, the relation between the X position reconstructed by FDC2 and the ID of the HODOSCOPE is shown. Here a linear correlation of X_{FDC2} and the ID of the HODOSCOPE is selected. On the right, reconstructed events which are outside the dimensions of FDC2 are rejected.*

4.1.2 Fragment moment reconstruction: $B\rho$ determination

The determination of the magnetic rigidity of charged fragments is fundamental in our analysis as it allows us to reconstruct their momenta and energies. As previously mentioned, the SAMURAI magnet bends the trajectory of ions, separating them isotopically as a function of their $B\rho$. The trajectory depends on multiple factors such as the initial velocity at the entrance of the magnet or the charge and mass of the isotopes. Since neither of these factors can be measured directly in our experiment, the $B\rho$ reconstruction is achieved by means of simulations based on Geant4 [58].

The simulations take into account the conditions of the experiment, including the distribution of the magnetic field in SAMURAI and the dimensions and positions of the different detectors in the experimental room. A large number of particles are randomly generated and propagated from the target, with known initial conditions of energy and $B\rho$. Their trajectory, their horizontal and vertical positions and incident angles in the drift chambers, can be therefore related to their energy and $B\rho$ (see Fig. 4.6). Since this relation is non-linear, the results of the simulations are used to generate a multidimensional polynomial function based on the *TMultiDimFit* library in ROOT. This function has as input parameters, the X and Y positions of the FDCs and the incident angles of the particle, and gives the $B\rho$ as an output value. The momentum is then calculated as

$$P_f = QB\rho \tag{4.1}$$

where Q is the charge of the fragment and P_f its total momentum. The direction of the momentum $\vec{p}_f = P_f\vec{u}$ can be calculated from the angle between the measured position in FDC1 and the vertex position in MINOS as follows

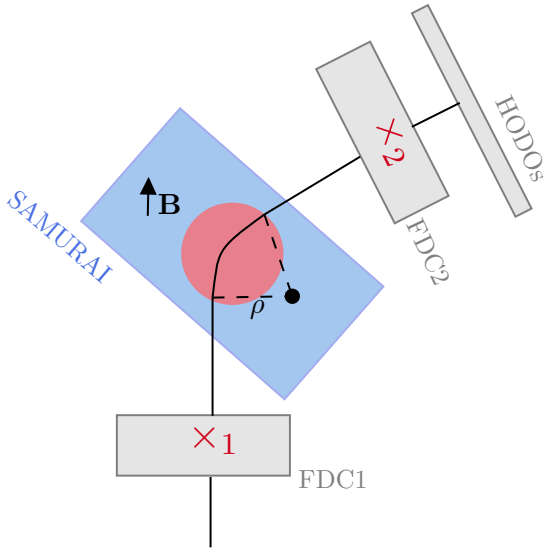

Figure 4.6: *Schematic overview of the Bρ determination using the positions measured in the FDCs for the heavy fragments. Once the Bρ is reconstructed, the momentum can be easily calculated following Eq. 4.1.*

$$
\begin{aligned}
u_{px} &= \frac{x_{FDC1} - x_{vertex}}{\sqrt{(\vec{r}_{FDC1} - \vec{r}_{MINOS})^2}} \\
u_{py} &= \frac{y_{FDC1} - y_{vertex}}{\sqrt{(\vec{r}_{FDC1} - \vec{r}_{MINOS})^2}} \\
u_{pz} &= \frac{z_{FDC1} - z_{vertex}}{\sqrt{(\vec{r}_{FDC1} - \vec{r}_{MINOS})^2}}
\end{aligned}
\tag{4.2}
$$

4.1.3 Fragment-neutron alignment

Given that different detectors are used to reconstruct the momenta of the fragment and the momenta of the neutron(s), it is necessary to align the multidetector setup altogether with respect to a common reference. This reference is chosen to be the momentum of the neutrons as it is unambiguously determined from the time of flight as

$$
P_n = m_n \beta_n \gamma_n \tag{4.3}
$$

where m_n corresponds to the neutron mass, $\beta_n = v/c$ the velocity of neutrons reconstructed from their ToF and γ_n the corresponding Lorentz factor. The alignment is performed using one neutron, the fastest one, and the charged fragment. The aim is to find a potential average shift $\Delta\beta_f$ for the velocity of the fragment, such as $\beta_f = \beta_f + \Delta\beta_f$, for which $\langle\beta_f\rangle = \langle\beta_n\rangle$. However, a change in the fragment velocity affects not only the value of β_f, but also the momentum of the fragment and consequently the relative energy between the fragment and the neutron (see Fig. 4.7). The optimal value of $\Delta\beta_f$ can be found by checking their evolution as a function of the shift applied to the fragment. Since

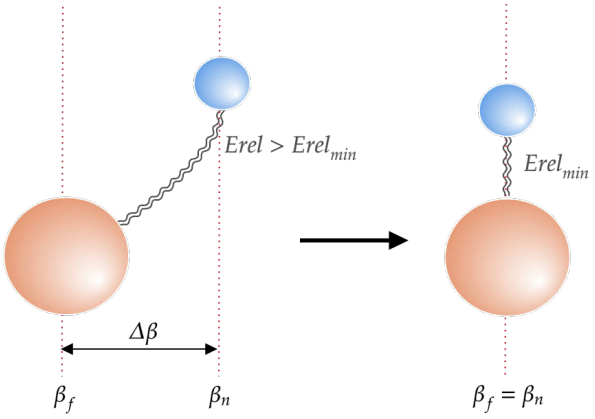

Figure 4.7: *A misalignment between the velocities of the fragment and the neutron has consequences in the reconstruction of other observables, such as the relative energy* E_{rel}.

a misalignment of only 1% of β can be significant in the reconstruction of the relative energy, the alignment is calculated independently with three different observables. If the alignment is correctly calculated, the results of each method should be consistent. The following observables are used:

- $\langle \Delta\beta \rangle = \langle \beta_n - \beta_f \rangle$, the average of the difference between the fragment and the neutron velocities.
- $\langle P_z(n)_f \rangle$, the average of the parallel momentum of the neutron in the rest frame of the fragment.
- $\langle E_{rel} \rangle$, the average of the fragment-neutron relative energy.

An example of the alignment method can be found in Fig. 4.8. As can be seen in this example, the distributions $\langle \beta_n - \beta_f \rangle$ and $\langle P_z(n)_f \rangle$ follow a linear evolution with respect to $\Delta\beta_f$. Both distributions are centered in zero as the fragment and the neutron are aligned. On the contrary, the average of the relative energy $\langle E_{rel} \rangle$ evolves as a polynomial function of second order. The minimum of the parabola defines the shift of the best alignment. The chosen $\Delta\beta_f$ is the average of the shift calculated by the three methods.

4.1.4 Invariant mass method

The main goal is to investigate unbound systems that decay immediately after being populated. Since the experiment is performed with the kinematic complete measurement of the reaction, the **invariant mass method** is used. At the beam energies of the experiment, ~ 250 MeV/nucleon, the energy and momenta have to be expressed in terms of special relativity. Indeed, the invariant mass is the total relativistic energy of the system reconstructed from the measured 4-momenta of all decay products in any reference frame.

The 4-momentum of a particle $P = (E, \vec{p})$ (we use natural units, $c = 1$) is given by its energy E and its spatial momentum $\vec{p}$, from where the rest mass is derived as follows

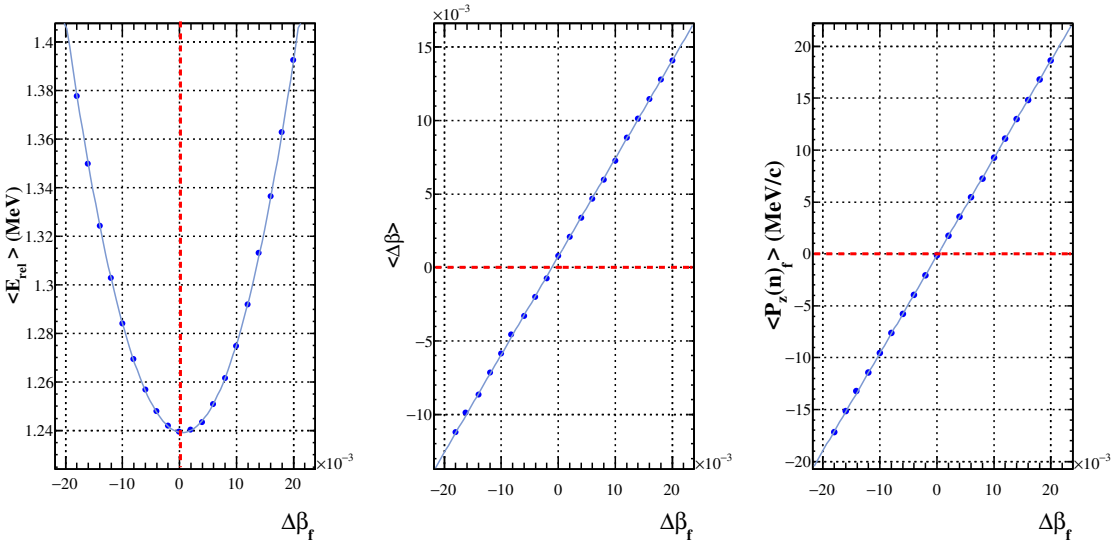

Figure 4.8: *Fragment-neutron alignment for the* $^{17}B\rightarrow\ ^{15}B{+}n$ *reaction channel. From left to right, the evolution of the observable* E_{rel}*,* $\langle\Delta\beta\rangle$ *and* $\langle\Delta P_z(n)_f\rangle$ *as a function of the fragment velocity shift* $\Delta\beta_f$ *are represented, respectively.*

$$m^2 \;=\; (E,\vec{p})^2 \;=\; E^2 - p^2 \tag{4.4}$$

The invariant mass, M_{inv}, for a N-body unbound system can be calculated using the energy and momentum of its decay products following the expression

$$M_{inv} \;=\; \sqrt{\left(\sum_{i=1}^{N} E_i\right)^2 - \left(\sum_{i=1}^{N} \vec{p}_i\right)^2} \tag{4.5}$$

where E_i is the energy of particle i and $\vec{p}_i$ its momentum. The relative energy E_{rel} is defined as the difference of the invariant mass of the system and all the rest masses m_i of the decay products

$$E_{rel} \;=\; M_{inv} - \sum_{i=1}^{N} m_i \tag{4.6}$$

In the case of an unbound system with a two-body decay, such as fragment+neutron, the previous equation becomes

$$E_{rel} \;=\; \sqrt{m_A^2 + m_n^2 + 2(E_A E_n - |\vec{p}_A|\,|\vec{p}_n|\,cos\theta)} - m_A - m_n \tag{4.7}$$

where the subscripts A and n denote a fragment of atomic number A and a neutron respectively, and θ the relative angle between the two particles. If the fragment is populated

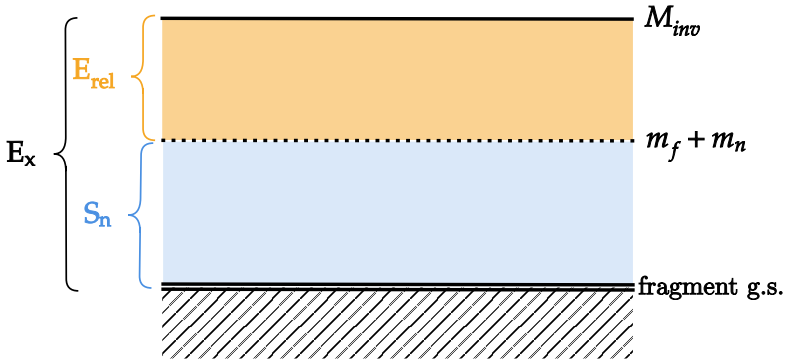

Figure 4.9: *Schematic representation between the relation of the invariant mass M_{inv} and the relative energy E_{rel} for a $f + n$ system assuming that the fragment is populated in its ground state. The excitation energy E_x can be then related to E_{rel} and the neutron separation energy as $E_x = E_{rel} + S_n$.*

in its ground state, the relative energy can be directly associated with resonances in the original system. The excitation energy E_x would be then (see Fig. 4.9)

$$E_x \;=\; S_n + E_{rel} \tag{4.8}$$

where S_n is the neutron emission threshold in the $A + 1$ nucleus.

4.2 Event generator: Monte-Carlo simulations

The reconstructed relative energy spectrum is described by means of **M**onte-**C**arlo (MC) simulations which take into account the response of the detectors as well as the parameters characterizing the resonances and decay mechanisms of the unbound system. The results of all experiments from the campaigns included in this work (s018, commissioning, DayOne) have been analyzed with the simulation MANGA (**M**ultiparticle **A**nalysis in a **N**eutron **G**eometrical **A**rray). MANGA has been specially developed for the description of unbound states decaying via the emission of one or several neutrons, such as $^{A+2}\mathrm{X}\rightarrow{}^{A}\mathrm{X}+n+n$, in experiments using the SAMURAI setup.

4.2.1 MC principle

The decay of an unbound system is constrained by the available energy of the decay E_d, which represents the maximum energy that N-particles can share. The decay is simulated by MANGA following MC principles: for each event, E_d is randomly generated according to a probability distribution that describes the nature of the unbound state.

Once the decay energy is set, it is randomly shared between the fragment and the neutron(s) following the corresponding N-body phase space. For simplicity, the momentum is calculated in the center of mass (CM) of the system. In the case of a two-body decay, both the momentum of fragment and neutron would have same norms but opposite directions. Moreover, the generation of particles in the CM frame becomes simpler as it allows an isotropic generation to be assumed. The momentum of a two-body decay in this

referential frame is defined by the following expression

$$\begin{aligned} P_{CM} &= \frac{\sqrt{[E_x^2 - (m_f + m_n)^2]\,[E_x^2 - (m_f - m_n)^2]}}{2E_x} \\ E_x &= E_{rel} + m_f + m_n \end{aligned} \tag{4.9}$$

where E_T is the total energy of the system and m_f and m_n the masses of the fragment and neutron, respectively.

However, in order to be fully comparable with experimental data, the momentum obtained by Eq. 4.9 has to be converted into a realistic distribution able to account for the effects of the experimental conditions. As detailed in the next section, general parameters such as the angular and momentum resolution of SAMURAI have a significant impact on the momentum distribution. The global resolution obtained by including all these effects is directly comparable to the experimental complex resolution of the multidetector setup.

The momentum in the CM is converted to the laboratory frame using the incident velocity of the beam. Since we use MINOS as a target, the depth of the reaction point is experimentally accessible and therefore also simulated randomly following an uniform distribution between 0 and 150 mm. Then, the energy of the fragment is affected by the energy loss and the straggling in the rest of the target, and the experimental resolutions are applied to the outgoing fragment and neutrons.

4.2.2 Characterization of the setup in MANGA

Given the complexity of the setup, the influence of each detector on the experimental resolution, as well as of all other parameters employed in the reconstruction of the momenta, cannot be straightforwardly identified. Hence, a simulation that intends to interpret the experimental data needs to include all these effects. In order to reproduce the experimental conditions, the setup and the reaction channel are characterized by a series of parameters. A brief description of all effects comprised in MANGA are detailed below.

Characterization of the beam. The beam is characterized following a flat distribution of energy within a given range. The average of this distribution and its spread, which defines the range of values covered by β, must be defined for every reaction channel.

Characterization of the target. The charged particles traveling inside the target are subject to energy loss and straggling. Due to the multiple microscopic processes encountered while going through the target, the energy distribution is broadened and the trajectory slightly deviated, effects referred to as energy and angular straggling, respectively. Consequently, the energy and trajectory of two fragments of the same nature that have the same initial energy, will be slightly different. These are simulated using energy-loss and straggling calculations with the LISE++ software based on the initial energy and the thickness traversed by a charged particle with defined Z and A numbers. The straggling is included in the simulation by randomizing using a Gaussian distribution of energy and angle, with sigma values defined by the average of the straggling of the beam and the fragment in a length of 150 mm (size of MINOS). Then, the straggling of the beam particle is included up to the reaction vertex, and then the straggling of the fragment up to the exit of MINOS.

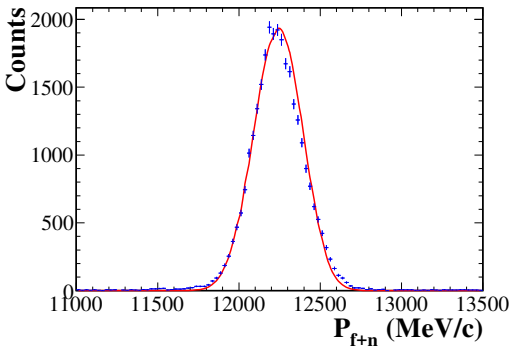

Figure 4.10: *Momentum distribution for ^{15}Be+n populated using a neutron knock-out reaction from a ^{17}B beam. The input parameters of the simulation (red) to reproduce the effect of the reaction on the momentum distribution are 85 MeV/c for the longitudinal axis and 140 MeV/c for the transverse axis.*

Characterization of the reaction. In the simulation, the fragment and the neutron(s) are generated at rest in the CM. However, experimentally the reaction mechanism plays an important role in the momentum distribution of the system. Indeed, a knock-out reaction, as used in our experiments, communicates a momentum to the system. This contribution to the total momentum is characterized by a Gaussian distribution in the longitudinal and transverse directions. The width of this distribution is taken from the experimental momentum distribution for each reaction channel and introduced in the simulation. In Fig. 4.10, an example for the $^{17}B \xrightarrow{-1n} {}^{15}B + n$ channel is presented. Here the values used are 85 MeV/c for the longitudinal component and 140 MeV/c for the transverse one.

Fragment resolution

The ideal conditions to determine the experimental resolution of the setup would involve the production of our nucleus of interest at the same energy as we experimentally have (including the energy loss in the target) and with a negligible momentum and angular spread. However, such conditions are difficult to obtain experimentally. Instead, we can select a *pencil beam* by applying conditions on the momentum and angle during empty target runs. Since it is not possible to produce a pencil beam for the nucleus of interest, we use several species of the beam to find a general trend for the experimental resolutions, which will be also applicable to our nucleus of interest.

The effects of the experimental resolution are significant if we look at the emission angles of the fragment and its total momentum. Different conditions are applied to produce the pencil beam to check the angular or momentum resolutions. For the former, the pencil beam is created by the following constraints

- Reaction centered on the target with a radius of 15 mm.
- $|\theta_x - \langle\theta_x\rangle| < 0.5$ mrad.
- $|\theta_y - \langle\theta_y\rangle| < 0.5$ mrad.
- No selection on the total momentum.

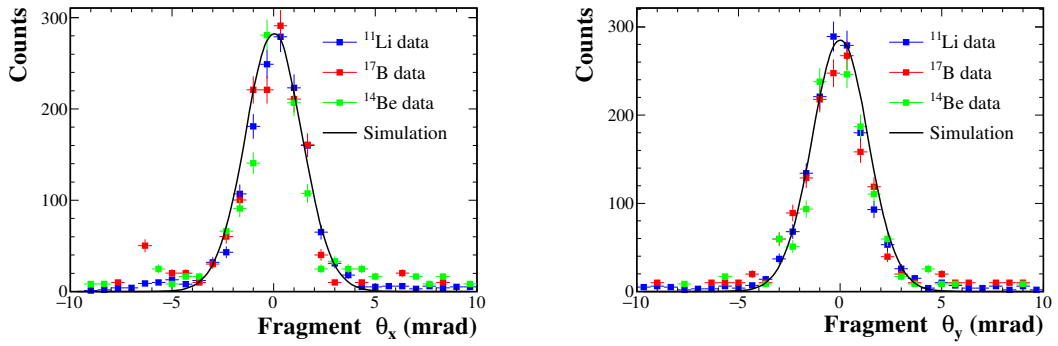

Figure 4.11: *Angular distributions for fragments obtained from pencil beams of ^{11}Li, ^{14}Be, ^{17}B. The simulation (black line) follows a Gaussian distribution of width σ = 1.2 mrad that reproduces the experimental angular resolutions.*

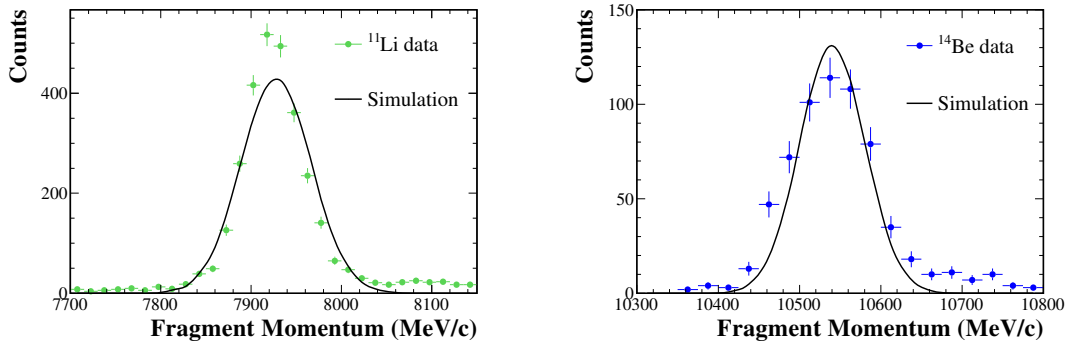

Figure 4.12: *Distributions of total momentum obtained for ^{11}Li and ^{14}Be pencil beams. The black line represents the best compromise to reproduce the experimental data using a Gaussian distribution of $\sigma = 32$ MeV/c.*

As can be seen in Fig. 4.11, the angular resolution for both x and y directions is very similar for different pencil beams (^{11}Li, ^{14}Be, ^{17}B). These distributions can be described by a single Gaussian of $\sigma = 1.2$ mrad.

The conditions applied to generate the pencil beam to define the momentum resolution are as follows

- Narrow dispersion for the momentum of the beam, $|P - \langle P\rangle|/\langle P\rangle < 0.5‰$.
- No selection on the target.
- No selection on the angles.

Figure 4.12 shows the experimental distributions of the reconstructed total momentum of the fragment for ^{11}Li (left) and ^{14}Be (right) pencil beams on empty target runs. Note that to get the best description of both, we need to find a compromise. The best result has been obtained for a Gaussian of width $\sigma = 32$ MeV/c.

Neutron detection

Once the momenta have been generated with the experimental resolutions and other related effects, it is necessary to simulate the response of the setup for the detection of the decay products. This is considered separately for the fragment and the neutron(s). While the efficiency of the detection of the fragment is experimentally close to 100% and not dependent on the momentum, the neutron efficiency is very much determined by its momentum. In the simulation, the fragment efficiency is then considered as 100%, and the resolution included as explained earlier. In the case of neutrons, the response of NEBULA is more complex and has to be simulated in MANGA.

Two main factors in the detector contribute to the neutron efficiency, namely the geometrical acceptance and the interaction probability. The former refers to the probability of a neutron to enter NEBULA. The latter, the probability of interaction inside the detector. The geometrical acceptance of the neutron detector depends on different conditions, such as the energy of the neutron, the dimensions of the detector or the distance from the target. In order to maximize the neutron detection, the distance from the target is optimized according to the beam energy. At the energies of our experiment $\sim$ 250 MeV/nucleon, emitted neutrons will be very focused at forward angles. Consequently, NEBULA can be located at a relatively far distance from the target, $\sim$ 11 m. The configuration of the setup is also included in the simulation.

Concerning the interaction in NEBULA, MANGA includes the detection probability in an effective way. Neutrons can be detected by the interaction with either a Carbon or a Hydrogen nucleus composing the plastic bars of NEBULA. By taking into account the experimental cross-section from the ensemble of processes, a constant probability per centimeter traversed can be estimated. Therefore, this approach allows the simulation of the main part of the complex detector response to multi-neutrons with one single parameter. With the assumption of this effective probability, whether each neutron is detected or not as well as its interaction point is determined as a function of the thickness that the neutron goes through in the plastic. Once the detection point is determined, the time for the light to reach both PMTs is calculated and folded with their time resolution, which is obtained experimentally.

In Fig. 4.13 the efficiency, including both the geometrical acceptance and the interaction probability, is shown for one-neutron (left) and two-neutron detection in NEBULA (right). As can be seen, the $1n$ efficiency is constant and maximum for low energies (between 0–2 MeV) and decreases for higher relative energies. When neutrons have very little relative energy with the fragment, they are emitted following trajectories close to the beam axis that go inside the dimensions of NEBULA. This means that at low relative energies the geometrical efficiency is close to 100%. The interaction probability for the whole thickness of the array, $\sim$ 48 cm, makes the maximum efficiency reach a value of $\sim$ 35% for one neutron. As neutrons become more energetic, their trajectories spread and deviate more from the beam axis. In such a case, their trajectories may escape the area covered by the detector, firstly in the vertical direction, and eventually in both vertical and horizontal directions.

As illustrated in the right panel of Fig. 4.13, the efficiency for $2n$ detection is significantly reduced when the cross-talk filter is applied. In particular, events with a very low relative energy $E_{rel} < 0.5$ MeV are more affected by the algorithm. At these energies

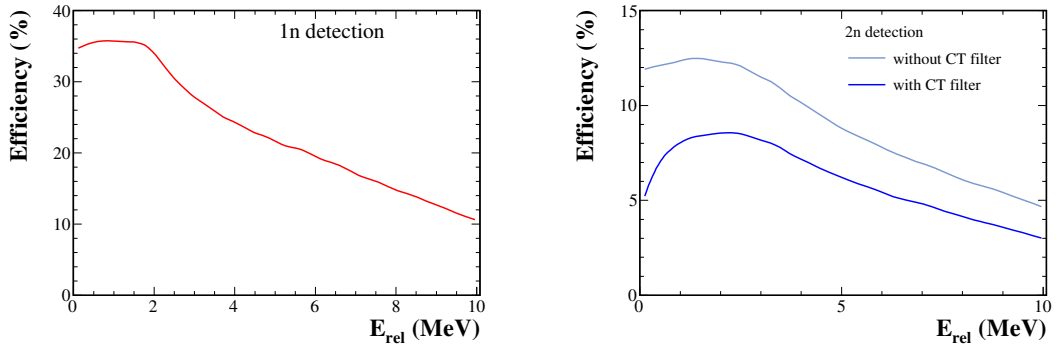

Figure 4.13: *Efficiency for neutron detection simulated with MANGA for the s018 experiment for a beam energy of* $\sim$ 280 *MeV/nucleon. On the left, the efficiency for the detection of 1n. On the right, the efficiency for 2n detection with and without the cross-talk (CT) filter, in blue and pale blue, respectively. Note that the main difference in shape is found at very low relative energy* $E_{rel} < 1$ *MeV.*

the emission angle of the two neutrons is very small, making them be detected in almost neighboring bars of NEBULA, and therefore difficult to distinguish by the filter. While the $1n$ efficiency varies from 35% to 10%, the $2n$ detection efficiency corresponds to an average of $\sim$ 7% in the range 0–5 MeV when the cross-talk filter is applied.

MANGA does not simulate the energy loss of neutrons in the plastic, nor the tracking inside the detector or the multiple interactions of each neutron. More complex simulations have been developed and put to the test giving very similar results on efficiency than MANGA. Given the similar results, and for reasons of time of calculation, MANGA has been preferred for this thesis work. Moreover, since one neutron can only interact once in this simulation, the coincident $2n$ events are always true $2n$ events. The effect of our cross-talk rejection algorithm on the efficiency can be studied using this simulation (see Sec. 3.6).

Global resolution of SAMURAI

The MANGA simulation allows us to evaluate the resolution of the setup with respect to the relative energy and the reaction channel. Taking into consideration the angular and momentum resolution of the fragment, as well as the time and position resolution of NEBULA, the total resolution of the setup can be estimated. The method consists in simulating states at a given E_{rel} that are folded with the input resolutions of SAMURAI. The evolution of the resolution with respect to the relative energy can be described approximately by FWHM $\sim a \times E_{rel}^{b}$, where a is a constant. As shown in Fig. 4.14, the resolution degrades as we go for higher values of relative energy. The evolution of the total experimental resolution can be described as a function of the relative energy with the following expression, FWHM $= 0.48 \times E_{rel}^{0.56}$ MeV. The parameters are the result of the fit shown in the right panel of Fig. 4.14.

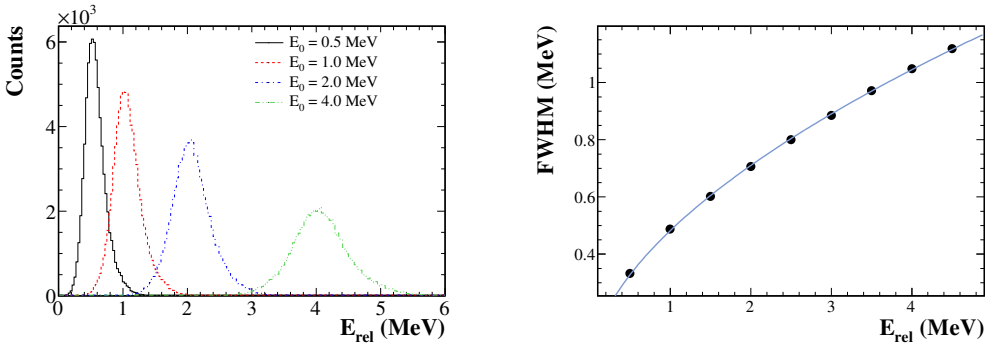

Figure 4.14: *Experimental resolution of SAMURAI for different fragment+n+n relative energies, for the s018 experiment at a beam energy of 280 MeV/nucleon. On the left, the ΔE distributions folded with a resonance at different relative energies. On the right, evolution of the experimental FWHM characterized by the equation $FWHM = 0.48 \times E_{rel}^{0.56}$ MeV.*

4.3 Energy spectra

4.3.1 Non-resonant contribution

The invariant-mass analysis is based on the study of the correlations between the charged fragment and the neutron(s) produced in the decay of the unbound system. However, the detection of these particles in coincidence does not indicate necessarily a correlation between them. Since we populate the unbound systems via knock-out reactions, we might either populate states in the non-resonant continuum or a final state for which the particles ^{A}X+xn do not interact. Moreover, in the case of the emission of excess neutrons, the detected neutrons might not correspond to the same neutrons interacting with the charged fragment. All these possibilities result in a non-correlated contribution that is essential to evaluate in order to differentiate the resonant structures.

Two different techniques are used to estimate the shape of the non-resonant contribution to the relative energy spectrum, the *event mixing* and the *"bck" simulation*. In our analysis, we employ the event mixing method for two-body systems, while in the case of N-body systems with N $>$ 2 the non-resonant component is simulated (*bck*) for simplicity. The basics concerning both techniques are explained in the following sections.

Two-body systems: Event Mixing

Let us consider two non-interacting particles, a fragment and a neutron, that are part of the exit channel of a given reaction, with four-momenta p_f and p_n. In an ideal case in which they do not "see" each other, the momentum distribution of each particle should be independent, *i.e.*, $d\sigma/dp_f$ and $d\sigma/dp_n$. However, it would be possible to measure these distributions only if we could select channels in which just one particle was emitted. Since in the breakup of an unbound system the fragment and neutron will be mostly emitted together, we can have only access to the two-particle momentum distribution $d^2\sigma/dp_f dp_n$, which is related to the independent momentum distributions of each particle as

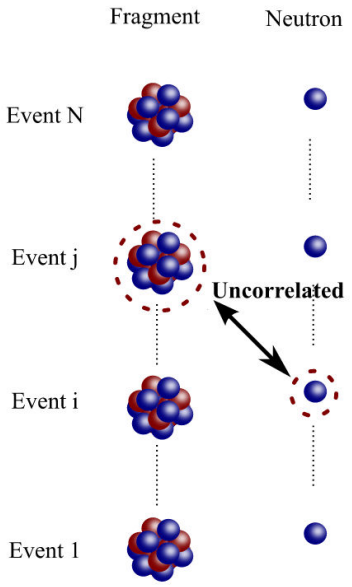

Figure 4.15: *Event mixing principle applied to experimental data. The detected fragment of a given event is associated to a neutron of a different event in order to create uncorrelated virtual pairs. Taken from [7].*

$$\frac{d^2\sigma}{dp_f dp_n} = \frac{d\sigma}{dp_f}\frac{d\sigma}{dp_n} \times C(p_f, p_n) \tag{4.10}$$

where $C(p_f, p_n)$ is the *correlation function* which by definition represents the correlations found in the measured momenta due to the non-independence of both particles in the final state. Therefore, the uncorrelated part of the spectrum corresponds to $C(p_f, p_n) = 1$ and is described by the independent momentum distribution of both particles, $\frac{d\sigma}{dp_f}\frac{d\sigma}{dp_n}$. In order to estimate the uncorrelated component, the independent distributions need to be extracted from the total distribution that we measure.

To remove correlation from experimental data, we can mix particles from different events, creating *virtual pairs* which did not coexist, and therefore, did not "see" each other (see Fig. 4.15 for a schematic representation of this principle). In addition, non-correlated distributions estimated from the mixing will include the experimental acceptances as they are built from actual detected particles. Mathematically, by mixing events we obtain the following distribution for the fragment,

$$\begin{aligned}\frac{d\sigma_{\otimes}}{dp_f} &= \int \frac{d^2\sigma}{dp_f\, dp_n}\, dp_n \\ &= \frac{d\sigma}{dp_f} \int C(p_n, p_f)\, \frac{d\sigma}{dp_n}\, dp_n \\ &= \frac{d\sigma}{dp_f}\, \langle C \rangle (p_f)\end{aligned} \tag{4.11}$$

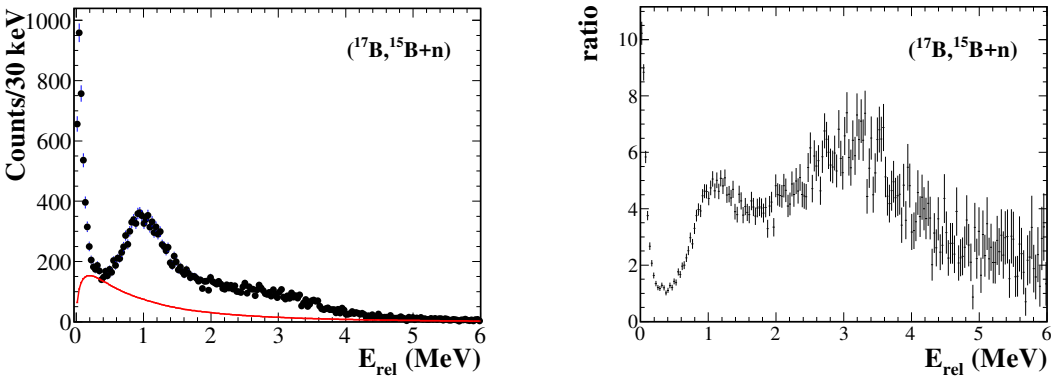

Figure 4.16: *Event-mixing technique for the (^{17}B,^{15}B+n) channel. On the left, the relative energy spectrum with the resulting non-resonant contribution in red. On the right, the ratio between the experimental data and the non-resonant contribution.*

where $\frac{d\sigma_{\otimes}}{dp_f}$ represents the mixing of the fragment with all other neutrons, obtained by integrating the two-particle distribution over the neutrons. The same stands for the neutron with respect to the fragments. Therefore the mixing distributions $d\sigma_{\otimes}/dp$ are the independent distributions we are trying to estimate times $\langle C \rangle(p)$. This factor represents the average correlation, with all the other virtual partners, of a particle with four-momentum p. When particles are weakly correlated, which is the case in most of the applications, this average correlation will be $\langle C \rangle(p) \approx 1$, and therefore $\frac{d\sigma_{\otimes}}{dp} \approx \frac{d\sigma}{dp}$.

However, if $\langle C \rangle(p)$ is significantly larger than 1, simply mixing events is not enough to erase all correlations. In cases of strong correlation, an iterative technique is used to enhance the method and eliminate the residual correlations. The details on the algorithm are explained in the appendix A.

Figure 4.16 illustrates the event mixing technique for the non-resonant contribution of the (^{17}B,^{15}B+n) channel. Although the amplitude of this distribution has to be determined by a fit with all the components contributing to the spectrum, yet its shape is precisely calculated with high statistics, from the mixing of N^2 virtual pairs where N is the number of coincident $f + n$ events. If we normalize the uncorrelated distribution with respect to the limit of the error bars of the experimental data for the whole energy range, we can study qualitatively the presence of structures in the spectrum. As shown in the right panel of Fig. 4.16, the ratio of the experimental data over this maximized uncorrelated distribution reveals the structures coming from resonant states populated in the reaction. This is specially useful for the identification of wide resonances that, depending on the experimental resolution, may be difficult to distinguish from an *a priori* unknown background.

Three-body systems: *bck* generator

The event mixing technique becomes very complex for N-body systems with $N > 2$. In a case in which more than one neutron is emitted, the algorithm used to estimate the non-resonant contribution has to, in addition, apply a cross-talk filter in order to reject virtual pairs that could have not been detected during the experiment. The reader can

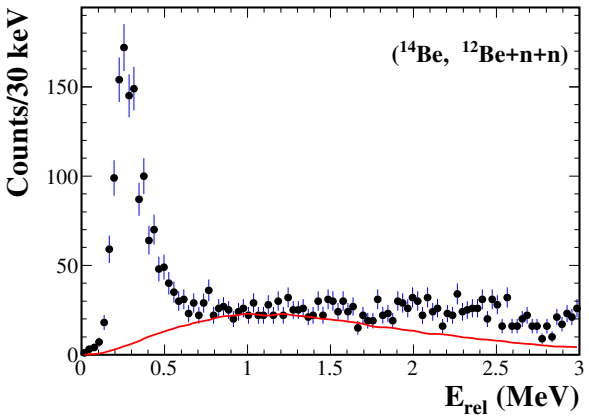

Figure 4.17: *Example of non-resonant contribution (red) generated from a* bck *simulation for the* $^{12}Be{+}n+n$ *relative energy.*

find more details on how to include a cross-talk algorithm in the event mixing method in Ref. [59].

Another possibility to estimate the uncorrelated distribution is to simulate a non-interacting N-body system, referred to in this work as *bck* simulation. In this case, the simulated momenta of the N particles would directly correspond to the independent momentum distributions $d\sigma_{\otimes}/dp$. Such simulation can be performed by the same code used for the simulation of resonances, MANGA. Hence this type of event generator takes into account the detector response and the experimental acceptances. Furthermore, the analysis of the simulated data, identical to the one followed for the analysis of experimental data, includes the cross-talk rejection algorithm. Similarly to the event mixing technique, the *bck* generator can only estimate the shape of the uncorrelated distribution, being necessary a fit of the spectrum with all components to determine its amplitude. An example of a non-resonant contribution generated with a *bck* simulation can be found in Fig. 4.17.

4.3.2 Resonant contribution

As already mentioned in Sec. 1.2.2, resonances are described using Breit-Wigner distributions. The shape of the resonance will be then described by the following parameters: *i)* the resonance energy E_r, *ii)* the width Γ and *iii)* the ℓ describing the angular momentum of the neutron with respect to the fragment. This resonance formalism is developed by treating a fragment-n resonance as a scattering problem. In the case of three-body resonances, however, several assumptions have to be considered in order to reduce the three-body scattering problem to the well-known two-body problem [16].

An important feature of the choice of the ℓ in Breit-Wigner distributions is its relation with the width of the resonance. In fact, the sensitivity to Γ is linked to the decay energy and the ℓ used for the description of the resonance. By way of example, we present in Fig. 4.18 the evolution of FWHM for a resonance energy $E_r = 1$ MeV (left) and $E_r = 0.25$ MeV (right) for $\ell = 0$–2. We can observe that for the $\ell = 2$ resonance the FWHM saturates in both cases at a certain value of Γ. Note that at a lower resonance energy, the saturation happens at smaller values of the width. This implies that regardless

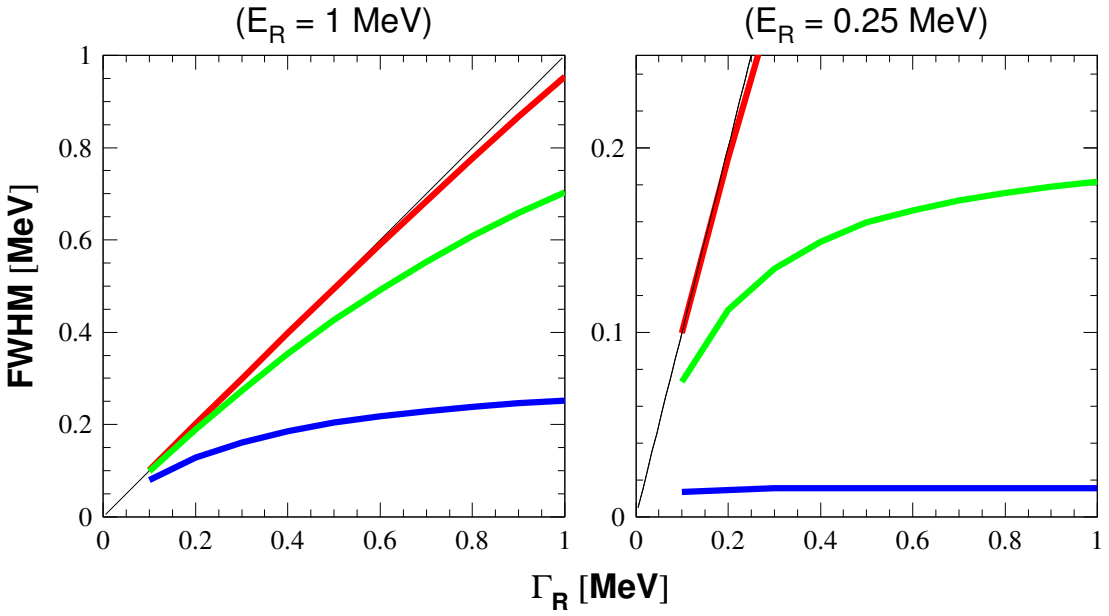

Figure 4.18: *FWHM as a function of the angular momentum of the valence neutron $\ell = 0, 1, 2$ (in red, green and blue respectively) for a Breit-Wigner with resonance energy $E_r = 1$ MeV (left) and $E_r = 0.25$ MeV (right).*

a very good experimental resolution, for certain resonances with $\ell > 0$ we may not be sensitive to the width with the use of a Breit-Wigner function, specially for low E_r and large Γ [16].

4.3.3 Data interpretation using simulations

In order to study the spectroscopy of unbound nuclei and their decay, first we need to identify and interpret the structures appearing in their experimental relative energy spectra. In this section, we briefly describe how to analyze a relative energy spectrum by using the simulations described in the previous sections. As already explained, we can consider two main contributions to the spectrum:

- A non-resonant component, which will be obtained either as a *bck* simulation in three-body resonances, or by the event-mixing technique in two-body systems.
- A resonant contribution described as a Breit-Wigner distribution.

By way of example, we present the analysis of the ^{15}B+n relative energy spectrum up to an energy of 0.3 MeV. As shown in Fig. 4.16, a very narrow resonant state is observed at $E \sim 50$ keV. Following the description given in Sec. 4.2, we can simulate this resonant state by taking into account the experimental resolution and response of the complete setup. In addition to this resonance, a non-correlated contribution is also needed in order to fully reproduce the spectrum. Since it is a two-body system, the event mixing technique is used to generate this contribution. The result of the non-resonant contribution can be found in Fig. 4.16. Then the best description of the spectrum can be achieved by fitting

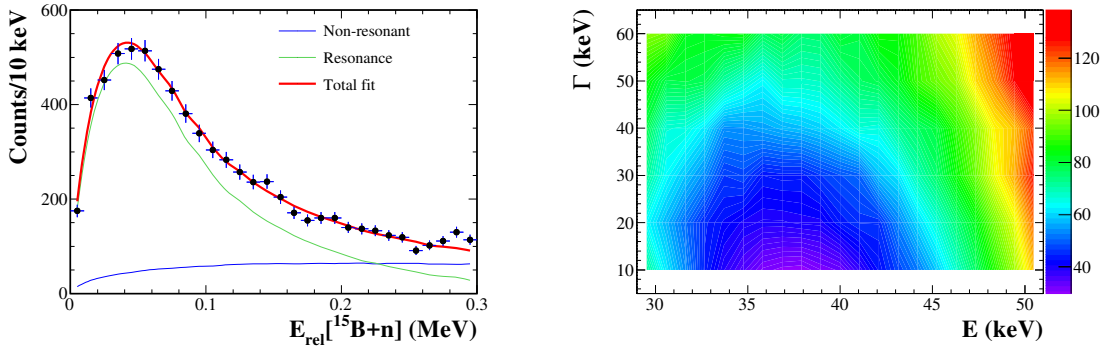

Figure 4.19: *On the left, result for the best fit to the relative energy spectrum of* ^{15}B+n *observed in the* $^{17}B(p,pn)^{15}B$ *reaction. In solid green line, the resonant Breit-Wigner distribution of energy* E_r=*38 keV, and in solid blue line, the non-resonant contribution. On the right, the* χ^2 *surface of the fit.*

	Degrees of freedom					
Confidence	1	2	3	4	5	6
68.3 %	1.00	2.30	3.53	4.72	5.89	7.04
90 %	2.71	4.61	6.25	7.78	9.24	10.6
95.4 %	4.00	6.17	8.02	9.70	11.3	12.8

Table 4.1: *List of* $\Delta\chi^2$ *used to calculate the uncertainties of the fit as a function of the degrees of freedom and the level of confidence.*

with these two components. Such fit consists in finding the parameters that best describe the experimental spectrum

$$N(E_{rel}) \;=\; w_1 R_1(E_r,\Gamma) \;+\; (1-w_1)\,U \tag{4.12}$$

where $N(E_{rel})$ is the number of events at a given energy, $R_1(E_r,\Gamma)$ represents the resonant component of energy E_r and width Γ which is normalized to the integral of the relative energy spectrum and weighed by the parameter w_1, and U the non-resonant contribution, also normalized to the integral of the relative energy spectrum and weighed by $w_2 = 1 - w_1$ (the sum of all the normalized components should give the total number of counts).

The best fit to the data can be found in Fig. 4.19 (left). The minimum of the χ^2 surface shown on the right plot represents the best description of the relative energy spectrum. Once the χ^2_{min} is determined, the error bars for the obtained values of E_r and Γ are calculated following the condition $\chi^2 \leq \chi^2_{min} + \Delta\chi^2$, where $\Delta\chi^2$ depends on the level of confidence and the degrees of freedom of the fit. Table 4.3.3 lists the values of $\Delta\chi^2$ as a function of the level of confidence and the degrees of freedom. In our case, we are fitting with only one resonance and a non-resonant contribution, which makes three degrees of freedom (E_r,Γ,w_1). For a level of confidence of 68.3%(1σ), $\Delta\chi^2$=3.53. By projecting onto the E_r and Γ axes we can easily obtain the uncertainties of the resonance parameters by taking into account the corresponding number of χ^2 units. In conclusion, the final parameters found for the low-energy resonance of ^{16}B are E_r = 38(4) keV and width

$\Gamma < 12$ keV.

4.4 Three-body correlations

Experiments in complete kinematics allow the investigation of the breakup of three-body systems from the particle correlations of the triple-coincidence events (fragment+n+n). The most basic correlations are those imposed by the energy and momentum conservation given by the N-body *phase space* [60] of the decay, which will define our baseline. The interaction between particles may give rise to "physical" correlations that are added to this baseline. In order to identify the correlations emerging from the interaction of particles, we use the *Dalitz plots* [61], where correlations lead to very characteristic structures.

4.4.1 Dalitz Plots

The Dalitz plot technique has been extensively used in particle physics to determine multi-particle correlations [61, 62]. In a three-body decay as the ones investigated in this work, the Dalitz plot can be obtained from the normalized invariant masses, by representing the reduced fragment-neutron mass, m^2_{fn}, as a function of the reduced neutron-neutron mass, m^2_{nn}. These variables are normalized and range from 0 to 1, which is one of the major advantages of this method[63]. If instead of m_{ij} we use directly the relative energy E_{ij} variables, which can go from 0 to the E_{rel} of the event, the resulting plot will not have a definite boundary as each event presents a different value of E_{rel}. The reduced variable m_{ij} is related to the invariant mass of the binary system as,

$$M_{ij} = m_i + m_j + E_{ij} \tag{4.13}$$

from where the reduced mass can be derived as

$$m^2_{ij} = \frac{M^2_{ij} - (m_i + m_j)^2}{(m_i + m_j + E_{rel})^2 - (m_i + m_j)^2} \tag{4.14}$$

In our case, the decay of fragment+n + n systems with an energy of few MeV, the Dalitz plot can be constructed using a simpler, more intuitive variable, the reduced relative energy, ε_{ij} that can be defined as

$$\varepsilon_{ij} = \frac{E_{ij}}{E_{rel}} \tag{4.15}$$

If we now introduce this expression in the invariant mass equation

$$M_{ij} = m_i + m_j + \varepsilon_{ij}\, E_{rel} \tag{4.16}$$

which allows us to express the reduced mass in terms of ε_{ij}

$$m_{ij}^2 = \frac{(m_i + m_j + \varepsilon_{ij}\, E_{rel})^2 - (m_i + m_j)^2}{(m_i + m_j + E_{rel})^2 - (m_i + m_j)^2}$$

$$= \varepsilon_{ij} \frac{2(m_i + mj) + \varepsilon_{ij}\, E_{rel}}{2(m_i + mj) + E_{rel}} \approx \varepsilon_{ij} \tag{4.17}$$

In nuclear physics the masses of the particles are much bigger than the relative energy, *i.e.*, $2(m_i + m_j) \gg E_{rel}$. Indeed, twice the particle masses are several GeV, while E_{rel} represents several MeV. This, together with the fact that $\varepsilon_{ij} \leq 1$, allows us to use the reduced energy ε_{ij} instead of the reduced mass m_{ij}^2 as a Dalitz variable.

4.4.2 Phase space correlations

The phase space is defined by the conservation laws of energy and momentum given by the N-body decay. In this sense, the phase-space correlations do not depend on the nature of the particles but on the available energy of the decay, their number and their masses [61]. In our case, we are interested in decays from $f + n + n$ resonances which can follow either a three-body phase space via a simultaneous $2n$ emission, or a two-body phase space if the decay is sequential. Depending on the nature of the mechanism, the phase space to consider as our baseline is different. This is particularly important since physical correlations are identified by comparison with the basic correlations that arise from the kinematics of the phase space.

Direct decay

In the absence of any interaction, a direct decay from a $f + n + n$ resonance follows a three-body phase space which leads to a uniform population of the Dalitz plot. As can be seen in Fig. 4.20 (a), the corresponding Dalitz plot is flat and does not show any structure. This makes the use of Dalitz plots a very suitable technique for the study of the dynamics of three-body decays, as any correlation coming from the interaction of particles will be easily spotted over this flat baseline. To analyze the correlations in a more quantitative manner, we can project onto the x- and y-axis to obtain the ε_{fn} and ε_{nn} distributions. These projections are presented in the plots (b) and (c) of Fig. 4.20, respectively. Note that since two neutrons are involved in the decay, the ε_{fn} is filled twice, one time for each neutron n_1 and n_2.

The cylindrical 2d flat structure leads to bell-like projections on both ε_{nn} and ε_{fn} axes. The phase space available is larger at the center of the "cylinder", while it reduces drastically at the limits, as it is unlikely for those two particles to leave along the exact same direction ($\varepsilon_{ij} = 0$) or for the other particle to stay at rest while they carry all the decay energy ($\varepsilon_{ij} = 1$).

Sequential decay

If an intermediate state is located at an energy below the energy of the three-body resonance, the decay can happen sequentially. This implies that one of the neutrons is emitted first while the remaining fragment and neutron form a resonance that, in turn, will

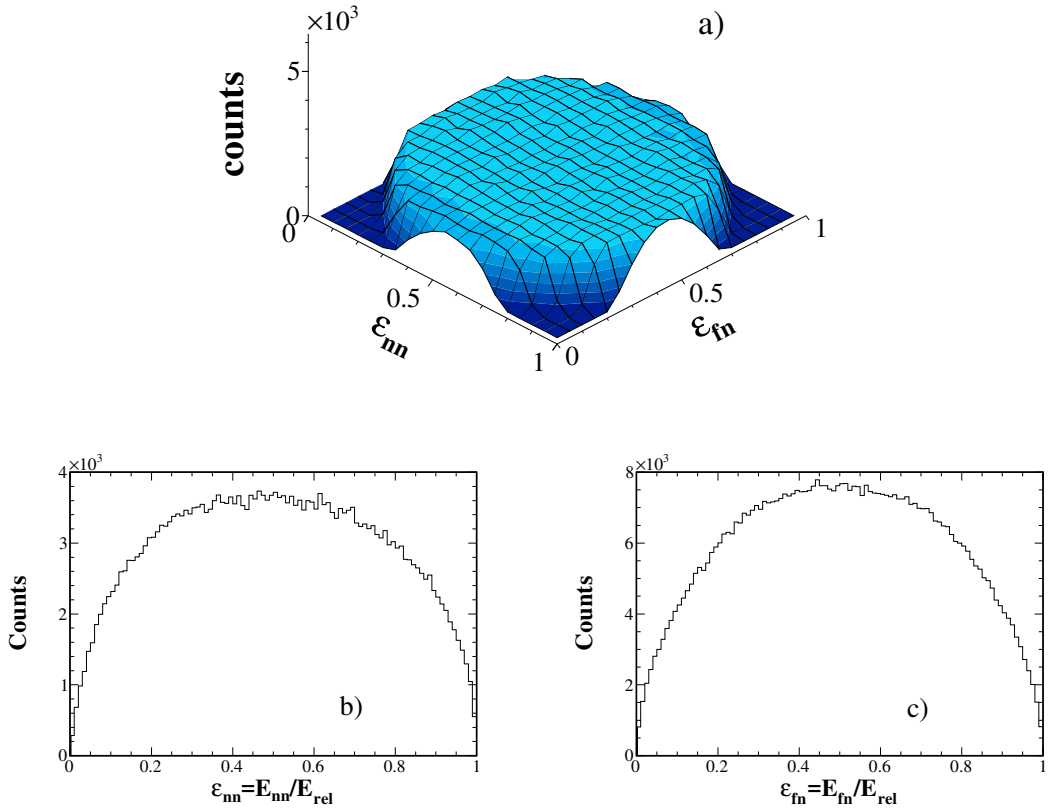

Figure 4.20: *Dalitz plot (a) for a simulation of the decay of ^{14}Be into ^{12}Be+n + n following a three-body phase space. The projections onto the axes ε_{nn} and ε_{fn} are represented in (b) and (c), respectively.*

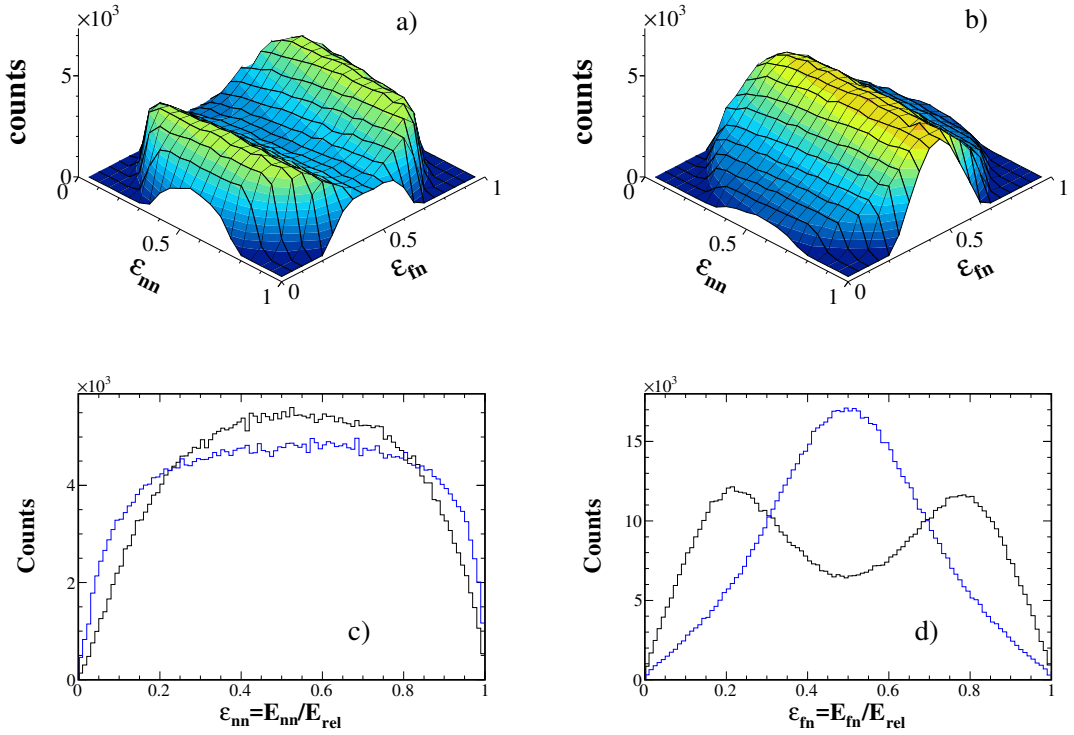

Figure 4.21: *Dalitz plot of the sequential decay of* ^{12}*Be+n+n from a state at an energy of 2 MeV through two different intermediate states: (a) a low energy state,* $E_r = 0.5$ *MeV and (b) an intermediate state at the middle of the resonance,* $E_r = 1$ *MeV. The projections onto* ε_{nn} *(c) and* ε_{fn} *(d) show the differences in shape depending on the energy of the intermediate state. In black, the corresponding distributions for an intermediate energy* $E_r = 0.5$ *MeV and in blue, for* $E_r = 1$ *MeV.*

subsequently decay. In this case the emission of the two neutrons cannot be considered simultaneous. Consequently, the kinematics governing the decay are not a three-body phase space but a double two-body phase space defined by the energy of the intermediate resonance E_r and its width Γ.

This decay mechanism is characterized in the Dalitz plot by "ridges" along the ε_{fn}-axis as illustrated in Fig. 4.21. These structures are the reflection of each other as $\varepsilon_{fn_1} \approx 1 - \varepsilon_{fn_2}$. Their positions depend directly on the energy of the intermediate state. To illustrate this effect, we have simulated the decay of ^{12}Be+$n + n$ from a Breit-Wigner resonance at 2 MeV through a sequential decay considering two different intermediate states, at $E_r = 0.5$ MeV (a) and $E_r = 1$ MeV (b). For an energy that corresponds to the middle of the decay-energy range, as in (b), we will observe a single ridge structure located in $\varepsilon_{fn} \sim 0.5$, due to the overlap of the two symmetrical wings. The effect of the position of the intermediate state can be seen in the ε_{fn} projection (d) where the lowest energy (black) shows very definite wings while the middle energy state shows a peak-like structure (blue). Since we are dealing with three-body decays, the ε_{nn} distribution is also dependent on the parameters E_r and Γ of the intermediate resonance, with a much smaller

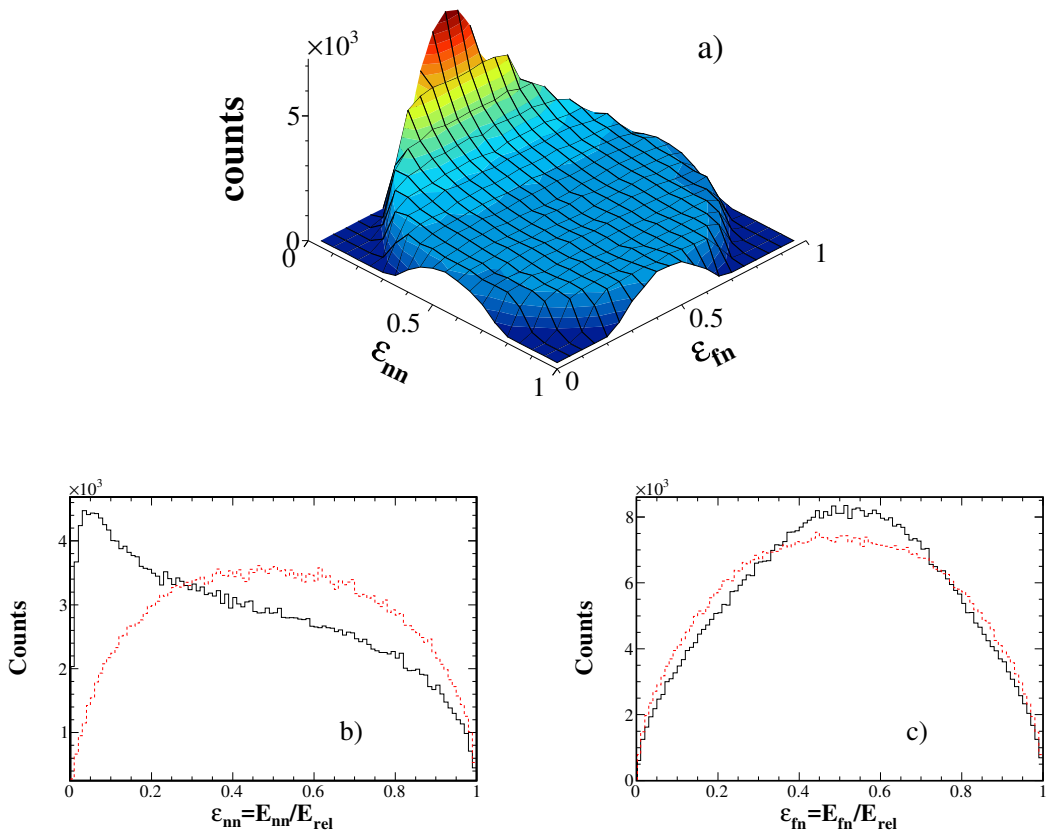

Figure 4.22: *Effect of the nn FSI on a three-body phase space for a simulation of the decay of* ^{14}Be *into* $^{12}Be+n+n$ *in the Dalitz plot representation (a). The projections onto* ε_{nn} *(b) and* ε_{fn} *(c) show the effect of the nn interaction (in black) with respect to the three-body phase space (in red).*

impact as can be seen in plot (c).

4.4.3 *nn* FSI

Physical correlations are revealed as they deviate from the phase space defined by the decay mechanism. In decays from $f+n+n$ systems, either direct or sequential, neutrons may interact with each other and give rise to characteristic correlation patterns. In order to identify *nn* correlations, a **correlation function** C_{nn} can be defined from the ratio between the experimental data and the corresponding phase space

$$C_{nn} = \frac{\sigma_{exp}(E_{nn})}{\sigma_{PS}(E_{nn})} \tag{4.18}$$

where σ_{exp} corresponds to the experimental distribution and σ_{PS} the distribution that we would obtain considering only the phase-space kinematics. If the experimental distribution

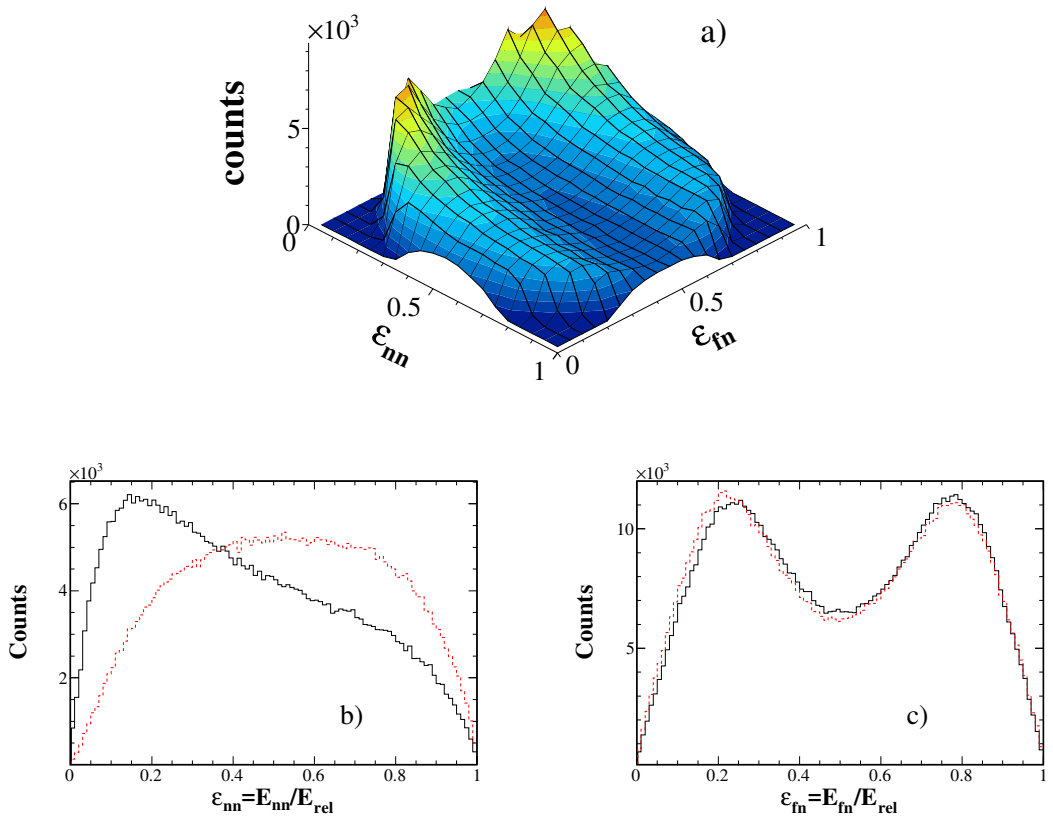

Figure 4.23: *Effect on the nn FSI on a two-body phase space for the simulation of a resonant state in ^{14}Be at $E_r = 2$ MeV decaying through an intermediate state at E_r=0.5 MeV. The Dalitz plot is presented in (a). The projections onto ε_{nn} (b) and ε_{fn} (c) show the effect of the nn FSI (in black) with respect to the initial sequential phase space (in red).*

is fully described by the phase space, then $C_{nn} = 1$. On the contrary, if the interaction between particles leads to a deviation from phase space, the function will show a signal $C_{nn} \geq 1$. In general, the nn FSI leads to correlation signals at low nn relative energies. In terms of correlation function, this translates into an exponential-like behavior at low relative energy.

In the Dalitz plot, the nn FSI can be observed as a low-energy enhancement in the ε_{nn}-axis. In Fig. 4.22 (a), an example of a typical nn correlation signal is shown on top of a three-body phase space. The projection onto ε_{nn} of this Dalitz plot (b) shows a clear low-energy increase with respect to phase space (in red). Moreover, strong nn correlations may have an important impact on the ε_{fn} distributions. This is depicted in plot (c), where the fn distribution presents a more peaked shape as compared with the three-body phase space as a consequence of the nn interaction.

On the other hand, if we now consider a sequential decay with the same nn FSI strength, as represented in Fig. 4.23 (a), the projection onto ε_{nn} (b) shows a slightly

different shape as compared with the three-body kinematics. This happens as a result of the influence of the fragment-n resonance on the relative energy of the two neutrons.

In conclusion, it is not possible to study the three-body correlations of a decay by looking at only one pair of correlations, that is, the influence of nn correlations on the fn relative energy cannot be neglected, and *vice-versa*. In this sense, the Dalitz plots allow us to relate the binary correlations and reconstruct the three-body picture.

4.5 Conclusions

In this chapter, we have shown the main techniques used in the analysis of the experimental data, namely the analysis of three-body correlations or the reconstruction of the physical observables. The relative energy spectrum is reconstructed by invariant mass analysis and interpreted by means of simulations. These simulations are a key factor in our experiments as they allow us to estimate the global resolutions of the complete multidetector setup SAMURAI. In order to compare data and simulation on a same basis, a unique analysis code is used in which all experimental filters and conditions are included.

Chapter 5

Results: Spectroscopy

Contents

In this chapter, the results obtained on the spectroscopy of the heaviest isotopes of beryllium from different experiments at RIKEN are presented. First, we investigate the ^{14}Be excited states populated by inelastic scattering during the SAMURAI commissioning. Then a systematic study of ^{15}Be states from multiple experiments in the DayOne campaign is presented. Finally, we probe the structure of the unbound ^{16}Be which was populated from ^{17}B$(-1p)$ during the SAMURAI18 campaign.

5.1 Beryllium 14

As mentioned in Sec. 1.4.3, a previous work has probed the first excited state of the most neutron-rich beryllium isotope by inelastic scattering [6]. A well-defined state was observed at $E_x = S_{2n} + E_{rel}$=1.55(13) MeV and its spin-parity determined as $J^\pi = 2^+$. The relative energy of ^{14}Be(2^+) was reconstructed from ^{12}Be+n+n measured in coincidence, for which $E_{rel} = 0.28 \pm 0.01$ MeV was found, giving a very precise value. Moreover, the use of the γ detector DALI allowed the measurement of the possible de-excitation γ-rays emitted from either the ^{14}Be projectile or the ^{12}Be fragment. The lack of γ-rays in coincidence indicated a direct decay to the ground state of ^{12}Be by emission of two simultaneous neutrons. Other studies have tentatively searched for excited states at higher energies[64], however, these states being much broader, their individual study becomes more difficult. The objective

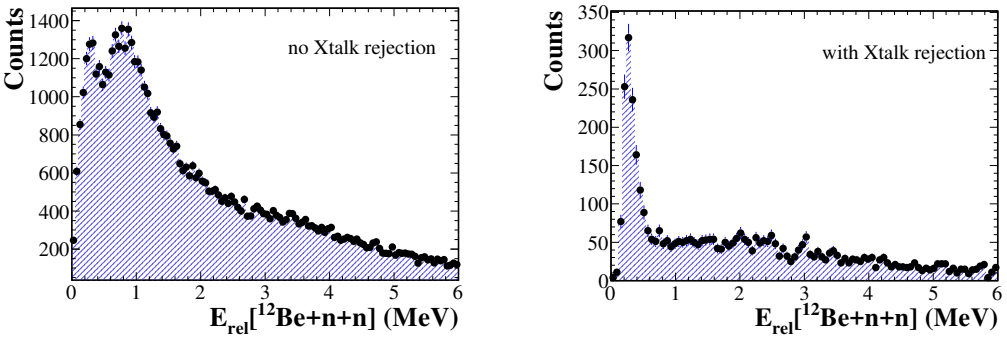

Figure 5.1: *Relative energy spectrum of ^{12}Be+n+n obtained via the inelastic scattering of ^{14}Be on a carbon target. On the left, the spectrum with no cross-talk filter. On the right, after the application of the cross-talk rejection algorithm.*

of our study is to confirm the energy of the first 2^+ state, but specially, to investigate its three-body decay and the correlations that the decay particles present.

5.1.1 Spectroscopy

Excited states in ^{14}Be have been populated by inelastic scattering on a carbon target, similarly to Ref. [6], during the SAMURAI commissioning at RIKEN. The relative energy spectrum is reconstructed from the coincident ^{12}Be+$n+n$ particles. The final spectrum is presented in Fig. 5.1 (right), where one main structure can be clearly observed and that we can identify as the first 2^+ excited state of ^{14}Be. Beyond this peak, no other structures are notable and therefore a non-resonant contribution is to be considered.

The very characteristic 2^+ state of ^{14}Be is also a benchmark for the $2n$ detection. As detailed in Sec. 3.6, one of the challenges of multineutron detection is the multihit events or cross-talk. The cross-talk rejection algorithm can be put to the test by means of simulations or very well-known experimental channels like this one. By way of example, the effect of the cross-talk filter is illustrated on the right panel of Fig. 5.1, where we can see that the non-application of this filter hides the very narrow peak at ~ 0.25 MeV. Even though the contribution of cross-talk can be simulated and included in the fit to reproduce the experimental data, if statistics are high enough, the most suitable is to eliminate this contribution in order to remove non-physical structures from the spectrum.

The analysis of the spectrum is performed taking into account a simple Breit-Wigner line shape with an energy-dependent width plus a non-resonant contribution, obtained from the simulation of a non-interacting system of the final particles ^{12}Be+n+n as described in Sec. 4.3.1 for three-body decays. The result of the fit is presented in Fig. 5.2. Since the objective is to describe only the low-energy part of the spectrum, we fit the data up to 1.5 MeV and neglect possible excited states beyond this value of energy.

The energy of the 2^+ state in terms of relative energy is found at E_{rel} =254(6) keV and Γ =40(20) keV. Since the two-neutron separation energy is measured at 1.27(13) MeV[44], the resulting excitation energy corresponds to E_x=E_{rel}+S_{2n}=1.52(13) MeV, consistent with the previous value of E_x=1.55(13) MeV. The difference in relative energy with respect to the previous work (E_{rel} = 280 keV) does not come from the experimental results by

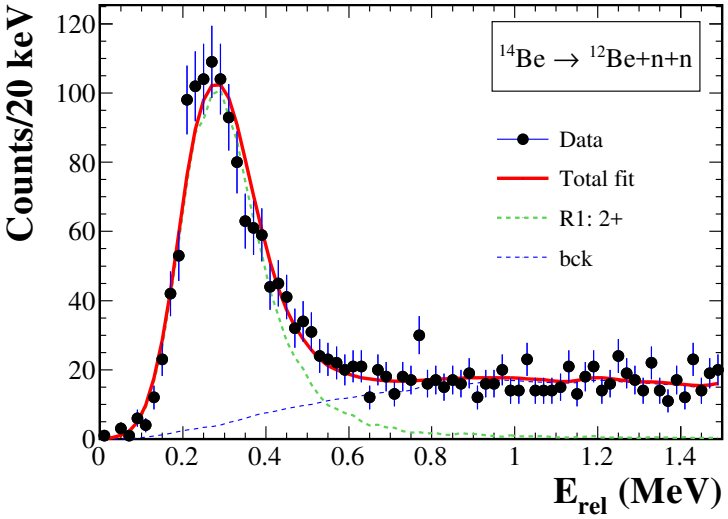

Figure 5.2: *Relative energy spectrum of* ^{12}*Be+n+n produced via the inelastic scattering of* ^{14}*Be on a carbon target. The red line corresponds to the best fit, including the non-resonant continuum (blue dashed line) and the* ^{14}*Be 2+ resonance at 254 keV (green dashed line).*

themselves but from the choice of the non-resonant component, whose contribution in the zone of the peak in our case is minimum and allows the fit to go to lower energies. On the other hand, and as in Ref. [6], although the uncertainty of the 2^+ state in relative energy is significantly small, the uncertainty of E_x is very much dominated by the much bigger uncertainty of the two-neutron separation energy measurement and can only be reduced by a more precise mass measurement of ^{14}Be.

5.1.2 Particle correlations

As the last isotope at the edge of the neutron dripline, ^{14}Be is an interesting candidate for the study of core-n-n correlations from the decay of its 2^+ state. Since the ground state of ^{13}Be is above the 2^+ energy, the decay is expected to be direct to ^{12}Be by emission of two simultaneous neutrons. The relative energy reconstructed from the coincident ^{12}Be+$n+n$ gives us the spectroscopy information of the states of ^{14}Be but does not tell us much about the decay mode itself. The study of particle correlations is, instead, a powerful tool that allows us to describe the three-body decay and therefore to complete the whole picture from the moment the unbound system is populated in the target to the detection of the coincident decay products.

The correlations of the three-body decay have been analyzed by means of Dalitz plots of the normalized two-body energies for which the effect of the nn interaction and intermediate resonances lead to very characteristic structures (see Sec. 4.4). References [6, 45] have shown evidence that the decay is indeed direct to the the g.s. of ^{12}Be. Under this assumption, particles involved in the decay should follow a three-body phase space, represented by a uniform Dalitz plot within the kinematic boundary defined by energy and momentum conservation. Although a direct decay does not necessarily imply the absence of nn correlations, in order to use as less hypothesis as possible in the description of the experimental data, this interaction is neglected as a first step comparison.

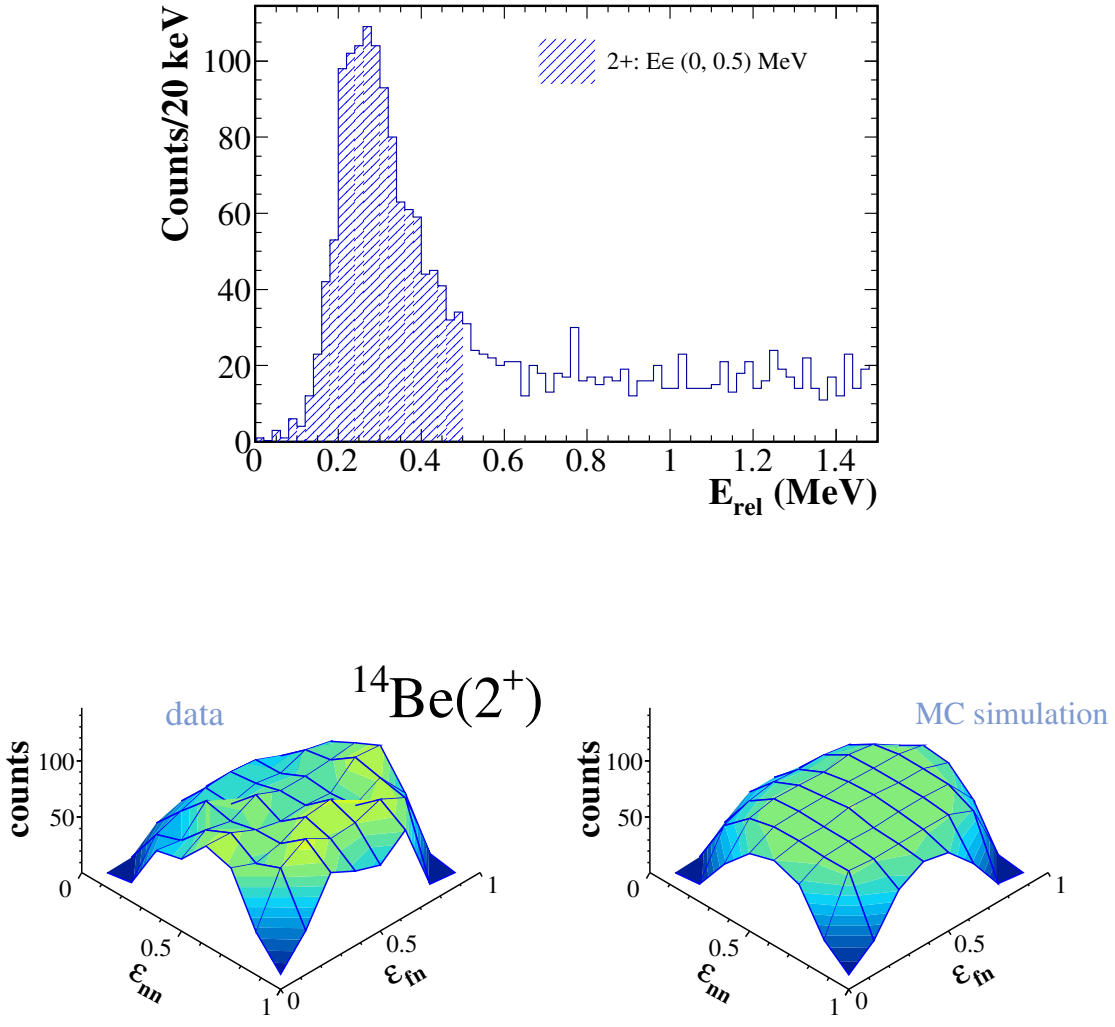

Figure 5.3: *On the top, selected range in the relative energy of $^{12}Be+n+n$ considered in the study of the decay of the 2^+ state of ^{14}Be. On the bottom, comparison of the experimental (lower left) and simulated (lower right) Dalitz plots for the 2^+ state of ^{14}Be in the above energy range. The simulation represents a decay following a three-body phase space with no interaction between particles.*

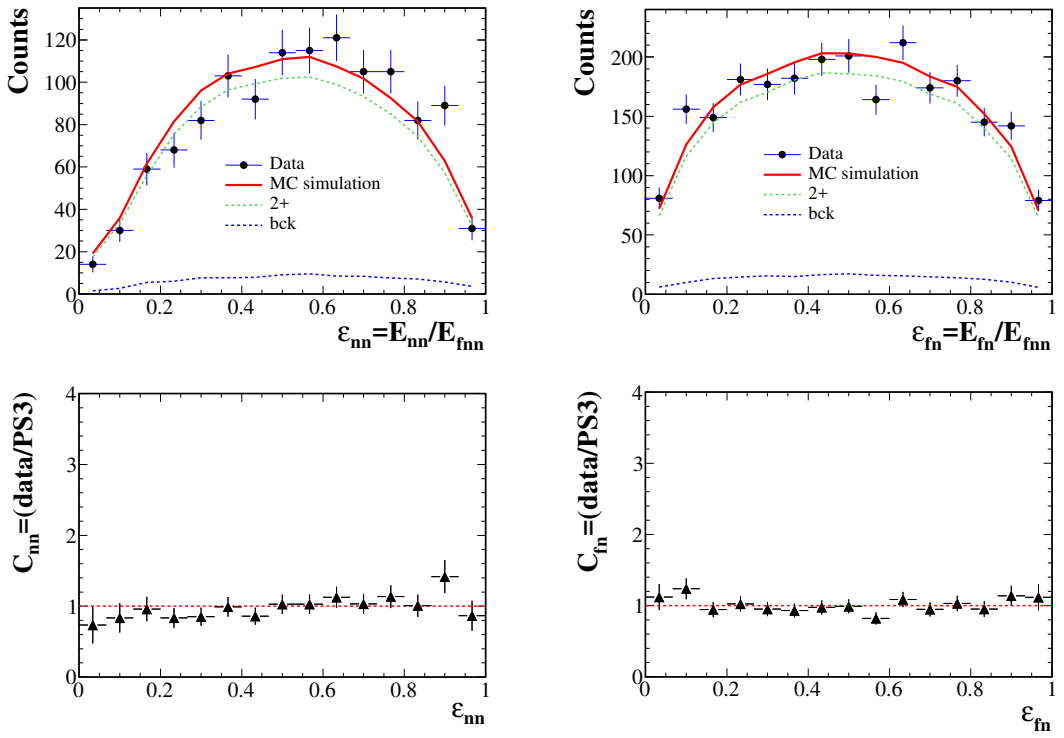

Figure 5.4: *Study of particle correlations in the decay of the ^{14}Be first excited state. On the top, nn (left) and fn (right) relative energy distributions. The red line represents a three-body phase space simulation, including both non-resonant and 2^+ resonant contribution in green and blue dashed lines, respectively. Note that the asymmetry observed at low nn energy in both data and simulation corresponds to the effect of the cross-talk filter. On the bottom, correlation function calculated as the ratio between the experimental data and the three-body phase space simulation. The flat distribution indicates a good agreement.*

Figure 5.3 illustrates the experimental Dalitz plot (lower left) for the decay of the 2^+ state, for which a range of $E_{rel} \in [0,0.5]$ MeV has been selected. Note that in this range, data are very little contaminated by the non-resonant contribution (less than 8%), and consequently correlation distributions correspond approximately to the "pure" distributions of the resonant state. However, the contribution of the non-resonant component is estimated from the fit of the relative energy and taken into account for the correlation distributions. *A priori*, we can observe that the experimental Dalitz plot does not show any significant structure and, except for some small fluctuations, looks compatible with the uniformity expected from a direct decay with no *nn* interaction. No noticeable increase towards $\varepsilon_{nn} = 0$ or any "winged" structures in ε_{fn} indicating clear trace of sequentiality appear in Fig. 5.3. The plot on the right corresponds to the simulated data of the decay following a three-body phase space, which seems to be qualitatively enough to reproduce the experimental data.

A more quantitative way of comparing the experimental distributions with a model is by projecting the Dalitz plots onto either axes ε_{nn} and ε_{fn}. In Fig. 5.4 experimental projections are compared to a three-body phase space taking into account contributions from both the 2^+ state and the non-resonant component. We can observe in the ε_{fn} plot that the distribution follows a three-body kinematics by which the decay can be considered

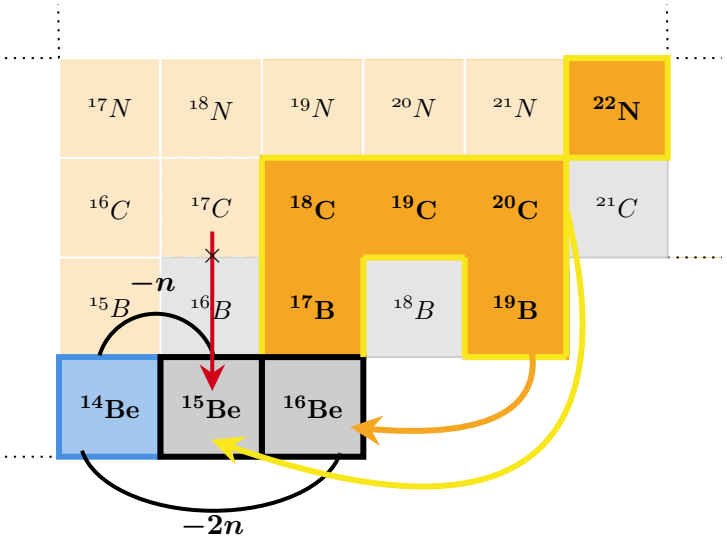

Figure 5.5: *Illustration of the different channels studied leading to the production of* ^{15}Be.

as exclusively direct. The C_{fn} correlation function between data and simulation showing a flat distribution confirms this scenario. We could expect that a simultaneous $2n$ emission would generate a very strong nn correlation from the interaction between both neutrons. On the contrary, the absence of a nn signal at low energies is evident in the experimental ε_{nn} projection (upper left). Here, the deviation from the usual shape of a ε_{nn} symmetric distribution from a non-interacting three-body decay is explained as the result of the cross-talk rejection algorithm, that preferentially rejects pairs of low relative-energy neutrons, an effect that is specially important for resonances as close to threshold as this ^{14}Be(2^+). Note that since the filter is applied to both the experimental and the simulated data, this effect is properly described.

5.2 Beryllium 15

The main goal of this thesis work is to investigate the three-body decay of ^{16}Be. However, whether the decay is direct or sequential is highly dependent on the energy of the ground state of ^{15}Be and its position with respect to the states in ^{16}Be. In order to fully understand the $2n$ decay from ^{16}Be, we have conducted a study on the spectroscopy of ^{15}Be from a wide range of experiments that took place during the DayOne experimental campaign at RIKEN. The potential states in ^{15}Be are probed through the use of knock-out reactions from different beams for which we select the ^{14}Be+n exit channel. The detailed spectroscopy of ^{16}Be could not be probed using these data due to the significantly lower statistics and worse resolution that were available during the DayOne campaign compared to s018, the main experiment of this work designed for the study of ^{16}Be (see next Sec. 5.3). An overview of the reaction channels used for this study is illustrated in Fig. 5.5 and listed in Table 5.1.

As detailed in Sec. 1.4.2, only one state in ^{15}Be, tentatively assigned to a spin and parity

Beam	N_{1n}	N_{2n}	E_{beam} (MeV/nucleon)	$E_{^{15}Be}$ (MeV)
^{17}B	4386	637	283	-
^{19}B	1788	493	219	-
^{22}N	1230	466	227	-
^{18}C	1351	185	242	1.8(1)
^{19}C	3327	547	214	1.8(1)
^{20}C	2222	363	280	1.9(1)

Table 5.1: *Summary of DayOne experiments leading to the ^{14}Be+xn exit channel used to study the spectroscopy of ^{15}Be. N_{1n} and N_{2n} refer to the number of counts for the ^{14}Be+n and ^{14}Be+$n+n$ exit channels, respectively. $E_{^{15}Be}$ corresponds the values of the ^{15}Be resonance energies obtained from the fits in Fig. 5.11.*

of $5/2^+$, has been observed at 1.8(1) MeV[5] with a width of 575(200) keV. Nevertheless, the level scheme of ^{15}Be remains uncertain. A $3/2^+$ state with an energy very close to that of the $5/2^+$ has also been predicted [34] but not yet observed, and after several experimental attempts the authors suggested that it could decay towards ^{12}Be(2^+) and thus proposed a lower limit of 1.54 MeV [34, 43]. Given the uncertainty surrounding the energy of the $3/2^+$ state, the question of which of the two predicted states, if any, corresponds to the ground state of ^{15}Be is still unknown.

5.2.1 Potential ^{16}Be contribution

Since in neither of the experimental campaigns conducted in SAMURAI so far we have access to the direct reaction $^{17}\mathrm{C}\xrightarrow{-2p}{}^{15}\mathrm{Be}$ that would populate directly states in ^{15}Be, we have undertaken a systematic search with heavier beams that potentially can produce ^{15}Be from more complex knock-out reactions. These reactions usually comprise the removal of several nucleons, such as for instance $-p2n$ knock-out reactions, which can populate states in isotopes other than ^{15}Be (see Fig. 5.5). As a result, structures in the relative energy spectrum do not necessarily involve the population of a state in ^{15}Be and could instead correspond to the decay of other heavier isotopes produced by the reaction. Indeed, through the application of this technique, only relatively narrow resonances, or at least narrower than the broad decay structures, can be identified. The list of channels used to populate ^{15}Be is summarized in Table 5.1.

The spectroscopy of ^{15}Be is investigated from the reconstructed relative energy of the coincident ^{14}Be+n events, with the selection of the fastest neutron arriving to the NEBULA detector. The spectra obtained for the different channels are presented in Fig. 5.6. We can observe that up to ∼3 MeV all spectra, except for the one obtained for the ^{22}N beam, show two similar structures, one between 0–1 MeV followed by a broader one between 1–3 MeV. In some of them, a well-defined structure around ∼1.8 MeV is also present, for example in the case of the reaction from a ^{18}C beam. We also note that in the spectrum obtained with the ^{22}N beam there is a clear decrease towards zero energy.

Despite the use of very complex knock-out reactions with beams that are far from ^{15}Be, all DayOne spectra show common structures. In fact, if we compare with the ^{14}Be+n relative energy spectrum obtained in the s018 campaign using a ^{17}B beam, these structures are also present. In s018 the comparison of both inclusive (all ^{14}Be+n events) and exclusive

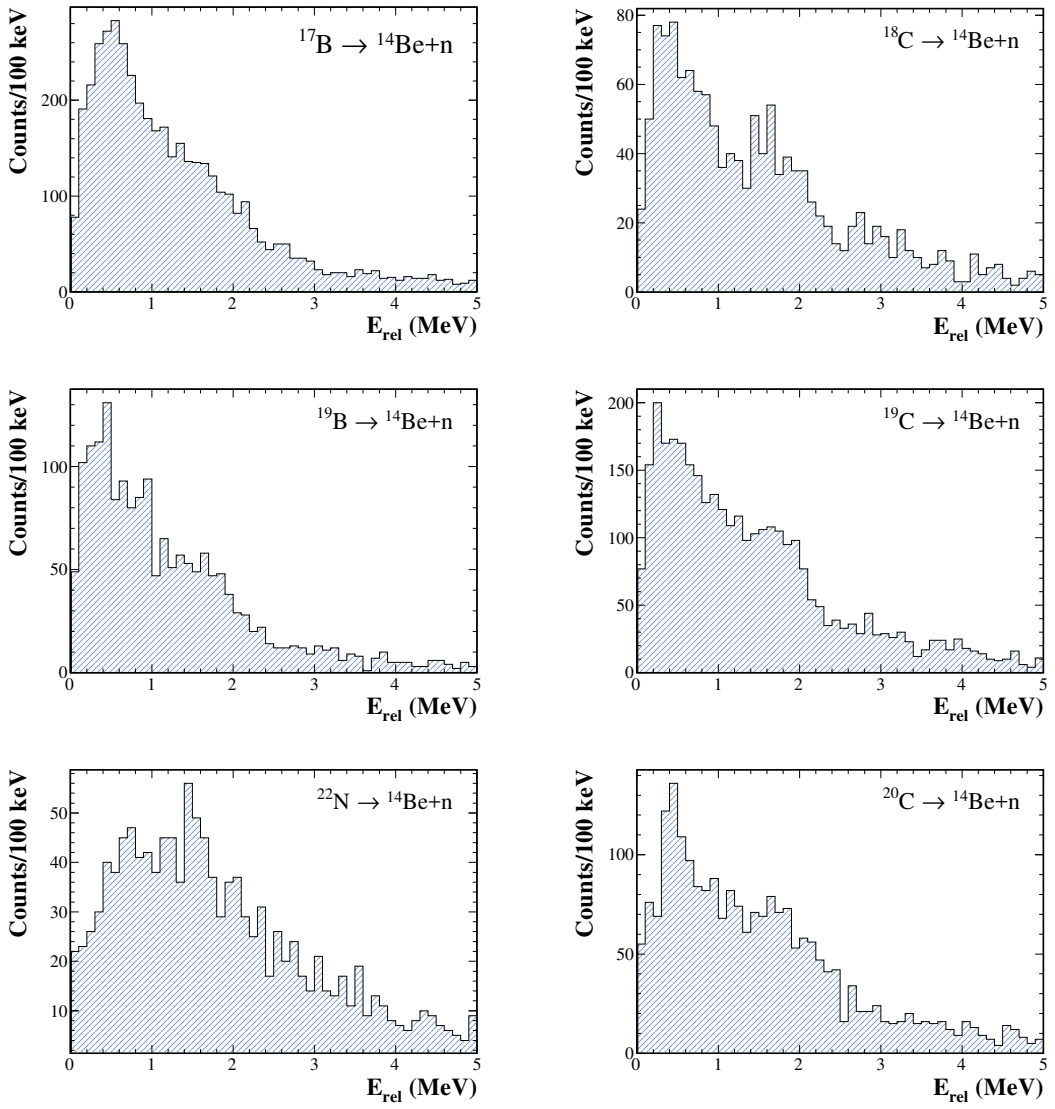

Figure 5.6: *Relative energy spectra reconstructed from ^{14}Be+n coincident events for DayOne experiments.*

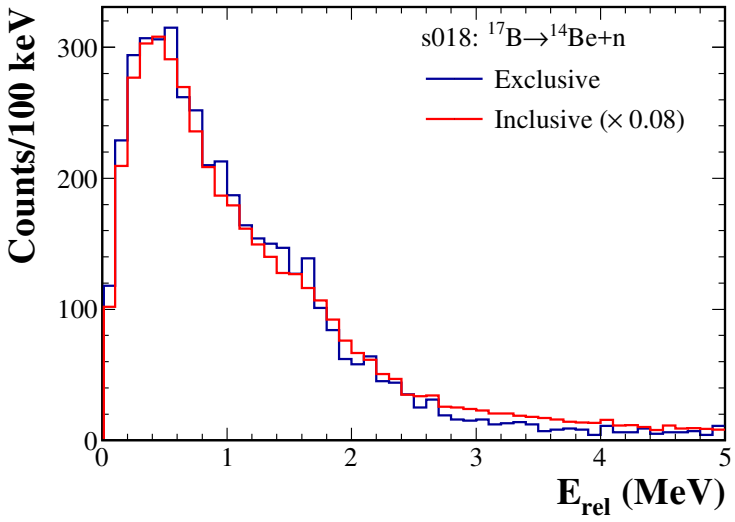

Figure 5.7: *^{14}Be+n energy relative reconstruction for the s018 experiment. In red solid line, the inclusive spectrum with all ^{14}Be+n events, and in blue solid line, the exclusive spectrum, where only events where two neutrons have been detected are selected.*

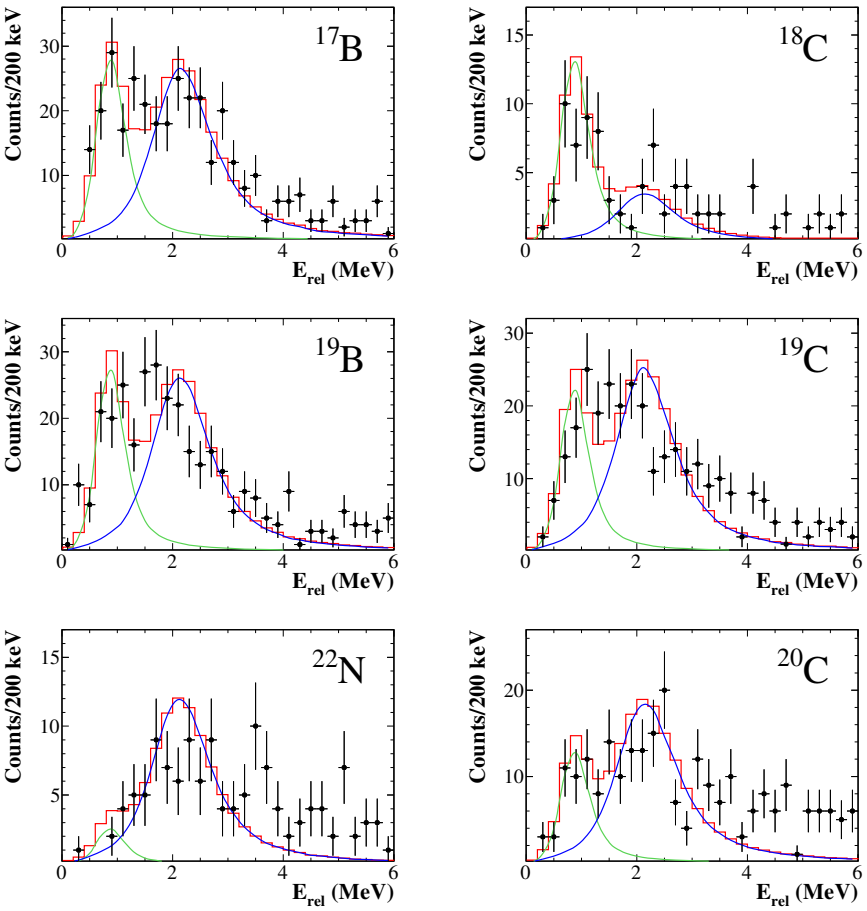

Figure 5.8: *Relative energy reconstruction for ^{14}Be+n+n coincident events from DayOne experiments.*

(the ^{14}Be+n part of triple coincidence ^{14}Be+n+n events) spectra is possible due to the high statistics. Figure 5.7 shows no significant difference between the inclusive (red) and the exclusive spectrum (blue). For the latter, as we will see in the next Sec. 5.3, these structures are clearly contributions from the decay of two states populated in ^{16}Be, and therefore do not correspond to a population of states in ^{15}Be. Therefore we can assume that all ^{14}Be+n events from the ^{17}B$\longrightarrow^{14}$Be+n reaction come almost exclusively from the contribution of decay of ^{16}Be$\longrightarrow^{14}$Be+$n+n$.

In order to test the validity of this assumption for DayOne experiments, we check the ^{14}Be+$n+n$ spectrum to determine if, despite the worse experimental conditions, we can associate structures to states in ^{16}Be. The three-body spectra in Fig. 5.8 can be roughly described up to 4 MeV with the two ^{16}Be structures that we will discuss in the next section, using different relative weights. As no other structures are observed beyond 4 MeV, in neither the ^{14}Be+$n+n$ or ^{14}Be+n spectra, only structures up to this energy are assumed to come potentially from a decay of ^{16}Be.

5.2.2 ^{14}Be+n spectroscopy

The contribution from the decay of both states in ^{16}Be is apparent, with varying weights, in all DayOne channels, indicating that at least a part of ^{14}Be+n events do not form ^{15}Be but are the result of populating ^{16}Be first. Due to low statistics in the triple events (^{14}Be+n+n), we cannot study separately the exclusive from the inclusive ^{14}Be+n spectra. For the same reason, it is not possible to perform a fit for ^{16}Be. The energies considered for the contribution of the decaying ^{16}Be states have been taken from the fit of ^{16}Be in the s018 experiment that we will discuss later (see Fig. 5.13). The non-resonant contribution is calculated following the technique of event mixing, as described in Sec. 4.3.1, separately for every reaction channel. The proportions of these three components are the free parameters that we vary for the description of the spectrum at this first stage.

In order to reveal resonances in ^{15}Be, we define the ratio C_{fn} between the data and the maximized contribution of the three identified channels not related with the population of ^{15}Be resonances: the fragment-n non-resonant component plus the contribution from the decay of the two ^{16}Be states. This ratio will highlight structures in the spectrum that potentially require states in ^{15}Be. Figure 5.9 shows the description of the spectra for knock-out reactions from ^{17,19}B and ^{22}N beams. The relative energy showing the explicit contribution of each non-resonant component is located on the left, while the ratio between the experimental spectrum and the simulated data is presented on the right. The comparison with the simulated data and the ratio plots does not indicate the need of any extra contribution. Although the description of the spectra is not completely accurate, their ratios do not show any clear structure that could be related to a state in ^{15}Be. Moreover, we have to keep in mind that we do not allow the variation of the energy nor the widths of the states in ^{16}Be in this description. This may explain the small differences in the spectra or modulations in the ratios that we observe.

On the other hand, ^{18,19,20}C reaction channels presented in Fig. 5.10 show a structure at around 1.8 MeV that cannot be fully explained by neither the decay of ^{16}Be nor the non-correlated contribution. In the particular case of ^{20}C, we can additionally observe another narrow structure at lower energy, at about $\sim$0.4 MeV. One important thing to determine the origin of these structures is to check whether the 1n spectrum is coherent

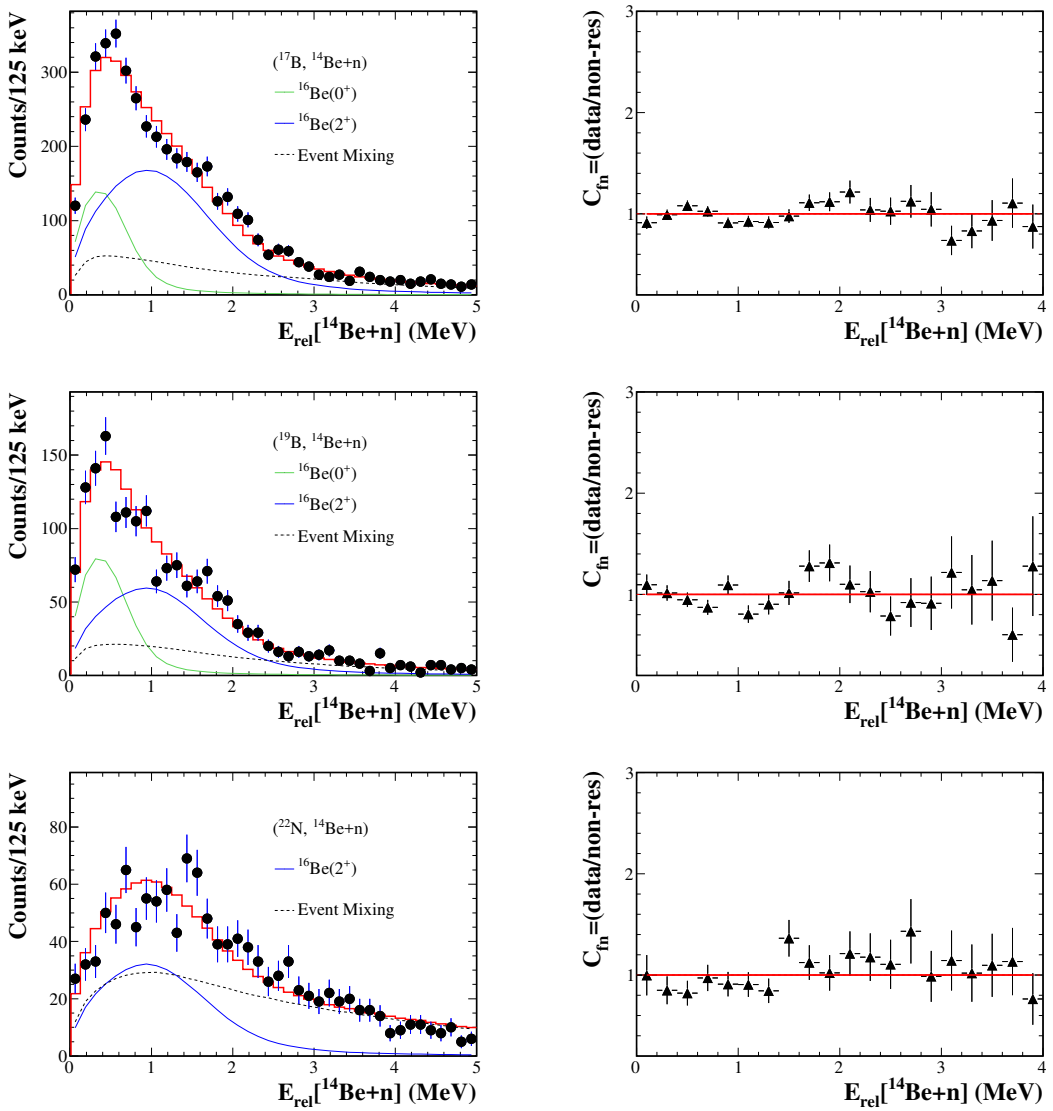

Figure 5.9: *On the left, ^{14}Be+n relative energy spectra obtained using a knock-out reaction from a ^{17}B (upper), ^{19}B (middle) and ^{22}N (lower) beam. The red line corresponds to the maximized contribution with no resonant states in ^{15}Be, including the non-correlated continuum generated by event mixing (dashed line) and the contribution from ^{16}Be decay (green and blue solid lines). On the right, the ratio between data and this non-resonant contribution.*

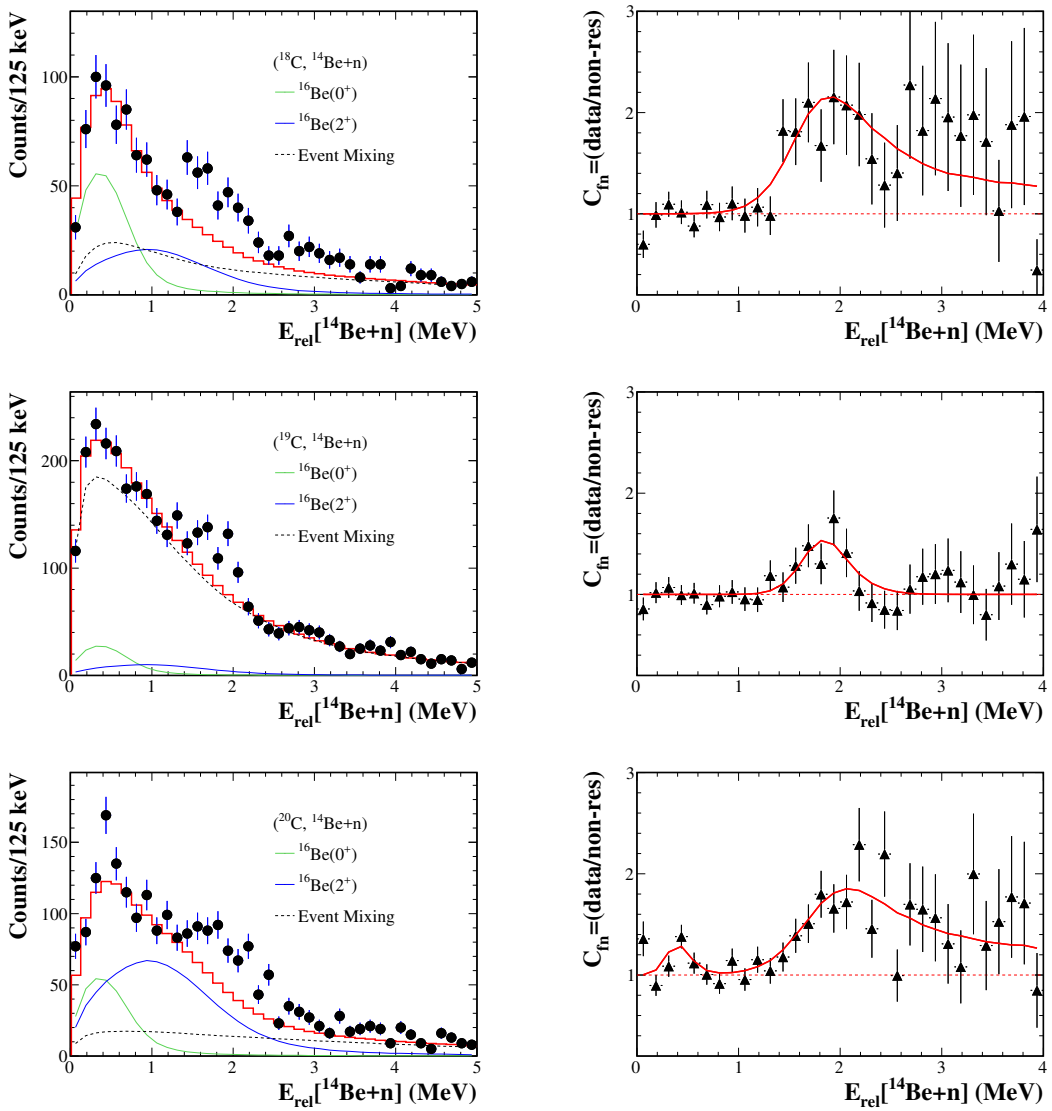

Figure 5.10: *On the left, ^{14}Be+n relative energy spectra obtained using a knock-out reaction from a ^{18}C (upper), ^{19}C (middle) and ^{20}C (lower) beam. The red line corresponds to the maximized contribution with no resonant states in ^{15}Be, including the non-correlated continuum generated by event mixing (dashed line) and the contribution from ^{16}Be decay (green and blue solid lines). On the right, the ratio between data and this non-resonant contribution. Here the red line corresponds to the best fit of the spectra presented in Fig. 5.11.*

with what we get in the $2n$ channel. If for instance, no ^{16}Be is formed or we just observe one of the two states, a description of the $1n$ decay with a similar contribution from both states in ^{16}Be would not be consistent. In Fig. 5.8 we note that very little ^{16}Be(2^+) is populated in ^{18}C, with a stronger contribution from the state at lower energy. This seems to be in agreement with the ^{14}Be+n spectrum. For ^{19,20}C, both states in ^{16}Be are populated, with equal contribution in ^{19}C and a major contribution for the higher-energy state in ^{20}C. While this scenario is consistent for ^{20}C, in the case of ^{19}C the $1n$ spectrum has a surprisingly big contribution from the non-resonant part that leaves very little room for ^{16}Be states. This channel is therefore to be considered carefully. One possibility to consider would be that the halo character of ^{19}C generated a lower-energy non-resonant component through event mixing, that then would not need any other contribution to reproduce qualitatively the spectrum.

In any event, the correlation functions of these three channels show a clear resonant structure at about 1.8 MeV. Therefore, a fit has been performed considering a resonance in ^{15}Be, or two in the case of ^{20}C beam, in addition to the structures from the decay of ^{16}Be (with fixed energy and width) and the non-resonant contribution. The best fit to the data are presented in Fig. 5.11, and show that ^{18,19}C fits (upper plots) give similar results for the potential ^{15}Be resonance around ∼2 MeV: *i)* $E = 1.80\pm0.10$ MeV and *ii)* $E = 1.80\pm0.06$ MeV, respectively, and in both cases with a width of $\Gamma = 1$ MeV. In the lower part of the figure, two different fits for ^{20}C are presented. On the left, a fit for which only a resonance at around 2 MeV is considered. The best description is achieved with an energy value of 1.90 ± 0.12 MeV, close to the other two obtained results. On the right, we have included a resonance at low energy. The latter results in two ^{15}Be resonances with energies of 0.4 ± 0.1 MeV and 1.9 ± 0.1 MeV. However, such a low-energy resonance is not predicted by theory and the low-energy narrow structure at about 0.4 MeV has little statistical significance. Any claim of a new state in ^{15}Be should therefore be taken with care. The best fits of these three channels have been compared to the correlation functions shown on the right of Fig. 5.10, confirming the good quality of our description.

The coincident observation of a structure at around 1.8 MeV in these three spectra indicates that we are likely populating a state in ^{15}Be. This would confirm the only observed state to date of ^{15}Be, also measured at the same energy and identified with a spin and parity of $5/2^+$. The direct $2p$ knock-out reaction from ^{17}C would be the natural next step in order to determine if there is a lower-energy resonance.

5.3 Beryllium-16

An investigation of the spectroscopy of ^{16}Be is conducted in this section. The current work is motivated by a previous study [4] in which a structure identified as the 0^+ ground state at an energy of 1.35(10) MeV and width of $0.8^{+0.1}_{-0.2}$ MeV was reported. In addition, a very strong low-energy enhancement was observed in the nn relative energy that was interpreted as the result of a new dineutron-decay mechanism. However, as explained in Sec. 1.4.1, the nn interaction was not included in the description of the three-body decay. Experimental data were only compared to either a non-interacting three-body decay, a sequential decay via an intermediate state in ^{15}Be or a dineutron model.

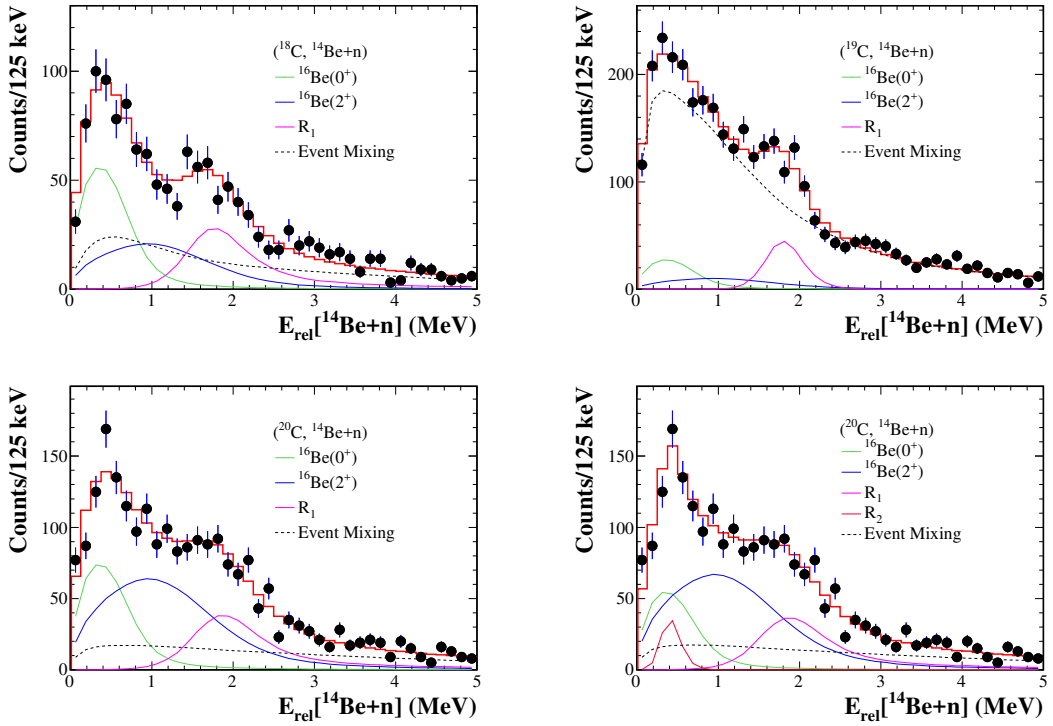

Figure 5.11: *Description of ^{14}Be+n spectra considering the direct population of a state in ^{15}Be at around 1.8 MeV for ^{18,19,20}C beams. The χ^2 values of the fits are 1.6, 1.3 and 1.8, respectively. The red line corresponds to the best fit to the data. In the case of ^{20}C, an additional low-energy resonance has also been added (lower right), which makes the χ^2 value slightly decrease, from 1.8 to 1.6.*

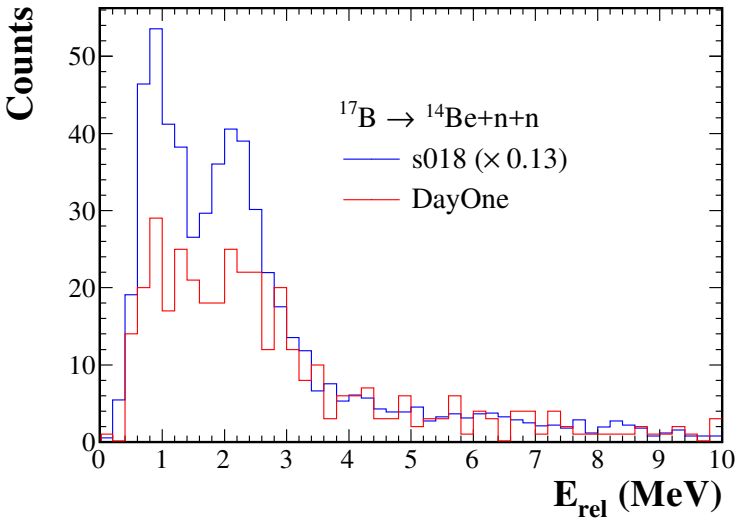

Figure 5.12: *Comparison of the relative energy spectrum of $^{14}Be+n+n$ following a proton removal from ^{17}B for DayOne (in red) and s018 (in blue) campaigns.*

5.3.1 Spectroscopy

The unbound ^{16}Be was populated using a proton removal reaction from a ^{17}B beam during the s018 experimental campaign at RIKEN. The relative energy spectrum is reconstructed from coincident ^{14}Be+n + n events by the invariant mass method and is presented in Fig. 5.12. For comparison, the relative energy spectrum obtained with the same reaction for the DayOne campaign is also included. Indeed, in the DayOne spectrum structures can be barely distinguished while two differentiated peaks can be easily observed in the spectrum from the s018 campaign. This improvement may be explained by the use of:

- The MINOS target, which allows the precise reconstruction of the vertex position of the reaction and therefore, the exact correction of energy loss of the fragment that improves significantly the resolution. This allows the use of a thicker target, 150 mm in s018, that consequently increases significantly the luminosity and statistics.
- a trigger logic specially thought for knock-out reactions, by which only reactions where a proton is ejected are taken into account, decreasing the background coming from reactions other than knock-out.

As already mentioned, the s018 spectrum clearly exhibits two different resonance-like structures below 5 MeV, which we can identify as the ground state and the first excited state. Following shell-model predictions [4], spin and parity of 0^+ and 2^+ are assigned respectively for both states. As shown in Fig. 4.13, the angular acceptance of NEBULA for the detection of two neutrons is large enough in the energy range between 0–10 MeV as well as for the neutron energies of the experiment. This allows to detect any potential structure in the whole relative-energy range considered. Since no distinct resonant features can be seen other than the two already mentioned, a non-resonant component may be assumed beyond 4 MeV.

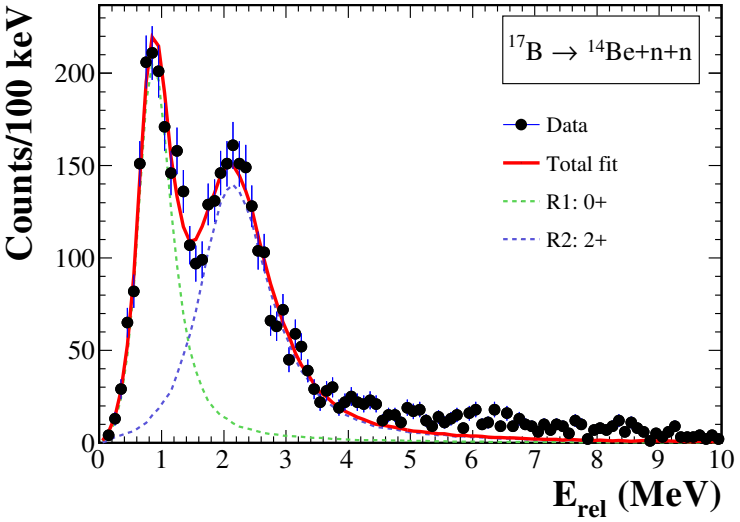

Figure 5.13: *Relative energy spectrum of $^{14}Be+n+n$ obtained using a proton knock-out reaction from a ^{17}B beam. The red line corresponds to the best fit to the data. The dashed lines represent the contribution of ^{16}Be resonances, the ground state at E_r=0.84 MeV (green) and the first excited state at E_r=2.15 MeV.*

The experimental relative-energy spectrum has been fitted between 0–4 MeV with a Breit-Wigner line shape with an energy-dependent width for both states, where the energy, width and normalization are free parameters. A non-resonant component is not required for the description of the data below 4 MeV. In fact, when allowed, such a component is set to zero in this range by the fit. The best description of the spectrum is achieved with E_{0^+} =0.84±0.03 MeV and E_{2^+} =2.15±0.05 MeV, and a respective width of Γ_{0^+} =0.32±0.08 MeV and Γ_{2^+} =0.95±0.15 MeV. The best fit to the data is represented in Fig. 5.13 by the red solid line and the individual components of the 0^+ and 2^+ resonances in green and blue dashed lines, respectively. Therefore, we have for the first time isolated and located the position of the ground state of ^{16}Be, which defines its mass and $S_{1n/2n}$, and observed its first excited state.

According to shell-model calculations with the WBP interaction [4], the predicted 0+ ground state is at approximately 0.9 MeV above the ground state of ^{14}Be, which is in agreement with the experimental result of 0.84 MeV. As for the 2^+ excited state, the same calculations give an energy of ∼2.5 MeV, close to our result. In the previous work, these two structures were not resolved, and only a broad resonance identified as the ground state was observed. The better resolution and statistics of the present work are due to the several improvements of our setup already mentioned, as it has been illustrated by the DayOne/s018 comparison in Fig. 5.12.

Furthermore, the reaction used to populate ^{16}Be in Ref. [4], although identical to the one used in s018, had a much lower beam energy, 53 MeV/nucleon, compared to ∼250 MeV/nucleon in our experiment. This is relevant to understand the difference in shape of both spectra as the beam energy has an important effect on the angular acceptance of the neutron detector. If the beam energy is high, neutrons will be emitted more forward focused, allowing to choose a distance between the target and the detector big enough to

get a good angular resolution and acceptance. Instead, if the energy is low, neutrons will be emitted in a wider angular range, and in order to collect enough statistics, the neutron detector is positioned closer to the target ($\sim$ 8 m in Ref. [4] and $\sim$ 11 m in s018), which reduces the angular resolution. The higher beam energy and the lower resolution could thus explain why the second structure that we see in Fig. 5.13 is not apparent in the previous work, as the beam energy indirectly cuts off the neutron acceptance beyond 2 MeV and part of it could be mixed up with the ground state.

5.3.2 Particle correlations

The type of decay to the ground state of ^{16}Be can be assessed from the study of the correlations between the decay particles. Following the same analysis as for ^{14}Be, the fn and nn relative energy distributions for both observed states in ^{16}Be have been compared to Monte-Carlo simulations. Similarly, a three-body direct decay with no interaction between the two neutrons is assumed as a first step.

The Dalitz plots showing the fn and nn correlations are presented in Fig. 5.14. The plots shown correspond to cuts in the three-body relative energy spectrum of $E_{rel} \in$[0, 1.2] MeV and $E_{rel} \in$[1.7, 3] MeV in order to select the 0^+ and 2^+ resonances. We can clearly see that there is a strong enhancement at low ε_{nn} while no evidence of sequential decay in the fn axis is *a priori* observed. The comparison with independent three-body decay simulations shows in both cases a big disagreement with the experimental data, indicating that a more complex hypothesis must be taken into account in order to describe the experimental data.

The ε_{nn} and ε_{fn} projections of the Dalitz plots are presented in Figs. 5.15 and 5.16 for the ground and first excited state, respectively. For the study of fn correlations, we have preferred to use E_{fn} instead of the reduced variable $\varepsilon_{fn} = E_{fn}/E_{rel}$ since in the case of a sequential decay, it is easier to determine the energy position in MeV of a potential intermediate state in ^{15}Be. The red solid line is a simulation of a three-body decay following phase space considerations alone. The green and blue dashed lines correspond to the contributions of each state in the selected energy range. Note that since both peaks are quite separated, the distributions approximately correspond to the "pure" distributions of both states in more than 90%.

Contrary to ^{14}Be, a pure three-body phase space is not consistent with any of the experimental ε_{nn} projections. The low energy nn enhancements observed indicate a strong correlation between the two neutrons that is usually interpreted as characteristic of the nn final state interaction (FSI). This type of enhancement is a distinguishing feature observed in many of the final states where the emission of two neutrons is involved. Therefore, if we want to describe at least qualitatively the experimental data we must consider a source of nn correlations. In chapter 6, the different models used to introduce such correlations will be discussed.

By contrast, the ε_{fn} distributions show a good agreement with simulations of a direct three-body decay. As explained in Sec. 4.4, the nn or fn correlations of a three-body decay cannot be understood separately. In particular, strong signals in the nn correlations may have a clear effect on the fn distributions, and the inclusion of this effect is essential for an accurate study of the sequentiality of the decay. Although this effect is normally

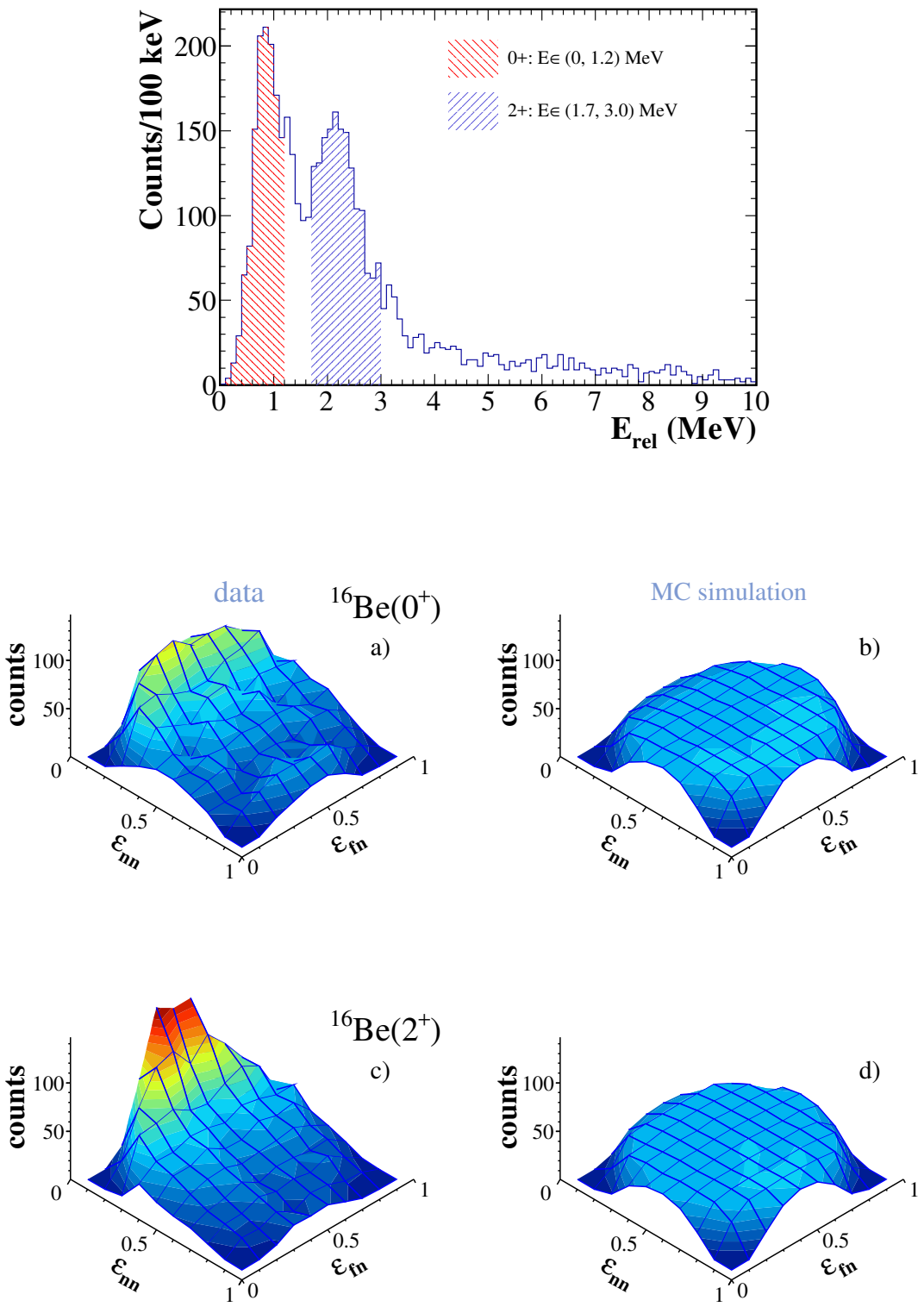

Figure 5.14: *On the top, the striped areas in the relative energy spectrum of $^{14}Be+n+n$ represent the energy ranges selected to study the correlations of the ^{16}Be ground state (red) and its first excited state (purple). Below, the Dalitz plots for both states are presented: $^{16}Be(0^+)$ (in the middle) and $^{16}Be(2^+)$ (on the bottom). Experimental data are on the left (a,c). The comparison with a simulated non-interacting three-body phase space is represented on the right (b,d).*

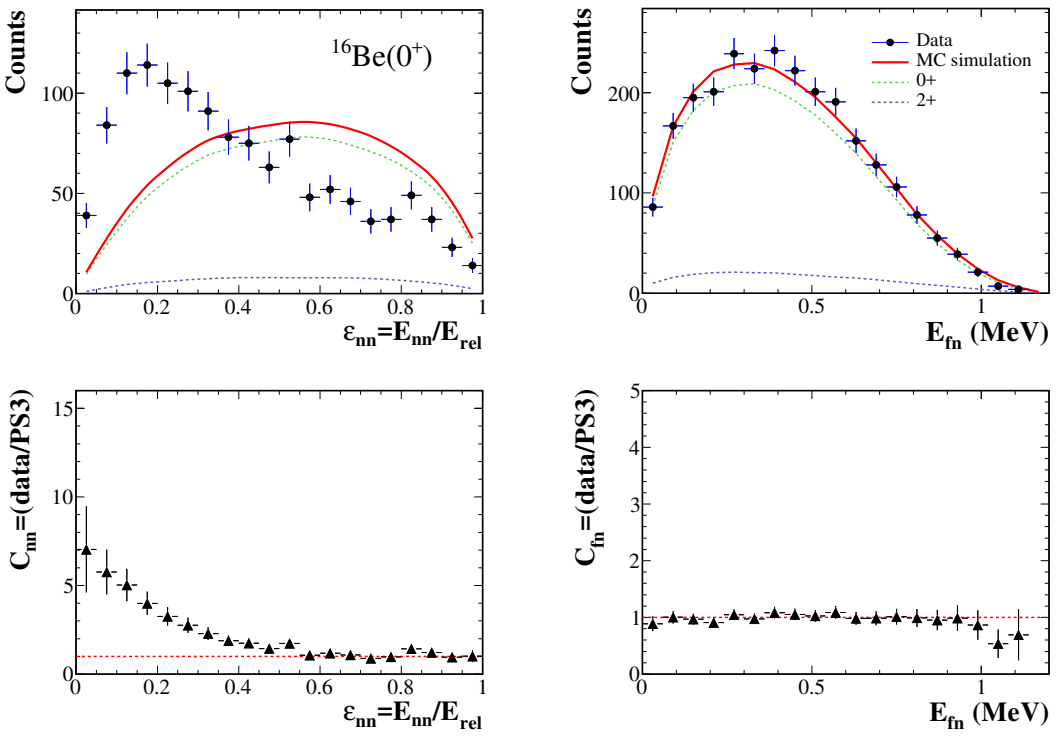

Figure 5.15: *ε_{nn} and E_{fn} distributions for ^{16}Be ground state for an energy $E_{rel} \leq$1.2 MeV. The red line corresponds to a three-body decay with no nn interaction. In dashed lines, the contributions from 0^+ and 2^+ states (in green and blue respectively) in the energy range considered. The lower plots represent the correlation functions (data divided by the MC simulation).*

small, the big difference between experimental and simulated nn distributions can make it more significant. For that reason, in the following the fn relative energy distributions have been simulated by taking into account a low-energy signal in the nn distribution that mimics the experimental signal, without entering into a discussion about the physical interpretation of the parametrization used. The latter will be addressed in detail during the next chapter.

The assumption of a spontaneous two neutron-emission to the ground state of ^{14}Be seems to be the main decay mode. Given the good agreement, it is not necessary to suppose any contribution from sequential decay through an intermediate state in ^{15}Be to reproduce the experimental data. For the ^{16}Be ground state, no states in ^{15}Be below 0.84 MeV have been neither predicted nor experimentally observed. However, that is not the case for the 2^+ state since a state in ^{15}Be has been observed below 2.15 MeV which, in principle, could allow a sequential decay. With the only objective of checking the compatibility of a sequential decay, we have studied the fn relative energy correlations allowing both direct and sequential decay through a state in ^{15}Be at 1.8 MeV. Such fit shows that the direct component is dominant, with more than 98 %. This indicates that the 2^+ decay through the observed intermediate state in ^{15}Be at 1.8 MeV is not favoured.

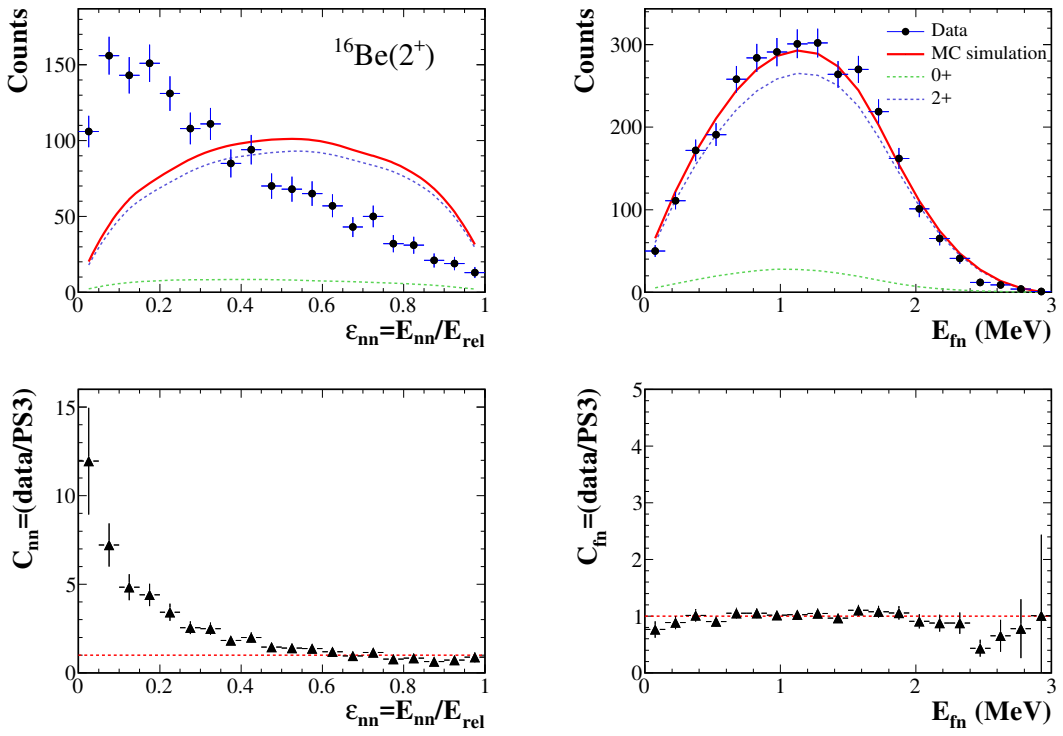

Figure 5.16: *ε_{nn} and E_{fn} distributions for ^{16}Be first excited stata for an energy range of $E_{rel} \in$(1.7, 3.0) MeV. The red line corresponds to a three-body decay with no nn interaction. In dashed lines, the contributions from 0^+ and 2^+ states in the energy range considered. The lower plots represent the correlation functions.*

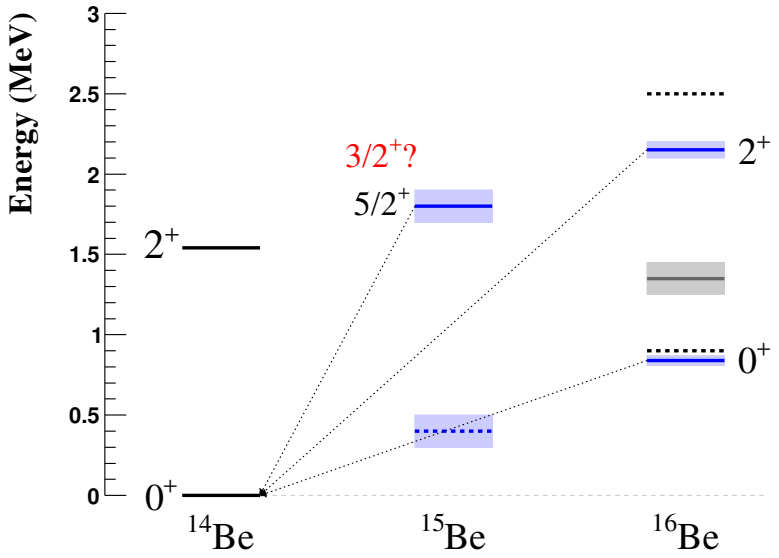

Figure 5.17: *Level scheme of the heaviest isotopes of Beryllium. The blue levels represent the contribution of this work. Note that for* ^{15}*Be*$(5/2^+)$ *the energy and uncertainty found are exactly the same as in previous works[5]. The black dashed lines are the theoretical predictions for* ^{16}*Be and in gray the previous value for the* S_{2n} *of* ^{16}*Be is represented for comparison.*

5.4 Conclusions on Beryllium spectroscopy

Beryllium-14. The first 2^+ excited state of ^{14}Be has been measured at an energy of 1.52(13) MeV by the reconstruction of the ^{12}Be+n+n relative energy. This value of energy is compatible with the previous one of 1.55(13) MeV. However, a more precise measure of the mass of ^{14}Be is required in order to reduce the uncertainty as the uncertainty of ^{14}Be(2^+) in terms of relative energy, only 6 keV, is negligible compared to the uncertainty of S_{2n} for ^{14}Be. Furthermore, the correlations between the decay products have been probed and a direct decay through the emission of two simultaneous neutrons into the ground state of ^{12}Be has been confirmed from the ε_{fn} relative energy distribution. In addition, no nn interaction seems to be needed in order to reproduce the experimental ε_{nn} distributions. It is concluded that the decay from ^{14}Be(2^+) to ^{12}Be(0^+) is a three-body decay that follows the energy and momentum conservation laws imposed by a three-body phase space, with no need for the inclusion of any two-body resonance or interaction.

Beryllium-15. We have investigated the spectroscopy of ^{15}Be from a series of experiments that involve different knock-out reactions. The relative energy spectra have been reconstructed from ^{14}Be+n. A clear population of a state at 1.8 MeV has been found, in agreement with Ref. [5], for knock-out reactions from ^{18,19}C beams, and at 1.9 MeV from a ^{20}C beam that, with an uncertainty of 0.1 MeV is also compatible with the previous measurement. Following Ref. [5], we could assign this state to a spin and parity of $5/2^+$. In addition, in the ^{20}C channel, a low-energy peak is also observed in the ^{20}C channel that cannot be reproduced with the only contribution of the decay of ^{16}Be. If this corresponds to a state in ^{15}Be, its energy would be 0.4 MeV according to the best fit of the data. However, more evidence is needed to confirm the existence of a low-energy state in ^{15}Be. The other analyzed channels, the knock-out reactions from ^{17,19}B and ^{22}N beams,

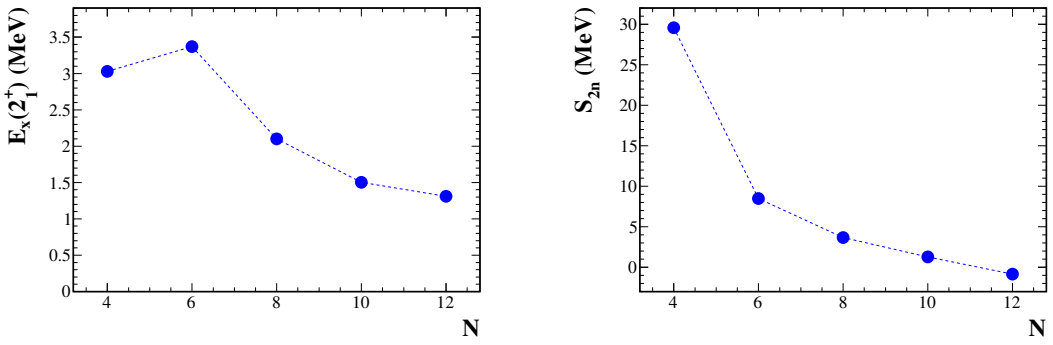

Figure 5.18: *Evolution of the excitation energy of the first excited 2^+ state with respect to the ground state (left), and the two-neutron separation energy (right) for the even-even nuclei of the Beryllium isotopic chain.*

are relatively well described with the only contribution of the ^{16}Be decay, though a small contribution of the $5/2^+$ state in ^{15}Be is also compatible with the data.

Beryllium-16. The ground state and first excited state of the unbound ^{16}Be have been observed unambiguously for the first time, at an energy of 0.84 MeV and 2.15 MeV, respectively. The good resolution and high statistics allow us to study separately for each state the correlations of the $2n$ decay to ^{14}Be. The Dalitz Plots from both states show that the two-neutron emission is likely to be simultaneous even for the first excited 2^+ state, which is energetically above the only known state of ^{15}Be at 1.8 MeV. However, in this case, a sequential decay via the intermediate state in ^{15}Be seems very unlikely given the experimental fn distribution observed. Nevertheless, the very strong low-energy correlations shown in its ε_{nn} distribution indicate that the decay is likely to be direct and not sequential. These strong nn correlations, which are as well observed in the nn relative energy of the ^{16}Be ground state, cannot be explained considering only a non-interacting three-body decay. In this sense, a more sophisticated nn treatment is needed in order to better understand the $2n$ emission from these resonances, and it will be presented in next chapter.

Figure 5.17 represents the level structure of the Beryllium isotopes studied in this work. Our contribution is marked in blue. For comparison, in ^{16}Be we have included the previous work in gray and the theoretical predictions from Ref. [4] in black dashed lines. Our new results on ^{16}Be allow as well to study the evolution of the nuclear properties in the whole isotopic chain of Beryllium. From Fig. 5.18 (right) we can see that, as expected, the S_{2n} of ^{16}Be, which is located beyond the neutron dripline and is unbound with respect to the emission of two neutrons, continues the decreasing trend of the Beryllium chain with N. On the left, the evolution of the excitation energies of the 2_1^+ states is represented, that shows a clear decreasing trend. A lower $E_x(2^+)$ might indicate a more deformed state and a larger transition probability [65]. However, to draw any reasonable conclusion about the collectivity of ^{16}Be a further analysis, including the determination of the $B(E2)$ parameter and a comparison with shell-model predictions, is needed.

Chapter 6

Interpretation: nn correlations

Contents

In the previous chapter, we have investigated the spectroscopy of the heaviest Beryllium isotopes: ^{14}Be, ^{15}Be and ^{16}Be. From the study of the particle correlations, we have determined that both 0^+ and 2^+ states observed in ^{16}Be decay directly to the ground state of ^{14}Be by emission of two simultaneous neutrons. The relative energy spectrum of the two emitted neutrons shows a significantly strong signal at low energies which cannot be reproduced by a non-interacting three-body phase space. This signal must therefore have its origin in a physical correlation between the two neutrons. In contrast, the first excited state of ^{14}Be, for which the decay is also found to be a three-body direct decay, does not show any deviation from a three-body phase space, and consequently presents no obvious nn correlation evidence. This is manifestly shown in Fig. 6.1 where we can find the correlation function C_{nn} for the decay of each of these three states: while the ^{14}Be(2^+) distribution is flat (left panel), ^{16}Be(0^+,2^+) show important low-energy correlations. The different pattern found in these two nuclei (three states) which present, *a priori*, similar decays, a direct two-neutron emission, is a very intriguing phenomenon.

The low-energy signal in the nn relative energy has been widely observed in decays of light exotic nuclei (see, for example, [37, 63, 66, 67]). Strong nn correlations are typically interpreted as the result of the emitted neutrons interacting in the final state. A phenomenological approach describing this final state interaction (FSI) can be sufficient to reproduce the low-energy enhancement in the nn channel. Such simple models cannot, however, envisage the connection of the correlations with the structure of the system.

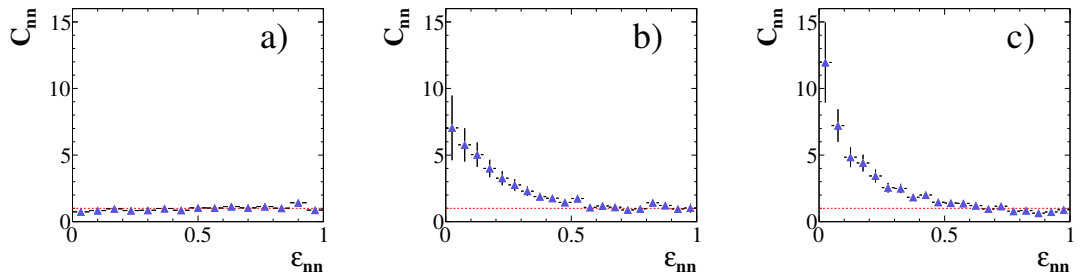

Figure 6.1: *Comparison of the nn correlation function obtained for (a) $^{14}Be(2^+)$, (b) $^{16}Be(0^+)$ and (c) $^{16}Be(2^+)$.*

What these correlations may reveal about the decay mechanism or the configuration of the neutrons within the original state requires a formalism capable of describing the two-neutron emission from microscopical principles. So far, a complete interpretation of the correlations in a *nn* emission remains an open question.

In this chapter two different approaches are studied in order to interpret the observed *nn* correlations. As a first step, a simple phenomenological model is introduced[19], in which the experimental data are reproduced using the *s*-wave FSI between two neutrons emitted independently by a structureless source, varying a single source-size parameter that we will call σ_{fsi}. A more realistic model based on a three-body microscopic calculation of the wave function is presented next. The components of the wave function as well as the *nn* relative energies are calculated for the ground state of ^{16}Be(0^+) and the first excited states 2^+ of both ^{14}Be and ^{16}Be. The comparison of both interpretations for the three systems studied will allow us to clarify the validity of the FSI model approach and establish the advantages of the three-body calculations.

6.1 Phenomenological model

As already mentioned throughout this thesis, the low-energy enhancement in the *nn* relative energy is a characteristic signal in many decays involving the emission of two neutrons. The FSI is a well-known effect present for any decay fragments, yet the *nn* channel is specially sensitive as no Coulomb barrier counteracts the *nn* nuclear attraction, characterized by a significantly big scattering length ($a_s \sim -18.5$ fm [68, 69]). As a result, the *nn* FSI usually governs the *nn* channel over other aspects such as the decay mechanism. The low-energy enhancement, typically discussed in terms of *nn* correlations, is something that deviates distinctively from the N-body phase space defined by the decay. In contrast with *fn* correlations which are generally linked to sequential decay through an intermediate resonance, the extraction of physical information from *nn* correlations is less straightforward, and requires a careful treatment of the FSI.

As observed in Fig. 6.1, the *nn* low-energy enhancement is characterized by an exponential-like behavior near zero relative energy or momentum when looking at its correlation function C_{nn} =data/PS. This exponential behavior, which has been systematically observed in most of the core+$n+n$ final states measured to date, is very similar to the one of a virtual state [18]. Accordingly, the low-energy signal can be very well reproduced by an *s*-wave *nn* interaction. This approach, that is known as the **Migdal-Watson ap-**

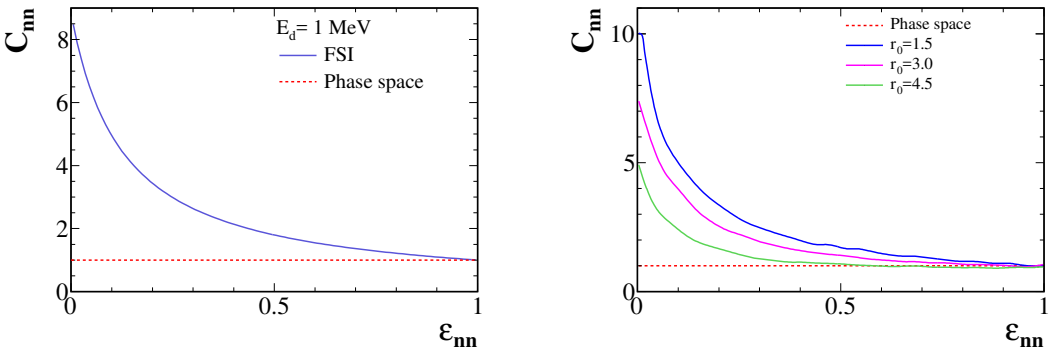

Figure 6.2: *C_{nn} function obtained within two FSI models: the Migdal-Watson aproximation (left) and the Lednicky formalism (right). The strength of the signal is modulated by adjusting the scattering amplitude of the nn interaction in the case of the former, or by modifying the relative distance between the two neutrons for the latter.*

proximation [70, 71], uses the simplest two-neutron final state, a virtual s-wave, and only one free parameter, the neutron scattering length a_s, to describe the nn spectra. The phase space is then modulated according to a probability distribution that depends on the relative momentum of the neutrons q_{nn} as

$$\sigma(q_{nn}) \approx \sigma_{PS}(q_{nn})\, C_{nn}(q_{nn}) \tag{6.1}$$

where $\sigma_{PS}(q_{nn})$ is the cross-section if we take into account only phase-space considerations. The correlation factor $C_{nn}(q_{nn})$ related to the FSI is expressed in terms of the effective range as:

$$C_{nn}(q_{nn}) = \frac{a_s^2}{1 + m_n E_{nn} a_s^2} \tag{6.2}$$

where m_n is the neutron mass and E_{nn} the nn relative energy. The nn correlation function obtained using this model for a fixed decay energy of, for example, 1 MeV and a scattering length of $a_s \sim -18$ fm would result in a low ε_{nn} signal as the Fig. 6.2 shows (left panel). The strength of the signal can be reduced or increased by modifying a_s.

The **FSI approach** described in [19] extends the formalism of the Migdal-Watson approximation by taking into account the distance between neutrons as having an effect on their interaction. In this model, the scattering length a_s is fixed and it is σ_{fsi} that is varied to reproduce the low nn energies. Similarly to Migdal-Watson, it considers the effect of the s-wave scattering amplitude, but also of the four-momentum distance that separates the neutrons, and integrates over a source distribution in space and time. Consequently, the nn FSI, characterized by the C_{nn} function, depends not only on the s-wave scattering amplitude of the nn interaction but also on the size of the source, introduced in the model through a parameter σ_{fsi}, and can be factorized as follows

$$C_{nn}(q_{nn}) \approx \int W(r_{nn}) F(r_{nn}, q_{nn}) dr_{nn} \tag{6.3}$$

where $W(r_{nn})$ is the spatial distribution of the source depending on the relative distance between the pair of neutrons, here taken as emitted by a Gaussian of sigma $\sigma_{\rm fsi}$, and $F(r_{nn}, q_{nn})$ the correlation factor that contains the nn interaction. The effect of the Fermi statistics for identical nucleons is also included in the latter. A more detailed description of the most relevant equations can be found in the appendix B.

However, this model, although it has described accurately the observed nn low-energy peaks of previous works [37, 38, 63, 66, 67], does not consider the core$+n+n$ structure of the original system. Instead, this formalism is developed for a *Gaussian* neutron source emitting *independent* neutrons. Certainly, considering that the wave function of the three-body system is Gaussian is by far a very simple approximation. However, as shown in [67], individual neutron distributions $W(r_n)$ of different shapes such as Yukawa-like or spherical, lead for independent neutrons to roughly Gaussian-like relative distance distributions $W(r_{nn})$.

On the other hand, the fact that the two neutrons move independently inside the source is also unrealistic as it implies neglecting the internal momentum correlations of the two neutrons, *i.e.*, $W(r_{nn}, q_{nn}) \approx W(r_{nn})$. These internal correlations could have an impact on the FSI by increasing (if momenta have parallel directions) or decreasing (if anti-parallel) the signal observed in the relative energy. Nevertheless, if these correlations were big enough to see their effects, a case could have been observed already where anti-parallel directions of momenta create a kind of anti-correlation in the relative energy, that is, a peak at high relative energy $\varepsilon_{nn} \sim 1$. Since such a signal remains unobserved, we assume that these potential correlations are small and/or negligible when integrating over the whole neutron source. In this respect, structures in the nn relative energy other than the typical enhancement at low energies, like anti-correlations or even oscillatory patterns, have been predicted within some recent formalisms [72] from the contribution of neutron configurations in p or d orbitals. However, these effects have not been yet observed in any nn final state.

Despite all these simplifications, this approach seems to be able to reproduce the characteristic C_{nn} functions, even for systems that are not Gaussian, and in addition it offers a possible scenario for its interpretation. The only free parameter of the model, the relative distance between neutrons $\sigma_{\rm fsi}$, is to be considered either as a mathematical input, with the only use of reproducing the data, or/and as a physical characteristic of the system. Since the assumption of a Gaussian source makes the equation 6.1 analytical, the correlation function obtained can be easily implemented in the simulation (see Sec. 4.2) as a probability function $P(q_{nn})$ that will accept or reject events according to the form of C_{nn}. The effect of the FSI on the three-body decay can therefore be included in the simulations where the only free parameter is the one related to the size of the two-neutron source $\sigma_{\rm fsi}$.

One should note that this model was derived assuming that the nn distances do not go significantly inside the nn potential, in order to lead to a formalism independent of the particular V_{nn} chosen and only dependent on the two FSI parameters, the effective range and specially the scattering length. Therefore, as noted in [19], the formulas can only be safely used for a minimum $\sigma_{\rm fsi}$ of 1.5 fm, that corresponds to a rms r_{nn} distance of $\sim$ 3.7 fm. At this value, the low-energy enhancement would be maximum, and as

we increase σ_{fsi}, and therefore neutrons become more distant, the strength of C_{nn} would decrease. This dependence with the relative distance between the neutrons is shown in Fig. 6.2 (right panel) for a total decay energy of 1 MeV.

6.1.1 Application to experimental data

In Sec. 5.3, we have analyzed the experimental Dalitz plots considering only the kinematic correlations arising from the decay and filtered by the experimental resolution and acceptance of the complete setup. The study of the core+n correlations, which are very sensitive to the sequentiality of the decay, have been found to be governed by the kinematics of a three-body phase space for all $2n$ decays investigated in this work. This implies that the two neutrons are likely to be emitted simultaneously. However, if we look at the nn relative distributions, strong deviations from phase space in ^{16}Be indicate that the nn FSI seems to be a key ingredient that cannot be neglected.

As a first step, the simplest way to include the FSI correlations in the analysis/simulation is by using a phenomenological model as the one described above which, by means of a simple correlation factor (see Eq. 6.1), allows us to modify the three-body phase space in order to take into account the FSI effects. In this section, we investigate the $2n$ decays of ^{16}Be(0^+, 2^+) and ^{14}Be(2^+) with simulations which include a phenomenological nn FSI, the kinematic constraints of the phase space, and the experimental conditions.

Beryllium-16. As discussed in Sec. 5.3, the experimental Dalitz plots are constructed in two energy ranges, E∈[0,1.2] MeV and E∈[1.7,3.0] MeV, which approximately correspond to the 0^+ and 2^+ states, respectively. The contribution of both states in each of the ranges is included in the fit. Figure 6.3 shows a comparison between the experimental Dalitz plot and the one obtained for the best fit of σ_{fsi}, which is found to be in good agreement with the experimental data. The values of σ_{fsi} corresponding to the best fit are 2.4(4) fm and 1.5(2) fm for the ground and first excited state, respectively. If we now project onto the nn axis, we can obtain the nn relative energy and its correlation function, as shown in Fig. 6.4. Here we can notice that the low-energy signals are reasonably well reproduced with this model.

We note that the best σ_{fsi} obtained for the 2^+ state is the minimum possible value considered in the model, 1.5 fm. The parameter σ_{fsi}, even in the case in which all the approximations of the model were fulfilled, is not to be taken straightforwardly as an average separation between the two neutrons. Within this formalism, σ_{fsi} is the sigma parameter of a Gaussian representing the source of independent neutrons [19] (see Appendix B). Assuming all the approximations, then the physical distance would be related to the parameter σ_{fsi} as $r_{nn}^{rms} = \sigma_{\text{fsi}} \times \sqrt{6}$. This would result in rms nn distances of $\sim 6\ fm$ and $\sim 4\ fm$ for the respective values of σ_{fsi}.

Following this interpretation, one could conclude that neutrons are more strongly correlated in the decay of ^{16}Be(2^+) given the more prominent peak in its nn distribution and the obtained value of σ_{fsi}=1.5 fm. On one hand, there is a kinematic focusing effect in the ε_{nn} variable, since a similar signal in E_{nn} will focus to lower values when we divide it by a higher total energy. On the other hand, we have to take into account that the effect of cross-talk is more important at low energies and that the filter is applied in both experimental and simulated distributions. Moreover, even if smaller values of σ_{fsi} are usually

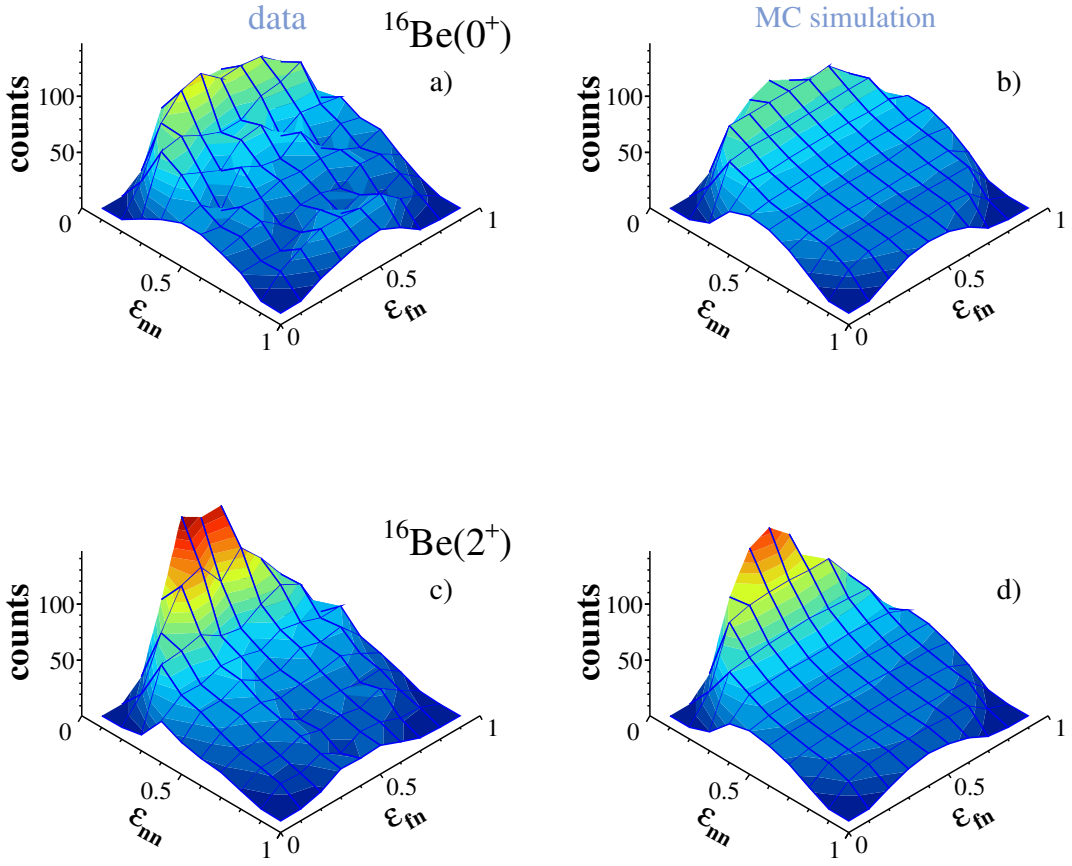

Figure 6.3: *Dalitz plots for the corresponding energy ranges of $^{16}Be(0^+)$ (a) and $^{16}Be(2^+)$ (c). The best description to the data using a MC simulation of a three-body phase space that includes a nn FSI interaction following the model described in this section is presented in plots (b) and (c), respectively for the two states.*

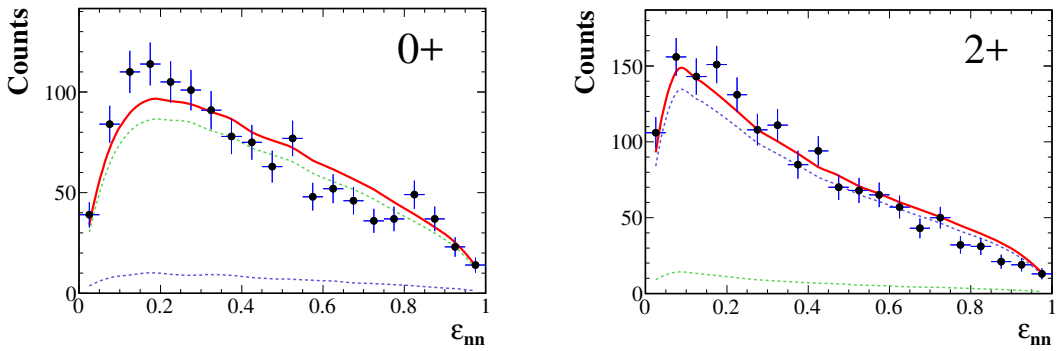

Figure 6.4: *ε_{nn} distribution for $^{16}Be(0^+)$ (left) and $^{16}Be(2^+)$ (right). The red line corresponds to a simulated three-body phase space that takes into account the nn FSI. The dashed lines represent the contribution from 0^+ (green) and 2^+ (blue) states to the energy range considered.*

connected to stronger nn signals, the sensitivity of the model to a fit in σ_{fsi} also depends on the total energy available in the decay. In decays from low-energy states, such as the ground state $E \sim 0.8$ MeV, the nn relative energy distributions are not very sensitive to σ_{fsi} around the minimum χ^2. This implies that, for the particular case of the $2n$ decay from ^{16}Be(0^+), the distribution from σ_{fsi}=1.5 to 3 fm are not very different from the value which best describes the data.

Beryllium-14. Contrary to ^{16}Be, the nn relative energy distribution follows a three-body phase space with no need to include FSI effects. In this context, this formalism, though not being essential in the description of the experimental data, allows us to deepen in the origin of the absence of nn correlations. In particular, there are some important aspects of the decay that can be investigated with this FSI model. First, the decay energy is very low, E_{2^+}=254 keV. At such low energies the cross-talk rejection algorithm is specially strong and cuts off a significant part of the nn low relative energy. Since the simulation as well as the experimental data are subject to the same cross-talk analysis, the inclusion of the FSI may determine whether the lack of nn FSI correlations is a consequence of the cross-talk filter. For this purpose, we have simulated multiple FSI signals of more or less strength to check the effects of the cross-talk rejection on them. Figure 6.5 shows the evolution of the simulated nn distributions with respect to the experimental data for a series of values of σ_{fsi}. We observe that the low-energy signal is able to overcome the cross-talk rejection and, though certainly suppressed, is present for values of $\sigma_{\text{fsi}} \leq$9 fm. This lets us assume that if the two neutrons were very strongly correlated in ^{14}Be, the correlation would survive the experimental conditions and filters. Therefore, the observed lack of correlations should come from the intrinsic properties of the system and/or the decay mechanism. In fact, some theoretical three-body calculations [72] predict nn correlations to be suppressed for $2n$ decays from very low-energy resonances. A phenomenological model as the one used in this section is not enough to determine the origin of this phenomenon.

We should note that this model, despite all the unrealistic simplifications, usually describes very accurately the nn FSI signals for values of σ_{fsi} which are not very unrealistic themselves. Therefore, it is interesting to check which value we would obtain for the model to describe the phase space. For the particular decay of ^{14}Be(2^+), the evolution of the nn distribution with σ_{fsi} shows that the best description of the spectrum does not tolerate the

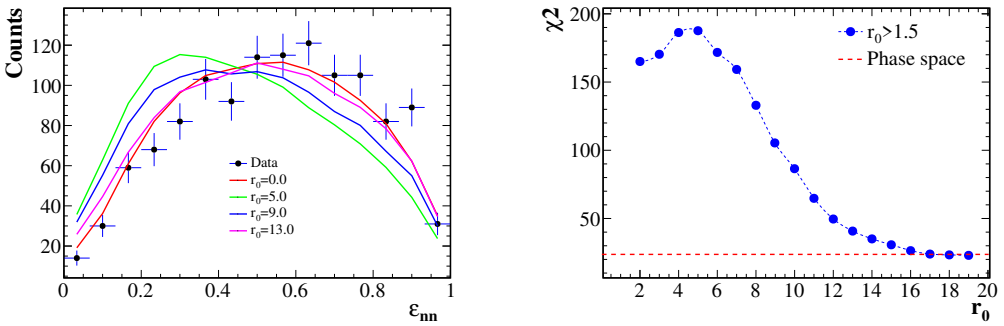

Figure 6.5: *Interpretation of nn correlations using a FSI model for $^{14}Be(2^+)$. On the left, nn energy distribution for different values of σ_{fsi}. On the right, evolution of χ^2 with respect to σ_{fsi}. The red line represents the phase space.*

slightest FSI correlation (see the χ^2 distribution in Fig. 6.5), confirming that the phase space not only seems to be compatible, but it is also the best fit. In fact, very large values of $\sigma_{\rm fsi}$, starting from $\sigma_{\rm fsi}$ ∼16 fm ($r_{nn}^{rms} \sim 40$ fm), do not present any correlation and lead to the three-body phase space. The fact that free phase space is reproduced by these large values seems reasonable.

6.2 Complete three-body calculations

We have seen in the previous section that a "structureless" model is able to reproduce the low-energy correlation patterns observed in experimental *nn* distributions. However, such a model does not illustrate the realistic scenario of a decay of a few-body nucleus, a system which has a definite structure and geometry, hardly comparable to a Gaussian source. The full understanding of the three-body decay and the role of the FSI during the process require a formalism able to take into account the internal structure of the system in all its complexity. The theoretical methods exploring the structure of three-body resonances and the energy distributions related to their $2n$ decays are still very few as their characterization is not trivial, since they require the solution of a three-body problem in the continuum. On top of this, the difficulties to experimentally access $2n$ emitters only offer a few candidates to test the reliability of the calculations. In this section, we present the investigation of the structure of the continuum states of ^{16}Be and ^{14}Be within a realistic formalism based on microscopic principles. It is the aim of this work to go beyond the mere reproduction of the experimental distributions and to establish a relation with the structure of the system through the comparison between theory and experiment.

The microscopic model developed by Casal and Gómez-Camacho[20, 73] has as main goal the description of the 3-body continuum as well as the identification and characterization of states in the continuum associated with core+n+n type resonances. For this purpose, the hamiltonian is diagonalized in a discrete basis of pseudostates built within the hyperspherical harmonics formalism. Among the large number of states constructed from this diagonalization, states which properties can be linked to resonances are extracted by means of a *resonance operator* that is defined specifically for this model.

The starting point of the model is the diagonalization of the three-body Hamiltonian

in a given basis, *i.e.*, solving the eigenvalue problem:

$$\mathcal{H}\,\psi_n^{j\mu} \;=\; \varepsilon_n\,\psi_n^{j\mu} \tag{6.4}$$

where $\psi_n^{j\mu}$ represents the eigenstates of the three-body resonance. The basis of states of the system is expanded in terms of a radial and angular function defined by $R_\beta^j(\rho)$ and $\mathcal{Y}_\beta^{j\mu}(\Omega)$. Within the hyperspherical harmonics (HH) formalism, these states are expanded in hyperspherical coordinates as

$$\begin{aligned}\psi^{j\mu}(\rho,\Omega) &= \rho^{-5/2}\sum_\beta R_\beta^j(\rho)\mathcal{Y}_\beta^{j\mu}(\Omega)\\ &= \sum_\beta\left[\sum_i D_{i\beta}^n U_{i\beta}(\rho)\right]\mathcal{Y}_\beta^{j\mu}(\Omega)\end{aligned} \tag{6.5}$$

where $\Omega=\{\alpha,\widehat{x},\widehat{y}\}$, with α the hyper-angle, and ρ is the so-called hyper-radius

$$\rho=\sqrt{x^2+y^2} \tag{6.6}$$

$$\tan\alpha=\frac{x}{y} \tag{6.7}$$

defined by the Jacobi coordinates x, y. The index i counts the number of functions in the basis $U_{i\beta}(\rho)$ and the label $\beta\equiv\{K,l_x,l_y,l,S_x,j_{ab}\}$ refers to the channel. The $D_{i\beta}^n$ denotes the diagonalization coefficients.

Angular functions $\mathcal{Y}_\beta^{j\mu}(\Omega)$ are states of good angular momentum which are expanded in analytical eigenfunctions of the hypermomentum operator, the hyperspherical harmonics $\Upsilon_{Klm_l}^{l_x l_y}$. In order to keep the resolution of the three-body Schrödinger equation as a standard eigenvalue problem, the pseudo-state method is used. The radial part is expanded in terms of the analytical transformed harmonic oscillator (THO) denoted by $U_{i\beta}(\Omega)$. The THO basis replaces the Gaussian asymptotic behaviour of the HO functions by an exponential decay while keeping the simplicity of the original HO functions. This transformation is performed as

$$U_{i\beta}^{\mathrm{THO}}(\rho)=\sqrt{\frac{ds}{dp}}U_{iK}^{HO}(s(\rho)) \tag{6.8}$$

where $s(\rho)$ is defined as follows,

$$s(\rho)=\frac{1}{\sqrt{2}b}\left(\frac{1}{(\frac{1}{\rho})^4+(\frac{1}{\gamma}\sqrt{\rho})^4}\right)^{1/4} \tag{6.9}$$

The parameters b and γ can be related to the density of pseudostates as a function of the energy. In the given THO basis, the energy of the pseudostates $\psi_n^{j\mu}$ are obtained by diagonalizing the three-body hamiltonian that requires the hyperradial coupling potentials,

$$V_{\beta'\beta}^{j\mu} = \langle \mathcal{Y}_\beta^{j\mu}(\Omega) | V_{nn} + V_{fn_1} + V_{fn_2} | \mathcal{Y}_{\beta'}^{j\mu}(\Omega) \rangle + \delta_{\beta\beta'} V_{3b}(\rho) \tag{6.10}$$

where V_{nn} and V_{fn_i} are the corresponding pair interactions, between both neutrons and between each of the neutrons and the core, and the term $V_{3b}(\rho)$ is a phenomenological three-body force. This last term is added since the three-body description with only realistic binary interactions is insufficient to reproduce the known spectra, and absorbs in an effective way effects beyond the strict three-body description of the system. The energy of the state can be therefore adjusted to the known experimental energy by modifying the parameters of this three-body force.

A large set of states is obtained from the diagonalization of the tree-body hamiltonian for a given channel. To characterize resonances among the continuum states found, a resonance operator $\widehat{M} = \widehat{H}^{-1/2}\widehat{V}\widehat{H}^{-1/2}$ is used. This operator is very sensitive to the interaction, a feature that allows the separation of resonances from the rest of the spectrum by diagonalizing $\widehat{M}$. The reader should refer to [20] for further details on the use of this operator.

6.2.1 $2n$ configuration

The structure and the $2n$ configuration in the three-body states of ^{16}Be and ^{14}Be have been studied from the pseudo-state approach using the THO basis. Within this formalism, solving the three-body problem requires as inputs: a nucleon-nucleon interaction, a core+n potential and a three-body force, with the latter two being adjusted to match the known experimental energies found in this work for ^{15}Be and ^{16}Be. Calculations are performed using the Jacobi-T set coordinates where the distance between the two neutrons r_{nn} is related to the x-axis, and the distance from the pair of neutrons to the core to the y-axis. The spatial correlations of the three-body resonance are revealed by its wave-function probability, which can be calculated as

$$P(r_x, r_y) \;=\; r_x^2\, r_y^2 \int |\Psi(r_x, r_y)|^2 \, d\widehat{x}\, d\widehat{y} \tag{6.11}$$

Application to ^{16}Be

The resulting spatial distributions are shown in Figs. 6.6 and 6.7 (left) for the ground and first excited states of ^{16}Be, respectively. In this particular case, the ^{14}Be+n interaction has been adjusted to reproduce the only known experimental state in ^{15}Be at 1.8 MeV, which has been assumed to be as its ground state. The parameters of the three-body term have been fixed in order to reproduce the experimental values E_{0^+} =0.84 MeV and E_{2^+} =2.15 MeV.

Ground state. The spatial correlations show three well defined maxima. The highest peak is found when the two neutrons are very close to each other, r_x ∼2 fm, but far from the core, r_y ∼3.5 fm. Such a configuration is commonly associated to a “dineutron”

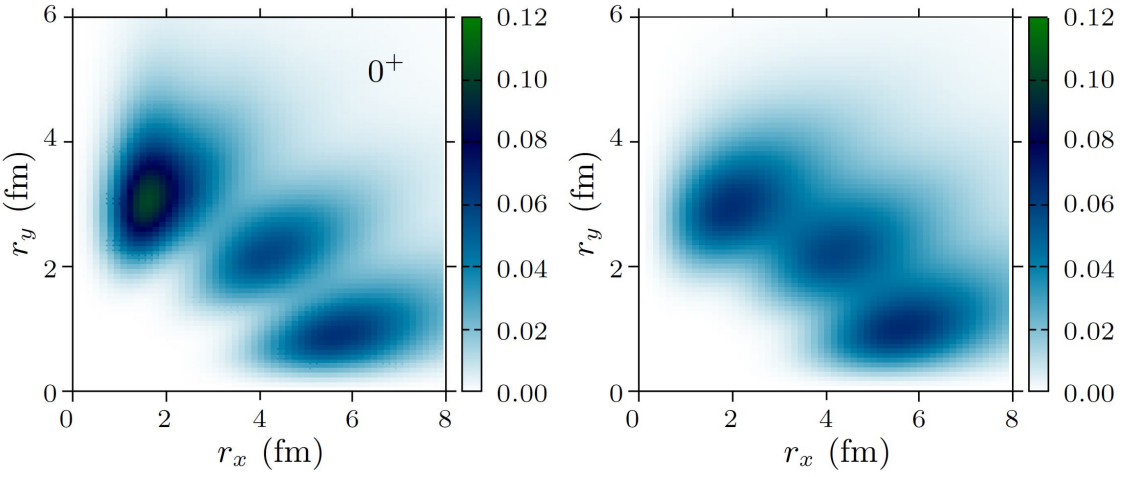

Figure 6.6: *Probability density for ^{16}Be ground state as a function of $r_x \equiv r_{nn}$ and $r_y \equiv r_{c-nn}$ with all potential terms described in Eq. 6.10 (left) and without the nn interaction term (right)[8].*

configuration, while the other two smaller peaks relate to triangular and cigar-like configurations, the latter corresponding to the case in which the two neutrons are very far from each other, $r_x \sim$6 fm, but very close to the core, $r_y \sim$1 fm. It is clear from Fig. 6.6 (left) that the dineutron configuration dominates the wave function of the ^{16}Be ground state.

The dominant dineutron component of the wave function can be explained as an effect of the *nn* interaction. This can be studied by diagonalizing the Hamiltonian without the *nn* interaction term of the potential, and adjusting the three-body term in order to obtain the same ^{16}Be energy. Although completely unrealistic, this allows to directly test how the *nn* interaction modifies the structure of the system and its relation with dineutron features. In Fig. 6.6 (right), the ground-state probability for this case is shown. From the absence of dineutron dominance in the spatial correlations, we can draw the conclusion that the strong dineutron character within this model derives from the *nn* interaction.

First excited state. Contrary to the ground state, the dineutron configuration in ^{16}Be(2^+) no longer dominates. In fact, the right panel on Fig. 6.7 shows a more diffused mixture of dineutron, triangular and cigar-like configurations. This fundamental difference with respect to the ^{16}Be ground state is interesting as they both show experimental *nn* correlation patterns. The absence of dineutron dominance may be a consequence of the intermediate state of ^{15}Be at 1.8 MeV included in the realistic ^{14}Be+*n* interaction. In that sense, an intermediate state could allow a sequential branch via ^{15}Be and dilute the *nn* interaction effect. However, as we explain in Sec. 6.2.3, calculations on excited three-body resonances using this model are very recent and still ongoing work, and therefore it is premature to draw any definite conclusions.

Application to ^{14}Be

Unlike the previously discussed ^{16}Be(2^+) $\rightarrow$^{15}Be case, it is known that no intermediate states in ^{13}Be lie below ^{14}Be(2^+). The right panel on Fig. 6.7 illustrates the spatial correlations obtained showing two clear structures. Similarly to the ^{16}Be ground state, a dineutron configuration clearly dominates the density distribution.

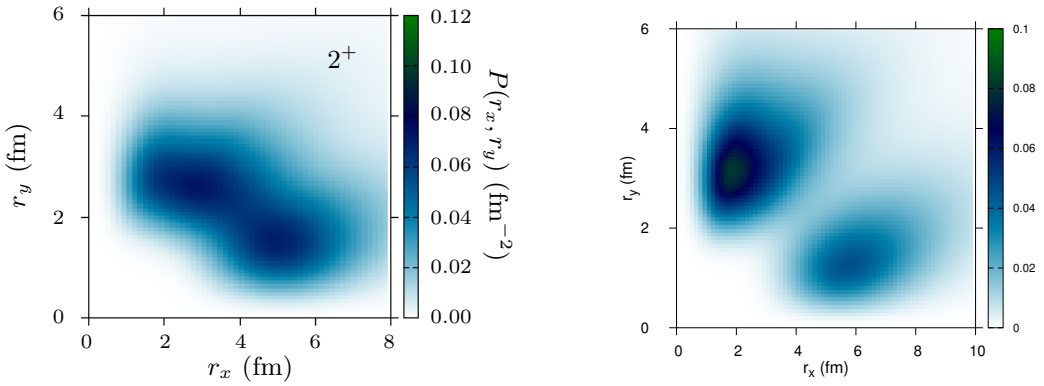

Figure 6.7: *Probability density as a function of $r_x \equiv r_{nn}$ and $r_y \equiv r_{c-nn}$ for for the 2^+ states of ^{16}Be (left) and ^{14}Be (right)[8].*

6.2.2 Gaussian source hypothesis

In Sec. 6.1, we have employed a structureless model to reproduce the characteristic *nn* low-energy enhancements observed in the experimental data. The strength of this signal depends on a single parameter which, within this formalism, is meant to be linked with the *nn* relative distance r_{nn}. This model, though able to reproduce relatively well the experimental distributions, is based on very unrealistic approximations. One of the major ones being the assumption of a Gaussian source. Since the different approximations do not correspond to a realistic scenario, the interpretation of $\sigma_{\rm fsi}$ as the distance between the two valence neutrons is highly questionable.

In order to investigate if the only free parameter of the FSI model has any physical meaning, we have studied the shape of a more realistic r_{nn} distribution, the one that would be deduced directly from the three-body wave functions. With that aim, we have projected the two-dimensional probability densities, presented in the previous section, onto the r_{nn} axis, and the results are shown in Fig. 6.8 (black dots). In order to check their similarity with a pure Gaussian source, we have fitted those projections with either one or two Gaussian distributions, of the form

$$P(r_{nn}) \propto r_{nn}^2 \exp\left(-r_{nn}^2/4\sigma_\psi^2\right) \tag{6.12}$$

In the case of the two 2^+ states, the distributions derived from the three-body wave function have a strong likelihood with a purely Gaussian source, although in the ^{14}Be(2^+) case (lower panel) a second Gaussian at smaller distances leads to a slight improvement in the fit. The values obtained from the one-Gaussian fit of the distributions are $\sigma_\psi = 2.1$ fm for ^{14}Be(2^+), and σ_ψ=2.0 fm for ^{16}Be(2^+).

For the ground state of ^{16}Be, the dineutron component that we observed already in the wave function is still apparent in the projection at short r_{nn} distances. Clearly, a two-Gaussian fit describes the distribution better, with two distinct values for both components of $\sigma_\psi = 0.7$ and 2.3 fm. Ideally, we could use the FSI model for each of those components and then add the results in order to test its validity, but as we saw earlier the FSI model is restricted to values of $\sigma_{\rm fsi} > 1.5$ fm, so the most compact component cannot be calculated

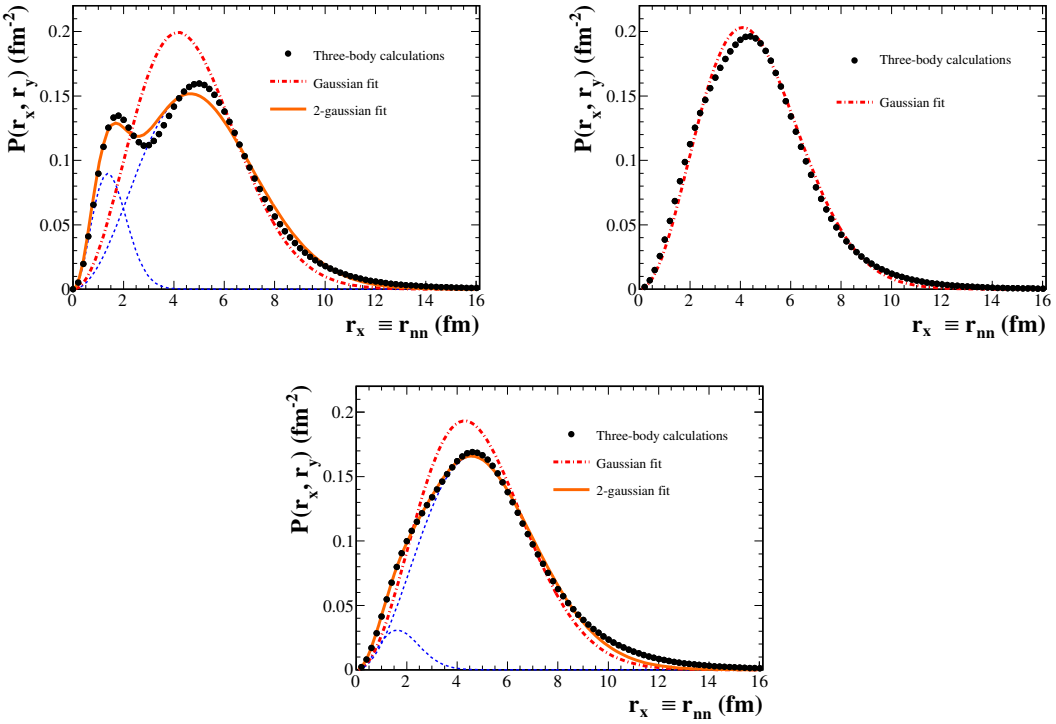

Figure 6.8: *Theoretical r_{nn} distribution obtained from the projection of the probability density of the three-wave function for $^{16}Be(0^+)$ (upper left), $^{16}Be(2^+)$ (upper right) and $^{14}Be(2^+)$ (lower) represented by black dots. The red twodash line corresponds to the fit with a single Gaussian and the solid orange line the total two-Gaussian fit. The individual components of the latter are in dashed blue lines.*

	^{16}Be(0^+)	^{16}Be(2^+)	^{14}Be(2^+)
$\sigma_{\rm fsi}$ (fm)	2.4(4)	1.5(2)	>16
σ_ψ (fm)	2.1	2.0	2.1

Table 6.1: *Summary of the σ values obtained for the description of r_{nn} with a Gaussian distribution: based on the FSI model and fitting to the experimental ε_{nn} (σ_{fsi}), and fitting the theoretical r_{nn} projection of the three-body wave function (σ_ψ)*

.

within this formalism. Therefore, we have made a one-Gaussian fit, that leads to an average value of $\sigma_\psi = 2.1$ fm for ^{16}Be(0^+). Even if the fit is worse, we see that the density projections of all three states are not radically different from a Gaussian distribution. A summary of the values obtained for both $\sigma_{\rm fsi}$ and σ_ψ can be found in Table 6.1.

6.2.3 Relative energy distribution

As shown in the preceding section, realistic three-body calculations can reveal interesting features about the internal structure of the system. Based on the microscopical model detailed in Sec. 6.2, the wave function of the three-body resonance allows us to study the spatial distribution of the two valence neutrons as a function of their distance to the core. These theoretical distributions have shown, for example, that a dineutron configuration dominates the ground state ^{16}Be(0^+) while the dineutron- and cigar-like contributions are equally important configurations for its first excited state ^{16}Be(2^+) (see Figs. 6.6 and 6.7). From a naive picture, one could expect that a strong dineutron configuration in the wave function would manifest a strong nn correlation in the final state, and *vice versa*. However, both states, with and without dineutron component, show strong correlations in their experimental nn relative energy distributions.

In order to put on equal footing theory and experiment, we need to transform the wave function into an observable we can directly compare with, as neither the wave function nor the distance between the two neutrons in the original resonant system can be directly measured in an experiment. Instead, the relative energy between the decay particles is experimentally accessible. From a theoretical approach, the connection between the wave function and the nn relative energy is, however, not straightforward since this entails the description of the evolution of the $2n$ correlations during the decay process. One solution to this problem has been developed by J. Casal *et al.*[74] and is briefly presented in this section.

As a first step, we need to describe the free evolution of the system during the decay. This can be assessed by calculating the *probability current* j of the wave function Ψ (see Sec. 6.2): this current shows how the two valence neutrons evolve within a given initial state. The time evolution of the wave function that describes the resonant state allows the definition of this current as a function of the hyperradius ρ, the hyperangle α and the time t, as $j(t, \rho, \alpha)$.

The time at which the decay particles would arrive at the detector, being no longer under the influence of the potential, would correspond to a time $t \to \infty$. However, the description of the asymptotic behavior of the hyperspherical current, which is related to

very large values of t, is not accurate since the discrete basis (see Eq. 6.2) used to describe the resonance is not complete at large distances. Yet for a time large enough, it is possible to find some optimal values of (ρ_0, t_0) for which the current is *i)* outgoing, *ii)* large and *iii)* stable $j(t, \rho, \alpha) \simeq j(\alpha)$. Around these values, the current would describe the flux of the wave function that "escapes" the potential. Therefore, within these conditions we can consider that particles do not feel the potential and move freely preserving their angular distribution.

In that region, the hyperangular probability of the decaying particles can be described as

$$\frac{dP(\alpha)}{d\alpha} = \frac{j(t_0, \rho_0, \alpha)}{J(t_0, \rho_0)} \tag{6.13}$$

where $J(t_0, \rho_0)$ is the hyperradial current obtained by integrating $j(t_0, \rho_0, \alpha)$ over the hyperangular part. For a three-body system of the type core$+n+n$ described in a Jacobi T set, the hyperangle α is related to the ratio between Jacobi momenta. If $E_x \equiv E_{nn}$ in our coordinate system, the relation between α and the momentum along the x-axis leads to $E_{nn} = E_r(\sin\alpha)^2$. The nn relative energy distribution is then,

$$\begin{aligned} \frac{dP(E_{nn})}{dE_{nn}} &= \frac{dP(\alpha)}{d\alpha}\frac{d\alpha}{dE_{nn}} \\ &= \frac{1}{E_r \sin 2\alpha}\frac{j(t_0, \rho_0, \alpha)}{J(t_0, \rho_0)} \end{aligned} \tag{6.14}$$

According to the above expression, the nn relative energy distribution would depend on the intrinsic correlations of the original system and its evolution over time. In a way, the possibility of transforming the three-body wave function into a measurable observable, which we can compare with experiment, allows us to indirectly have access to its structural information.

6.2.4 Energy distribution of ^{16}Be ground state

The theoretical $\varepsilon_{nn} = E_{nn}/E_{rel}$ distribution for ^{16}Be ground state obtained from its three-body wave function is presented on the left panel of Fig. 6.9. We can clearly observe a prominent peak at low energies ε_{nn} ~0.05 which indicates a very strong correlations between the two valence neutrons. In order to be directly comparable with experiment, the same experimental conditions have to be applied to the nn relative energy calculated from Eq. 6.14. In particular, we have to take into consideration *i)* the angular and energy resolution and acceptance of the setup, which distort the measured energy of neutrons, and *ii)* the cross-talk filter as this eliminates a big part of "true" $2n$ events.

The application of these experimental factors substantially changes the theoretical distribution. Figure 6.10 shows in blue line the nn relative energy from three-body calculations filtered by the detector response and the cross-talk rejection algorithm in comparison with experimental data. We note that the strong low-energy correlation that we had initially in the theoretical distribution is reduced, mainly due to the cross-talk rejection. The

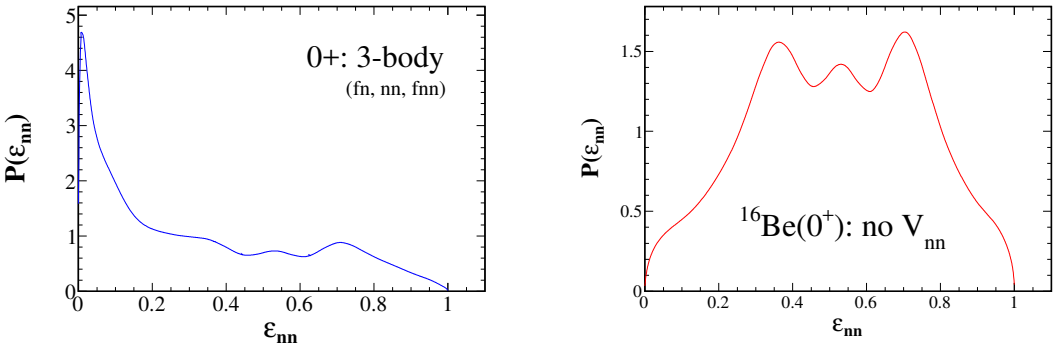

Figure 6.9: *Theoretical ε_{nn} distributions for ^{16}Be ground state. On the left, with the complete potential and on the right, removing the nn interaction term from the potential.*

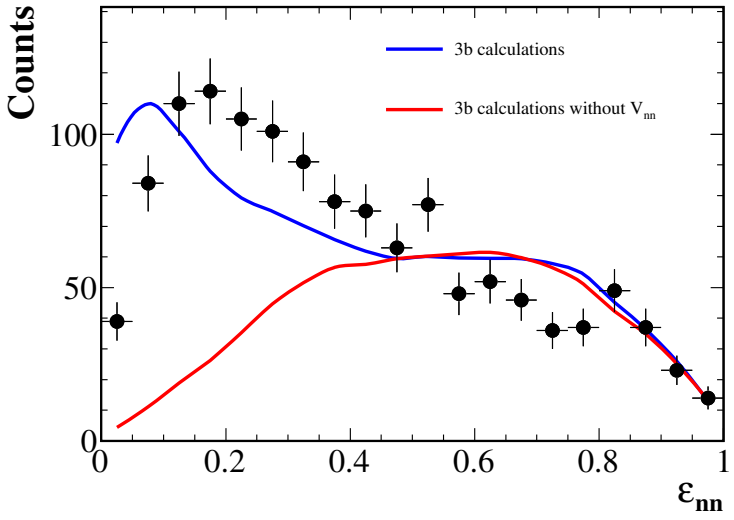

Figure 6.10: *ε_{nn} from three-body calculations for the ground state of ^{16}Be with experimental filters. The red solid line represents the case where we do not take into account the nn interaction for the diagonalization of the three-body hamiltonian.*

agreement with data is reasonably good, specially if we consider that we are not fitting the experimental spectrum but just comparing theory and experiment straightaway. The fact that both distributions show low-energy correlations, though a bit shifted, indicates that such a configuration for ^{16}Be(0^+) could represent a realistic picture able to describe the structure of the resonance.

Effect of the *nn* interaction

The connection between the structures that we see in the energy distribution and the ones in the spatial correlations, such as the dineutron configuration, are not directly equivalent, nor straightforward. From the perspective of FSI models, the low-energy *nn* enhancements have always been related to a strong *nn* interaction in the final state. Within the three-body approach we can actually study the effect of the *nn* interaction directly on the relative energy of the neutrons as the *nn* potential term can be easily "disconnected"

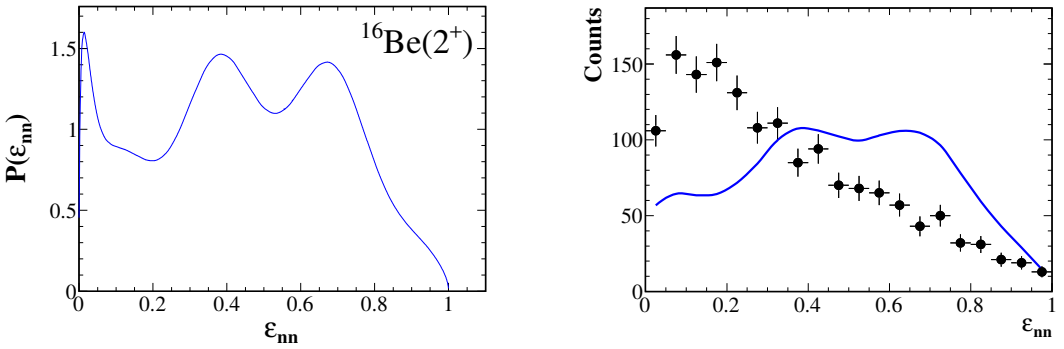

Figure 6.11: *On the left, theoretical ε_{nn} distributions for the 2^+ state of ^{16}Be. On the right, comparison with the experimental nn distribution after application of the experimental filter.*

in the diagonalization of the three-body problem.

The *nn* relative energy distribution that results from removing the *nn* interaction is radically different. As illustrated in Fig. 6.9 (right), even before any experimental filter, the low-energy peak has completely disappeared. In fact, the shape of the distribution is now centered at $\varepsilon_{nn} \sim 0.5$. When we apply the experimental conditions, the shape is smoothened and the low-energy part is even more suppressed. The distribution is presented in Fig. 6.10 in red solid line. Without the *nn* interaction, the resulting *nn* energy correlations are very similar to the *nn* correlations of a decay following a three-body phase space. This indicates that the *nn* enhancement at low energies is a result of the *nn* interaction or that, at least, is a very important factor in the description of the structure and decay of the three-body resonance.

6.2.5 Energy distribution of 2^+ excited states

In a similar way, the *nn* relative energy distributions for the 2^+ states of both ^{16}Be and ^{14}Be have been calculated. The result for ^{16}Be(2^+), before applying the experimental filter (Fig. 6.11, left), shows a very narrow peak at very low energies ε_{nn} ∼0.05. This peak, which could be as well associated with the effect of the *nn* interaction, does not seem to be a dominant feature as other broader structures at higher energies are equally important. In any event, the *nn* correlation at low energy is by far a less important feature than it was in the ground state of ^{16}Be. Once we apply the experimental filter and the cross-talk rejection algorithm, the very narrow low-energy contribution is considerably reduced (Fig. 6.11, right). Clearly, the result is not in agreement with the strong experimental low-energy *nn* signal observed.

In the case of ^{14}Be(2^+), the calculation (Fig. 6.12, left) shows a dominant strength at low energies, with a significant part of the distribution at $\varepsilon_{nn} < 0.5$. Even after the application of the experimental and cross-talk filters, the dominant strength at lower energies remains, which is in qualitative disagreement with the experimental distribution. As we have seen in the previous chapter, these data are very well described with a three-body phase space of non-interacting particles, without the necessity of including any *nn* FSI. Similarly to the ^{16}Be ground state, the wave function of this resonance is found to have

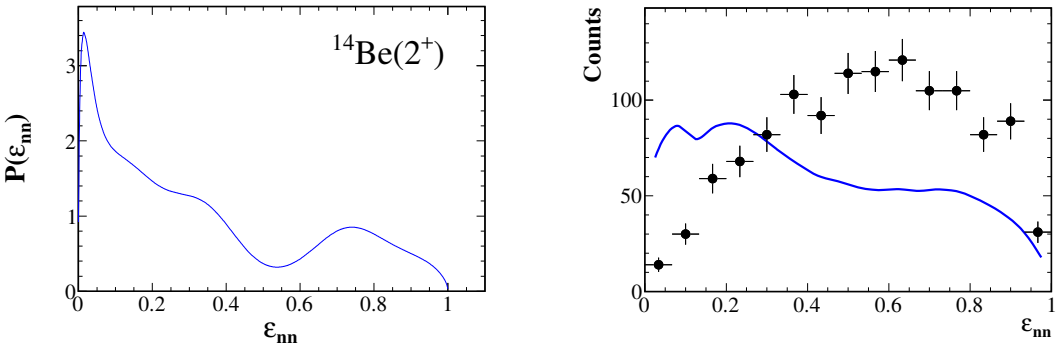

Figure 6.12: *On the right, theoretical ε_{nn} distributions for the 2^+ state of ^{14}Be. On the left, comparison with the experimental nn distribution after aaplication of the experimental filter.*

a dominant dineutron configuration while we find an absence of the dineutron component in ^{16}Be(2^+). Therefore, this would suggest that very strong low-energy correlations within this formalism are a consequence of the *nn* interaction together with a dominant dineutron configuration.

While the theoretical prediction for the ^{16}Be ground state seems to be in good agreement with the data, we find that the predicted distributions of the excited 2^+ states, of either ^{16}Be or ^{14}Be, do not describe the basic features of the experimental *nn* correlations. One should note that the microscopic model described in Sec. 6.2 has been developed for the study of ground state resonances of three-body systems. The study of the currents and their associated relative energy distributions is a very recent work that aims to better understand the observed $2n$ correlations from the point of view of the specific structure of the initial system. By extending this model to excited states, we find that the discrete basis that we use to describe the three-body resonance is incomplete. As a consequence, the asymptotic behavior of the current, defined by large values of the hyperradius ρ and time t (see Sec. 6.2.3), cannot be calculated in an accurate way. Comparison with these data will help the model to locate the different aspects that presently escape the theoretical description. Authors from [20] are currently working in a more robust model suitable for the excited resonant states in which the issues with the asymptotic currents would be fixed.

6.3 Conclusions

We have investigated the experimental *nn* correlations from two different perspectives. First, from a phenomenological approach using a FSI model with the main objective of reproducing the experimental data. By fitting the spectrum with a single free parameter σ_{fsi} we have succeeded in reproducing the strong low-energy signals observed in the *nn* relative energy of the ^{16}Be ground and first excited state. Despite all the simplifications used in the model, some of them probably in contrast with the physics related to the structure and decay of these systems, this approximation is able to reproduce quite accurately the experimental *nn* correlations.

In order to obtain a more realistic and physical interpretation we have studied next

the nn correlations from complete three-body calculations that take into consideration the internal distribution of the valence neutrons in the original system. Using this microscopic approach, the wave function as well as the spatial correlations derived from its configuration have been probed for the continuum of ^{16}Be and ^{14}Be. A direct comparison with experimental distributions has been made possible through the theoretical calculation of the nn currents or flux from the three-body wave functions. Without any fit parameter, in the case of the ^{16}Be ground state the agreement is remarkably good. The nn low-energy correlations are associated with the nn interaction. Indeed, if we remove the nn term from the potential, the missing low-energy signal of the resulting nn distribution confirms that nn low-energy enhancements appear as a consequence of the interaction between the two valence neutrons.

The treatment of the excited 2^+ states in the model faces additional issues that ground-state resonances do not encounter. Moreover, their results disagree with our experimental distributions: in ^{16}Be(2^+) we find a low-energy signal that the model lacks, and in ^{14}Be(2^+) the model predicts such a signal that clearly is absent in the data. The collaboration with theoretician colleagues is still ongoing and more work is in progress to improve the model. In that respect, our experimental 2^+ distributions will be of great value in guiding and validating the new methods still in development.

Chapter 7

Conclusions and perspectives

This thesis work is focused on the structure of neutron-rich nuclei that lie at the edge or beyond the neutron dripline. In particular, we have investigated the heaviest Beryllium isotopes ^{14}Be, ^{15}Be and ^{16}Be. One of the foremost topics studied has been the three-body decay of two-neutron unbound states, a phenomenon that can be observed in both ^{14}Be and ^{16}Be.

All the experiments presented in this work have been performed at the RIBF-RIKEN facility using the **SAMURAI** multidetector setup (gamma, neutron and charged-particle detector arrays) during different experimental campaigns: the SAMURAI commissioning, the DayOne and the s018 campaigns. For the latter, the state-of-the-art MINOS target was added to the standard SAMURAI setup that includes the neutron array NEBULA, allowing us to improve qualitatively both resolution and statistics as compared with previous studies.

The unbound states in the nuclei of interest have been populated using nucleon **knock-out** reactions. All studied resonant states lie above the neutron emission threshold and decay by neutron emission. We have used the invariant mass method to reconstruct the relative energy from their decay products that required the detection in coincidence of the fragment and the neutron(s) in flight and the measurement of their momenta and energy. Multi-neutron detection has been successfully analyzed by means of **cross-talk** rejection algorithms.

The complexity of the multidetector setup has required the use of simulations able to take into account the experimental resolutions and acceptances in order to interpret the data. The relative energy spectrum has been analyzed using two main contributions: a non-resonant component representing the continuum of these final states, plus potential resonances with different energies and widths. The non-resonant contribution has been generated either by simulations or by event mixing techniques, avoiding the *a priori* subjective analytical assumptions used in other works. The resonant contribution has been characterized with Breit-Wigner line shapes with energy-dependent widths.

The **three-body correlations** in core+n+n decays have been probed using the Dalitz plot technique. In order to get a better understanding about the relation between the internal structure of the system and the role of the nn interaction in the observed final

correlations, full three-body calculations have been performed. A new theoretical method has been developed to calculate the nn relative energy distribution from the three-body wave function. We have developed a technique to integrate the experimental conditions in the theoretical distributions and make experiment and theory directly comparable.

These are the main results of this thesis work for each of the systems studied:

- **^{16}Be**

  In a previous work, a new type of decay, a dineutron emission, was claimed in ^{16}Be. However, the analysis of the three-body correlations that led to this conclusion did not include the nn final state interaction, and only accounted for phase space considerations. Moreover, a structure identified as the ground state was observed at an energy and width of E =1.35 MeV and Γ =0.85 MeV, respectively. The questions raised by the broad width of the resonance and the peculiar $2n$ decay mode motivated a new experimental campaign.

  Spectroscopy. ^{16}Be was populated using a proton knock-out reaction from a ^{17}B beam during the s018 campaign, with high resolution and large energy acceptance. The ^{14}Be+$n+n$ relative energy spectrum showed two clear structures:

  - a low-energy resonance identified as the ground state of spin and parity $J^\pi = 0^+$. The energy and width is found to be $E = 0.84(3)$ MeV and $\Gamma = 0.32(8)$ MeV, respectively.
  - a second resonant state identified with the first excited state of spin and parity $J^\pi = 2^+$. The energy and width is found to be $E = 2.15(5)$ MeV and $\Gamma = 0.95(15)$ MeV, respectively.

  Three-body correlations. The correlations of the $2n$ decay of ^{16}Be have been investigated. The analysis of the experimental fn and nn relative energy distributions and the comparison with a theoretical model based on microscopic principles led to the following conclusions:

  - The study of experimental fn correlations have indicated that both 0^+ and 2^+ states in ^{16}Be have a direct decay to ^{14}Be by emission of two simultaneous neutrons.
  - The experimental nn relative energy spectra have shown strong low-energy nn correlations for both states.
  - Three-body calculations predict a wave function for the ^{16}Be ground state dominated by a dineutron configuration. The theoretical nn distributions calculated from this wave function were able, without any fit parameter, to reproduce the low-energy enhancement observed experimentally, which has been demonstrated to be related to the nn interaction.

- **^{15}Be**

  The level structure of ^{15}Be is still unknown. Only a state identified with spin and parity $J^\pi = 5/2^+$ at an energy $E = 1.8$ MeV was observed. The predicted $3/2^+$ ground state remained unobserved, and the position of the ground state in ^{15}Be may have an important influence on the decay of ^{16}Be.

Spectroscopy. ^{15}Be has been studied from different experiments performed during the DayOne campaign:

- **(^{17}B,^{14}Be+n)**, **(^{19}B,^{14}Be+n)** and **(^{22}N,^{14}Be+n)** knock-out reactions show no clear population of ^{15}Be. Their relative energy spectrum can be well described by the contributions of the decay from the two observed states in ^{16}Be plus the direct population of the ^{14}Be+n continuum.
- One resonant state at 1.8 MeV was observed in **(^{18}C,^{14}Be+n)**, **(^{19}C,^{14}Be+n)** and **(^{20}C,^{14}Be+n)** knock-out reactions. In the latter, a possible low-energy resonance located at $\sim$ 0.4 MeV could correspond to another resonance in ^{15}Be, although the statistical significance is small.

These results seem to confirm a resonance at 1.8 MeV identified with the $5/2^+$ state in previous works. The nature of this state (J^π, ground or excited state) is still unresolved.

- **^{14}Be**

  The 2_1^+ state of ^{14}Be is known to lie only 254 keV above the two-neutron threshold emission. However, its $2n$ emission is assumed to be direct to ^{12}Be but neither the three-body correlations nor the decay mechanism had never been formally studied.

  This state has been populated using an inelastic scattering reaction from a ^{14}Be beam. The correlations between its decay products have been deeply investigated. Our study leads to the following conclusions:

  - The decay follows a three-body phase space. Therefore the decay of ^{14}Be can be considered as direct via the emission of two simultaneous neutrons.
  - The nn relative energy distribution does not show any evidence of nn interaction or correlations.

Other than all the specific results listed above, the main result of this work is the pioneering bridge that has been extended between the experimental observations of $2n$ observables and the microscopic description of their initial wave functions. Within a simple FSI picture based on the nn s-wave scattering, the experimental distributions can be more or less accurately reproduced. However, it cannot answer many open questions. Why don't we see any nn signal in the decay of ^{14}Be(2^+), a system very similar to its ^{16}Be partners? Why do we observe a stronger signal in the decay of ^{16}Be(2^+), that seems to have an open sequential path available that the ground state has not? Why should we see only s-wave type of signals in systems that have important p and d components in their wave functions?

A joint important effort between our state-of-the-art experimental approaches and the theoretical development of three-body formalisms has allowed a first direct comparison on equal footing. The good description of the ^{16}Be(0^+) ground state decay connects the experimental nn signal we observe with the component of the three-body wave function in which the neutrons orbit together the core of ^{14}Be, the dineutron configuration. Somehow, in a system with a three-lob structure, reminiscent of a dominant d-wave, we can "measure" the most dineutron-like lob.

As we have seen in Sec. 6.2.5, the description of the decay of the other two 2^+ excited states is not satisfactory. Nevertheless, the higher difficulty of the exercise in these excited states was to be expected, since the three-body formalism uses an incomplete basis and the lack of completeness plays a more important role the higher the energy in the continuum. Work is in progress in order to succeed in the description and understanding of these excited states, and in this task our experimental results will be a firm and clear guide.

On the experimental side, our work has opened some perspectives. The resolution and acceptance of our setup has provided a clear picture of the spectroscopy and decay of ^{16}Be. If other states were to be populated, we do not need a better setup or technique, but a different reaction. In the case of ^{15}Be, our systematic quest for states has overcome the possible selection rules that were invoked in previous works and the 1.8 MeV state was clearly confirmed. Since in one of the channels a small low-energy signal was also observed, it could be worth to undertake a dedicated experiment using this channel, that could confirm whether the ground state is much lower than expected.

In the subject of dineutron emission, the most promising future may lie higher in mass, in ^{26}O. A new experiment will be conducted at RIBF with a higher granularity neutron detector, in order to access the decay correlations. This seems to be a very favorable case in every sense. From the experimental point of view, the energy of its states is known to the keV level, and the cross-sections have been accurately measured. From the theoretical side, there are very few states involved. Moreover, the energies are so low that they are close to binding, and ^{24}O can be confidently treated as a spherical core nucleus. However, as we have seen in the ^{14}Be(2^+) decay and as some theoreticians predict[72], it could be that the low energies "erase" the correlations. Such an interesting effect is to be studied in future experiments.

Appendices

Appendix A

Event Mixing

As we have seen in Sec. 4.3.1, when the correlation function is small, or if it acts on a small portion of the data set, we can consider that $\langle C \rangle \approx 1$, and therefore the correlation function will be approximately,

$$C(p_1, p_2) \;\approx\; \frac{d^2\sigma/dp_1 dp_2}{(d\sigma_\otimes/dp_1)\,(d\sigma_\otimes/dp_2)} \tag{A.1}$$

However, if particles are strongly correlated $\langle C \rangle > 1$, a simple event mixing will not be enough to remove all correlations. In general, mixing the events will lead us to underestimate, more or less, the correlation function

$$\frac{d^2\sigma/dp_1 dp_2}{(d\sigma_\otimes/dp_1)\,(d\sigma_\otimes/dp_2)} \;\leq\; C(p_1, p_2) \tag{A.2}$$

If we are able to calculate the residual correlation factors of each particle, we can use them as weights to calculate the exact value of $C(p_1, p_2)$,

$$\underbrace{\frac{d^2\sigma/dp_1 dp_2}{(d\sigma_\otimes/dp_1)\,(d\sigma_\otimes/dp_2)}}_{\times \frac{1}{\langle C\rangle(p_1)}\frac{1}{\langle C\rangle(p_2)}} \;=\; C(p_1, p_2) \tag{A.3}$$

with the residual factor defined as

$$\begin{aligned} \langle C\rangle(p_1) &= \int C(p_1, p_2)\,\frac{d\sigma}{dp_2}\,dp_2 \\ &= \int C(p_1, p_2)\,\frac{d\sigma_\otimes/dp_2}{\langle C\rangle(p_2)}\,dp_2 \end{aligned} \tag{A.4}$$

Therefore, this implies to construct the correlation function using the correlation function itself. In addition, as can be deduced from A.4, we would need the "independent"

distribution of particle 2 in order to calculate the weights of the particle 1, but experimentally we cannot measure this independent function. In order to solve this problem, we need to use an double iterative algorithm, a first loop to estimate the weight and a second loop to estimate the independent contribution of one particle at each step.

Iterative technique. First, we need to project the 8-dimensional space into 1 dimension:

$$(p_i, p_j) \;\rightarrow\; x_{ij} \tag{A.5}$$

where x_{ij} is the relative variable we want to study, such as the fragment-n relative energy. This variable contains the correlations that we want to extract. If we now rewrite Eq. A.3 in terms of x_{ij}

$$\frac{\sigma(x_{12})}{[\sigma_{\otimes}(x_{12})]_{w_{12}}} \;=\; C(x_{12}) \tag{A.6}$$

with $\sigma(x_{12})$ the measured two-particle distribution and $[\sigma_{\otimes}(x_{12})]_{w_{12}}$ the mixed distribution obtained through the event mixing weighed by

$$w_{12} \;=\; w_1\, w_2 \;=\; \frac{1}{\langle C\rangle(p_1)}\,\frac{1}{\langle C\rangle(p_2)} \tag{A.7}$$

Each particle has an associated weight w_i, that is, we have to build an array of $2N$ weights such as

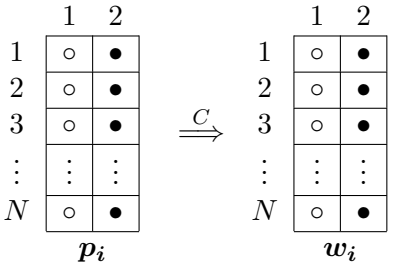

In the first iteration, all weights will be set to 1, and we will build an initial mixed distribution. To obtain the correlation function, we will divide the data by the obtained distribution, as described by the Eq. A.6. Since in this correlation function a part of the correlations is erased, it can be used to calculate the second weights. These weights will be similarly used to mix the distributions to construct a second correlation function, which will be again used to obtain the third weigths...*etc.*

$$\begin{aligned}
w^{(1)}=1 \;&\rightarrow\; [\sigma_{\otimes}]_{w^{(1)}} \rightarrow \frac{\sigma}{[\sigma_{\otimes}]_{w^{(1)}}} = C^{(1)} \\
\rightarrow\; w^{(2)} \;&\rightarrow\; [\sigma_{\otimes}]_{w^{(2)}} \rightarrow \frac{\sigma}{[\sigma_{\otimes}]_{w^{(2)}}} = C^{(2)} \\
\rightarrow\; w^{(3)} \;&\rightarrow\; \cdots \rightarrow \frac{\sigma}{[\sigma_{\otimes}]_{w^{(n)}}} = C^{(n)}
\end{aligned} \tag{A.8}$$

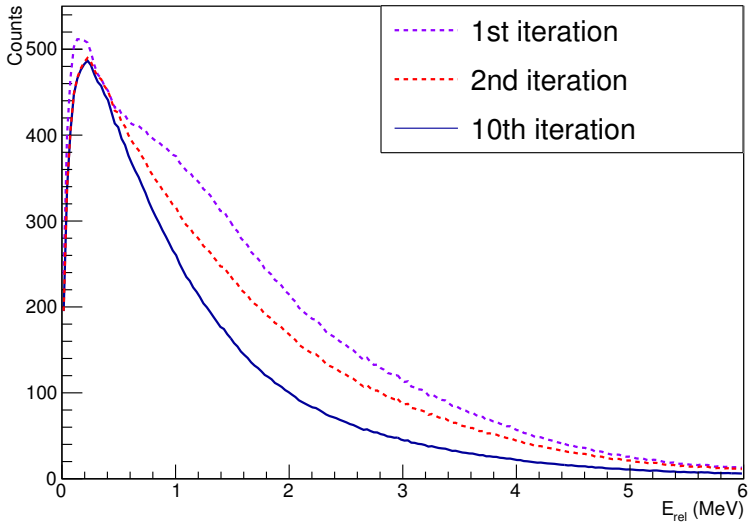

Figure A.1: *Fragment-n non-resonant contribution to the relative energy for the* ^{15}B*+n channel.*

The second loop that we mentioned above implies that the calculation of the array of weights described in Eq. A.4 becomes,

$$\langle C\rangle^{(n)}(p_i) \;=\; \frac{1}{N-1}\sum_{j=1\neq i}^{N}\frac{C^{(n-1)}(x_{ij})}{\langle C\rangle^{(n)}(p_j)} \tag{A.9}$$

since we calculate this array at every step of the general iteration, and for the calculation of each weight $1/\langle C\rangle^{(n)}(p_i)$ we need the weights $1/\langle C\rangle^{(n)}(p_j)$ of all possible partners, that at the same time will need the former.

After a certain number of general iterations, the correlation function will converge. Figure A.1 shows how the non-resonant contribution changes with the number of iterations. A total number of 10 iterations is usually enough to achieve the convergence.

Appendix B

Lednicky formalism

In the formalism of Ref. [19], the correlation function for neutrons of four-momenta p_i emitted at a space-time relative distance $x = (\vec{r}, t)$ has two terms: *i)* a term originating from Fermi statistics and *ii)* the s-wave FSI, averaged over the distribution of distances contribution. This correlation function is then written as

$$C_{nn}(p_1, p_2) = 1 + \langle b_0 \rangle + \langle b_i \rangle \tag{B.1}$$

$$\langle b_0 \rangle = -\frac{1}{2} \langle \cos(qx) \rangle \tag{B.2}$$

$$\langle b_i \rangle = \frac{1}{2} \Big\{ |f(k^\star)|^2 \langle |\phi_{p_1 p_2}(x)|^2 \rangle + 2\, \Re \left[f(k^\star) \langle \phi_{p_1 p_2}(x) \cos(qx/2) \rangle \right] \Big\} \tag{B.3}$$

where the superscript * refers to the $2n$ center of mass, $q = p_1 - p_2$ is the relative four-momentum, $k^\star = \sqrt{q^2}/2$ is the four-momentum of each neutron, and f is their scattering amplitude. The latter can be expressed as

$$f(k^\star) = \left(-1/a_s + k^{\star 2} d_0/2 - i k^\star \right)^{-1} \tag{B.4}$$

where a_s and d_0 are the scattering length and effective range, respectively. In this formalism, we use $a_s = -18.5$ and $d_0 = 2.8$ fm.

The $2n$ wave function is factorized assuming $r^\star \gtrsim d_0$ as $f(k^\star)\phi_{p_1 p_2}(x)$, with the exact form of $\phi_{p_1 p_2}(x)$ given in Ref. [19]. However, the final expression of C_{nn} (B.8) does not depend on the form of $\phi_{p_1 p_2}(x)$. If we consider a spherically symmetric source W and *neglect the momentum dependence* inside this source, we can rewrite the parameters that define the correlation function $\langle b_0 \rangle$ and $\langle b_i \rangle$ as,

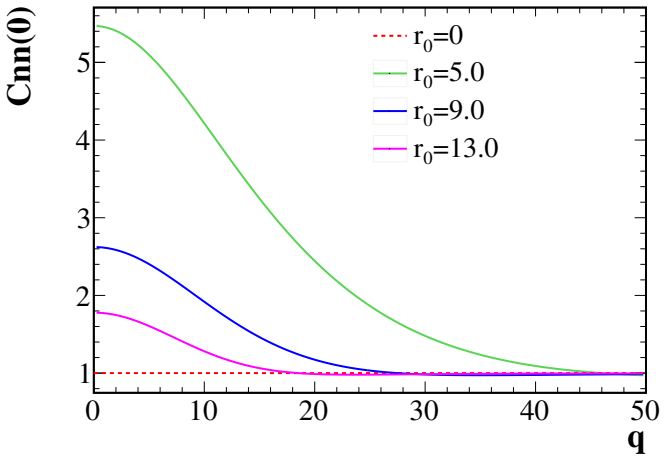

Figure B.1: *Evolution of the nn relative momentum with respect to different values of the phenomenological parameter r_0. Here r_0 is equivalent to r_0.*

$$\langle b_0 \rangle = -\frac{1}{2}\int W(x)\,\cos(qx)\,d^4x \tag{B.5}$$

$$\langle b_i \rangle = \int 2\pi r_T dr_T dr_L dt\; W(x)\left\{|f(k^\star)\phi_{p_1p_2}(x)|^2 + 2\Re[f(k^\star)\phi_{p_1p_2}(x)]J_0\left(\frac{q_T r_T}{2}\right)\cos\left(q_0\frac{r_L - vt}{2v}\right)\right\} \tag{B.6}$$

with L/T the directions parallel/perpendicular to the velocity v of the pair. This expression can be simplified if we assume a *Gaussian source* of the form $W(x) = \exp(-r^2/4r_0^2 - t^2/4\tau_0^2)$, where r_0 corresponds to σ_{fsi} used in Sec. 6.1. For small enough energies ($k^\star \ll m$), the integration over $t^\star$ would result in,

$$\langle b_0 \rangle = -\frac{1}{2}\exp(-4k^{\star 2}r_0^2 - q_0^2\tau_0^2) \tag{B.7}$$

$$\langle b_i \rangle = \frac{1}{2\sqrt{\pi}r_0^2\gamma\rho}\int r_T dr_T dr_L^\star \exp(-r_T^2/4r_0^2 - r_L^{\star 2}/4\gamma^2\rho^2) \times\left\{\frac{|f|^2}{2r^{\star 2}} + \Re\left[f\frac{\exp(ik^\star r^\star)}{r^\star}\right]J_0\left(\frac{q_T r_T}{2}\right)\cos\left(\frac{q_0 r_L^\star}{2\gamma v}\right)\right\} - (1/8\sqrt{\pi})|f|^2 d_0/\gamma\rho r_0^2 \tag{B.8}$$

with $\rho = \sqrt{r_0^2 + v^2\tau_0^2}$ where τ is the relative time between the emitted neutrons. The last term in (B.8) is a first-order correction of the integration of the expression used for $\phi_{p_1p_2}(x)$ in the region $r^\star < d_0$.

In the case of simultaneous emission with $\tau = 0$ and/or very small velocities ($\gamma\rho \approx r_0$) the final expression becomes analytical and dependent on only one free parameter r_0

$$C_{nn}(q_{nn}) = 1 - \frac{1}{2}\exp(-q_{nn}^2 r_0^2) + \frac{|f|^2}{4r_0^2}\left(1 - \frac{d_0}{2\sqrt{\pi}r_0}\right) + \frac{\Re f}{\sqrt{\pi}r_0}F_1(q_{nn}r_0) - \frac{\Im f}{2r_0}F_2(q_{nn}r_0) \quad \text{(B.9)}$$

with $F_1(z) = e^{-z^2}/z \int_0^z e^{x^2} dx$ and $F_2(z) = (1 - e^{-z^2})/z$. Otherwise one should use (B.7,B.8), with the two free parameters (r_0, τ_0). From the parametrization of the gaussian source W used, one obtains $rms = \sqrt{6}r_0$ and $\tau = \sqrt{2}\tau_0$.

Note that this model cannot be applied for $r_0 \lesssim 1.5$ fm ($rms \lesssim 2.5$ fm), since then the result is completely determined by the short-distance behavior of $\phi_{p_1 p_2}(x)$ in (B.3), sensitive to the form of the n-n potential.

Appendix C

Résumé

Contents

Dans ce document, nous présenterons des travaux portants sur les noyaux très riches en neutrons qui se situent aux limites de la stabilité et au-delà, dans la région de masse légère de la carte nucléaire. En particulier, nous nous intéresserons à la spectroscopie et la désintégration à deux neutrons de l'isotope non lié ^{16}Be. Les corrélations nn de la désintégration ont été largement examinés et interprétés à partir d'un point de vue microscopique. Afin de compléter le tableau et de donner un meilleur aperçu de l'évolution des propriétés nucléaires vers le ^{16}Be, les deux isotopes précédents de la chaîne isotopique, le non lié ^{15}Be et le dernier isotope lié ^{14}Be, sont également étudiés.

Ce travail est divisé en 6 chapitres. Le premier présente le contexte et les motivations de cette thèse. Nous décrirons ensuite le dispositif expérimental qui a été utilisé afin d'observer les noyaux d'intérêt. Les méthodes liées à l'analyse des données expérimentales ainsi que les simulations effectuées sont décrites dans le troisième chapitre. Le chapitre suivant est consacré a la présentation des résultats obtenus pour la spectroscopie du ^{14,15,16}Be. L'analyse des corrélations nn pour les états qui présentent une émission "deux neutrons" est détaillé dans le chapitre 6. Finalement, les conclusions et les perspectives sont résumées dans le dernier chapitre.

C.1 Introduction

Noyaux riches en neutrons

L'une des questions fondamentales de la structure nucléaire est de savoir où se situent les limites de l'existence nucléaire, c'est-à-dire, les limites de la stabilité où plus aucun proton

ou neutron ne peut être lié au noyau. Ces frontières sont communément appelées *driplines*, à savoir la dripline proton et neutron, pour le côté déficient en neutrons et le côté riche en neutrons, respectivement. Au fur et à mesure que nous nous rapprochons de la dripline neutron, vers des rapports plus extrêmes $N/Z \gg 1$, les isotopes deviennent très instables, leur durée de vie pouvant être aussi courte que plusieurs millisecondes. Cela les rend très difficiles à produire et à étudier expérimentalement. En effet, la dripline neutron reste très inexplorée et n'a été atteinte que pour des noyaux très légers, avec un petit nombre de protons $Z \lesssim 10$.

Des phénomènes "exotiques" apparaissent dans les noyaux instables loin de la stabilité comme conséquence de l'évolution de la structure nucléaire avec le nombre des nucléons, comme par exemple, des nouveaux modes de décroissance. Jusqu'à présent, aucune théorie nucléaire actuelle ne peut expliquer pleinement l'ensemble des phénomènes qui se produisent du côté riche en neutrons, ni la position exacte de la dripline. La détermination exacte de la dripline neutron est un test important pour les formalismes théoriques car elle peut aider à vérifier l'exactitude de leurs hypothèses en les comparant aux données expérimentales.

Émission de neutrons

Les noyaux pour lesquels le nombre de neutrons ou de protons est en excès deviennent plus faiblement liés et, par conséquent, les nucléons peuvent plus facilement "s'échapper" du noyau. L'émission de nucléons par des noyaux riches en neutrons ou en protons a été établie comme un phénomène caractéristique se produisant à l'approche des driplines, où l'énergie nécessaire pour enlever un proton ou un neutron devient suffisamment faible, voire négative [9, 10, 11].

L'émission "deux neutrons" à l'état fondamental peut se produire une fois que nous dépassons les driplines en raison de l'évolution des corrélations neutron-neutron. L'une des manifestations les plus évidentes de ces corrélations se retrouve dans les oscillations paires-impaires des énergies de séparation neutronique S_n. Ces oscillations proches de zéro rendent les voisins pairs-N liés et les voisins impairs-N non liés en ce qui concerne l'émission à un neutron. Au contraire, l'énergie de séparation à deux neutrons S_{2n} a tendance à diminuer de façon monotone vers la dripline. Au-delà de la dripline neutron, les oscillations S_n peuvent donner lieu à des situations dans lesquelles S_{2n} atteint des valeurs négatives tandis que S_n reste positif. Cela se traduit en systèmes liés par rapport à l'émission neutron et non liés par rapport à l'émission deux neutrons. Dans ces systèmes, une désintégration spontanée à deux neutrons à partir de l'état fondamental a plus de chances de se produire. Cependant, étant donné que le dripline neutron n'est accessible que pour les noyaux légers, très peu d'émetteurs à deux neutrons sont connus. Les deux seuls candidats sont ^{26}O et ^{16}Be, qui est le sujet de notre étude.

Structure à trois corps

Les noyaux légers riches en neutrons, tels que ^{6}He ou ^{11}Li, présentent souvent des structures avec un caractère à trois corps manifeste composé d'un noyau lié et deux neutrons faiblement liés, core+n+n. Ces systèmes, étant presque impossible à décrire comme un problème à N-corps, peuvent être plus facilement abordés en termes d'interactions à deux et trois corps. En effet, l'étude expérimentale des résonances à trois corps peut révéler des pro-

priétés directes des interactions core+n ou nn qui peuvent aider les théories à développer des interactions nucléaires plus réalistes. En particulier, l'interaction nn peut être étudiée en profondeur car cela se manifeste sous la forme de signaux caractéristiques à faible énergie dans le spectre d'énergie relative qui s'écartent clairement de la distribution d'énergie que nous obtiendrions en suivant uniquement des contraintes cinématiques. Les corrélations nn auront également un impact sur l'énergie relative de base $+n$, et éventuellement, sur l'énergie relative des trois corps. Afin de bien comprendre la désintégration des résonances à trois corps, il est essentiel de prendre en considération l'effet de l'interaction entre les neutrons.

Dans ce travail, nous étudions plusieurs systèmes qui présentent une émission de deux neutrons. Les corrélations nn mesurées ont été étudiées avec deux approches différentes : en utilisant d'abord un modèle phénoménologique, le formalisme FSI [19], avec lequel nous supposerions que la partie asymptotique du potentiel nn domine l'état final, négligeant la structure de la source, et ensuite, un modèle microscopique [20] qui effectue des calculs complets à trois corps en tenant compte des corrélations internes dans le système d'origine. L'interprétation des corrélations de désintégration ainsi que la comparaison entre les deux approches sont présentées au chapitre 6.

Noyaux d'intérêt

Béryllium-16. Le système ^{16}Be a été auparavant étudié par [4] à partir d'une réaction knock-out ($-1p$) avec un faisceau ^{17}B à une énergie de 53 MeV/nucléon en utilisant une cible de Béryllium. Une large structure à une énergie de 1.35(10) MeV au-dessus du seuil ^{14}Be+n + n + n a été identifiée avec son état fondamental, avec une largeur de $\Gamma = 0,8(1)$ MeV et une spin et parité attribuées de 0^+. De plus, des forts signaux de corrélations ont été observées à faibles énergies relatives nn (E_{nn}) et angles (θ_{nn}). Ce signal observé, ne peut être décrit,parmi les hypothèses utilisées dans cet étude, que par celui qui suppose une désintégration dineutron. Cependant, cette simple interprétation ne tient pas compte de l'interaction nn dans l'état finale, largement observé dans un grand nombre de systèmes qui présentent une émission deux neutrons.[37, 38, 39].

Ce travail de thèse présente des nouveaux résultats sur ^{16}Be obtenus avec la campagne s018 à RIKEN en utilisant le dispositif SAMURAI, qui inclut le détecteur de neutrons NEBULA et la cible active MINOS. ^{16}Be a été peuplé a partir de la même réaction que celle de [4]. Une amélioration est attendue au niveau de la résolution, les statistiques et l'efficacité de la détection de deux neutrons grâce a l'utilisation de la cible MINOS. Outre ces améliorations expérimentales, un autre objectif serait l'étude de l'émission $2n$ dans un formalisme plus réaliste, à partir de principes microscopiques pour mieux comprendre la structure des résonances à trois corps et le rôle de l'interaction nn. En ce sens, le déploiement du FSI est essentiel pour étudier les corrélations qui manifestent les particules lors de la désintégration.

Béryllium-15. L'existence d'un état intermédiaire dans ^{15}Be est fondamentale pour l'interprétation de la désintégration à deux neutrons de ^{16}Be. Pourtant, sa structure de niveau n'est pas complètement déterminée et comprise. Les études de spectroscopie précédentes de ^{15}Be ne résolvent pas la question de savoir quel état, soit un $3/2^+$ ou $5/2^+$, correspond à l'état fondamental. Une seul structure résonante a été observée pour ^{15}Be et, sous critères des calculs de modèle en couches, a été identifiée avec l'état $5/2^+$ à une énergie

de 1.8(1) MeV. L'état $3/2^+$, prédit par la théorie, reste sans observation expérimentale.

Le but des nouvelles expériences sur ^{15}Be serait de peupler les $3/2^+$ non observés et de confirmer l'énergie de l'état $5/2^+$ à 1.8 MeV. Dans ce contexte, nous avons sondé la spectroscopie de ^{15}Be peuplée à partir de différentes expériences effectuées à RIKEN en utilisant la configuration SAMURAI qui inclut une large gamme de réactions d'inactivation. Les résultats obtenus à partir de ces expériences et son influence sur la désintégration de ^{16}Be sont présentés dans ce travail de thèse.

Béryllium-14. ^{14}Be est l'isotope le plus lourd du béryllium avec un état lié connu. Il s'agit également d'un exemple classique de noyau halo, pouvant être décrit comme un noyau de ^{12}Be plus deux neutrons faiblement liés. Son premier état excité 2^+ est non lié et se trouve à 280(10) MeV [6] par rapport au seuil d'emission $2n$. Le meme etude a confirmé la désintégration directe de ^{14}Be(2^+) à ^{12}Be via l'émission de deux neutrons. Des études ultérieures ont indiqué que l'énergie relative des deux neutrons émis lors de la désintégration peut être reproduite en prenant simplement en considération la cinématique à trois corps sans l'inclusion d'interaction dans l'état final [45].

Dans le cadre de cette thèse, l'étude de l'émission $2n$ de ^{14}Be(2^+) permettrait de mieux comprendre les caractéristiques de la désintégration à trois corps impliquant l'émission de deux neutrons simultanés. Bien que les désintégrations de ^{16}Be et ^{14}Be impliquent l'émission de deux neutrons, elles présentent des caractéristiques différentes. Alors que la FSI semble être très important dans la désintégration de ^{16}Be, l'énergie relative nn de la décroissance ^{12}Be+n+n ne montre aucune corrélation venant du FSI. Afin de déterminer si ces différences sont importantes ou non, il serait intéressant de comparer l'émission spontanée à deux neutrons que nous trouvons dans l'état fondamental de ^{16}Be avec celle "induite" qui se produit dans ^{14}Be. Le but de ce travail est d'étudier et de comparer les corrélations montrées dans la désintégration des deux systèmes dans le même formalisme.

C.2 Approche expérimentale

La campagne expérimentale SAMURAI 18 (s018), réalisée au **R**adioactive **I**sotope **B**eam **F**actory (RIBF) à RIKEN Nishina Center [46], est l'expérience principale analysée pour ce travail. Dans notre cas particulier, le noyau d'intérêt était ^{16}Be, peuplé avec une réaction knock-out a partir d'un faisceau de ^{17}B en utilisant la cible MINOS, et détecté à l'aide de la configuration standard SAMURAI et du détecteur de neutrons NEBULA. La structure nucléaire des précédents isotopes du béryllium, ^{15}Be et ^{14}Be, a également été étudiée à travers d'une série d'expériences de la campagne SAMURAI comissioning et DayOne, aussi réalisées à RIKEN.

Production du faisceau

Pour atteindre des noyaux riches en neutrons très éloignés de la stabilité ($N/Z \gg 1$) des faisceaux d'isotopes radioactifs (RI) intenses doivent être utilisés. La technique la plus appropriée pour générer ce type de faisceaux est la **fragmentation en vol** : le faisceau RI de haute intensité est produit par la fragmentation en vol d'un faisceau primaire d'ions lourds stable, préalablement accéléré. Le faisceau secondaire résultant de la fragmentation est ensuite dirigé vers une cible secondaire où des isotopes très riche en neutrons peuvent

être peuplés. Au RIBF, le séparateur BigRIPS [49] est spécialement conçu pour la production de faisceaux RI très intenses en utilisant cette technique. Dans ce cas, la cible de production est située au début du séparateur.

Les faisceaux RI produits par la technique en vol sont communément appelés faisceaux **cocktail**, car ce type de collisions d'ions lourds à haute énergie génèrent une grande variété de noyaux. Comme la quantité d'espèces générées est importante, la sélection des espèces de faisceaux secondaires devient une partie essentielle. Cette sélection se fait en vol dans la première partie du séparateur (F0-F2). Considérant que la trajectoire d'une particule dans un champ magnétique constant dépend de sa charge, de sa masse et de sa vitesse, les noyaux peuvent être séparés selon leur A/Z. Le champ magnétique le long de la ligne de faisceau est ainsi ajusté pour contrôler le mouvement des particules et purifier le faisceau. Dans la deuxième partie du détecteur le faisceau est transporté et les différents espèces composant le faisceaux identifiés événement par événement à l'aide de détecteurs situés dans les plans focaux qui mesurent leur perte d'énergie (ΔE), temps de vol (ToF) et position (x,y). À continuation, le séparateur BigRips est suivi d'une ligne de transport qui conduit le faisceau vers la salle d'expérimentation SAMURAI, à partir de F13. En fonction des exigences expérimentales, les réglages dans l'optique des lignes de faisceaux peuvent être ajustés pour obtenir les caractéristiques souhaitées.

Dispositif expérimental SAMURAI

SAMURAI signifie "**S**superconducting **A**analyser for **MU**lti-particle from **RA**dio **I**sotope beam" [51] et il est spécialement conçu pour détecter plusieurs particules en coïncidence dans des mesures cinématique complètes. La configuration SAMURAI standard se compose d'un grand nombre de détecteurs qui incluent les suivantes détecteurs :

- Aiment super-conducteur SAMURAI

  L'aimant SAMURAI est un dipôle de type H avec un pôle cylindrique de 2 m de diamètre. Si le système non lié produit lors de la réaction a une structure de type fragment+n+n, comme dans le cas de ^{16}Be, les deux neutrons seront émis vers l'avant tandis que la trajectoire du fragment lourd sera courbée par l'aimant SAMURAI selon ses propriétés de masse, de charge et de quantité de mouvement décrites par B_ρ. L'aimant SAMURAI permet ainsi la séparation de fragments lourds produits dans la cible, ce qui permet, en association avec les autres détecteurs SAMURAI, l'identification et la cinématique complète de tous les produits de désintégration.

- Les chambres à dérive BDC1, BDC2, FDC1 et FDC2

  La position du faisceau entrant est déterminé à l'aide de deux chambres de dérive identiques appelées BDC1 et BDC2 (**B**eam **D**rift **C**hamber). Ces deux détecteurs sont séparés de 1 m et elles sont situés entre le *beam trigger* (SBT) et la cible. En combinant la position mesurée par les deux chambres de dérive, les trajectoires des isotopes incidents sont déterminées événement par événement.

  De la même manière, la position du faisceau sortant est mesurée en utilisant deux chambres de dérive appelées **F**orward **D**rift **C**hambers (FDC), et elles sont positionnées à l'entrée et à la sortie de l'aimant de la SAMURAI. A partir de la trajectoire reconstruite entre les deux détecteurs, la rigidité magnétique B_ρ nécessaire pour la reconstruction du moment des fragments peut être calculée.

- Détecteurs HODOSCOPEs

  Deux hodoscopes scintillateurs conventionnels (HODOF et HODOP) sont placés après la FDC2 afin de mesurer le temps de vol (ToF) et la charge des fragments. L'utilisation de deux hodoscopes permet la détection d'un plus grand nombre de particules comprises dans une large gamme de masse et de charge. En combinaison avec la position donnée par la FDC2, les particules chargées sont identifiées.

- Détecteur de neutrons NEBULA

  NEBULA signifie "**NE**utron-detection system for **B**reakup of **U**nstable-Nuclei with **L**arge **A**cceptance"[54]. Le détecteur est conçu pour mesurer des neutrons rapides à des énergies de plusieurs centaines de MeV avec une large acceptance. NEBULA est placé à environ 11m de la cible après l'aiment SAMURAI. Contrairement aux particules chargées, les neutrons émis par la cible traverseront directement SAMURAI sans se dévier. Les neutrons ne sentant pas le champ magnétique, ce qui rend possible la reconstruction de la quantité de mouvement directement à partir du ToF mesuré entre la cible et la position de détection dans NEBULA.

  Un problème important concernant la détection de neutrons est leur identification :

  i) Les particules chargées peuvent être identifiées erronément comme des neutrons, puisqu'elles peuvent interagir dans NEBULA. Pour éviter toute erreur d'identification de particules chargées en tant que neutrons, des détecteurs de particules chargées (VETO) sont placés devant chaque mur de NEBULA.

  ii) Un neutron peut générer plusieurs signaux qui peuvent être interprétés comme des événements neutron multiples, un phénomène appelé **diaphonie**. L'identification du nombre de neutrons réels est essentielle pour l'étude des canaux dans lesquels on attend plus d'un neutron à l'état final, ce qui rend nécessaire le développement d'un algorithme d'analyse capable de rejeter la diaphonie.

D'autres peuvent être ajoutées en fonction des spécifications de l'expérience. Pour la campagne s018, notamment destinée aux réactions quasi libres (*p*,*pn*) sur une cible de protons (MINOS), un détecteur de neutrons supplémentaire (WINDS) et deux détecteurs de protons (RPD, RPTOF) ont été ajoutés au dispositif standard.

- Cible active MINOS

  MINOS (**M**ag**I**c **N**umbers **O**ff **S**tability)[52] est la cible de réaction utilisée dans l'expérience, spécialement conçu pour des réactions de knock-out induites par protons. Elle est composé d'une cellule d'hydrogène liquide de 15 cm d'épaisseur, couplée à une TPC (**T**ime **P**rojection **C**) de 30 cm. La TPC est utilisé en tant que *vertex tracker* : les trajectoires des protons émis dans le TPC sont reconstruites en trois dimensions, à partir desquelles le point d'interaction dans la cible peut être déterminé. La détermination du point de réaction dans MINOS nous donne la possibilité de calculer plus précisément la perte d'énergie des produits de réaction sortants ou des particules entrantes du faisceau. Cela permet d'utiliser des cibles plus épaisses, non seulement sans dégrader la résolution en énergie, mais même en l'améliorant tout en augmentant considérablement les statistiques, ce qui est particulièrement utile dans les réactions où des isotopes rares sont étudiés.

C.3 Techniques d'analyse et simulations

Le dispositif SAMURAI a une configuration de multidétecteurs complexe pour laquelle de nombreux étalonnages doivent être effectués afin de convertir et de rendre "lisibles" les données brutes. La reconstruction d'observables physiques, tels que le moment des particules, combine données de détecteurs individuels ou, ultérieurement, de groupes de détecteurs. Par conséquent, la résolution globale est une convolution des résolutions de détecteurs individuels en amplitude, temps, position, *etc.* À cet égard, les simulations constituent une partie essentielle de l'analyse car elles permettent de déduire les résolutions globales et les réponses des détecteurs, mais aussi interpréter physiquement les spectres. Afin de rendre les simulations parfaitement comparables aux données expérimentales, toutes les deux sont analysées de façon identique.

Reconstruction d'observables physiques

Afin de reconstruire l'énergie relative des systèmes non liés produits dans la cible, il faut déterminer la quantité de mouvement des produits de désintégration. Une identification précise du fragment et des neutrons est essentielle pour rejeter les événements parasites et obtenir un spectre propre.

- **Sélection dans la cible :** La reconstruction du vertex de la réaction dans MINOS est un aspect important de l'analyse qui permet de calculer avec précision la perte d'énergie des particules chargées. Seuls les événements pour lesquels la distance minimale D_{min} entre les trajectoires reconstruites dans la TPC est inférieure à 5 mm sont sélectionnés. De la même façon, les événements pour lesquels le vertex reconstruit est en dehors de la cellule cible cylindrique de MINOS sont également rejetés : Z_{vertex} est sélectionné de 0 à 150 mm tandis que le rayon sélectionné dans le plan XY est égal à $R(X,Y) = \sqrt{X^2_{\mathrm{vertex}} + Y^2_{\mathrm{vertex}}} < 19$ mm.
- **Sélection dans NEBULA :** Le détecteur de neutrons est non seulement sensibles aux neutrons mais également à d'autres particules telles que les raies γ. Pour les éliminer, nous appliquons un seuil de $L > 6$ MeVee en combinaison avec une limite inférieure de ToF > 44 ns, nous pouvons sélectionner environ 90 % de neutrons en éliminant environ 80% des raies γ.
- **Sélection de fragments** : Pour assurer une bonne reconstruction de la position du fragment, si les positions X_{FDC2}, Y_{FDC2} reconstruites sont hors des dimensions du FDC2 ($|Y| > 200$ mm et $|X| > 1000$ mm) l'événement est rejeté. De plus, seuls les événements présentant une corrélation linéaire entre FDC2 et HODOSCOPE sont sélectionnés.

Reconstruction du B_ρ du fragment

L'aimant SAMURAI courbe la trajectoire des ions en les séparant isotopiquement en fonction de leur $B\rho$. La trajectoire dépend de nombreux facteurs tels que la vitesse initiale à l'entrée de l'aimant ou la charge et la masse des isotopes. Comme aucun de ces facteurs ne peut être mesuré directement dans notre expérience, la reconstruction de $B\rho$ est réalisée au moyen de simulations basées sur Geant4[58]. Les simulations prennent en

compte les conditions expérimentales de l'expérience, y compris la distribution du champ magnétique dans SAMURAI et les dimensions et positions des différents détecteurs dans la salle d'expérimentation. Les paramètres d'entrée de la simulation sont les positions X et Y des FDC et les angles d'incidence de la particule. A partir de cette simulation, $B\rho$ est donné comme valeur de sortie. La quantité de mouvement est alors calculée comme $P_f = QB\rho$.

Alignement fragment-neutron

Étant donné que différents détecteurs sont utilisés pour reconstituer les impulsions du fragment et les impulsions des neutrons, il est nécessaire d'aligner complètement la configuration des multidétecteurs sur une référence commune. Cette référence est choisie comme étant la quantité de mouvement des neutrons, car elle est déterminée sans ambiguïté à partir du temps de vol. L'alignement est effectué en utilisant un neutron, le plus rapide, et le fragment chargé. Le but est de trouver un décalage moyen potentiel pour la vitesse du fragment, tel que $\beta_f = \beta_f + \Delta\beta_f$, pour lequel $\langle\beta_f\rangle = \langle\beta_n\rangle$.

Méthode de la masse invariante

Aux énergies du faisceau de l'expérience, ~ 250 MeV / nucléon, l'énergie et les moments doivent être exprimés en termes de relativité restreinte. En effet, la masse invariante est l'énergie relativiste totale du système reconstruite à partir des 4 impulsions mesurés de tous les produits de désintégration dans n'importe quel cadre de référence. Elle est déterminée par l'équation :

$$M_{inv} = \sqrt{\left(\sum_{i=1}^{N} E_i\right)^2 - \left(\sum_{i=1}^{N} \vec{p}_i\right)^2} \tag{C.1}$$

L'énergie relative E_{rel} est définie comme la différence de la masse invariante du système et de toutes les masses restantes m_i des produits de désintégration,

$$E_{rel} = M_{inv} - \sum_{i=1}^{N} m_i \tag{C.2}$$

Simulations Monte-Carlo

Le spectre d'énergie relative reconstruit est décrit en utilisant de simulations **M**onte-**C**arlo (MC) qui prennent en compte la réponse des détecteurs ainsi que les paramètres caractérisant les mécanismes de résonance et de désintégration du systèmes non liés. Les résultats de toutes les expériences des campagnes incluses dans ce travail (s018, commissioning, DayOne) ont été analysés avec la simulation MANGA. Cette simulation a été développé pour la description des états non liés se désintégrant via l'émission d'un ou de plusieurs neutrons, tels que $^{A+2}\mathrm{X}\rightarrow{}^{A}\mathrm{X}+n+n$, dans des expériences utilisant le dispositif SAMURAI.

Caractérisation du dispositif expérimental

La configuration et le canal de réaction sont caractérisés par une série de paramètres dans la simulation.

- **Faisceau** : Le faisceau est caractérisé par une distribution uniforme d'énergie. La moyenne de cette distribution et sa largeur, déterminé par les valeurs couverte par β, doivent être définis pour chaque réaction.
- **Cible :** En raison des multiples processus microscopiques rencontrés lors de la traversée de la cible, la distribution en énergie des particules est élargie et la trajectoire légèrement déviée, des effets étant appelés *straggling* en énergie et angulaire, respectivement. Celles-ci sont simulées à l'aide du logiciel LISE ++ basés sur l'énergie initiale et l'épaisseur traversée par une particule chargée ayant des nombres définis de Z et A.
- **Réaction :** Dans la simulation, le fragment et les neutrons sont générés au repos. Cependant, expérimentalement une réaction de knock-out, telle qu'utilisée dans nos expériences, communique une impulsion au système. Cette contribution à la quantité de mouvement totale est caractérisée par une distribution gaussienne dans les directions longitudinale et transversale. La largeur de cette distribution est déterminée à partir de la distribution de la quantité de mouvement expérimentale.

Résolution globale de SAMURAI

En tenant compte de la résolution angulaire et en moment du fragment, ainsi que de la résolution temporelle et de la position de NEBULA, la résolution totale de la configuration peut être estimée. La méthode consiste à simuler des états à un E_{rel} donné qui sont convolués avec les résolutions de SAMURAI. La résolution se dégrade à mesure que nous passons à des valeurs d'énergie relative plus élevées. L'évolution de la résolution pour la campagne s018 en ce qui concerne l'énergie relative peut être décrite approximativement par l'expression suivante : $\mathrm{FWHM} = 0.48 \times E_{rel}^{0.56}$ MeV. Les paramètres sont le résultat d'un fit.

Efficacité de détection de neutrons

Deux facteurs principaux dans le détecteur contribuent à l'efficacité des neutrons, à savoir, l'acceptation géométrique et la probabilité d'interaction. Le premier fait référence à la probabilité qu'un neutron entre dans NEBULA. Le dernier, la probabilité d'interaction à l'intérieur du détecteur. À faibles énergies relatives, l'efficacité géométrique est proche de 100%. La probabilité d'interaction dans une barre de NEBULA avec une épaisseur de $\sim$ 48 cm réduite l'efficacité de 100% à une valeur maximale de $\sim$ 35% pour la détection d'un neutron. Au fur et à mesure que les neutrons deviennent plus énergétiques, leurs trajectoires s'écartent davantage de l'axe du faisceau. Dans un tel cas, leurs trajectoires peuvent s'échapper de la zone couverte par le détecteur, d'abord dans la direction verticale, puis dans les deux directions verticale et horizontale, et par conséquence, l'efficacité est est réduite.

L'efficacité de détection de $2n$ est considérablement réduite lorsque le filtre de diaphonie est appliqué. En particulier, les événements avec une énergie relative très faible $E_{rel} <$

0.5 MeV sont davantage affectés par l'algorithme. À ces énergies, l'angle d'émission des deux neutrons est très petit, ce qui les rend détectables dans les barres de NEBULA presque voisines, et donc difficiles à distinguer par le filtre. Alors que l'efficacité de 1 n varie de 35% à 10%, l'efficacité de la détection de $2n$ correspond à une moyenne de $\sim 7\%$ entre 0 et 5 MeV lorsque le filtre de diaphonie est appliqué.

Corrélations à trois corps

Des expériences en cinématique complète permettent d'étudier la rupture de systèmes à trois corps à partir des corrélations entre particules des événements en triple coïncidence (fragment+n+n). Les corrélations les plus fondamentales sont celles imposées par la conservation de l'énergie et de la quantité de mouvement donnée par le N-corps *espace de phase*[60] de la décroissance, ce qui définira notre ligne de base. L'interaction entre les particules peut donner lieu à des corrélations «physiques» qui s'ajoutent à cette ligne de base. Pour identifier les corrélations émergeant de l'interaction des particules, nous utilisons les *Dalitz plots* [61], qui se manifestent comme des structures très caractéristiques.

Le diagramme de Dalitz peut être obtenu à partir des énergies relatives réduites, en représentant l'énergie réduite fragments-neutron, $\varepsilon_{fn} = E_{fn}/E_{rel}$, en fonction de l'énergie réduite neutron-neutron, $\varepsilon_{nn} = E_{nn}/E_{rel}$. Ces variables sont normalisées et vont de 0 à 1, ce qui est l'un des principaux avantages de cette méthode [63].

Dans notre cas, nous nous intéressons aux désintégrations de résonances f+n+n qui peuvent suivre une phase de phase à trois corps via une émission simultanée de $2n$ ou une espace de phase à deux corps si la désintégration est séquentielle. En fonction de la nature du mécanisme, l'espace de phase à considérer comme base de référence est différent. Ceci est d'autant plus important puisque les corrélations physiques sont identifiées par comparaison avec les corrélations de la ligne de base issues de la cinématique de l'espace de phase.

Espace de phase à trois corps. En l'absence de toute interaction, une décroissance directe d'une résonance f+n+n suit un espace de phase à trois corps qui conduit à une population uniforme du plot de Dalitz : plate avec aucune structure. Toute corrélation provenant de l'interaction des particules sera facilement repérable sur cette ligne de base plate. Pour analyser les corrélations de manière plus quantitative, nous pouvons projeter la distribution de Dalitz sur les axes x et y pour obtenir les distributions ε_{fn} et ε_{nn}. Ces projections présentent une forme de cloche pour les deux distributions correspondantes. L'espace de phase disponible est plus grand au centre du "cylindre", alors qu'il diminue considérablement aux limites, car il est peu probable que deux particules partent dans la même direction ($\varepsilon_{ij} = 0$) ou pour l'autre particule de rester au repos pendant que les autres deux transportent toute l'énergie de désintégration ($\varepsilon_{ij} = 1$).

C.4 Résultats : Spectroscopie

Béryllium-14

Les états excités de ^{14}Be ont été peuplés par diffusion inélastique sur une cible de carbone, de la même manière que pour Ref. [6], pendant la campagne expérimentale SAMU-

RAI comissioning. Le spectre d'énergie relative est reconstruit à partir des particules ^{12}Be+n+n détectées en coïncidence. Une structure principale peut être clairement observée et identifiée comme le premier état excité 2^+ de ^{14}Be. Au-delà de ce pic, aucune autre structure n'est notable et, par conséquent, une contribution non résonante doit être prise en compte. L'état 2^+ du ^{14}Be est également un point de repère pour la détection $2n$: la non-application du filtre de diaphonie masque le très étroit pic à 0,25 MeV.

L'énergie de l'état de 2^+ en termes d'énergie relative est trouvée à E_{rel}=254(6) keV et Γ=40(20) keV. Puisque l'énergie de séparation des deux neutrons est mesurée à 1.27(13)[44], l'énergie d'excitation obtenue correspond à E_x=E_{rel} + S_{2n} = 1.52(13) MeV, cohérent avec la valeur précédente de E_x = 1.55(13) MeV. La différence en énergie relative par rapport au travail précédent (E_{rel} = 280 keV) ne provient pas des résultats expérimentaux eux-mêmes, mais du choix de la composante non résonante, dont la contribution dans la zone de la le pic dans notre cas est minimum et permet au fit d'aller aux énergies inférieures.

^{14}Be est un candidat intéressant pour l'étude des corrélations core-n-n de la décroissance de son état 2^+. *A priori*, le plot expérimental de Dalitz ne montre aucune structure significative et, à part quelques petites fluctuations, semble compatible avec l'uniformité attendue d'une décroissance directe sans interaction nn. Aucune augmentation notable vers ε_{nn} = 0 ni aucune autre structure dans ε_{fn} indiquant des traces de séquentialité n'apparaissent dans le plot. Le simulations d'un espace de phase à trois corps semblent être suffisant pour reproduire les données expérimentales. Également, la projection expérimentale ε_{fn} suit une cinématique à trois corps selon laquelle la décroissance peut être considérée comme exclusivement directe. La fonction de corrélation C_{fn} entre données et simulation montrant une distribution plate confirme ce scénario.

On pourrait s'attendre à ce que l'émission simultanée de $2n$ génère une très forte corrélation nn à partir de l'interaction entre les deux neutrons. Au contraire, l'absence de signal nn aux basses énergies est évident dans la projection expérimentale ε_{nn}. Ici, l'écart par rapport à la forme habituelle d'une distribution ε_{nn} correspondante à une désintégration à trois corps sans interaction est expliqué comme le résultat de l'algorithme de rejet de diaphonie, qui rejette de préférence les paires à faible énergie relative nn, un effet particulièrement important pour des résonances aussi proches du seuil comme celui-ci de ^{14}Be(2^+). Notez que puisque le filtre est appliqué aux données expérimentales et simulées, cet effet est correctement décrit.

Béryllium-15

L'objectif principal de ce travail de thèse est d'étudier la décroissance à trois corps de ^{16}Be. Cependant, que la décroissance soit directe ou séquentielle dépend fortement de l'énergie de l'état fondamental de ^{15}Be et de sa position par rapport aux états de ^{16}Be. Afin de bien comprendre la désintégration $2n$ de ^{16}Be, nous avons mené une étude sur la spectroscopie de ^{15}Be à partir d'un large éventail d'expériences ayant eu lieu au cours de la campagne expérimentale DayOne à RIKEN. Les états potentiels dans ^{15}Be sont détectés via réactions knock-out à partir de différents faisceaux pour lesquels nous sélectionnons en sortie ^{14}Be+ n en coïncidence.

La contribution de la décroissance des deux états de ^{16}Be est évidente, avec des poids variables, dans toutes les voies de DayOne, ce qui indique qu'au moins une partie des

événements ^{14}Be+n ne forme pas ^{15}Be mais sont le résultat du peuplement de ^{16}Be. Les énergies considérées pour la contribution des états de ^{16}Be ont été extraites du fit de ^{16}Be dans l'expérience s018 dont nous parlerons plus tard. La contribution non résonante est calculée selon la technique de mélange d'événements, séparément pour chaque voie de réaction. Les proportions de ces trois composantes sont les paramètres libres que nous varions pour la description du spectre à cette première étape. Afin de révéler les résonances dans ^{15}Be, nous définissons le rapport C_{fn} entre les données et ces trois contributions identifiés non liés à la population de résonances ^{15}Be. Ce rapport mettra en évidence les structures du spectre pouvant nécessiter des états dans ^{15}Be.

Bien que la description des spectres ne soit pas tout à fait précise, leurs rapports ne montrent aucune structure claire pouvant être liée à un état dans ^{15}Be pour les voies des faisceaux ^{17,19}B et ^{22}N. D'autre part, les voies de réaction ^{18,19,20}C montrent une structure autour de 1.8 MeV qui ne peut pas être entièrement expliquée par la décroissance de ^{16}Be ni la contribution non corrélée. Dans le cas particulier de ^{20}C, nous pouvons également observer une autre structure étroite à plus basse énergie, à environ 0 ∼0,4 MeV. Pour ces trois voies, un fit a été effectué en considérant une résonance dans ^{15}Be, ou deux dans le cas du faisceau de ^{20}C, en plus des structures issues de la désintégration de ^{16}Be (à énergie et largeur fixes) et de la contribution non résonante.

Le meilleur ajustement aux données montre que pour ^{18,19}C ajustements donnent des résultats similaires pour la résonance potentielle de ^{15}Be à environ ∼2 MeV : *i)* $E = 1.80\pm$ 0.10 MeV et *ii)* $E = 1.80\pm0.06$ MeV, respectivement, et dans les deux cas avec une largeur de $\Gamma = 1$ MeV. Deux fits différents pour ^{20}C sont effectués. Le premier, avec une seule résonance autour de 2 MeV donne une valeur pour la résonance de ^{15}Be de 1.90 ± 0.12 MeV, proche des deux autres résultats obtenus. Pour le deuxième fit, nous avons inclus une résonance à basse énergie. Ce dernier donne deux résonances pour ^{15}Be avec les suivantes énergies : 0.4 ± 0.1 MeV et 1.9 ± 0.1 MeV. Cependant, une telle résonance à aussi faible énergie n'est pas prédite par la théorie et la structure étroite à basse énergie observée a peu de signification statistique. Toute revendication d'un nouvel état dans ^{15}Be doit donc être prise avec précaution. L'observation d'une structure autour de 1.8 MeV dans ces trois spectres indique que nous sommes probablement en train de peupler un état dans ^{15}Be. Cela confirmerait le seul état observé à ce jour de ^{15}Be, également mesuré à la même énergie et identifié avec un spin et une parité de $5/2^+$.

Béryllium-16

L'isotope non lié ^{16}Be a été peuplé à l'aide d'une réaction knock-out proton à partir d'un faisceau de ^{17}B pendant la campagne expérimentale s018 à RIKEN. Le spectre d'énergie relative est reconstruit par masse invariante à partir des événements ^{14}Be+n+n coïncidents. En comparaison avec la campagne DayOne, les structures du spectre de DayOne peuvent être à peine distinguées alors que deux pics différenciés peuvent être facilement observés dans le spectre de la campagne s018. Cette amélioration peut s'expliquer par l'utilisation de :

- MINOS, qui permet la reconstruction précise de la position du vertex de la réaction et, par conséquent, la correction exacte de la perte d'énergie du fragment qui améliore considérablement la résolution. Cela permet d'utiliser une cible plus épaisse, 150 mm, ce qui augmente considérablement les statistiques.

- une logique de déclenchement spécialement pensée pour les réactions knock-out, qui prend en compte uniquement les réactions d'éjection d'un proton, diminuant le bruit de fond provenant d'autres réactions.

Nous pouvons identifier ces deux structures qui sont présents dans les 5 premiers MeV du spectre comme l'état fondamental et premier état excité du ^{16}Be. Suivant les prédictions du modèle en couches [4], le spin et la parité de deux états 0^+ et de 2^+, respectivement. Le spectre expérimental d'énergie relative a été ajusté entre 0 et 4 MeV avec une Breit-Wigner avec une largeur dépendante de l'énergie pour les deux états, où l'énergie, la largeur et la normalisation sont des paramètres libres. Un composant non résonant n'est pas nécessaire pour la description des données inférieures à 4 MeV. En fait, lorsque cela est autorisé pour le fit, ce composant est mis à zéro. La meilleure description du spectre est obtenue pour E_{0^+}=0.84±0.03 MeV et $E_{2^+} = 2.15 \pm 0.05$ MeV, et une largeur respective de $\Gamma_{0^+} = 0.32 \pm 0.08$ MeV et $\Gamma_{2^+} = 0.95 \pm 0.15$ MeV.

Le type de désintégration des états de ^{16}Be peut être évalué à partir de l'étude des corrélations entre les particules de désintégration. Suite à la même analyse que pour ^{14}Be, les distributions d'énergie relative fn et nn pour les deux états observés dans ^{16}Be ont été comparées aux simulations Monte-Carlo pour une désintégration directe à trois corps sans interaction entre les deux neutrons. Les diagrammes de Dalitz illustrent clairement qu'il y a une forte signal à basse énergie pour ε_{nn} alors qu'aucune preuve de décroissance séquentielle dans l'axe fn n'est observée *a priori*. La comparaison avec des simulations de désintégration à trois corps montre dans les deux cas un désaccord important avec les données expérimentales, ce qui indique qu'une hypothèse plus complexe doit être prise en compte pour décrire les données expérimentales, notamment, l'inclusion de l'interaction entre les deux neutrons.

Les projections ε_{nn} et ε_{fn} des plot de Dalitz montrent, contrairement au ^{14}Be, qu'un espace de phase pur à trois corps n'est cohérent avec aucune des projections expérimentales ε_{nn}. Les signaux observées en nn à basse énergie indiquent une forte corrélation entre les deux neutrons, qui est généralement interprétée comme une caractéristique de l'interaction dans l'état finale. Ce type d'amélioration est une caractéristique distinctive observée dans de nombreux états finaux où l'émission de deux neutrons est impliquée. Par conséquent, si nous voulons décrire au moins qualitativement les données expérimentales, nous devons considérer une source de corrélations nn.

En revanche, les distributions ε_{fn} montrent un bon accord avec les simulations d'une décroissance directe à trois corps. L'hypothèse d'une émission spontanée de deux neutrons dans l'état fondamental de ^{14}Be semble être le principal mode de désintégration. Compte tenu du bon accord, il n'est pas nécessaire de supposer une quelconque contribution de la désintégration séquentielle via un état intermédiaire dans ^{15}Be pour reproduire les données expérimentales. Pour l'état fondamental de ^{16}Be, aucun état dans ^{15}Be inférieur à 0,84 MeV n'a été ni prédit ni observé expérimentalement. Cependant, ce n'est pas le cas pour l'état 2^+ puisqu'un état dans ^{15}Be a été observé en dessous de 2.15 MeV, ce qui, en principe, pourrait permettre une décroissance séquentielle. Dans le seul but de vérifier la compatibilité d'une désintégration séquentielle, nous avons étudié les corrélations d'énergie relative fn permettant une désintégration directe et séquentielle dans un état dans ^{15}Be à 1.8 MeV. Cet ajustement montre que la composante directe est dominante, avec plus de 98 %. Cela indique que la désintégration de 2^+ à travers l'état intermédiaire

observé dans ^{15}Be à 1.8 MeV n'est pas favorisée.

C.5 Interprétation : corrélations nn

Le signal de faible énergie dans l'énergie relative nn a été largement observé dans les désintégrations de noyaux exotiques légers (voir, par exemple, [37, 63, 66, 67]). Les corrélations fortes nn sont généralement interprétées comme le résultat de l'interaction des neutrons émis dans l'état final. Une approche phénoménologique décrivant cette interaction d'état final (FSI) peut suffire à reproduire ces signaux de corrélation. De tels modèles simples ne peuvent toutefois pas envisager la connexion des corrélations avec la structure du système. Ce que ces corrélations peuvent révéler sur le mécanisme de désintégration ou la configuration des neutrons dans l'état initial nécessite un formalisme capable de décrire l'émission de deux neutrons à partir de principes microscopiques.

Modèle phénoménologique

Le signal de corrélation nn à basse énergie se caractérise par un comportement de type exponentiel proche de zéro en énergie relative ou impulsion lorsque l'on regarde sa fonction de corrélation C_{nn} = data/PS. Ce comportement exponentiel est très similaire à celui d'un état virtuel [18]. En conséquence, le signal de basse énergie peut être très bien reproduit par une interaction d'onde-s pour nn. L'approche **FSI** décrite dans [19] tient compte de la distance entre les neutrons comme ayant un effet sur leur interaction. Dans ce modèle, la longueur de diffusion a_s est fixe et c'est σ_{fsi} qui est varié pour reproduire les faibles énergies nn. Par conséquent, la FSI de nn dépend non seulement de l'amplitude de diffusion des ondes-s de l'interaction nn, mais également de la taille de la source, introduite dans le modèle via le paramètre σ_{fsi}.

Cependant, ce modèle, bien qu'il ait décrit avec précision les distributions expérimentales observés lors de travaux antérieurs [37, 38, 63, 66, 67], ne prend pas en compte la structure interne du système d'origine. Au lieu de cela, ce formalisme est développé pour une source de neutrons *gaussienne* émettant des neutrons *indépendants*. Certes, considérer que la fonction d'onde du système à trois corps est gaussienne est de loin une approximation très simple. D'autre part, le fait que les deux neutrons se déplacent indépendamment à l'intérieur de la source est également irréaliste dans la mesure où cela implique de négliger les corrélations de moment internes des deux neutrons. Malgré toutes ces simplifications, cette approche semble pouvoir reproduire les fonctions caractéristiques C_{nn}, même pour des systèmes non gaussiens, et offre en outre un scénario possible pour son interprétation. Le seul paramètre libre du modèle, la distance relative entre les neutrons σ_{fsi}, doit être considéré soit comme une entrée mathématique, avec la seule utilisation de reproduire les données, soit comme caractéristique physique du système.

Application aux données expérimentales

- *Béryllium-16* : Le plot de Dalitz obtenu pour le meilleur ajustement de σ_{fsi} de deux états du ^{16}Be s'avère bien concorder avec les données expérimentales dans les deux cas. Les valeurs de σ_{fsi} correspondant au meilleur ajustement sont 2.4(4) fm et 1.5(2) fm pour l'état fondamental et le premier état excité, respectivement. Si nous projetons maintenant sur l'axe nn, nous pouvons obtenir l'énergie relative nn

et sa fonction de corrélation. Ici, nous pouvons remarquer que les signaux de basse énergie sont raisonnablement bien reproduits avec ce modèle. Cela entraînerait des distances nn en rms de $\sim 6\ fm$ et $\sim 4\ fm$ pour les valeurs respectives de σ_{fsi}.

- *Béryllium-14* : Contrairement à ^{16}Be, la distribution d'énergie relative nn suit un espace de phase à trois corps sans avoir besoin d'inclure des effets FSI. Dans ce contexte, ce formalisme, bien que non essentiel dans la description des données expérimentales, permet d'approfondir l'origine de l'absence de corrélations nn. Premièrement, l'énergie de désintégration est très faible, E_{2^+}=254 keV. Avec des énergies aussi faibles, l'algorithme de rejet de diaphonie est particulièrement fort et coupe une partie importante de l'énergie relative basse de nn. Étant donné que la simulation et les données expérimentales font l'objet de la même analyse de diaphonie, l'inclusion de la FSI peut déterminer si l'absence de corrélations nn de la FSI est une conséquence du filtre de diaphonie. Pour ce faire, nous avons simulé plusieurs signaux FSI plus ou moins forts pour vérifier les effets du rejet de la diaphonie sur eux. Nous observons que le signal de basse énergie est capable de surmonter le rejet de diaphonie et, bien que certainement supprimé, est présent pour des valeurs de σ_{fsi} $\leq$9 fm. Cela nous laisse supposer que si les deux neutrons étaient très fortement corrélés dans ^{14}Be, la corrélation survivrait aux conditions expérimentales et aux filtres. Par conséquent, l'absence de corrélations observée devrait provenir des propriétés intrinsèques du système et/ou du mécanisme de désintégration.

Calculs théoriques à trois corps

Nous avons vu qu'un modèle "sans structure" est capable de reproduire les signaux de corrélation à basse énergie observés dans les distributions expérimentales nn. Cependant, un tel modèle n'illustre pas le scénario réaliste d'une désintégration d'un noyau à quelques corps, un système qui a une structure et une géométrie définies, difficilement comparables à une source gaussienne. Les méthodes théoriques explorant la structure des résonances à trois corps et les distributions d'énergie liées à leurs désintégrations à $2n$ sont encore très peu nombreuses car leur caractérisation n'est pas triviale, puisqu'elles nécessitent la solution d'un problème à trois corps dans le continuum. De plus, les difficultés d'accès expérimental à des émetteurs $2n$ n'offrent que quelques candidats pour tester la fiabilité des calculs.

Fonction d'onde à trois corps

Le modèle microscopique développé par Casal et Gómez-Camacho [20, 73] a pour objectif principal la description du continuum à 3 corps ainsi que l'identification et la caractérisation d'états dans le continuum associés aux résonances qui peuvent être décrites de la forme fragment+n+n. À cette fin, le hamiltonien est diagonalisé dans une base discrète de pseudoétats construits dans le formalisme des harmoniques hypersphériques. Parmi le grand nombre d'états construits à partir de cette diagonalisation, les états dont les propriétés peuvent être liées aux résonances sont extraits.

Le point de départ du modèle est la diagonalisation de le hamiltonien à trois corps dans une base donnée, *i.e.*, Résolvant le problème des valeurs propres :

$$\mathcal{H}\,\psi_n^{j\mu} \;=\; \varepsilon_n\,\psi_n^{j\mu} \tag{C.3}$$

en utilisant le potentiel à trois corps suivant :

$$V^{j\mu}_{\beta'\beta} = \langle \mathcal{Y}^{j\mu}_{\beta}(\Omega)|V_{nn} + V_{fn_1} + V_{fn_2}|\mathcal{Y}^{j\mu}_{\beta'}(\Omega)\rangle + \delta_{\beta\beta'}V_{3b}(\rho) \tag{C.4}$$

où V_{nn} et V_{fn_i} sont les interactions de paires correspondantes, entre les neutrons et entre chacun des neutrons et le fragment, et le terme $V_{3b}(\rho)$ est un terme phénoménologique à trois corps. Ce dernier terme est ajouté car la description à trois corps avec uniquement des interactions binaires réalistes est insuffisante pour reproduire les spectres connus. L'énergie de l'état peut donc être ajustée à l'énergie expérimentale connue en modifiant les paramètres de cette force à trois corps. La diagonalisation de le hamiltonien permet d'obtenir un grand ensemble d'états. Pour caractériser les résonances parmi les états de continuum trouvés, un opérateur de résonance $\widehat{M} = \widehat{H}^{-1/2}\widehat{V}\widehat{H}^{-1/2}$ est utilisé. Cet opérateur est très sensible à l'interaction, une fonctionnalité qui permet de séparer les résonances du reste du spectre en diagonalisant $\widehat{M}$. Le lecteur devrait se référer à [20] pour plus de détails sur l'utilisation de cet opérateur.

Les corrélations spatiales de la résonance à trois corps sont révélées par sa probabilité de fonction d'onde, qui peut être calculée comme suit :

$$P(r_x, r_y) \;=\; r_x^2\, r_y^2 \int |\Psi(r_x, r_y)|^2 \, d\widehat{x}\, d\widehat{y} \tag{C.5}$$

État fondamental du Béryllium-16

Les corrélations spatiales montrent trois maxima bien définis. La configuration la plus probable se trouve lorsque les deux neutrons sont très proches l'un de l'autre, $r_x \sim 2$ fm, mais loin du coeur, $r_y \sim 3{,}5$ fm. Une telle configuration est généralement associée à une configuration "dineutron", alors que les deux autres plus petits pics concernent des configurations triangulaires et en forme de cigare, cette dernière correspondant au cas où les deux neutrons sont très éloignés l'un de l'autre, $r_x \sim$6 fm, mais très proche du coeur, $r_y \sim 1$ fm. La configuration en dineutron domine la fonction d'onde de l'état fondamental ^{16}Be.

La composante dineutron dominante de la fonction d'onde peut être expliquée par un effet de l'interaction nn. Cela peut être étudié en diagonalisant le hamiltonien sans le terme d'interaction nn du potentiel et en ajustant le terme à trois corps afin d'obtenir la même énergie ^{16}Be. Bien que totalement irréaliste, cela permet de tester directement comment l'interaction nn modifie la structure du système et sa relation avec les caractéristiques dineutron. La probabilité de l'état fondamental pour ce cas montre l'absence de dominance dineutron dans les corrélations spatiales. Nous pouvons en conclure que le fort caractère dineutron de ce modèle découle de l'interaction nn.

Distribution en énergie relative

Afin de mettre la théorie et l'expérience à égalité, nous devons transformer la fonction d'onde en une observable mesurable expérimentalement, étant donné que ni la fonction d'onde ni la distance entre les deux neutrons dans le système résonant d'origine ne peuvent être directement mesurées. L'énergie relative entre les particules de désintégration est

expérimentalement accessible. D'un point de vue théorique, la connexion entre la fonction d'onde et l'énergie relative *nn* n'est toutefois pas simple, car elle implique la description de l'évolution des corrélations $2n$ au cours du processus de désintégration. Pour cela, nous devons décrire l'évolution libre du système pendant la désintégration. Ceci peut être évalué en calculant le *probabilité de la courent j* de la fonction d'onde Ψ : ce courant montre comment les deux neutrons de valence évoluent dans un état initial donné.

La distribution théorique $\varepsilon_{nn} = E_{nn}/E_{rel}$ pour l'état fondamental de ^{16}Be obtenue montre un pic important aux basses énergies ε_{nn} ∼0.05, ce qui indique une très forte corrélation entre les deux neutrons de valence. Pour être directement comparables à l'expérience, les mêmes conditions expérimentales doivent être appliquées à l'énergie relative *nn*. En particulier, nous devons prendre en compte de *i)* la résolution angulaire et en énergie et l'acceptante du dispositif et *ii)* le filtre de diaphonie pour la fausse identification de neutrons, ce qu'il élimine egalement une grande partie des "vrais" $2n$ événements.

L'application de ces facteurs expérimentaux modifie considérablement la distribution théorique. Nous notons que la forte corrélation basse énergie que nous avions initialement dans la distribution théorique est réduite, principalement en raison du rejet de la diaphonie. La concordance avec les données est raisonnablement bonne, surtout si nous considérons que nous n'ajustons pas le spectre expérimental, mais nous ne faisons que comparer la théorie et l'expérience. Le fait que les deux distributions montrent des corrélations à basse énergie, bien que légèrement décalé, indique qu'une telle configuration pour ^{16}Be(0^+) pourrait représenter une image réaliste capable de décrire la structure de la résonance.

La distribution d'énergie relative *nn* résultant de la suppression de l'interaction *nn* est radicalement différente : le pic à basse énergie a complètement disparu. En fait, la forme de la distribution est maintenant centrée sur $\varepsilon_{nn} \sim 0.5$. Lorsque nous appliquons les conditions expérimentales, la forme est lissée et la partie basse énergie est encore plus supprimée.

C.6 Conclusion

Ce travail de thèse porte sur la structure des noyaux riches en neutrons situés au bord ou au-delà de la dripline neutron. En particulier, nous avons étudié les isotopes les plus lourds du béryllium : ^{14}Be, ^{15}Be et ^{16}Be. L'un des principaux sujets étudiés a été la désintégration à trois corps d'états non liés à deux neutrons, un phénomène qui peut être observé à la fois dans ^{14}Be et ^{16}Be.

Toutes les expériences présentées dans ce travail ont été réalisées au RIBF-RIKEN à l'aide du multidétecteur **SAMURAI** au cours de différentes campagnes expérimentales : SAMURAI comissioning, DayOne et s018. campagnes. Pour cette dernière, la cible MINOS a été ajoutée à la configuration standard du SAMURAI, qui inclut le détecteur de neutrons NEBULA, nous permettant d'améliorer qualitativement la résolution et les statistiques par rapport aux études précédentes.

Les états non liés des noyaux d'intérêt ont été peuplés à l'aide de réactions **knock-out**. Tous les états résonants étudiés se situent au-dessus du seuil d'émission de neutrons et se désintègrent par émission de neutrons. Nous avons utilisé la méthode de la masse invariante pour reconstruire l'énergie relative à partir de leurs produits de désintégration nécessitant

la détection en coïncidence du fragment et d'un ou plusieurs neutrons en vol, ainsi que la mesure de leur quantité de mouvement et de leur énergie. La détection plusieurs neutrons a été analysée avec succès au moyen d'algorithmes de rejet de la **diaphonie**.

La complexité de la configuration multidétecteurs a nécessité l'utilisation de simulations capables de prendre en compte les résolutions et acceptances expérimentales afin d'interpréter les données. Le spectre d'énergie relative a été analysé à l'aide de deux contributions principales : une composante non résonante représentant le continuum de ces états finaux, ainsi que des résonances d'énergie et de largeur différentes. La contribution non résonante a été générée soit par des simulations, soit avec la technique de mélange d'événements. La contribution de résonances a été caractérisée par des formes de lignes de Breit-Wigner avec des largeurs dépendantes de l'énergie.

Les **corrélations à trois corps** dans les désintégrations fragment+n+n ont été sondées à l'aide de la technique des plots de Dalitz. Afin de mieux comprendre la relation entre la structure interne du système et le rôle de l'interaction nn dans les corrélations finales observées, des calculs complets à trois corps ont été effectués. Une nouvelle méthode théorique a été développée pour calculer la distribution d'énergie relative nn à partir de la fonction d'onde à trois corps. Nous avons développé une technique permettant d'intégrer les conditions expérimentales dans les distributions théoriques et de rendre l'expérience et la théorie directement comparables.

Voici les principaux résultats de ce travail de thèse pour chacun des systèmes étudiés :

- **^{16}Be**

  Dans un travail précédent, un nouveau type de désintégration, une émission de dineutron, a été revendiqué dans ^{16}Be. Cependant, l'analyse des corrélations à trois corps qui ont conduit à cette conclusion n'incluait pas l'interaction d'état final nn et ne tenait compte que des considérations d'espace de phase. De plus, une structure identifiée comme état fondamental a été observée à une énergie et une largeur de E = 1.35 MeV et Γ = 0,85 MeV, respectivement. Les questions soulevées par la largeur de la résonance et le mode particulier de décroissance $2n$ ont motivé une nouvelle campagne expérimentale.

  spectroscopie. ^{16}Be a été peuplé lors de la campagne s018 à l'aide d'une réaction knock-out proton à partir d'un faisceau de ^{17}B, avec une grande résolution et acceptance. Le spectre d'énergie relative ^{14}Be+n+ n présentait deux structures claires :

  - une résonance basse énergie identifiée comme l'état fondamental de spin et de parité $J^\pi = 0^+$. L'énergie et la largeur sont respectivement égales à $E = 0.84(3)$ MeV et $\Gamma = 0.32(8)$ MeV.
  - un deuxième état de résonance identifié au premier état excité de spin et parité $J^\pi = 2^+$. L'énergie et la largeur sont respectivement $E = 2.15(5)$ MeV et $\Gamma = 0.95(15)$ MeV.

  Corrélations à trois corps. Les corrélations de la désintégration $2n$ de ^{16}Be ont été étudiées. L'analyse des distributions d'énergie relative fn et nn expérimentales et la comparaison avec un modèle théorique basé sur des principes microscopiques ont conduit aux conclusions suivantes:

- L'étude des corrélations expérimentales fn a montré que les états 0^+ et 2^+ de ^{16}Be ont une désintégration directe vers ^{14}Be par émission de deux neutrons simultanés.
- Les spectres d'énergie relative nn expérimentaux ont montré de fortes corrélations nn pour les deux états.
- Les calculs à trois corps prédisent une fonction d'onde pour l'état fondamental de ^{16}Be dominée par une configuration dineutron. Les distributions nn théoriques calculées à partir de cette fonction d'onde ont été capables, sans aucun paramètre d'ajustement, de reproduire les corrélations à faible énergie observé expérimentalement, ce qui a été démontré qu'il est lié à l'interaction nn.

- **^{15}Be**

  La structure de ^{15}Be est toujours inconnue. Seul un état identifié avec spin et parité $J^\pi = 5/2^+$ à une énergie $E = 1.8$ MeV a été observé. L'état fondamental $3/2^+$ prédit par la théorie n'a pas été observé. La position de l'état fondamental de ^{15}Be peut avoir une influence importante sur la décroissance de ^{16}Be.

  spectroscopie. ^{15}Be a été étudié à partir de différentes expériences réalisées lors de la campagne DayOne :

  - **(^{17}B,^{14}Be+n)**, **(^{19}B,^{14}Be+n)** et **(^{22}N,^{14}Be+n)** ne montrent aucune population claire de ^{15}Be. Leur spectre énergétique relatif peut être bien décrit par les contributions de la désintégration des deux états observés dans ^{16}Be plus la population directe du continuum ^{14}Be + n.
  - Un état de résonance à 1.8 MeV a été observé dans les réactions de **(^{18}C,^{14}Be+n)**, **(^{19}C,^{14}Be+n)** et **(^{20}C,^{14}Be+n)**. Dans ce dernier cas, une éventuelle résonance de basse énergie située à ~ 0.4 MeV pourrait correspondre à une autre résonance en ^{15}Be, bien que la signification statistique soit faible.

  Ces résultats semblent confirmer une résonance à 1.8 MeV identifiée à l'état $5/2^+$ dans les travaux précédents. La nature de cet état (J^π, état fondamental ou excité) n'est toujours pas résolue.

- **^{14}Be**

  L'état 2^+_1 de ^{14}Be est connu pour ne dépasser que 254 keV au-dessus du seuil d'émission à deux neutrons. Cependant, son émission $2n$ est supposée être directe vers ^{12}Be mais ni les corrélations à trois corps ni le mécanisme de désintégration n'ont jamais été formellement étudiés.

  Cet état a été peuplé en utilisant une réaction de diffusion inélastique d'un faisceau ^{14}Be. Les corrélations entre ses produits de désintégration ont fait l'objet de recherches approfondies. Notre étude conduit aux conclusions suivantes :

  - La désintégration suit un espace de phase à trois corps. Par conséquent, la désintégration de ^{14}Be peut être considérée comme directe via l'émission de deux neutrons simultanés.
  - La distribution d'énergie relative de nn ne montre aucune preuve d'interaction ou de corrélation nn.

Autres que tous les résultats spécifiques énumérés ci-dessus, le principal résultat de ces travaux est le pont qui a été prolongé entre les observations expérimentales d'observables $2n$ et la description microscopique de leurs fonctions d'onde initiales.Avec une modèle FSI basée sur la diffusion nn d'onde-s les distributions expérimentales peuvent être reproduites plus ou moins précisément. Cependant, il ne peut pas répondre à beaucoup de questions ouvertes. Un effort important conjoint entre nos approches expérimentales de pointe et le développement théorique de formalismes à trois corps a permis une première comparaison directe sur un pied d'égalité. La bonne description de la désintégration de l'état fondamental ^{16}Be(0^+) relie le signal expérimental nn observé à la composante de la fonction d'onde à trois corps dans laquelle les neutrons gravitent autour du noyau de ^{14}Be, la configuration dineutron.

Bibliography

[1] J. P. Delaroche, M. Girod, *et al.* "Structure of even-even nuclei using a mapped collective hamiltonian and the D1S Gogny interaction". *Phys. Rev. C*, **81**, 2010. https://link.aps.org/doi/10.1103/PhysRevC.81.014303.

[2] Y. Kondo, T. Nakamura, *et al.* "Nucleus ^{26}O: A barely unbound system beyond the Drip Line". *Phys. Rev. Lett.*, **116**, 2016. https://link.aps.org/doi/10.1103/PhysRevLett.116.102503.

[3] Q. Deshayes. *Les isotopes d'azote au-delà de la limite de stabilité neutronique: ^{23}N, ^{24}N et ^{25}N.* PhD Thesis, Université de Caen Normandie, 2017. http://www.theses.fr/2017NORMC243.

[4] A. Spyrou, Z. Kohley, *et al.* "First Observation of Ground State Dineutron Decay: ^{16}Be". *Phys. Rev. Lett.*, **108**, 2012. https://link.aps.org/doi/10.1103/PhysRevLett.108.102501.

[5] J. Snyder, T. Baumann, *et al.* "First observation of ^{15}Be". *Phys. Rev. C*, **88**, 2013. https://link.aps.org/doi/10.1103/PhysRevC.88.031303.

[6] T. Sugimoto et al. "The first 2^+ state of ^{14}Be". *Phys. Lett. B*, **654**, 2007. https://linkinghub.elsevier.com/retrieve/pii/S037026930701057X.

[7] S. Leblond. *Structure des isotopes de bore et de carbone riches en neutrons aux limites de la stabilité.* PhD Thesis, Université de Caen Normandie, 2015. https://tel.archives-ouvertes.fr/tel-01289381.

[8] J. Casal. "Private communication".

[9] M. D. Cable, J. Honkanen, *et al.* "Discovery of beta-delayed two-proton radioactivity: ^{22}Al". *Phys. Rev. Lett.*, **50**, 1983. https://link.aps.org/doi/10.1103/PhysRevLett.50.404.

[10] B. Blank and M. Borge. "Nuclear structure at the proton drip line: Advances with nuclear decay studies". *Progress in Particle and Nuclear Physics*, **60**, 2008.
http://www.sciencedirect.com/science/article/pii/S0146641007000956.

[11] I. Dillmann, D. Abriola, *et al.* "Recent activities for β-decay half-lives and β-delayed neutron emission of very neutron-rich isotopes". *AIP Conference Proceedings*, **1594**, 2014.
https://aip.scitation.org/doi/abs/10.1063/1.4874091.

[12] V. Goldansky. "On neutron-deficient isotopes of light nuclei and the phenomena of proton and two-proton radioactivity". *Nuclear Physics*, **19**, 1960.
http://www.sciencedirect.com/science/article/pii/0029558260902583.

[13] M. Pfützner, E. Badura, *et al.* "First evidence for the two-proton decay of ^{45}Fe". *The European Physical Journal A - Hadrons and Nuclei*, **14**, 2002.
https://doi.org/10.1140/epja/i2002-10033-9.

[14] Z. Kohley, T. Baumann, *et al.* "Study of two-neutron radioactivity in the decay of ^{26}O". *Phys. Rev. Lett.*, **110**, 2013.
https://link.aps.org/doi/10.1103/PhysRevLett.110.152501.

[15] L. V. Grigorenko, I. G. Mukha, *et al.* "Lifetime and fragment correlations for the two-neutron decay of ^{26}O ground state". *Phys. Rev. Lett.*, **111**, 2013.
https://link.aps.org/doi/10.1103/PhysRevLett.111.042501.

[16] J. Gibelin. *États résonants de noyaux loin de la stabilité*. Habilitation à diriger des recherches, Université de Caen Normandie, 2018.
https://tel.archives-ouvertes.fr/tel-01729016.

[17] A. Messiah. *Mécanique quantique*, volume 1. Dunod, 1959.

[18] K. McVoy. "Virtual states and resonances". *Nuclear Physics A*, **115**, 1968.
http://www.sciencedirect.com/science/article/pii/0375947468907410.

[19] R. Lednicky and V. L. Lyuboshits. "Final state interaction effect on pairing correlations between particles with small relative momenta". *Sov. J. Nucl. Phys.*, **35**, 1982.
https://www.researchgate.net/publication/236441107_Effect_of_the_final-state_interaction_on_pairing_correlations_of_particles_with_small_relative_momenta.

[20] J. Casal and J. Gómez-Camacho. "Identifying structures in the continuum: Application to ^{16}Be". *Phys. Rev. C*, **99**, 2019.
https://link.aps.org/doi/10.1103/PhysRevC.99.014604.

[21] W. von Oertzen. "Dimers based on the $\alpha + \alpha$ potential and chain states of carbon isotopes". *Zeitschrift für Physik A - Hadrons and Nuclei*, **357**, 1997. https://doi.org/10.1007/s002180050255.

[22] M. Freer, E. Casarejos, *et al.* "α : 2n : α Molecular Band in ^{10}Be". *Phys. Rev. Lett.*, **96**, 2006. https://link.aps.org/doi/10.1103/PhysRevLett.96.042501.

[23] C. Scholl, Y. Fujita, *et al.* "High-resolution study of the ^{9}Be(^{3}He,t)^{9}B reaction up to the ^{9}B triton threshold". *Phys. Rev. C*, **84**, 2011. https://link.aps.org/doi/10.1103/PhysRevC.84.014308.

[24] A. Navin, D. W. Anthony, *et al.* "Direct Evidence for the Breakdown of the N=8 Shell Closure in ^{12}Be". *Phys. Rev. Lett.*, **85**, 2000. https://link.aps.org/doi/10.1103/PhysRevLett.85.266.

[25] F. C. Barker. "T=2 states of the A=12 nuclei". *J. Phys. G: Nucl. Phys.*, **2**, 1976. http://stacks.iop.org/0305-4616/2/i=4/a=001?key=crossref.ebb94a3cc59d01bb6fe7db8f5333eb94.

[26] S. D. Pain, W. N. Catford, *et al.* "Structure of ^{12}Be: Intruder d-Wave Strength at N=8". *Phys. Rev. Lett.*, **96**, 2006. https://link.aps.org/doi/10.1103/PhysRevLett.96.032502.

[27] I. Talmi and I. Unna. "Order of Levels in the Shell Model and Spin of ^{11}Be". *Phys. Rev. Lett.*, **4**, 1960. https://link.aps.org/doi/10.1103/PhysRevLett.4.469.

[28] D. J. Millener, J. W. Olness, *et al.* "Strong E1 transitions in ^{9}Be, ^{11}Be, and ^{13}C". *Phys. Rev. C*, **28**, 1983. https://link.aps.org/doi/10.1103/PhysRevC.28.497.

[29] W. Nörtershäuser, D. Tiedemann, *et al.* "Nuclear Charge Radii of ^{7,9,10}Be and the One-Neutron Halo Nucleus ^{11}Be". *Phys. Rev. Lett.*, **102**, 2009. https://link.aps.org/doi/10.1103/PhysRevLett.102.062503.

[30] E. Liatard, J. F. Bruandet, *et al.* "Matter Distribution in Neutron-Rich Light Nuclei and Total Reaction Cross-Section". *Europhys. Lett.*, **13**, 1990. http://stacks.iop.org/0295-5075/13/i=5/a=004?key=crossref.fb5c6ad9af0cb9ef47e8049c6f9ddc76.

[31] I. Tanihata, T. Kobayashi, *et al.* "Measurement of interaction cross sections using isotope beams of Be and B and isospin dependence of the nuclear radii". *Physics Letters B*, **206**, 1988. http://www.sciencedirect.com/science/article/pii/0370269388907022.

[32] T. Suzuki, R. Kanungo, *et al.* "Nuclear radii of ^{17,19}B and ^{14}Be". *Nuclear Physics A*, **658**, 1999.
http://www.sciencedirect.com/science/article/pii/S0375947499003760.

[33] D. F. Geesaman, R. L. McGrath, *et al.* "Particle decay of ^{6}Be". *Phys. Rev. C*, **15**, 1977.
https://link.aps.org/doi/10.1103/PhysRevC.15.1835.

[34] A. Spyrou, J. K. Smith, *et al.* "Search for the ^{15}Be ground state". *Phys. Rev. C*, **84**, 2011.
https://link.aps.org/doi/10.1103/PhysRevC.84.044309.

[35] F. M. Marqués, N. A. Orr, *et al.* "Comment on "First Observation of Ground State Dineutron Decay: ^{16}Be"". *Phys. Rev. Lett.*, **109**, 2012.
https://link.aps.org/doi/10.1103/PhysRevLett.109.239201.

[36] A. Spyrou, Z. Kohley, *et al.* "Spyrou et al. Replies:". *Phys. Rev. Lett.*, **109**, 2012.
https://link.aps.org/doi/10.1103/PhysRevLett.109.239202.

[37] A. Revel, F. M. Marqués, *et al.* "Strong Neutron Pairing in core + 4n Nuclei". *Phys. Rev. Lett.*, **120**, 2018.
https://link.aps.org/doi/10.1103/PhysRevLett.120.152504.

[38] F. Marqués, M. Labiche, *et al.* "Two-neutron interferometry as a probe of the nuclear halo". *Phys. Lett. B*, **476**, 2000.
http://www.sciencedirect.com/science/article/pii/S0370269300001416.

[39] K. Ieki, D. Sackett, *et al.* "Coulomb dissociation of ^{11}Li". *Phys. Rev. Lett.*, **70**, 1993.
https://link.aps.org/doi/10.1103/PhysRevLett.70.730.

[40] R. W. Brown, B. A. "The Shell-Model Code NuShellX@MSU". *Nuclear Data Sheets*, **120**, 2014.
http://www.sciencedirect.com/science/article/pii/S0090375214004748.

[41] E. K. Warburton *et al.* "Effective interactions for the 0p1s0d nuclear shell-model space". *Phys. Rev. C*, **46**, 1992.
https://link.aps.org/doi/10.1103/PhysRevC.46.923.

[42] V. Maddalena, T. Aumann, *et al.* "Single-neutron knockout reactions: Application to the spectroscopy of ^{16,17,19}C". *Phys. Rev. C*, **63**, 2001.
https://link.aps.org/doi/10.1103/PhysRevC.63.024613.

[43] A. N. Kuchera, A. Spyrou, *et al.* "Search for unbound ^{15}Be states in the $3n$+^{12}Be channel". *Physical Review C*, **91**, 2015.
https://link.aps.org/doi/10.1103/PhysRevC.91.017304.

[44] M. Wang, G. Audi, *et al.* "The AME2016 atomic mass evaluation (II). Tables, graphs and references". *Chinese Physics C*, **41**, 2016.
https://doi.org/10.1088%2F1674-1137%2F41%2F3%2F030003.

[45] T. Nakamura and Y. Kondo. "Neutron halo and breakup reactions". *Lecture Notes in Physics*, **848**:67, 2012.

[46] T. Kubo. "The RIKEN radioactive beam facility". *Nucl. Instrum. Meth. B*, **70**, 1992.
http://www.sciencedirect.com/science/article/pii/0168583X9295947P.

[47] A. Revel. *Nuclear forces at the extremes.* PhD thesis, Université de Caen Normandie, 2018.
https://tel.archives-ouvertes.fr/tel-02082089.

[48] Y. Kubota. *Neutron-neutron correlation in Borromean nucleus ^{11}Li via the (p, pn) reaction.* PhD thesis, University of Tokyo, 2017.

[49] T. Kubo. "In-flight RI beam separator BigRIPS at RIKEN and elsewhere in Japan". *Nucl. Instrum. Meth. B*, **204**, 2003.
http://www.sciencedirect.com/science/article/pii/S0168583X02018967.

[50] H. Okuno, N. Fukunishi, *et al.* "Progress of RIBF accelerators". *Progress of Theoretical and Experimental Physics*, **2012**, 2012.
https://academic.oup.com/ptep/article-lookup/doi/10.1093/ptep/pts046.

[51] T. Kobayashi, N. Chiga, *et al.* "SAMURAI spectrometer for RI beam experiments". *Nucl. Instrum. Meth. B*, **317**, 2013.
https://linkinghub.elsevier.com/retrieve/pii/S0168583X13007118.

[52] A. Obertelli, A. Delbart, *et al.* "MINOS: A vertex tracker coupled to a thick liquid-hydrogen target for in-beam spectroscopy of exotic nuclei". *The European Physical Journal A*, **50**, 2014.
http://link.springer.com/10.1140/epja/i2014-14008-y.

[53] C. Santamaria. *Quest for new nuclear magic numbers with MINOS.* PhD thesis, Université Paris Sud, 2015.
http://www.theses.fr/2015PA112153.

[54] Y. Kondo. "Calibration methods of the neutron detector array NEBULA". *RIKEN Accel. Prog. Rep.*, **45**:131, 2012.
http://www.nishina.riken.jp/researcher/APR/index_e.html.

[55] H. Baba, T. Ichihara, *et al.* "New data acquisition system for the RIKEN radioactive isotope beam factory". *Nucl. Instrum. Meth. A*, **616**, 2010.
http://www.sciencedirect.com/science/article/pii/S0168900210003761.

[56] R. Tanaka. Master's thesis, Tokyo Institute of Technology.

[57] W. R. Leo. *Techniques for nuclear and particle physics experiments: a how-to approach.* Springer, 1994.

[58] S. Agostinelli, J. Allison, *et al.* "Geant4 - a simulation toolkit". *Nucl. Instrum. Meth. A*, **506**, 2003.
http://www.sciencedirect.com/science/article/pii/S0168900203013688.

[59] G. Normand. *Investigation of correlations in light neutron-rich nuclei.* PhD thesis, Université de Caen, 2004.
https://tel.archives-ouvertes.fr/tel-00008393.

[60] Nikolic. *M. Kinematics and Multiparticle System.* Gordon and Breach, 1968.

[61] D. H. Perkins. *Introduction to high energy physics.* Cambridge Univ. Press, 2000.

[62] E. M. Aitala, S. Amato, *et al.* "Experimental Evidence for a Light and Broad Scalar Resonance in $D^+ \to \pi^-\pi^+\pi^+$ Decay". *Phys. Rev. Lett.*, **86**, 2001.
https://link.aps.org/doi/10.1103/PhysRevLett.86.770.

[63] F. M. Marqués, M. Labiche, *et al.* "Three-body correlations in Borromean halo nuclei". *Phys. Rev. C*, **64**, 2001.
https://link.aps.org/doi/10.1103/PhysRevC.64.061301.

[64] Y. Aksyutina, T. Aumann, *et al.* "Study of the ^{14}Be Continuum: Identification and Structure of its Second 2^+ State". *Physical Review Letters*, **111**, 2013.
https://link.aps.org/doi/10.1103/PhysRevLett.111.242501.

[65] S. RAMAN, C. NESTOR, *et al.* "Transition probability from the ground to the first excited 2^+ state of even–even nuclides". *Atomic Data and Nuclear Data Tables*, **78**, 2001.
http://www.sciencedirect.com/science/article/pii/S0092640X01908587.

[66] J. Smith, T. Baumann, *et al.* "Neutron correlations in the decay of the first excited state of ^{11}Li". *Nuclear Physics A*, **955**, 2016.
http://www.sciencedirect.com/science/article/pii/S0375947416301439.

[67] B. Laurent, F. M. Marqués, *et al.* "Chronology of the three-body dissociation of ^{8}He". *J. Phys. G: Nucl. Part. Phys.*, **46**, 2019.
http://stacks.iop.org/0954-3899/46/i=3/a=03LT02?key=crossref.ba1874425840a554ac8c103070491e44.

[68] M. Preston and R. Bhaduri. *Structure of the Nucleus.* Addison-Wesley, Reading, 1975.

[69] B. Gabioud, J.-C. Alder, *et al.* "nn Scattering parameters a_{nn} and r_{nn} from the photon spectrum of the reaction $\pi^- d \to \gamma nn$". *Nuclear Physics A*, **420**, 1984.
http://www.sciencedirect.com/science/article/pii/0375947484906699.

[70] A. Migdal. *Sov. Phys. JETP*, **1**, 1955.

[71] K. M. Watson. "The effect of final state interactions on reaction cross sections". *Phys. Rev.*, **88**, 1952.
https://link.aps.org/doi/10.1103/PhysRev.88.1163.

[72] L. V. Grigorenko, J. S. Vaagen, *et al.* "Exploring the manifestation and nature of a dineutron in two-neutron emission using a dynamical dineutron model". *Phys. Rev. C*, **97**, 2018.
https://link.aps.org/doi/10.1103/PhysRevC.97.034605.

[73] J. Casal. "Two-nucleon emitters within a pseudostate method: The case of ^{6}Be and ^{16}Be". *Physical Review C*, **97**, 2018.
https://link.aps.org/doi/10.1103/PhysRevC.97.034613.

[74] J. Casal *et al. In preparation.*

Résumé

À la limite de stabilité nucléaire, où l'énergie nécessaire pour enlever un nucléon tend vers zéro, l'émission de neutrons est un phénomène caractéristique des noyaux riches en neutrons. La désintégration "deux neutrons" d'un noyau à l'état fondamental est un cas particulier qui peut se produire au-delà de cette limite. La spectroscopie et la désintégration des isotopes les plus riches en neutrons du béryllium ^{14}Be, ^{15}Be et surtout ^{16}Be ont été étudiées lors de différentes campagnes expérimentales au RIBF-RIKEN en utilisant le dispositif SAMURAI couplé au détecteur de neutrons NEBULA. Dans ce dernier cas, la cible MINOS a été ajoutée à la configuration standard.

L'approche expérimentale et un traitement approfondi des événements multi-neutron ont rendu possible une analyse détaillée des corrélations à trois corps fragment+n+n à partir d'états non liés à deux neutrons. Pour la première fois, l'état fondamental et le premier état excité du ^{16}Be ont été observés sans ambiguïté, et les analyses des corrélations montrent clairement une émission directe de paires de neutrons à partir des deux états. Afin d'interpréter les distributions expérimentales, l'émission de paires de neutrons (nn) a été caractérisée à partir d'une approche théorique microscopique. La comparaison directe entre les résultats expérimentaux et les prédictions théoriques a permis de relier le signal expérimental nn que nous observons à la fonction d'onde à trois corps.

Mots clés: Physique nucléaire, Structure nucléaire, Spectroscopie nucléaire, Réactions directes, Isotopes radioactifs, Corrélations de particules, Décroissances à trois corps, Analyse de données, Simulation par ordinateur.

Abstract

Near the dripline, where the energy needed to remove one nucleon is low enough or even negative, neutron emission from neutron-rich nuclei is a characteristic phenomenon. Ground state two-neutron decays are a special case that may occur once we go beyond the dripline. The spectroscopy and neutron decay of the most neutron-rich isotopes of Beryllium ^{14}Be, ^{15}Be and especially ^{16}Be have been investigated during different experimental campaigns at RIBF-RIKEN using the SAMURAI setup and the NEBULA neutron array. For the latter, the state-of-the-art MINOS target was added to the standard setup.

The experimental approach and a thorough treatment of multi-neutron events have made possible an extensive analysis on the three-body correlations in fragment+n+n decays from two-neutron unbound states. For the first time, the ground state and first excited state of ^{16}Be have been unambiguously observed, and the correlation analyses show a clear direct neutron-pair emission from both states. In order to interpret the experimental distributions, the neutron-pair emission (nn) has been characterized from microscopic principles. A joint effort between experiment and theory has allowed a direct comparison to connect the experimental nn signal we observe with the three-body wave-function.

Keywords: Nuclear physics, Nuclear structure, Nuclear spectroscopy, Direct reactions, Radioactive isotopes, Particle correlations, Three-body decays, Data Analysis, Computer simulations.